DESIGN ISSUES FOR GRID-CONNECTED PHOTOVOLTAIC SYSTEMS

**A Ph.D. Thesis
Presented to**

The Academic Faculty

by

Michael Eugene Ropp

in partial fulfillment of the requirements of the degree of

Doctor of Philosophy in Electrical Engineering

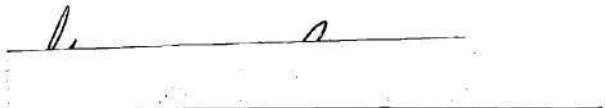## October 12, 1998

Advisors:

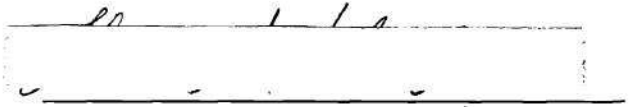**Dr. Ajeet Rohatgi**

Dr. Miroslav Begovic

DESIGN ISSUES FOR GRID-CONNECTED PHOTOVOLTAIC SYSTEMS

APPROVED:

Dr. Ajeet Rohatgi, Chairman

Dr. Miroslav Begovic, Co-chairman

Dr. Richard Bass

Dr. Tom Habetler

Dr. Samuel Shelton

Date approved by chairmen: 11 | 10 | 98

ii

DEDICATION

I dedicate this thesis with love and affection to my wife, Susan, for all of her support, and also to everyone who sees the wisdom of sustainability.

ACKNOWLEDGMENTS

TABLE OF CONTENTS

LIST OF TABLES

LIST OF FIGURES

NOMENCLATURE

List of symbols

$\alpha_{sun,k}$	solar azimuth angle at time t_k
α_{array}	azimuth angle of PV array
β	array tilt angle up from horizontal
$\Delta\omega$	deviation of the frequency of the node **a** voltage away from the nominal utility line voltage (rad/sec)
ΔP	real power flowing from utility into potential island (W)
ΔP^-	ΔP immediately before opening of the switch to form an island (W)
ΔQ	reactive power flowing from utility into potential island (VAR)
ΔQ^-	ΔQ immediately before opening of the switch to form an island (VAR)
ϕ	phase angle of an RLC load = $\tan^{-1}[R(\omega_0 C - (\omega_0 L)^{-1})]$
ϕ_{th}	dpf threshold for PJD method
$\eta_{PV,k}$	PV system DC efficiency at time t_k
η_{rated}	rated efficiency of PV modules
η_{dust}	1 - fractional power loss resulting from dust/soiling of PV array
$\eta_{mismatch}$	1 - fractional power loss resulting from module parameter variation
η_{DCloss}	1 - fractional power loss resulting from I^2R losses in the DC system
η_{MPPT}	1 - fractional power loss resulting from MPPT error/imperfection
η_T	thermal efficiency derating term
ρ	albedo (reflectance) of the ground
ω	frequency of υ_a (rad/sec)
ω_0	nominal utility frequency (rad/sec)
ω_m	mechanical (rotational) speed of an induction machine (rad/sec)
ω_{res}	resonant frequency
ω_s	synchronous speed of an induction machine
A_{array}	PV array effective area (m^2)
C	load capacitance (F)
CI	clearness index
$\hat{d}_k$	unit vector antiparallel to the direct irradiance (normal to the surface that is normal to the direct irradiance) at time t_k
E_{curv}	energy produced by a curved PV array (Wh)
E_{pl}	energy produced by a planar PV array (Wh)
F	positive feedback function used in the AFDPF method; also brightness coefficients for Perez diffuse irradiance model
FF	fill factor of a solar module
$G_{d,H,k}$	diffuse horizontal irradiance at time step t_k (W/m^2)
$G_{d,poa,k}$	diffuse plane of array irradiance at time t_k (W/m^2)
$G_{D,poa,k}$	direct plane of array irradiance at time t_k (W/m^2)
$G_{D\perp,k}$	direct normal irradiance at time t_k (W/m^2)
$G_{mismatch,k}$	difference between north and south-side irradiances on the GTAC PV

	array (W/m^2)
$G_{North,k}$	total plane of array irradiance in the plane of the average tilt of the north side of the GTAC PV array at time t_k (W/m^2)
$G_{poa,k}$	total plane of array irradiance at time t_k (W/m^2)
$G_{refl,poa,k}$	ground-reflected component of plane-of-array irradiance at time step t_k (W/m^2)
$G_{South,k}$	total plane of array irradiance in the plane of the average tilt of the south side of the GTAC PV array at time t_k (W/m^2)
$G_{T,H,k}$	total (global) horizontal irradiance at time step t_k (W/m^2)
H	terrestrial total average daily radiant energy flux ($kWh/m^2/day$)
H_0	extraterrestrial total average daily radiant energy flux ($kWh/m^2/day$)
i_{load}	instantaneous load current (A)
I_{load}	RMS value of i_{load} (A)
$\vec{I}_{load}$	phasor load current (A)
i_{PV}	instantaneous PV system output current (A)
I_{SC}	solar module short-circuit current (A)
K_{curv}	time-averaged curvature derating factor
$K_{curv,k}$	curvature derating factor at time t_k
K_T	PV module thermal derating coefficient (%/°C)
L	load inductance (H)
$\hat{n}$	unit vector normal to the PV array surface
P_{in}	input power (irradiance) to a solar module (W or W/m^2)
$P_{k,curv}$	power production of a curved PV array at time t_k (W)
$P_{k,pl}$	power produced by a planar PV array at time t_k (W)
P_{load}	real power consumption of the load (W)
P_{PV}	real power production of the PV system (W)
Q_{load}	reactive power consumption of the load (VAR)
Q_{PV}	reactive power production of the PV system (VAR)
R	load resistance (Ω)
S	slip in an induction machine
$T_{cell,k}$	solar cell temperature at time t_k
T_{lpv}	period of the sinusoidal portion of the AFD waveform (sec)
t_k	time at which sample number k is taken; also the interval between t_k's (sec)
T_{STC}	Standard Test Condition temperature (25°C)
T_{Vutil}	period of the utility voltage waveform (sec)
t_z	zero time in the AFD waveform per half-cycle (sec)
v_a	instantaneous voltage at PV system terminals or at node **a** (V)
V_a	RMS value of v_a (V)
$\vec{V}_a$	phasor voltage at node **a** (V)
$V_{a,high}$	upper threshold of the magnitude of v_a at which the overvoltage relay will trip (V)
$V_{a,low}$	lower threshold of the magnitude of v_a at which the undervoltage relay will trip (V)
V_{OC}	open-circuit voltage of a solar module (V)
Z_{load}	impedance of the RLC load (Ω)

List of abbreviations

AFD   active frequency drift method of islanding prevention

AFDPF   active frequency drift method of islanding prevention with positive feedback

cf   "chopping fraction"; the fraction of zero time in the AFD waveform per half-cycle

dpf   displacement power factor; the phase-angle power factor of the load, excluding the effects of nonlinearity

GTAC   Georgia Tech Aquatic Center

NDZ   nondetection zone

OFR   overfrequency relay that disconnects the PV system from the utility if the frequency of v_a exceeds a threshold value

OVR   overvoltage relay that disconnects the PV system from the utility if the RMS value of v_a exceeds a threshold value

PCU   power conditioning unit; power electronic converter that provides system control, regulation and waveshaping functions

PFCC   power factor correction capacitor

PJD   phase-jump detection method of islanding prevention

PLL   phase-locked loop

POCC   point of common coupling; the point at which a PV system is connected to a utility system and load (usually the electric meter)

PV   photovoltaic(s)

SMS   slide-mode frequency shift method of islanding prevention

UFR   underfrequency relay that disconnects the PV system from the utility if the frequency of v_a drops below a threshold value

UVR   undervoltage relay that disconnects the PV system from the utility if the RMS value of v_a drops below a threshold value

SUMMARY

Photovoltaics (PV) is the direct conversion of sunlight to electrical energy. In areas without centralized utility grids, the benefits of PV are such that they easily overshadow the present shortcomings of the technology. However, in locations in which a centralized utility system is in place, significant technical challenges remain before utility-interactive PV (UIPV) systems can be fully integrated as an important part of the mix of electricity sources.

One of these challenges lies in the area of modeling PV systems which are integrated into buildings, because the needed computer design tools for optimal and accurate design of PV systems with curved PV arrays are not available, and even those tools that are available do not facilitate monitoring and maintenance of the system once it is built.

A second significant technical challenge to UIPV systems arises from the issue of islanding. Islanding occurs when a UIPV system continues to energize a section of a utility system after that section has been isolated from the utility voltage source. Islanding is potentially dangerous to both personnel and equipment, and therefore it is important that it be prevented. Unfortunately, islanding is a particularly difficult problem to solve fully, and no existing techniques for preventing it have gained the approval of equipment manufacturers, utilities, and standards-writing bodies.

The work contained within this thesis targets both of these technical challenges. In the work under Task 1, a method for modeling a PV system with a curved PV array using only existing, proven computer software packages is developed. This methodology allows accurate modeling of BIPV systems on curved roof structures and also facilitates comparison of measured and modeled data for use in system maintenance and

monitoring. These goals are accomplished by introducing a "curvature derating factor", a coefficient that adjusts the PV system's efficiency to account for the effect of the PV array curvature. This procedure is applied to the Georgia Tech Aquatic Center (GTAC) PV system, a large roof-mounted PV system with a curved PV array, and it is shown that the goals of reasonably accurate modeling of curved PV arrays combined with preservation of diagnostic capabilities are achieved through the use of the curvature derating factor. Also within this task, the use of computer modeling in the design, optimization, and monitoring of such a large system is described and applied. The performance penalty incurred by the non-optimal orientation of the PV array is quantified using two different optimization criteria, and the choice of PCU for the GTAC system is justified on the basis of overall system efficiency. Also, modeling is used to show that the DC voltage of the PV system will not exceed allowable limits under realistic conditions for Atlanta.

In the work contained under Task 2, the difficult problem of islanding is considered. First, the existing state-of-the-art in islanding prevention is thoroughly reviewed. Then, in Subtask 2.1, an analysis is performed which suggests that standard protective relays used on all UIPV systems are in fact insufficient to guarantee protection against islanding. In Subtask 2.2, several existing islanding prevention methods are compared in a novel way by mapping into a load space the ranges of RLC loads for which the various methods fail. The superiority of this type of mapping over those used previously is demonstrated. These mappings allow quantitative comparison of the methods. A new islanding prevention method that had not previously been studied is the subject under Subtask 2.3. This method is thoroughly characterized, and it is shown that in fact it does not compare favorably with other existing techniques. However, in Subtask 2.4, a novel method for dramatically improving this new islanding prevention method is described. It is shown, both by computer modeling and

experiment, that this new method is one of the most effective available today, if not *the* most effective. Finally, under Subtask 2.5, the effects of certain types of loads on the effectiveness of islanding prevention methods are discussed. It is shown that nonlinear and constant-power loads should not significantly affect the performance of islanding prevention techniques, but the effects of motor loads are still uncertain and may be very significant.

CHAPTER I

INTRODUCTION

Photovoltaics (PV) is the direct conversion of sunlight into electricity using a semiconductor device called a solar cell. It is a technology that has long captured the fancy of both scientists and the public alike because it has the potential to simultaneously solve energy and environmental problems. Its input energy source, sunlight, is free, essentially unlimited, and nonpolluting, and is available over the vast majority of the earth's surface in quantities sufficient to be useful. The conversion process itself is both nonpolluting and noiseless, and the converters, the photovoltaic cells, can have useful lifetimes in excess of 25-30 years.

During the energy crisis of the 1970s, interest in renewable generation technologies such as PV increased rapidly. At that time, the primary drivers behind this interest were the rising cost of oil and the fear that oil supplies were limited. The free and unlimited aspects of sunlight brought the attention to PV. However, today the world is awash in inexpensive oil, prices have plummeted, and new supplies are being found continuously. Because other forms of energy remain so inexpensive, PV is cost-competitive today only in remote areas without utility access or for very small loads, in spite of nearly a factor of fifty reduction in the cost of PV in the last two decades.

However, a new set of concerns has arisen: pollution and the effects of human activities on the environment and climate. It has long been known that the burning of fossil fuels releases compounds such as carbon dioxide (CO_2), nitrous oxides (NO_x) and sulfur oxides (SO_x) into the atmosphere, but it has only recently begun to become clear

that these compounds can have harmful effects on climate, property, and human health. NO_X and SO_X are the compounds that cause rain to become acidic, and CO_2 is the most common of the so-called "greenhouse gases", which are mostly transparent to visible wavelengths of light but which strongly absorb or reflect longer wavelengths. The generation of electricity from fossil fuels is a major source of these pollutants. Reducing the emissions of these compounds is becoming a new driver for PV development.

It has been shown [1,2] that the use of photovoltaics can significantly reduce the emissions of these harmful compounds into the atmosphere. In particular, each GWh of electrical energy produced by PV instead of by burning coal reduces the amount of CO_2 released into the atmosphere by 1000 tons. This fact, coupled with the concern over the environmental effects of these compounds, is now being reflected in the actions of the public and also those of state and national legislatures in the U.S. and around the world. For example, Japan, a country long concerned with natural resources, has recently completed its Sunshine Project and initiated the New Sunshine Project. Both of these projects have among their goals the development and promotion of utility-interactive photovoltaic (UIPV) systems [3]. Similarly, in Germany the Thousand Roofs Project has led to the installation of nearly 5 MW of distributed roof-mounted UIPV systems throughout that country since 1991 [4], and the recently announced Million Roofs Project in the United States calls for the installation of one million distributed UIPV systems on public and private buildings in this country by the year 2010 [5]. These are merely three of several examples of such programs worldwide. UIPV, it would seem, is a technology that is definitely on the increase in terms of deployment, and this trend shows no signs of slowing in the near future.

An important part of this trend is the integration of UIPV systems into buildings. PV modules can actually be used as part of the exterior surface of a building, or as

2

roofing in overhangs, various types of shelters, or walkway or parking lot shades. Such systems are called building-integrated PV (BIPV) systems. BIPV systems are important because if the PV modules can replace building materials in addition to providing electricity, and if the building can provide the support structure for the PV modules, a great deal of redundancy in terms of materials and installation is avoided, reducing the effective cost of PV.

However, there are concerns about the rapid deployment of multiple small UIPV systems, particularly among the utility companies themselves. The utilities must decide what is a fair price for PV-produced electricity. To do this, they must determine the value of this electricity. A critical component in making this valuation is the ability to accurately predict the power and energy output of a PV system in a given location. This requires accurate PV system performance models. Many such models exist, but unfortunately they generally do not work for BIPV systems in which the PV array is not planar (that is, if the array is curved or has multiple "facets"). Of course, another significant benefit of accurate computer models is that more optimized systems can be designed, which improves system economics without sacrificing system reliability and performance.

Another concern, perhaps one of greater significance, is the potential of UIPV systems to island. Islanding is a condition that occurs when a UIPV system continues to energize a section of the utility system after that section has been isolated from the utility voltage source. Islanding is undesirable for several reasons. First, it can pose a serious safety hazard to utility personnel who may be unaware that the isolated section of the utility is being energized by a nonutility generator (NUG). Second, while the system is isolated, a phase difference between the utility voltage and the voltage in the isolated system can arise, and if the utility were to attempt to reconnect to the isolated system, the resulting large overcurrents could damage the UIPV system or the customer

3

load within the isolated section. Islanding could potentially interfere with the operation of other utility equipment as well. Clearly, another critical challenge for UIPV is that the problem of islanding be solved. Under most circumstances, standard protective relays included in PV systems will prevent islanding. In fact, PV system manufacturers have long argued that the likelihood of failure of these relays is so low that no additional islanding protection is needed. However, utilities generally do not accept this. Currently, there is little solid evidence to support this claim.

To address this concern and make UIPV systems acceptable to utilities, manufacturers of PV system power conditioning units (PCUs) have devised many methods to prevent islanding. One method proposed recently is called the active frequency drift (AFD) method. This method is thought to have a great deal of promise, but very little quantitative research has been done on it to demonstrate its potential and/or shortcomings.

In response to the problems outlined above, the research described within this dissertation was conducted. The research was subdivided into two primary tasks: 1) Modeling and Optimization of PV Systems and 2) Islanding Prevention for Grid-Connected PV systems. Under Task 1, the work is divided into two subtasks: 1.1) development of a method for modeling curved PV arrays using existing software; 1.2) performance prediction and optimization of the Georgia Tech Aquatic Center (GTAC) PV array. Under Task 2, the proposed research is divided into five subtasks: 2.1) determination of the probability of the conditions that could lead to failure of the four standard protective relays; 2.2) comparison of existing islanding prevention methods on the basis of NDZ location; 2.3) analysis and characterization of the AFD method and its nondetection zone (NDZ); 2.4) development of a novel and improved AFD method based on positive feedback (AFDPF); and 2.5) impact of different (non-RLC) loads on the size of NDZ of AFD and AFDPF.

CHAPTER II

TASK #1--MODELING OF PV SYSTEMS

History, literature review, and motivation

The ability to accurately predict the performance of a PV system is important for a variety of reasons, particularly the ability to produce optimized designs. If accurate predictions are not available, then the only method available to the designer for increasing the PV system availability, reliability, and safety is to overdesign the system when sizing cables, fuses, PCUs, and PV arrays. Overdesigning leads to an excessively complex and expensive system. In the case of UIPV, accurate performance predictions also are required to enable the utility company to accurately determine the value of the PV-produced electricity. This value is a complex function of how much energy can be delivered by the PV system, when the energy will be delivered, and how likely a given system is to meet performance predictions. Accurate performance predictions are clearly important to the economic viability of UIPV systems.

Fortunately, much work has already been done in this area, and many computer software packages are available that give results of varying levels of accuracy. Unfortunately, all of the currently available models assume that the entire PV array has the same tilt and azimuth angles. For BIPV systems that are fitted to nonplanar roofs or to faceted structures, this will not be the case. There is no currently available modeling package that can accurately predict the performance of PV systems with nonplanar arrays. In addition, even if such a program were available, the computational intensity of the problem would necessitate very long calculation times,

limiting the utility of the program. Finally, even if such a program were available, it would not allow diagnostic comparisons of measured PV system output against the expected output calculated using models and measured meteorological conditions. These shortcomings will be addressed in more detail in the section entitled "The Problem: Variable-Tilt PV Arrays" beginning on Page 17.

These PV system modeling difficulties provided the motivation for the research contained within Task 1. First, those aspects of PV system modeling that are pertinent to the problem of modeling curved PV arrays will be introduced, and the ways in which some of the existing models are implemented in the existing software packages are described. This material is used as the foundation for the following section, in which an existing computer program is adapted for modeling the GTAC PV system, a BIPV system that has a non-planar PV array.

The general structure of a PV system modeling program

In the design, analysis, and performance assessment of PV systems, the following equation is used to describe a system's DC efficiency at a time step k:

$$\eta_{PV,k} = \eta_{rated}\eta_{dust}\eta_{mismatch}\eta_{DCloss}\eta_{MPPT}\eta_T \qquad (1)$$

where η_{rated} is the rated efficiency of the PV modules under standard test conditions (STC), η_{dust} is (1 - the fractional power loss resulting from dust and debris on the PV array), $\eta_{mismatch}$ is (1- the fractional power loss resulting from module parameter mismatch), η_{DCloss} represents (1 - the DC-side I^2R, diode and other losses), η_{MPPT} is (1 - the power loss resulting from DC current ripple and "algorithm error" caused by the switching converter that performs the maximum power point tracking function), and

$$\eta_T = 1 + K_T[T_{cell,k} - T_{STC}]\tag{2}$$

where $T_{cell.k}$ is the module temperature at time step k, T_{STC} is the STC temperature (25°C), and K_T is the modules' thermal derating coefficient in %/°C and is negative.

The factor $\eta_{PV,k}$ can then be used to predict the power output of a planar PV array at time step k:

$$P_{k,pl} = \eta_{PV,k} G_{poa,k} A_{array}\tag{3}$$

or energy output over n time steps of length t_k:

$$E_{pl} = \sum_{k=1}^{n} \eta_{PV,k} G_{poa,k} A_{array} t_k\tag{4}$$

where $G_{poa,k}$ is the plane of array (POA) irradiance in W/m² at time step k and A_{array} is the area in m² of the PV array.

However, in using a single irradiance value, Equations (3) and (4) assume that the entire PV array has the same tilt and azimuth angles, as indicated by the "pl" (planar) subscript on E and P. To understand why this is so, the following section describes how $G_{poa,k}$ is calculated.

Translation of irradiance components into the plane of the array

The *total* or *global solar irradiance* on a plane, expressed in W/m², is comprised of three components: the *direct irradiance*, which comes straight from the solar disk; the *diffuse irradiance*, which strikes the plane after having been scattered by various

atmospheric effects; and the *ground-reflected irradiance*. In meteorological databases or from charts, the most commonly available irradiance data are the total irradiance on a horizontal surface, called the *global horizontal irradiance,* and the *direct normal irradiance,* which is the power per unit area coming directly from the solar disk and striking a surface normal to the irradiation [6,7]. Since the array is usually neither horizontal nor always normal to the direct irradiance (we are assuming the array not to have tracking capability), models for translation of the normal and horizontal irradiance data into the plane of the array and for determining the ground-reflected component are needed. Methods for dealing with each of these components are described in the following sections.

Direct irradiance

The translation of direct irradiance from that incident on a normal surface to that incident on the plane of the array is straightforward and determined mostly by geometric factors. Referring to the geometry in Figure 1, the direct irradiance on a tilted plane is

$$
G_{D,POA,k} = \begin{cases} G_{D\perp,k}\cos\theta_k, & \left[-90^\circ + \alpha_{array}\right] \le \alpha_{sun,k} \le \left[90^\circ + \alpha_{array}\right] \\ 0, & \alpha_{array} \le \left[-90^\circ + \alpha_{array}\right] \text{ or } \alpha_{array} \ge \left[90^\circ + \alpha_{array}\right] \end{cases} \tag{5}
$$

where $G_{D,POA,k}$ is the direct plane of array (POA) irradiance, $G_{D\perp,k}$ is the direct normal irradiance, θ_k is the angle of incidence of the direct radiation on the tilted plane, and $\alpha_{sun,k}$ and α_{array} are the azimuth angles of the sun and the PV array respectively, with due South = 0° and positive angles measured west of south. The subscript k denotes that the value is taken at time t_k. θ_k can be readily determined for any time of day and day of the year using a vector construction and the quantities defined in Figure 1:

8

$$\hat{d}_k \cdot \hat{n} = \left| \hat{d}_k \right| \left| \hat{n} \right| \cos\theta_k$$
$$\Downarrow \qquad\qquad\qquad (6)$$
$$\theta_k = \cos^{-1}\left[\cos(\zeta_k)\cos(\beta) + \cos(\alpha_{sun,k})\cos(\alpha_{array}) + \sin(\alpha_{sun,k})\sin(\alpha_{array}) \right]$$

where $\hat{d}_k$ and $\hat{n}$ are unit vectors antiparallel to the direct irradiance and normal to the array, respectively, ζ_k is the solar zenith angle at time t_k, and β is the array tilt angle. The angles ζ_k and $\alpha_{sun,k}$ can be readily determined using well-known solar geometry equations [8]. Many textbooks give a different form of Equation (5) that ignores the azimuthal effects [9]. This can lead to significant errors early and late in the day and if α_{array} is not zero. Note that the stipulation that $G_{D,POA,k} = 0$ for $\alpha_{sun,k} - \alpha_{array} > 90°$ is important; this corresponds to a situation in which the solar disk is actually behind the array, so no direct radiation reaches the active portion of the PV modules. Equations (5) and (6), coupled with accurate values for $G_{D\perp,k}$, allows for modeling of the direct component on the array with essentially zero error [10].

Diffuse irradiance

Modeling the diffuse radiation on a tilted surface is considerably more involved. POA diffuse irradiance models, often called sky dome models or simply sky models, can be divided into two categories, isotropic and nonisotropic. Isotropic models consider the entire sky to be of uniform brightness. This leads to simple, easy-to-use models. The

9
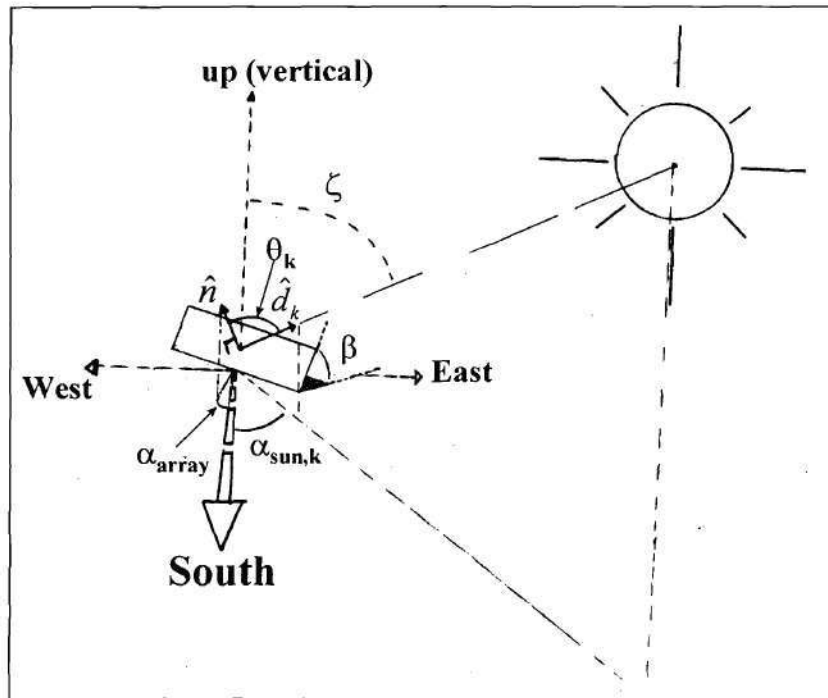
Figure 1. **Diagram defining direct irradiance angles and geometry used in Equations (5) and (6).**

simplest, in fact, merely considers the diffuse irradiation to be some fraction of the direct radiation and independent of the array tilt [9]. A more realistic isotropic sky model that accounts for the array tilt and is frequently used was developed by Liu and Jordan [8]:

$$G_{d,POA,k} = \frac{1}{2} G_{d,H,k} [1 + \cos(\beta)]$$

(7)

where $G_{d,POA,k}$ is the POA diffuse irradiance and $G_{d,H,k}$ is the horizontal diffuse

irradiance, both at time t_k.

Anisotropic models divide the sky hemisphere into regions of different brightness. One common model is the "three-region model" shown in Figure 2, in which the sky is divided into the near-horizon band, the circumsolar region, and the "sky dome". Anisotropic models give more accurate estimates of the POA diffuse component.

One of the most widely used and tested of the anisotropic models was developed by Perez et al. in 1983. This model uses the three-region sky model and is given by [10]:

$$G_{d,POA,k} = G_{d,H,k}\left[\frac{0.5(1 + \cos(\beta)) + a(F_1 - 1) + b(F_2 - 1)}{1 + c(F_1 - 1) + d(F_2 - 1)}\right] \qquad (8)$$

where a and b are solid angles subtended by the circumsolar and near-horizon regions weighted by their average incidences on the tilted array, c and d are the same as a and b except referenced to the horizontal, and F_1 and F_2 are empirically-determined brightness coefficients for the circumsolar and near-horizon regions respectively. Expressions for a, b, c, and d are given in [10]. In practice, values for F_1 and F_2 are selected from a table, the selection being based on the values of the solar zenith angle z_k, $G_{d,H,k}$, and the quantity $(G_{d,H,k} + G_{D\perp,k})/G_{d,H,k}$, thus accounting for solar position and cloudiness. Four years later, a simplified version of the Perez model was presented. After rewriting Equation (8) in terms of "reduced brightness coefficients" [10] that represent the percentage contributions of the circumsolar and near-horizon regions to $G_{d,H,k}$, and making some approximations, Equation (9) is derived:

$$G_{d,POA,k} \approx G_{d,H,k}\left[0.5(1 + 0.5\cos(z_k))(1 - F_3) + F_3\left(\frac{a}{c}\right) + F_4\sin(z_k)\right] \qquad (9)$$

11
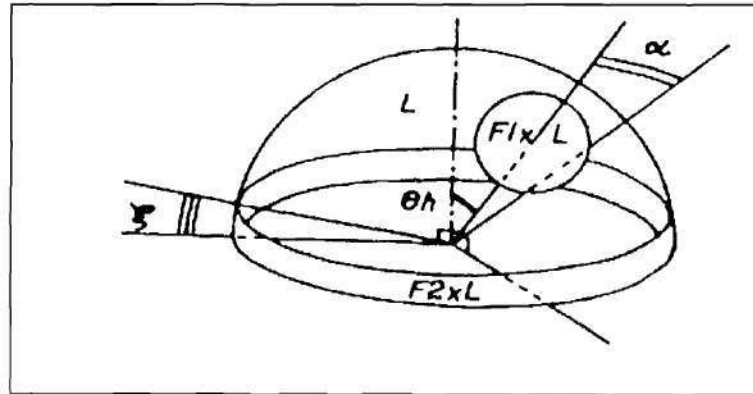
Figure 2. **Diagram showing the three sky regions (near-horizon band, circumsolar region, and the "sky dome") for the diffuse irradiance models [10].**

where F_3 and F_4 are the reduced brightness coefficients.

Tests of the original and simplified Perez models and the isotropic (Liu and Jordan) model [10] using measured data from one location showed that the original Perez model outperformed the other models for all of the orientations tested (vertical orientation facing north, south, east, and west, and also south-facing at a 45° tilt). The simplified Perez model gave only slightly less accurate results than the original, adding less than 1% error. The worst performance was given by the isotropic model, which consistently underpredicted the diffuse component and had 183% more error than the original Perez model. Similar tests for other locations [8] yielded similar results, with the Perez model outperforming all others under most conditions, including two-axis tracking, and the isotropic (Liu and Jordan) model consistently underestimating the diffuse component and giving the least accurate results.

Ground-reflected irradiance

Accurate assessment of the ground-reflected component of the POA irradiance is somewhat challenging. Many simulation programs do not account for this component at all, but this can lead to large errors in situations where the array tilt angle and the reflectance of the surrounding ground are both high [11]. A better method would be to consider the ground surrounding the array as a diffuse or isotropic reflector; that is, the intensity of the reflected radiation is independent of direction. Making this assumption, we can then specify the *albedo*, or *reflectance*, of the ground in a single time-independent parameter, the reflectance ρ [8,12]:

$$G_{refl,POA,k} = \frac{1}{2} G_{T,H,k} \, \rho (1 - \cos(\beta)) \qquad (10)$$

where $G_{refl,POA,k}$ is the irradiance reflected from the ground onto the tilted array and $G_{T,H,k}$ is the total horizontal irradiance, both at time t_k. $G_{refl,POA,k}$ is zero for a horizontal surface, because a horizontal surface does not "see" the surrounding ground at all, and increases to a maximum of $(0.5\rho G_{T,H,k})$. The factor of 0.5 can be understood by realizing that the array has a hemispherical field of view. As the array is tilted up from the horizontal, half of its surroundings are immediately excluded from this field because they fall behind the array.

Review of existing PV system modeling software packages

Many software packages have been developed for modeling of PV systems. Most of these use the previously-described irradiance models or variants of them, along with

other models for calculating such things as the solar cell temperature and the behavior of other system components. Two such packages, which have been extensively tested and shown to predict PV system performance reasonably well, are PVFORM, written by James Fernandez and David Menicucci of Sandia National Laboratories in the mid-80s, and PVGRID, a program written more recently by Howard Wenger of the Pacific Energy Group in California. In this research, two other programs that model PV arrays electrically were used. These do not utilize any irradiance models, but rather simulate the PV array as an electrical circuit given the POA irradiance, cell temperature, and other parameters. These two programs are PVSIM, created by David King at Sandia National Laboratories, which is a full PV array electrical model, and IVCURVE, written by Photovoltaic Resources International, which is a more approximate but much faster electrical model.

PVFORM

PVFORM is intended to be a rigorous, accurate, complete simulator for grid-connected and stand-alone PV systems. It accepts TMY-format meteorological input data, and it uses the Perez model for the POA diffuse irradiance and the most accurate available cell temperature model. PVFORM also includes a PCU model which accounts for the variation of PCU efficiency with PV power production. Because of its strong theoretical foundations, as well as a substantial amount of field corroboration [13,14], it is generally the PV system simulator of choice for academic work [15,16,17]. PVFORM also allows the user to extract many non-system parameters, such as modeled POA irradiance, modeled cell temperature, and several of the meteorological inputs as a function of time at hourly resolution. Finally, since the FORTRAN source code of the program is supplied, it is possible to customize PVFORM for specific installations. However, it has no electrical modeling capability and assumes a planar PV array. Such capability could be added to PVFORM by integrating it with a model such as that

14

presented by Bishop [18], but as we will shortly see the computation time involved in simulating an array like the one on the Aquatic Center would be extreme.

PVGRID

PVGRID is a more recent addition to the PV systems modeling arsenal, but it has undergone rigorous testing by the Pacific Energy Group and several California utilities, including SMUD and PG&E. PVGRID accepts TMY2 data as its meteorological inputs. It uses the Perez diffuse irradiance model, and its cell temperature model is similar to the Fuentes model in that it is based on an energy balance on a PV module. It differs from the Fuentes model in its handling of the convective heat transfer, but experiments have shown the two models both to very closely predict the operating temperatures of rack-mounted systems. PVGRID also allows I-V curve modeling of modules, but it treats them all as identical and does not allow for more than one orientation. The DC-AC conversion model in PVGRID allows the user to enter up to eight points on the PCU's efficiency vs. fractional loading curve. Alternatively, the user can enter a constant efficiency and bypass the curve. PVGRID has several other capabilities, including the abilities to optimize of the operating voltage of a fixed-voltage (non-MPPT) PCU and to perform a shading analysis for ground-mounted arrays. The shading analysis allows the user to determine the correct spacing between modules such that they do not shadow each other when the sun is low in the sky.

PVSIM

PVSIM calculates an array I-V curve including the effects of blocking and bypass diodes. It calculates individual I-V curves for each solar cell in the array using an equivalent circuit for the solar cell [ref] and combines these in series and parallel to obtain the PV array I-V curve. PVSIM is useful in determining potential hot spots in a PV array, verification of the bypass diode configuration, and examination of an array I-V

curve. However, as was previously mentioned, this program does not accept meteorological data and does no calculations of POA irradiance or cell temperature, and it only accepts single values for these parameters and therefore still cannot model a curved PV array. In addition, we have alluded several times to the fact that, for a large system, a program that electrically models the entire system can take a very long time to run. As an example, we note that to simulate the entire GTAC PV array using PVSIM on a 166-MHz Pentium PC takes slightly over four hours. This clearly limits the use of such a program as a design tool, unless significantly more efficient calculation algorithms or greater simplification can be achieved.

IVCURVE

IVCURVE is a PV array I-V curve estimation program. Given either the type of modules (selected from a module database) or the module parameters, the array configuration, the POA irradiance, and either the cell or ambient air temperature, IVCURVE estimates the I-V curve of the entire array. Also, if given an operating voltage, IVCURVE calculates the power produced by the array at that voltage. This program has much shorter execution times than does PVSIM because it does not contain the level of detail that PVSIM does; it does not account for blocking or bypass diodes, uses a simplified equation for computing the I-V curve (neglects series resistance), and uses simpler interconnection models. IVCURVE does not have the capability of calculating the POA irradiance or cell temperature from meteorological data and is therefore not a PV system design or analysis program.

The problem: variable-tilt PV arrays

All of the above-described models for determining the POA irradiance from available data show a dependence on the array tilt angle, and the most important component (the direct irradiance) also depends on the array's azimuth angle. These angles will be known for a given system, but they may not have single values. BIPV systems may be mounted onto existing roof structures, which may be curved or have multiple facets and therefore could have multiple azimuth and tilt angles. In this case, the irradiance on the array at any given time will be nonuniform, and each section of the array at a different tilt or azimuth will produce a different amount of DC power. Equations (3) and (4) cannot be used simply because there is no single value for G_{poa}.

There is another effect that must also be considered. PV modules have a distinctive current-voltage characteristic that is dependent upon the irradiance. Examples of this characteristic for a PV module under four different irradiance levels are shown in Figure 3. The PV module's output current is strongly dependent on the irradiance, but the module voltage shows a much weaker dependence on irradiance.

Consider the case of two series-connected modules under different irradiances. Since they are connected in series, they must operate with the same current. This means that the module under lower irradiance will limit the current of the module under higher irradiance to a much lower value than it could otherwise produce. Similarly, if two PV modules connected in parallel (and thus having the same voltage) are under different irradiances, the module under lower irradiance will cause the more brightly lit module to be unable to produce its full voltage, but since the voltage dependence on irradiance is much weaker, this effect will not be as strong as the current reduction in series-connected modules under differing irradiance. In short, interconnected PV modules under different irradiances will interact electrically, making their operating points interdependent.
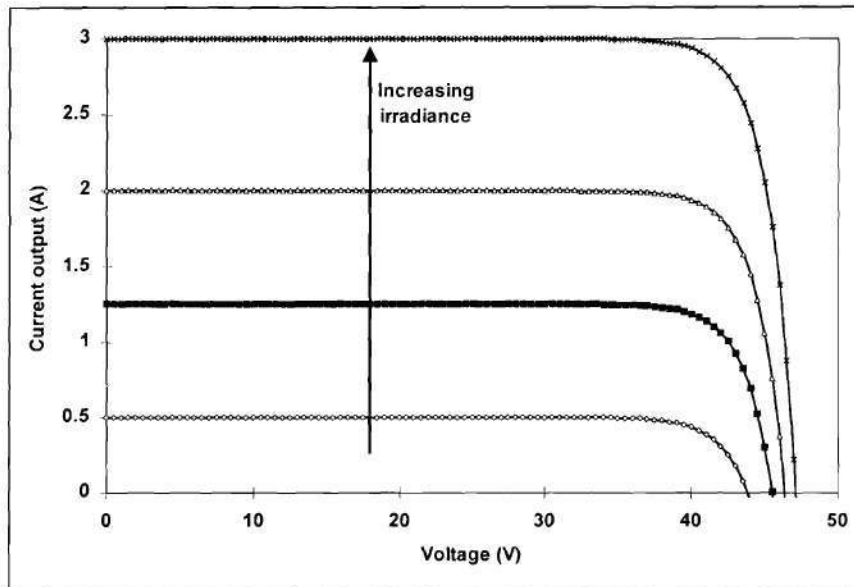
Figure 3. Solar module I-V curves, neglecting series and shunt resistances, for different levels of irradiance.

For a complete solution that takes into account the electrical interactions of the modules, the irradiance on each section of the array at a different tilt must be calculated, and from this and the module parameters, the temperatures must be found and the I-V curves constructed. The array power can then be calculated by combining the I-V curves according to the series-parallel configuration of the array and calculating the array's maximum power point. However, for large systems, this solution is computationally intensive, and for all systems it requires solar cell parameters for which accurate values are usually not available.

There is one final problem associated with curved PV arrays. Comparisons between "expected" PV system energy production calculated using Equation (4) and measured energy production can be very valuable in diagnosing PV array problems such as blown fuses and broken connectors. However, if the PV array is equipped with irradiance-measuring devices (i.e., pyranometers), it will usually have only one oriented at some "average" tilt, possibly augmented by a horizontal measurement. Mathematical relationships exist for translating these into other array planes, but not without error and computational overhead. This lack of measurements in all of the planes of the curved array complicates accurate comparison of measured and modeled results. To understand this difficulty, consider the case of the GTAC PV system. $G_{poa,k}$ is measured only in the plane of the average tilt of the south-facing side of the array, augmented by a horizontal measurement. This "plane of array" irradiance measurement is clearly not accurate for the entire array, and therefore the calculated system performance using this value will also be inaccurate.

Subtask 1.1: development of a modeling procedure for curved PV arrays

The literature review in the previous section revealed that no modeling program currently combines multiple POA irradiance capability with electrical I-V curve modeling, execution times for such a program could be prohibitively long in many practical cases, and even if such a program were available it would not facilitate comparisons between measured and predicted array performance. However, for PV systems with a narrow range of tilts and azimuths, a simpler approach may be possible. In these cases, the deviation of the real system's performance from that predicted by

Equations (3) and (4) can be modeled by introducing an additional parameter, similar to the other loss parameters in Equation (3). This method is developed and utilized in the following two subtasks.

Procedure

To model a curved PV array using existing software packages in such a way as to facilitate diagnostic comparisons, we will first introduce a new factor, called the "curvature derating factor", K_{curv}, into Equations (3) and (4) to obtain correct power and energy values for curved PV arrays. In the following section, this parameter is mathematically defined. Then, procedures for using existing modeling software (PVFORM) to obtain values for K_{curv} will be described. The procedure will include a set of PV array configuration criteria, relating to the array's series-parallel configuration and range of orientations, which a given PV system must meet in order for this procedure to be used with validity. It is then shown that the GTAC PV system meets these criteria, and the modeling procedure is applied to obtain its K_{curv} values. Finally, to verify the results, a procedure for obtaining K_{curv} values experimentally for the GTAC PV system is described, applied to the GTAC PV array, and its results compared with K_{curv} values for the GTAC system determined using the modeling procedure.

Definition of the curvature derating factor

The curvature mismatch factor K_{curv} is defined using Equations (3) and (4):

$$E_{curv} = \sum_{k=1}^{n} \eta_{PV,k} G_{poa,k} A_{array} t_k (1 - K_{curv,k}) = \sum_{k=1}^{n} P_{k,curv} t_k$$

$$= (1 - K_{curv}) \sum_{k=1}^{n} \eta_{PV,k} G_{poa,k} A_{array} t_k = (1 - K_{curv}) \sum_{k=1}^{n} P_{k,pl} t_k$$

(11)

20

where E_{curv} and $P_{k,curv}$ are the energy and power produced by the curved PV array at time step k under irradiance $G_{poa,k}$ and with efficiency $\eta_{PV,k}$, $P_{k,pl}$ is the power produced by a planar array with the same efficiency (i.e. temperature), and t_k is the length of the time step in hours. Solving for K_{curv},

$$K_{curv} = 1 - \left(\frac{\sum_{k=1}^{n} P_{k,curv} t_k}{\sum_{k=1}^{n} P_{k,pl} t_k} \right) \qquad (12)$$

The planar array used in Equation (12) could be one whose orientation is in some way optimized (for maximum annual energy, maximum wintertime energy, maximum peak-shaving energy, etc.). Alternatively, it could be a planar array whose orientation is the same as that of an available irradiance measuring device. In this case K_{curv} can be used to facilitate comparison between expected and measured PV system performance.

K_{curv} is a function of four parameters:

1.) The array geometry, the effect of which is what K_{curv} is intended to model;

2.) The time of day, since K_{curv} depends on the solar position in the sky;

3.) The day or season of the year, for the same reason as in #2;

4.) The amount of cloud cover, because as the cloudiness increases, the remaining sunlight is increasingly diffuse or isotropic, and the ratio in Equation (12) approaches unity.

Estimation of K_{curv} by computer modeling: development of the simplified method

Having defined K_{curv}, a method for calculating its value is required. The summation in the numerator of the ratio in Equation (12) is simply the energy produced by the curved array during n equal-length time intervals, and the summation in the denominator is the energy produced by the previously-described planar array during this same set of time intervals. The latter of these can be computed using any presently available modeling software, but to obtain the former we must devise a method for modeling the curved array.

PVFORM v. 3.3 was previously described as the PV systems simulation program of choice for academic purposes for a variety of reasons, and for these same reasons it was chosen for this portion of this work. As has already been stated, PVFORM can only model planar PV arrays. Therefore, it was necessary to model the GTAC PV array as a set of planar "subarrays". This procedure seems intuitive; however, there was a second difficulty. When each individual planar subarray is modeled, PVFORM assumes that it is operating at its own maximum power point (MPP), and therefore that the planar subarrays are electrically noninteracting, or decoupled. This is clearly untrue in the real system. What was required, then, was to determine the conditions under which ignoring the electrical interaction of the planar subarrays would introduce minimal error. PV systems not meeting these conditions cannot be modeled using this procedure.

First, consider a generalized curved PV array, and recall that the voltage produced by a PV module is only logarithmically dependent on the irradiance, whereas the current is approximately linear with irradiance. Therefore, the effect of varying the irradiance level affects the currents produced by the different sections of the array much more strongly than it does their voltages. Another way of stating this is that two individual PV arrays at different tilts, and therefore under different irradiances, will

22

produce very similar voltages but significantly different currents. In electrical circuits, if two connected nodes are at the same voltage, they may be modeled as being disconnected without changing the operation of the circuit. Therefore, two planar subarrays having similar tilts and producing the same voltage may be decoupled without significantly altering the accuracy of the calculation.

Of course, this simplification will be valid over a restricted range of tilt angles. If the difference in tilts between the subarrays is too large, even the voltage will differ significantly between them, and breaking the connections will lead to incorrect results. When breaking two subarrays apart it is therefore advisable to check their maximum power voltages under the worst-case irradiance difference to make certain that the difference in their voltages at that time is still sufficiently small.

We also require a method for selecting the tilts of the planar subarrays with which we will replace sections of the curved array. One simple method would be to use the average tilt of the curved array section. However, this could lead to a small error in certain circumstances because, as indicated by Equations (6), (9), and (10), the irradiance varies nonlinearly with tilt. Therefore, the average tilt of the curved array may not receive the average irradiance of the curved array. In order to eliminate this effect, the following symmetry condition must be checked:

$$G_{\text{largest tilt},k} - G_{\text{pl},k} = -\left(G_{\text{smallest tilt},k} - G_{\text{pl},k} \right) \tag{13}$$

where $G_{\text{largest tilt},k}$ and $G_{\text{smallest tilt},k}$ are the irradiances on the parts of the curved array with the largest and smallest tilt angles respectively, and $G_{\text{pl},k}$ is the irradiance on the planar subarray, all at time step k.

These criteria can be summarized by the three criteria listed below:

1) The PV array contains no modules under different illumination that are connected in series.

2) The difference in tilts between parallel-connected subarrays that are to be separated for modeling purposes must be sufficiently small that their maximum power voltages do not differ significantly at any time.

3) The tilts of planar subarrays with which the curved array will be represented must be selected such that the irradiances on the planar subarrays and the irradiances on the extreme tilts of the curved array being replaced satisfy Equation (13).

If a curved PV system meets the first two criteria, it may then be represented by a group of independent planar subarrays with tilts selected according to the third criterion. The system can then be modeled by simulating each (planar) subarray separately and summing the results. This final step may now be accomplished with currently available PV system simulators.

Results

Applicability of the modeling method to the GTAC PV system

The Georgia Tech Aquatic Center PV system is a 342-kW system with its PV array mounted on the roof of the Georgia Tech Aquatic Center, which was the venue for the swimming events of the 1996 Summer Olympic and Paralympic Games. A full description of this system is provided in Appendix I. An aerial photograph of the GTAC and the PV array are shown in Figure 4. The array consists of 2856 120-W multicrystalline silicon modules arranged as shown in Figure A1-1. Twelve modules are connected in series to form a series string, and then 34 series strings are connected in parallel to form a source circuit. There are seven source circuits on the roof, each with

24

Figure 4. Aerial view of the Georgia Tech Aquatic Center (GTAC) rooftop PV array, showing the roof curvature.

its own fuses, disconnect switches, and cables routing power to the PCU. The source circuits are also connected in parallel.

Before applying the simplified modeling method to and finding K_{curv} values for the GTAC PV system, a detailed analysis was performed to ascertain whether it meets the three above-listed criteria. First, all of the series strings in the array are coplanar; there is no irradiance mismatch between series-connected modules, and Criterion 1 is satisfied. To check the second criterion, the following procedure was used. Note that on the south-facing side of the roof, the tilt angles of the modules vary from about 13° up from horizontal to 0°, with an average tilt of 6.4°. On the north-facing side, the variation is from about 2° to about 10°, with an average tilt of 5.9°. The full range of tilts, as measured using a self-leveling protractor, is listed in Table A1-11. To test

whether this range is small enough that Criterion 2 is satisfied, the POA irradiance on the average tilt of each side (north and south) of the array was modeled using the TMY in PVFORM. Then, from these model results a time point at which the POA irradiance difference between the two average tilts was the largest was selected, thus yielding a worst-case scenario. It was found that the maximum irradiance mismatch occurred on January 16 of the TMY at 1pm, when there was 645 W/m^2 of irradiance on the south-facing side. The difference in the irradiances on the average north-side and south-side tilts at that time was 165 W/m^2. Using the modeled south-side irradiance, the simplified equations in [9], and an assumption that the diffuse irradiance is 10% of the direct irradiance, the irradiances on three additional tilts were calculated: 13° facing south, 10° facing north, and 0°. These three additional tilts represent the extreme tilts of both sides of the GTAC array. Based on this set of five irradiances (tilts), I-V curves of one series string of identical modules at each of the five tilts were constructed using the program IVCURVE and the parameters of the modules used in the GTAC system. Finally, from these I-V curves, taking V as a parameter, the power-versus-voltage (P-V) curve of each series string was calculated, again using IVCURVE. A plot of these P-V curves over a narrow range of voltages near the maximum power voltage (MPV) is shown in Figure 5. The range of MPVs overlaps for most of the strings, and even the extreme values differ by only 15V. Recalling that this small voltage difference is the result of the largest irradiance difference encountered during the entire year of simulation, it can be concluded that the difference in MPVs over the entire range of tilts is therefore negligible, and Criterion 2 is satisfied. Finally, if the curved array is modeled by two planar arrays, one at the average tilt of the south-facing side (6.4°) and the other at the average tilt of the north-facing side (5.9°), Equation (13) is approximately satisfied over the entire year. The average disagreement between the two sides of Equation (13) is
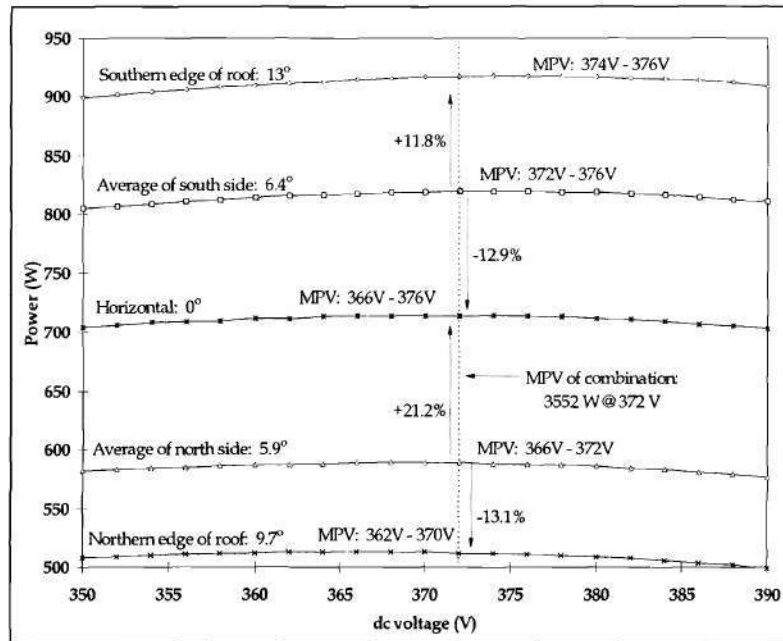
Figure 5. P-V curves of five series strings at different tilts. The region near the maximum power point is shown.

about 3 W/m² on the south side and about 2 W/m² on the north side. Therefore, these two planar subarrays may be used to model the GTAC system.

Based on the above analysis, it was concluded that the simplified modeling procedure could be applied to the GTAC PV array. Therefore, the curved array was divided into two planar subarrays, one at the average tilt of the south-facing side, the other at the average tilt of the north-facing side. Each subarray was then simulated individually using PVFORM, and the results were summed. For the planar array (the denominator in Equation (12)), an array with the same area as the GTAC array (3175 m²), azimuth equal to that of the south-facing side of the GTAC array, and a tilt equal to the average tilt of the south-facing side was used. This is the same orientation as one of

the two pyranometers, and therefore this choice of orientation will facilitate experimental validation of the results and diagnostic comparisons between calculations and measurements. In order to demonstrate that no more than two planar subarrays are needed to model this system reasonably well, we also divided the GTAC array into two, three, four, seven, and eleven equal-area sections, substituted planar subarrays at the average tilt of each subarray, and calculated K_{curv} values using the above procedure and Equation (12). This calculation is shown in Figure 6. Theoretically, as the number of subarrays increases, the agreement between the simplified and actual system performances should converge. We see that increasing the number of subarrays for this system leads to very little change in the predicted K_{curv} values. Therefore, the two-subarray model should provide adequate accuracy with minimal effort. The K_{curv} values for the two-subarray model alone are reproduced in Figure 7.

Experimental verification of K_{curv} values for the GTAC system

In order to verify the modeling procedure, K_{curv} values were calculated from the data being acquired from the GTAC system. Fortunately, the GTAC system is heavily instrumented with two data acquisition systems (DASs), a rooftop DAS and a DAS in the electrical room. The rooftop DAS measures meteorological parameters and also the temperatures of six randomly-selected solar modules, while the electrical room DAS measures the system's electrical performance. The parameters measured by each DAS and the sensors used to make the measurements are listed in Table A1-12 and Table A1-13.
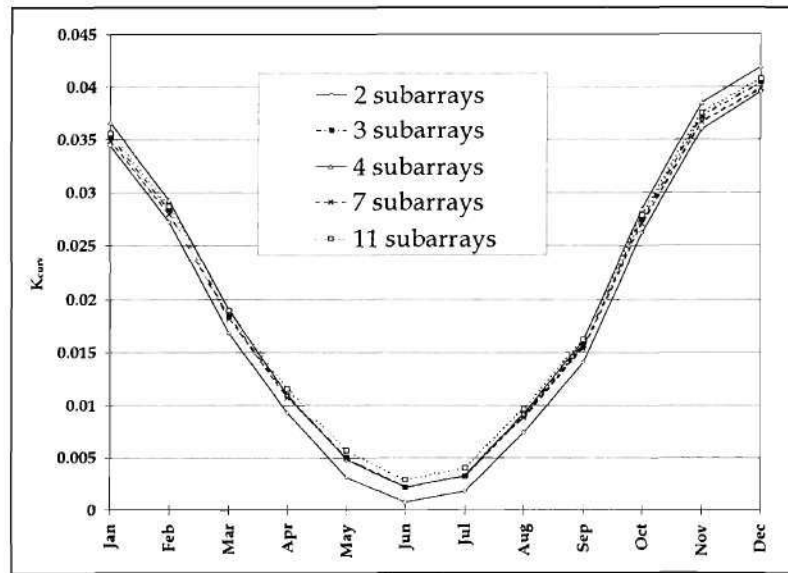
Figure 6. K_curv values for the GTAC PV system calculated using different numbers of subarrays.
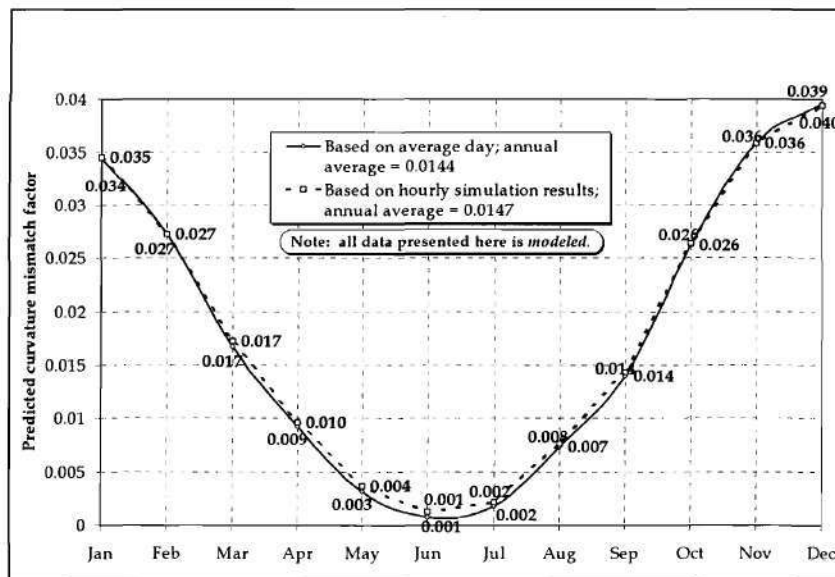
Figure 7. Plot of the curvature mismatch factor K_curv as a function of month, modeling the GTAC system using two subarrays.

Using Equation (12), it is possible to solve for K_{curv} in terms of measured quantities:

$$K_{curv} = 1 - \frac{\displaystyle\sum_{k=1}^{n} P_{k,curv}}{\displaystyle\sum_{k=1}^{n} P_{k,pl}} \qquad (14)$$

$$= 1 - \frac{\displaystyle\sum_{k=1}^{n} P_{k,curv}}{\displaystyle\sum_{k=1}^{n} \eta_{PV,k} G_{poa,k} A_{array}}$$

The numerator of Equation (14) represents the summation of the DC power as measured by the electrical room DAS. In the denominator, $\eta_{PV,k}$ is found using the measured temperatures, the derating factor values given in Table 1, and Equation (1), and $G_{poa,k}$ is the plane-of-array global irradiance measured by the rooftop DAS. The denominator therefore represents the energy production of a fictitious planar array with the same efficiency and area as the GTAC array, but with all modules at the tilt and orientation of the irradiance measurement.

However, if the efficiency calculated in the denominator is inaccurate, so will be the calculated K_{curv} values. Thus, before experimentally testing the modeled K_{curv} values, it was necessary that the values of the other η parameters in Equation (3) be known with sufficient accuracy. Unfortunately, this presented some difficulty. K_T was given by the manufacturer and independently verified by ISPRA in Italy. Reasonable values for the mismatch parameter $\eta_{mismatch}$ and the DC loss parameter η_{DCloss} were suggested by the system designer and component manufacturers. However, the other two derating factors, η_{dust} and η_{MPPT}, are not known with certainty. Furthermore, they

both vary with time. A value for η_{dust} frequently used in PV system simulations is 10%; however, experienced field personnel [19,20] agreed that this value is far too high, and suggested that a value less than 5% is probably more accurate. To experimentally determine η_{dust} for the GTAC system, the following approach was developed. The efficiency η of a solar module can be expressed as [21]

$$\eta = \frac{V_{OC} I_{SC} FF}{P_{in}} \qquad (15)$$

where V_{OC} and I_{SC} are the open-circuit voltage and short-circuit current of the module, FF is the module fill factor, and P_{in} is the input power to the module. The experiment can be conducted in such a way that P_{in} does not change appreciably during the time of the experiment (i.e. rapidly on a clear day), and FF is constant for a given module. Note also that all of the other parameters in Equation (1) are approximately constant, and if the module has no dust or soiling then $\eta_{dust} = 1$. Therefore, we can calculate the dust factor for a module by measuring V_{OC} and I_{SC} with and without dust and inserting these values into

$$\frac{\eta_{\text{with dust}}}{\eta_{\text{without dust}}} = \eta_{dust} = \frac{\left(V_{OC} I_{SC} \right)_{\text{with dust}}}{\left(V_{OC} I_{SC} \right)_{\text{without dust}}} \qquad (16)$$

V_{OC} and I_{SC} for several modules in the array were measured, then the modules were cleaned, and the same parameters were measured again. This experiment was repeated several times under different conditions, and the results are shown in Figure 8. On May 14, 1998, the dust factors were nearly unmeasurable (zero), and on August 24, 1998, only one valid measurement was possible. These results make it quite clear that
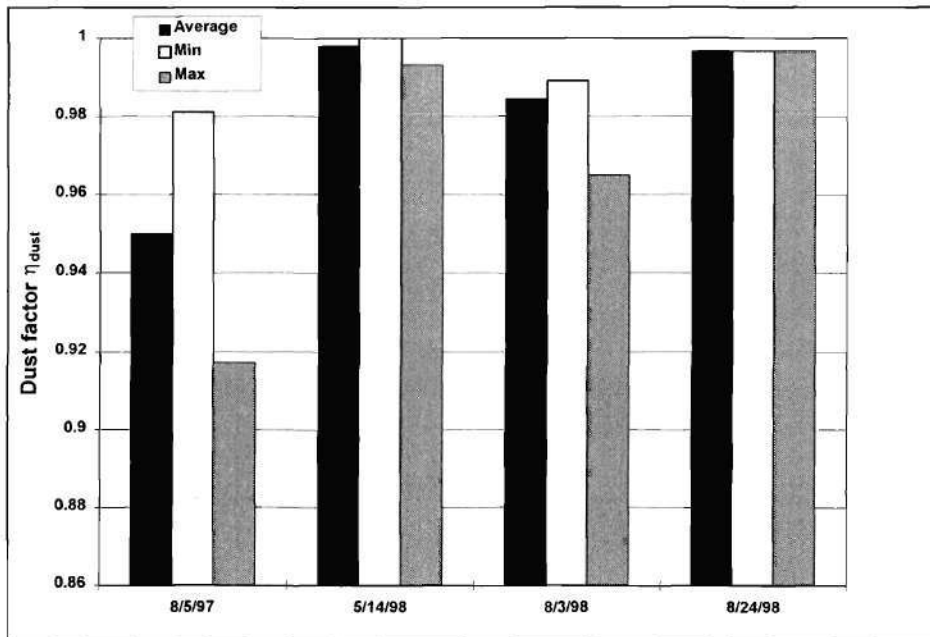
Figure 8. Results of dust factor measurements.

η_{dust} is time-varying, and that the range of variation is significant—in fact, the average values vary by over 3%, which is nearly as large as the largest values of K_{curv}.

In addition to this problem, the results indicate that the dust factor is nonuniform over the array. This in fact is an additional loss mechanism, a "mismatch factor due to dust nonuniformity" which can be viewed as tending to increase η_{dust}. This additional loss is difficult to quantify. The average measured value of η_{dust} is 97.8%; however, in this work, a value of 96% was used to account for nonuniformity.

Of the five derating factors, the maximum power point tracker derating factor, η_{MPPT}, was probably the one whose value was the least well known. Perez et al. [13] suggest a value of 95%. However, the results presented here showed that a value of

93%, which is quite close to Perez's suggested value, leads to a better matching between the measured and predicted K_{curv} values. The values used for all five derating factors are given in Table 1.

Table 1. Parameter values for Equation (3).

Parameter	Value
η_{dust}	0.96
$\eta_{mismatch}$	0.98
η_{Dcloss}	0.98
η_{MPPT}	0.93
K_T	-0.0037 (°C)$^{-1}$

The results of this calculation are shown in Figure 9. During this time period, two of the 238 series strings in the array were inoperative. The results in Figure 9 were adjusted to compensate for this factor by altering A_{array} appropriately. The error bars indicate the best estimate of the amount of variation which is expected to be introduced by the dust and MPPT derating factors. When one considers the potential sources of error, coupled with the fact that the value of the parameter being measured is very small, it is clear that the agreement between the measurements and predictions is in general quite excellent. It should also be noted that the expected seasonal variation is apparent in the measured K_{curv} values. This indicates the validity of the modeling procedure. The exact reason for the disagreement in September of 1997 is unclear, but is thought to be due to a pyranometer problem. The PCU suffered from intermittent thermal shutdowns during June and July of 1998 because of a cooling fan failure and
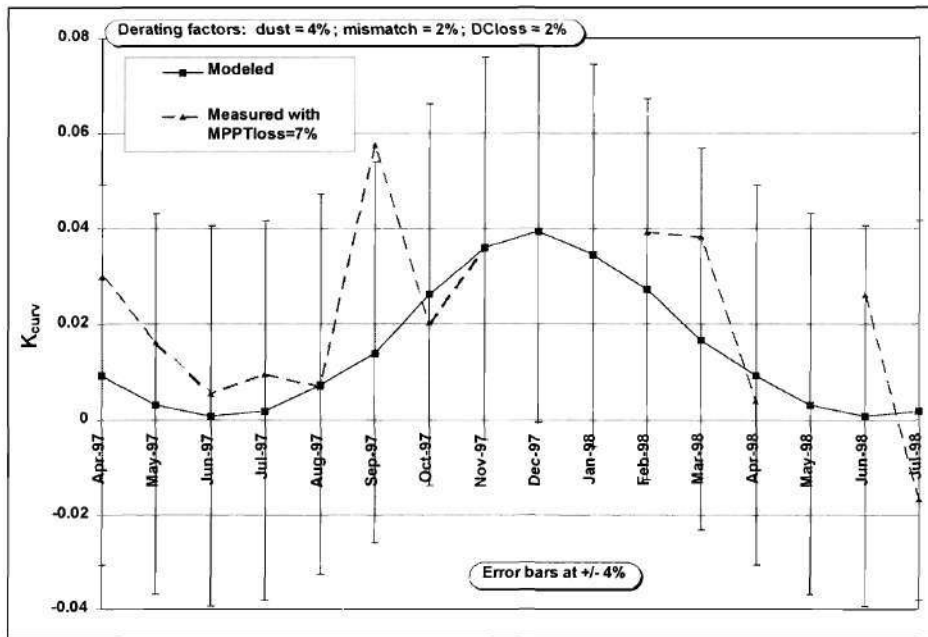
Figure 9. Comparison between measured and computed K$_{curv}$ values.

therefore the K$_{curv}$ values for those two months have an additional source of error not present in the other months, which may account for the disgreement during that time. No irradiance data was available during December 1997 or January 1998 because the pyranometers were being recalibrated, and a synchronization problem between the roof and electrical room DASs has rendered the data for May 1998 unusable.

One additional source of error that was investigated was the aforementioned affect of cloud cover: if during a month of measurements the skies are unusually cloudy compared with the corresponding month in the TMY, the measured K$_{curv}$ would be much lower than the modeled one. This possible error source was investigated by

calculating the clearness indices (CI) for five of the months of measurements and the corresponding five months of the TMY. The clearness index is given by [22]

$$CI = \frac{H}{H_0} \qquad (17)$$

where H and H_0 are the terrestrial and extraterrestrial (outside the atmosphere) total average daily radiant energy fluxes (kWh/m²/day). The values of CI based on the measurements and the model are shown in Table 2. H was calculated from the measured data or the TMY as appropriate, and H_0 was taken from the literature [8]. CI values for other months were unavailable because of a malfunction of the horizontal pyranometer.

Table 2. Clearness index values based on

measurements and models.

Month	CI based on measurements	CI based on PVFORM/TMY
April	0.3949	0.3650
May	0.3841	0.4155
June	0.2998	0.3852
July	0.3819	0.3898
August	0.3679	0.3763

The *CI* values from the meteorological database and the measurements agree fairly well with the exception of June, in which the measured value of K_{curv} was very near to the predicted value in spite of the difference in *CI*. It may therefore be concluded that a change in cloudiness does not appear to have been a significant factor in these five months.

Subtask 1.2: Performance prediction and optimization of the GTAC PV array

The procedure for modeling the curved GTAC PV array established in Subtask 1.1 was used to predict the performance of the GTAC PV system in order to aid in the design process for this system. Modeling was also used to quantify the performance penalty incurred by the PV array's non-optimal orientation compared to a system optimized for maximum annual energy production and also to one optimized for maximum peak-shaving effectiveness. Finally, a simple method for matching a PV PCU to a PV array using a parameter, called the "effective inverter efficiency", was introduced and utilized to determine the optimality of the match between the PV array and the PCU.

Determination of an Appropriate PCU Power Capacity

For economic reasons, it is desirable to use the smallest-capacity PCU possible that can still handle the full power output of the array. The designers of the system selected a PCU for the GTAC system that was rated at 315 kW. However, by the time this PCU was selected it had already been decided that the rated array output power would be 342 kW, almost 9% larger than the PCU. The PCU's maximum power point (MPP) tracking circuitry incorporates a power-limiting self-protection mechanism

36

against PCU damage resulting from overload. If either the PV power or current production exceeds preset thresholds (315 kW and 900 A), the MPP tracker limits the power or current to that threshold value by moving the array off of its MPP. For this reason, damage to the PCU was not the primary reason for the concern over the seeming mismatch between the size of the PV array and the rating of the PCU. Rather, the concern was that, if this "clipping" condition could occur frequently under actual operating conditions, the result would be a waste of significant amounts of PV power.

The 342-kW nameplate rating of the array corresponds to the array's performance at STC, which are conditions that will rarely be duplicated in the field and which does not include the five system derating factors or the effect of the array curvature. Thus, the array will probably never produce that much power, and therefore an exact knowledge of the maximum power that the array will produce under "real" conditions was needed to facilitate PCU selection. Using the two-subarray model for the GTAC system, the array's power output over the course of a year was calculated. Figure 10 shows the predicted monthly energy output of the GTAC PV system, and Figure 11 shows a histogram of the array DC power output based on the original Typical Meteorological Year (TMY1) for Atlanta. Note that the maximum array power output (which occurs on April 1 of the TMY1) is 279.7 kW, well below the PCU's rated capacity. Therefore, it was decided that the 315 kW PCU is sufficient for this installation and that its self-protection against overload will not result in a significant loss of power.

Another important factor in PCU selection was the optimality of the match between the PCU and the PV array in terms of overall system efficiency. The efficiency of the PCU is not constant, but rather is a function of the amount of power being processed and therefore of the PV array's power production. A plot of the efficiency curve for the GTAC PCU is shown in Figure 12 (the black curve). The system's efficiency
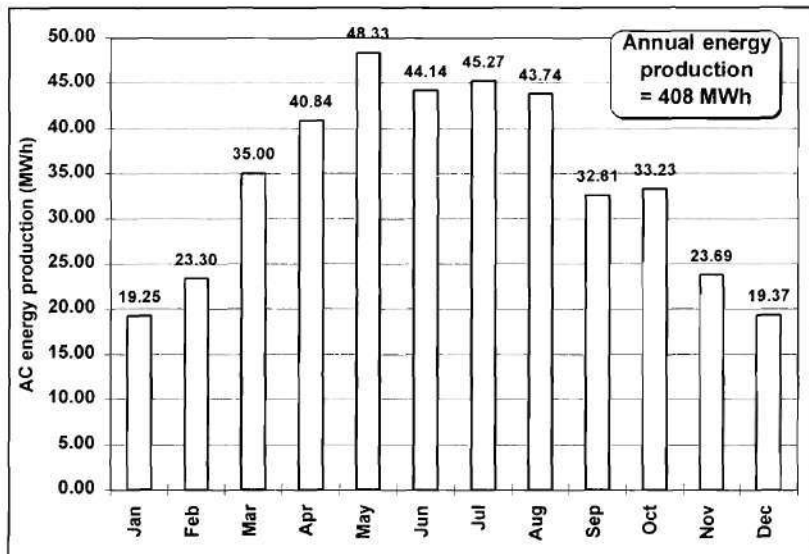
Figure 10. Predicted monthly energy production of the GTAC PV system using PVFORM, the TMY database, and the two-subarray modeling procedure.
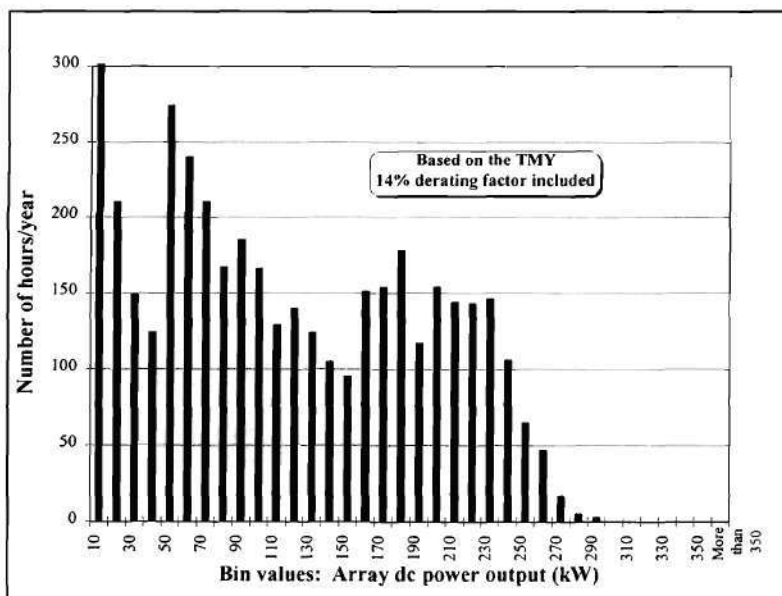
Figure 11. Histogram of the GTAC PV system's DC power output.
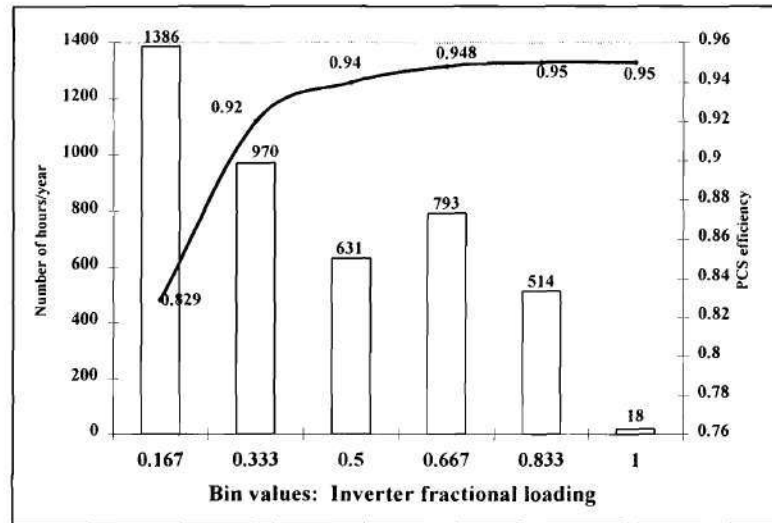
Figure 12. Comparison between the DC power histogram for the GTAC system and the PCU's efficiency-vs.-fractional loading curve.

can be maximized by selecting a PCU whose efficiency curve has a maximum at a PV power level which occurs with maximum frequency; that is, the PCU is most efficient at the power level at which the PV array produces the most energy. Using the previously-calculated DC power histogram, which is also shown in Figure 12 (the six white bars), an "effective PCU efficiency" may be calculated using the expression

$$\eta_{inv,eff} = \frac{\sum_{j=1}^{N_b} \{N(F_j) \cdot P_j \cdot \eta_{inv,j}(F_j)\}}{\sum_{j=1}^{N_b} N(F_j) \cdot P_j} \tag{18}$$

where $\eta_{inv,j}(F_j)$ is the PCU efficiency at fractional load F_j (determined from the actual curve), $N(F_j)$ is the number of hours during the year that the PV power production results in fractional loading F_j, P_j is the power production corresponding to bin j, and N_b is the number of bins (discrete values of F considered), as demonstrated in Figure 12. Note that the effective PCU efficiency depends not only on the PCU efficiency itself but also on the power production of the array. This parameter can thus be used as a measure of how well the PCU is matched to the PV array by comparing the effective PCU efficiency to the full-load PCU efficiency. Using this expression and the information in Figure 12, the PCU's effective efficiency for this installation was found to be approximately 90.5%. This compared favorably with the PCU's full-load efficiency of 95%, supporting the choice of this PCU for this PV array.

The effective PCU efficiency also provided an easy way to determine the system's AC output. Note that the two-subarray modeling procedure prevents the use of PVFORM's internal PCU submodel, because it is the sum of the subarray powers that needs to be fed into the PCU submodel. The effective PCU efficiency was used in lieu of writing additional software to allow the use of this model. Using the 90.5% effective PCU efficiency, PVFORM predicted that the annual energy production of the PV system will be almost 409 MWh.

Maximum Voltage vs. PCU DC Input Rated Voltage

The 315 kW PCU has a maximum DC open-circuit input voltage of 600V, as do the DC-side conductors and switchgear. Therefore, care was required to ensure that the series-parallel configuration of the array was such that the array voltage would not exceed 600 V. Since the array has a negative voltage temperature coefficient, and temperatures lower than the STC-specified 25°C could be encountered in the field, PVFORM was used to model the temperature of the cells for an entire year, using the TMY as input. The output was then scanned for the lowest cell temperature that

occurred during daylight hours. This temperature was -7.3°C. Assuming an irradiance of 1 kW/m² , the maximum voltage produced by the array was calculated using the equation

$$V_{max} = \left[V_{OC} + (K_{V_{oc}})(\Delta T_{max}) \right] \times N \tag{19}$$

where N is the number of series modules (12), ΔT_{max}= (T_{min} - 25°C), V_{OC} is the open-circuit voltage (42.6V), and $K_{V_{oc}}$ is the voltage derating coefficient per module given by the manufacturer (-0.146 V/°C). Substituting the values for this system into Equation (19), V_{max} was found to be 568 V. It is important to note that when this low temperature occurs there will be very little usable sunlight, so the actual voltage under these conditions would be lower than 568 V. Therefore, based on PVFORM modeling, the array design was deemed acceptable and will not produce voltages in excess of the 600 V_{dc} rating of the DC-side equipment.

It should also be noted that Underwriters' Laboratories (UL) standards dictate that the lowest expected ambient temperature at the site should be used in determining the maximum array voltage [23]. In order to determine this temperature, all 30 years of the NSRDB-SAMSON database were scanned for the minimum temperature during that time period in Atlanta, which was -22.2°C (occurring on January 21, 1985). Substituting this value into Equation (19) gave

$$\Delta T = -47.2^\circ C$$
$$V_{max} = 594V$$

This is still below the 600 V_{dc} limit, again supporting the suitability of the array design.

41

Investigation of the Effects of Standoff Height

One of the novel features of this PV installation is that the array is mounted to the roof directly using clamps connected to the standing seams (Figure 13). The standing seam height is about 2.5 inches, and the mounting clamps hold the modules about 1 inch above the standing seams, resulting in an array-roof standoff height of about 3.5 inches. From a photovoltaic standpoint, the standoff height is important because it strongly affects the ventilation behind the array and thus the array temperature, which in turn affects the array's efficiency. An additional concern from a design standpoint is that the cables selected which run beneath the array must have temperature ratings which are high enough to ensure that the cables will tolerate the thermal conditions experienced on the roof and not reduce the system's operational lifetime. PVFORM was utilized to quantify this effect. In the program, the standoff height is reflected in the choice of INOCT, where INOCT is the Installed NOCT (Nominal Operating Cell Temperature) and is calculated using the manufacturer's specified NOCT and a set of empirically-determined rules [24]. INOCT values of 56°C, 50°C, and 48°C, which correspond to standoff heights of 2", 4" and 6" respectively, were used. An additional "penalty" of +4°C was also added to INOCT as specified by the rules because the underlying standing-seam roof is "channelized", meaning that the standing seams will partially restrict airflow behind the array and increase INOCT. To investigate the importance of the standoff height, the array annual AC energy production and the maximum temperature attained by the array were calculated as functions of standoff height (Figure 14). [Note: the annual energy productions given are for a *planar* array at the average tilt of the south-facing side. The two-subarray model was not used in this calculation.] As expected, the model calculations revealed that as the array-roof standoff height increases, the maximum cell temperature attained during the year

42
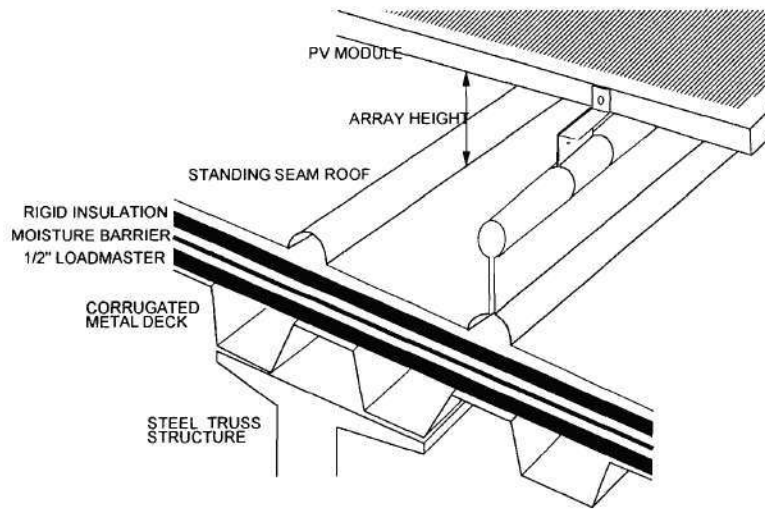
Figure 13. Schematic representation of the module mounting scheme for the GTAC PV array.
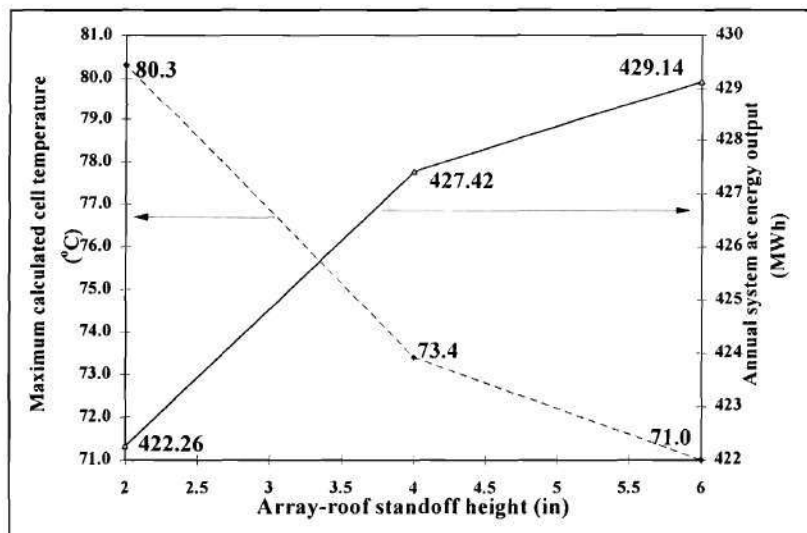
Figure 14. Maximum calculated solar cell temperature and annual AC energy output as functions of the roof-to-module standoff height.

43

decreases and as a result the annual energy production of the array increases. Notice that the maximum temperatures attained by the cells in the array are quite high, approaching 77°C for the 3.5" array-roof distance. However, the temperature rating of the cables selected was 90°C, which is comfortably above the maximum cell temperature and is therefore more than adequate for this installation.

Investigation of the Optimum Orientation of the PV Array

From the PV performance standpoint, the orientation of the Aquatic Center PV array is not optimized. The tilt and azimuth of the array were determined by the shape of the roof, which in turn was selected according to architectural and aesthetic considerations. The performance penalty incurred by this unoptimized orientation was estimated using PVFORM. To allow isolation of the effect of unoptimized orientation from that of the roof curvature, the GTAC array was modeled as being a planar array at the average tilt of the south-facing side (6.4°), whose annual AC energy production as computed by PVFORM is about 427 MWh. A matrix of 84 PVFORM simulations covering tilt angles from 0° (horizontal) to 60° up from horizontal and azimuth angles of 20° east of south to 90° west of south at 10° increments was constructed. Figure 15, which is a 3-D plot of the array's annual energy production as a function of array orientation, shows that the optimum array orientation for maximum annual energy production is a tilt of about 30° with a due-south azimuth. To increase the accuracy of this figure, further simulations with an angle increment of 1° were performed, and it was found that 30° is the true optimum to within 1°. Notice that the optimum tilt is slightly less than the site latitude (33.7°N). This is to be expected, since the optimum tilt for maximum annual energy production is roughly equal to the site latitude, but high-humidity locations can have slightly lower optimum tilts because high humidity will increase the diffuse component [25], and this component decreases with increasing

tilt, as indicated by Equations (7)-(9). However, Figure 15 also demonstrates that the sensitivity of the system performance to such small deviations is fairly small (performance penalties of only about 1% or less). The model calculations show that the annual energy output could be increased from about 427 MWh/year to about 462 MWh/year (an 8% increase) by changing the tilt angle to 30° from its installed orientation (6.4°). Recall that the 427 MWh/year baseline figure was computed for a coplanar array. If the comparison is instead made to the curved array as represented by the two-subarray model, thus adding the effect of the roof curvature, we find that the output could have been increased by almost 14%, from 407 MWh to 462 MWh, by placing the entire array at the same (optimized) tilt.

An additional orientation optimization was also carried out as a part of this work. Since peak shaving is an important potential application of PV systems, the "peak-shaving effectiveness" of the GTAC system as a function of orientation was also examined. To optimize the array for peak shaving, one might intuitively believe that the array should be oriented by the position of the sun at the peak demand time on the local utility's system. For the Georgia Power Company, the peak demand occurs at about 3-4pm during the four summer months of June-September. According to the well-known set of equations for determining solar position [8,9] or solar geometry charts [8], the "rule of thumb" optimum array orientation should be approximately 43° tilt and about 82° azimuth west of south to achieve maximum peak shaving at the peak demand time (3-4pm). To look for the peak shaving optimum, the array's energy production during "peak hours", defined by Georgia Power as noon-7pm during the four summer months, was calculated as a function of array orientation (again for a planar array). The results of these simulations are shown in Figure 16, and they indicate that the peak shaving optimum is approximately 30° tilt and 70° W of S azimuth. This time, the resolution of the simulation matrix near this point was increased by reducing the

45
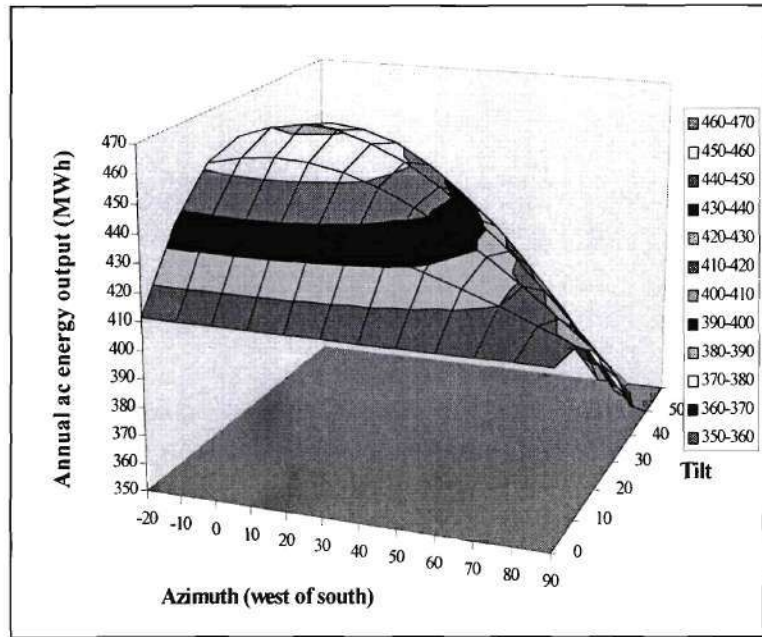
Figure 15. Plot showing the annual AC energy production of the GTAC PV system as a function of orientation.
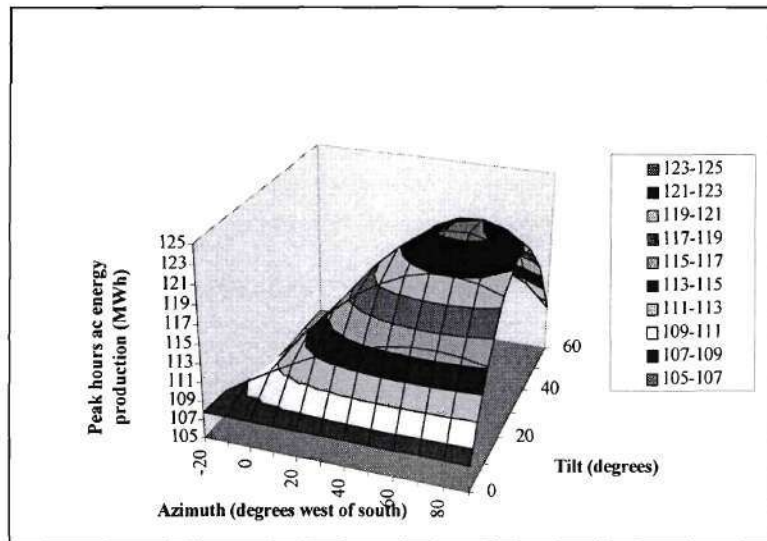
Figure 16. Plot showing the annual peak-hours AC energy production of the GTAC system as a function of orientation.

46

angular increment to 1°, and it was found that the optimum is actually approximately 35° tilt and 75° W of S azimuth. These results demonstrate that applying the previously mentioned intuitive method for determining orientation in Atlanta yields values that are slightly high, although again the sensitivity of the system performance to small deviations from the optimum orientation is essentially negligible. The small discrepancy between predicted optimum tilts can be explained as before: as the tilt angle is increased, more and more diffuse irradiation is lost because it strikes the back of the array. In the case of the azimuth, the disagreement arises because the peak demand time falls relatively late in the day, at a time when less solar energy is available, and orienting the array for maximum production at that time sacrifices energy production at earlier times in the window, when more irradiance is available. Too great an azimuth results in an excessive loss of this midday solar energy and an eventual reduction of peak shaving capability, with the peak window as defined here (noon-7pm). The model calculations (Figure 16) show that the annual electricity generation of the Aquatic Center array during the peak window could be increased from about 109.1 MWh/year to 123.6 MWh/year, an increase of 13%, by moving the orientation to 35° tilt and 75° azimuth west of south.

Use of modeling in system monitoring

Using the value for K_{curv}, an "effective PV array efficiency" may be defined by

$$\eta_{eff,PV,k} = \eta_{curv}\eta_{rated}\eta_{dust}\eta_{mismatch}\eta_{DCloss}\eta_{MPPT}\eta_{T} \tag{20}$$

where $\eta_{curv} = (1-K_{curv})$. This is called an "effective" efficiency because the curvature of the array actually decreases the energy output of the array by decreasing the energy *input*, not the efficiency. However, this notation is used here because $\eta_{eff,PV,k}$ represents

47

the efficiency value which would be calculated using measured irradiance and DC power output and is therefore the number required to facilitate diagnostic comparisons between predictions and measurements.

Such diagnostic capability can be extremely important. In early July, 1996, just before the start of the Summer Olympics, it was noted that the power output of the GTAC PV system recorded by the DAS was much lower than had been predicted by modeling. However, the power production by itself does not indicate a problem, because this effect could be caused by higher-than-normal temperatures or lower-than-normal sunlight. Therefore, to check the state of the PV array, the meteorological measurements and readings of the module temperatures were used to calculate $\eta_{eff,PV,k}$. It was found that $\eta_{eff,PV,k}$ values of 7.5% should have been achieved, but actual DC-side system efficiencies were as low as 5%. This made it clear that the system was not functioning properly and signaled a need for a detailed inspection of the system. This inspection revealed that Source Circuit G (see Figure A1-1) was producing no power. It was later discovered that the roof had received a direct lightning strike in early July, and this strike blew all of the fuses and surge arrestors in Source Circuit G's string combiner boxes. Fortunately, the problem was detected in time to allow for repairs before the Olympics. However, without the forewarning provided by the lack of consistency with performance expectations obtained from both simple and detailed models, the situation might have been very different, and the opportunity to showcase the system before a worldwide audience could have been lost.

Comparison of predicted and measured GTAC PV system performance

Since the system's activation in July of 1996, its performance data has been collected, analyzed and archived. For each month, the system's measured AC energy production has been calculated, and Figure 17 shows a comparison between the

predicted and measured monthly AC energy production of the system, without any correction mechanisms applied.

In general, the measured system output has been lower than the predicted system output. The primary reason for this has been that the amount of downtime has been much higher than anticipated. Another important factor is that the module temperatures appear on average to be somewhat higher than originally predicted, particularly during the critical summer months, as illustrated in Figure 18. This figure shows the average daylight-hours module temperatures from PVFORM and the GTAC. "Daylight hours" are defined as any hours in which there is nonzero POA irradiance (in the PVFORM case) or when the POA irradiance exceeds 10 W/m² (in the GTAC case, with the threshold value chosen to eliminate "noise" that may occur at night). This discrepancy indicates that the value of INOCT used in the modeling may have been too low, and in fact the roof curvature and the standing-seam roof effectively eliminate any air circulation behind the array. Finally, the amount of sunlight received on the roof is not always the same as that which the models predicted.

It is possible to compensate for these mechanisms. The procedure adopted for correcting for downtime is as follows. For a given month, the average energy produced each day is the total energy produced during the month in W-h, E, divided by the number of days in the measurement, D_l. Note that D_l is also the number of days in the month minus the number of days during which the system was off ("downtime days"). If it is assumed that the system's energy production during the downtime days would have been average, and if the total number of days in the month is D_0, then the monthly energy production can be scaled to compensate for the downtime as follows:

$$E_{corrected,downtime} = E \frac{D_0}{D_l} \tag{21}$$
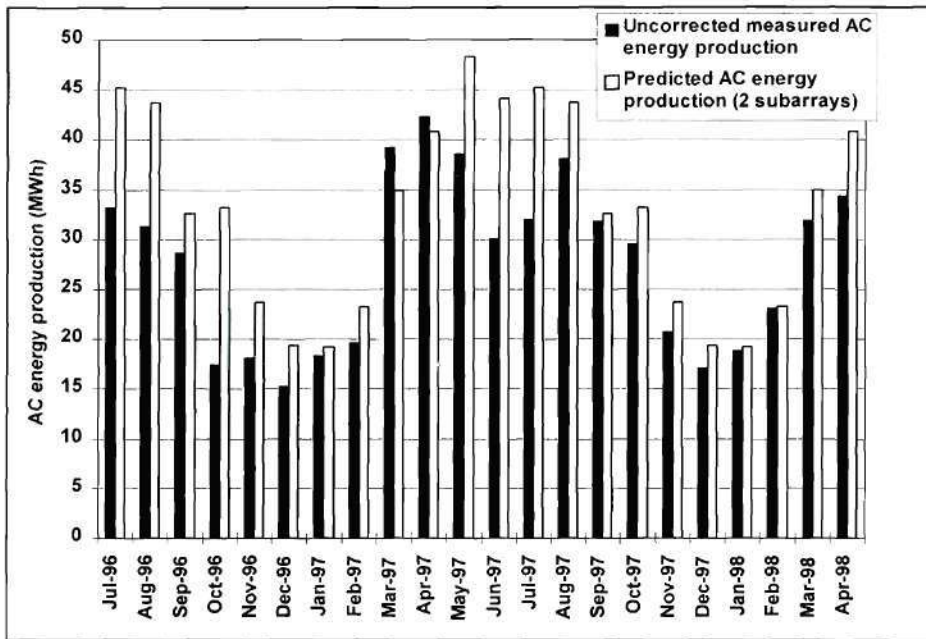
Figure 17. Comparison between predicted and measured AC energy production of the GTAC PV system since July, 1996.
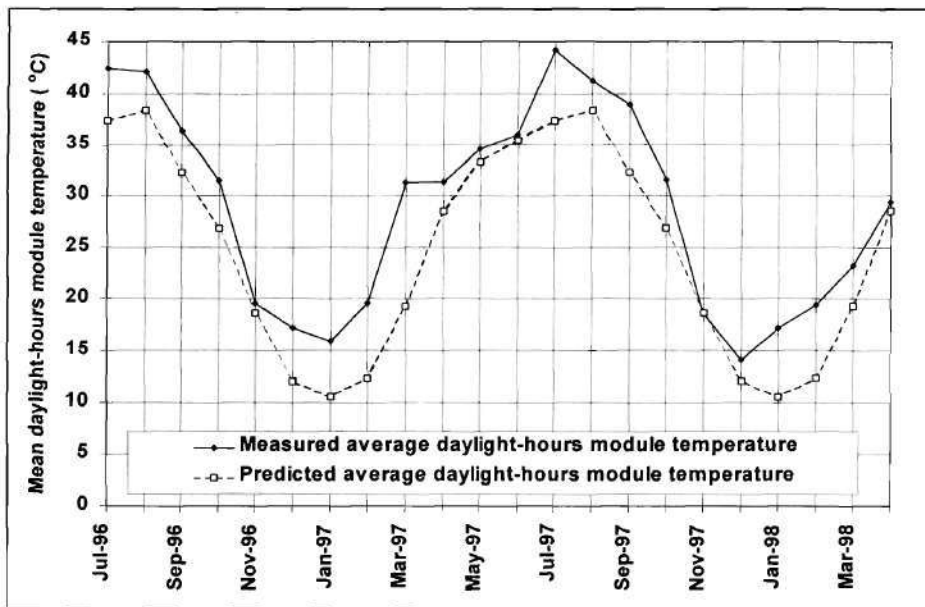
Figure 18. Comparison between predicted and measured average daylight-hours module temperatures.

50

A similar approach is followed to correct for differences between the measured and predicted amounts of sunlight. The "amount of sunlight" is quantified using the mean daily solar energy per unit area E_{avg}, which is calculated by

$$E_{avg} = \frac{\sum\limits_{all\ measurements} G_{poa} \cdot \Delta t_{meas}}{N} \qquad (22)$$

where N is the number of days in the month, and Δt_{meas} is the measurement interval in hours (1/6 for the GTAC system or 1 for PVFORM). The units of E_{avg} are W-h/m^2/day. Note that this procedure assumes that the sunlight can be approximated as constant over the measurement interval Δt_{meas}. Values for this parameter must be calculated using the measured data from GTAC and also from PVFORM. Either the POA or horizontal irradiance may be used, but consistency must be ensured. Then, the monthly energy production may be approximately corrected by substituting the values into the following expression:

$$E_{corrected,sunlight} = E \frac{E_{avg,PVFORM}}{E_{avg,meas}} \qquad (23)$$

To correct for differences between predicted and measured temperatures, the following approximation may be used. First, one must calculate the mean daylight-hours module temperature for each month by simply averaging all daylight-hours module temperatures. This must be done both for the measurements and the predicted values from PVFORM. Then, the average monthly energy production may be approximately corrected by multiplying it by

$$E_{corrected,temp} = E \frac{\left[1 - K_T \left(T_{mod,pred} - T_{STC}\right)\right]}{\left[1 - K_T \left(T_{mod,meas} - T_{STC}\right)\right]} \qquad (24)$$

where $T_{mod,pred}$ and $T_{mod,meas}$ are the predicted and measured mean daylight-hours module temperatures respectively, and T_{STC} is the standard test conditions temperature (25°C).

Applying these mechanisms to the measured monthly AC energy production leads to the results shown in Figure 19. No corrections are available for October 1997-January 1998 due to a malfunction of one of the pyranometers. In general, the corrected measurements are much closer to the predictions than the raw measurements. The anomalies in September 1996 and September 1997 are suspected to be caused by pyranometer malfunctions.
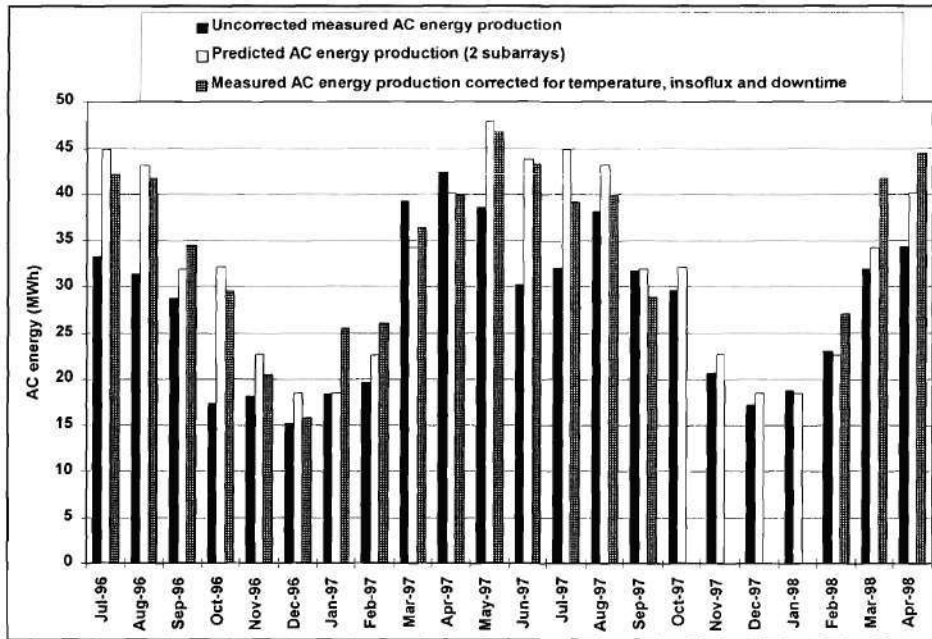
Figure 19. Measured and predicted monthly AC energy production of the GTAC system, along with measured AC energy corrected for the effects of downtime, temperature, and irradiance.

CHAPTER III

TASK #2--ISLANDING PREVENTION FOR UIPV SYSTEMS

History, literature review and motivation

Islanding occurs when a PV system feeds power into a section of the utility system that has been isolated from the utility voltage source. Consider the configuration shown in Figure 20, a PV system connected to a feeder line that is in turn connected to the utility voltage source through a transformer and a switch (a recloser, breaker, fuse etc.). The PV system consists of a PV array and a PCU. A local load is also connected to the feeder line. The PV system acts as a current source, supplying a nearly sinusoidal current which has the same frequency and (in general) the same phase as the voltage at the PV system's terminals. If the switch were opened, under certain conditions it is possible for the PV PCU to continue to supply current to the isolated section of the grid and the local load. This is islanding, and the isolated section of the utility being powered by the PV system is referred to as an island.

The time interval between the disconnection of the utility and the shutdown of the PCU is referred to as the *run-on time*. Islanding events are typically subdivided into two categories: long-term, with run-on times of one second or more, and short-term, with run-on times of less than one second [26,27].

The primary concern with long-term islanding is one of safety [26,27,28,29,30,31,32,33]. Maintenance or repair personnel arriving to service the isolated feeder may be unaware that it is still energized, which could lead to personal

54
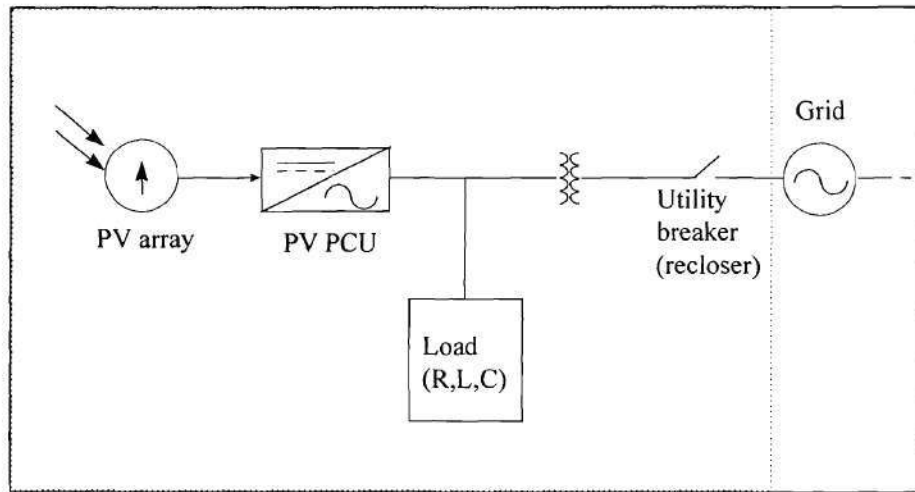
Figure 20. Schematic of a PV system connected to a utility feeder that can be isolated from the utility by the switch at the right.

injury. This is of particularly great concern in the case of scheduled maintenance, when the switch could be manually operated by service personnel who would immediately commence work on the isolated system. In this case, islanding of even a few tens of seconds could be dangerous.

Another problem associated with both long- and short-term islanding is that the PV system, which relies on the utility voltage to provide a phase and frequency reference for its output current, may lose synchronism with the utility while the switch is open; that is, the frequency of the PV system's output current may drift away from the utility frequency, and over time a sizable phase error between the PV current and utility voltage can develop. The change in frequency itself can lead to malfunctioning of many types of equipment, but the phase difference is particularly serious because the utility may reclose on the out-of-phase island [27,34]. Such an *asynchronous reclosure* would

result in large surge currents, which could quickly damage the PV system and the local load.

It has been postulated that another possible problem with short-term islanding is that it can interfere with the arc-clearing function of protective relays [34]. However, there is much debate over whether this is a significant issue.

One final problem that is increasing in relevance is that some islanding prevention methods interfere with each other, leading to longer run-on times and possibly failure to detect islanding if several PV systems are present in the island. In some cases, this can happen even if all the PV systems in the island are using the same islanding prevention scheme. This situation has been termed the "multi-inverter case", and it could become increasingly common with the proliferation of small, roof-mounted PV systems and the development of PCUs for AC PV arrays, in which case there could be tens or even hundreds of PCUs in an island.

In general, an islanding prevention method should accomplish the following goals:

I.) Detect islanding and disconnect the PV system from the utility, regardless of the initial state of the system, perturbations, composition of the load, or presence of other equipment such as other PV systems (i.e. the multiple inverter case);

II.) Detect islanding rapidly enough to guarantee safety and safeguard the reliability and integrity of the utility and PV systems;

III.) Disconnect the PV system only when islanding is actually occurring to avoid nuisance trips.

A considerable body of work exists on islanding and islanding prevention methods. However, there is a considerable lack of consensus and understanding about

islanding. Specifically, there is much debate over the need for more than basic protective relays for islanding prevention, and there is little agreement about the effectiveness of current prevention schemes. This lack of consensus provided the motivation for the research contained within Task 2. The purpose of the next section is to critically review the literature on islanding, including the status and performance of existing islanding prevention methods. The section describes the mechanism of operation of each method, including the four standard relays, and then compares them, thereby providing a fundamental understanding of each method which will establish the necessary background for understanding the research proposed in following sections.

Islanding prevention by standard protective relays

Grid-connected PV systems are required to have an overvoltage relay (OVR), an undervoltage relay (UVR), an overfrequency relay (OFR), and an underfrequency relay (UFR) that disconnect the PV system from the utility in the event that the magnitude or frequency of the PCU's terminal voltage goes beyond certain limits [35]. Under most circumstances, these relays will prevent islanding. Consider the configuration shown in Figure 21, in which power flows and node **a** have been labeled. Node **a** is also referred to as the "point of common coupling" between the utility and PV systems, and therefore the PV system is required to disconnect from node **a** in order to prevent islanding. When the recloser is closed and the utility is connected, real and reactive power P_{PV} + jQ_{PV} flows from the PV system to node **a**, and power P_{load} + jQ_{load} flows from **a** to the load. Summing power flows at node **a**,

$$\Delta P = P_{load} - P_{PV}$$
$$\Delta Q = Q_{load} - Q_{PV}$$

(25)
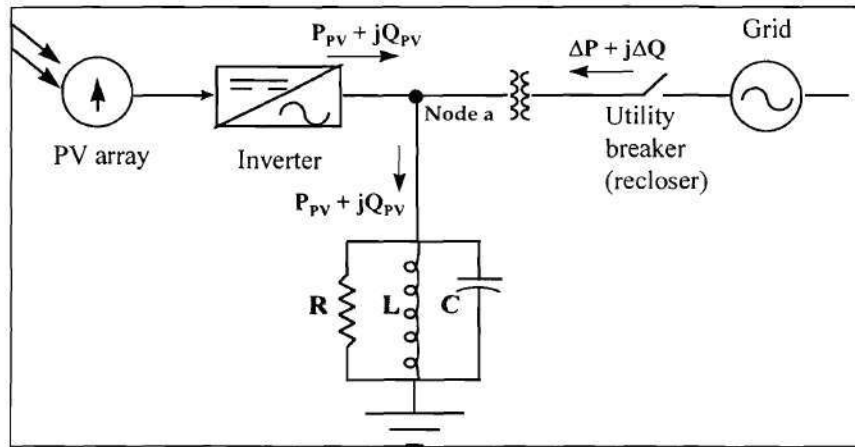
Figure 21. PV system/utility feeder configuration showing definitions of power flows and terms.

are the real and reactive power flowing into node **a** from the utility. Typically, PV PCUs operate with a unity power factor (that is, the PV output current is in phase with the voltage at node **a**), so $Q_{PV} = 0$ and $\Delta Q = Q_{load}$. The real and reactive power being consumed by the load are given by

$$
P_{load} = \text{Re}\left[\vec{V}_a * \vec{I}_{load}^*\right] = V_a I_{load} \cos\phi
$$

$$
Q_{load} = \text{Im}\left[\vec{V}_a * \vec{I}_{load}^*\right] = -V_a I_{load} \sin\phi
$$

(26)

where $\cos(\phi)$ is the load displacement power factor (dpf) and V_a and I_{load} are the RMS values of v_a, the instantaneous voltage at **a,** and i_{load}, the load current. The superscript

asterisk denotes complex conjugation. Assuming that the load can be represented as a parallel RLC circuit, these expressions may be written in terms of V_a as follows:

$$P_{load} = V_a \frac{V_a}{R_{load}} \qquad (27)$$

$$Q_{load} = V_a \left[\frac{V_a}{\omega L} - \frac{V_a}{\frac{1}{\omega C}} \right] \qquad (28)$$

where ω is the frequency of v_a. When the recloser opens, ΔP and ΔQ will both go to zero. The behavior of the isolated system will depend on ΔP and ΔQ at the instant before the recloser opens to form the island, denoted ΔP^- and ΔQ^-. There are four cases in which the OVR/UVR or OFR/UFR will prevent islanding [36]:

1.) $\Delta P^- > 0$. In this case, the PV system is producing less real power than is required by the local load ($P_{load} > P_{PV}$). From Equation (27), we see that when the switch opens and ΔP becomes zero, P_{load} will decrease, meaning that V_a must also decrease since R_{load} can be assumed to be constant over this time interval. This decrease in voltage can be detected by the UVR, and islanding is prevented.

2.) $\Delta P^- < 0$. In this case, $P_{load} < P_{PV}$, and power is flowing into the utility system. Now, when ΔP becomes zero, P_{load} must increase and V_a will also increase. This condition can be detected by the OVR, and again islanding is prevented.

3.) $\Delta Q^- > 0$. This case corresponds to a lagging power factor load, or a load whose reactive component is inductive. After the recloser opens, $\Delta Q = 0$. However, as previously mentioned, Q_{PV} is usually zero, and therefore $Q_{load} = 0$. This requires the

term in square brackets in Equation (28) to become zero, meaning that the inductive part must drop and the capacitive part must increase. Equation (28) shows us that in order for this to occur the frequency ω of v_a must increase until $\omega = \omega_{res} = (LC)^{-0.5}$. If this increase in ω is sufficiently large, it can be detected by the OFR.

4.) $\Delta Q^- < 0$. This case corresponds to a leading power factor load, or one that is primarily capacitive. As in case 3, when ΔQ becomes zero, the inductive and capacitive parts of Equation (28) must balance so that $Q_{load} = 0$, and this requires ω to decrease, again to $\omega = \omega_{res} = (LC)^{-0.5}$. This frequency decrease, if it is large enough, can be detected by the UFR.

It bears repeating at this point that all PV PCUs for utility interface applications are required to have OVR/UVR and OFR/UFR protection [35]. Therefore, if *either* the real power of the load and PV system are not matched, *or* the load's resonant frequency does not lie near the utility frequency, islanding will not occur.

Shortcomings of the standard protection systems: the nondetection zone

We have thus far examined four cases in which the OVR/UVR and OFR/UFR of a PV system will prevent islanding. Unfortunately, there is another possible case: $\Delta P^- = \Delta Q^- = 0$. This corresponds to a case in which the PV power production is matched to the load power requirement, and the load dpf at ω_0 is unity; that is, $\omega_0 = \omega_{res}$. In this case, when the switch is opened no change occurs in the isolated system, and the OVR/UVR and OFR/UFR do not operate. In reality, ΔP^- and ω_{res} do not have to be exactly equal to zero and ω_0 respectively for this to occur because the magnitude and frequency of the utility voltage can be expected to deviate slightly from nominal values, and therefore the thresholds for the four relays cannot be set arbitrarily small or else the PV system will be subject to nuisance trips. This limitation leads to the formation of a *nondetection*

zone (NDZ), as shown schematically in Figure 22 for a fixed RLC load. There are two possible definitions for the NDZ:

1.) For a given (fixed) load, there is a finite range of ΔP and ΔQ for which islanding is not detected. In other words, in a "power mismatch space" defined as the space defined by the values of ΔP and ΔQ (Figure 22), there is a subspace in which islanding prevention methods will fail. This range of ΔP and ΔQ values for which the islanding prevention method fails is defined as the NDZ of that method.

2.) For a fixed ΔP (usually zero) and assuming a parallel RLC load, there is a range of values of R, L and C for which islanding is not detected. In other words, in a "load space" defined as the space defined by the values of R, L and C, there will be a subspace in which islanding prevention methods fail. This range of RLC loads for which the islanding prevention method fails is defined as the NDZ of that method.

The "power mismatch space" representation shown in Figure 22 is the one traditionally used in the islanding literature. However, henceforth in this work, the latter definition will be adopted. The reasons for this will become clear shortly.

One earlier study indicates that under certain (unspecified) conditions the probability of ΔP- and ω_{res} falling into the NDZ of the OVR/UVR and OFR/UFR can be significant [37]. However, in spite of this, there is still much disagreement between PV PCU manufacturers and utility engineers over whether further islanding protection equipment beyond the four standard relays is really necessary. Many in the field still believe that the conditions under which the relays will not protect against islanding are so rare that no effort is warranted to develop methods to handle these cases. Still, utilities and bodies that establish standards generally require that additional islanding

61

Within the figure:

ΔQ

OF

OV

UV

ΔP

UF

For ΔP and ΔQ in this region, islanding is not detected
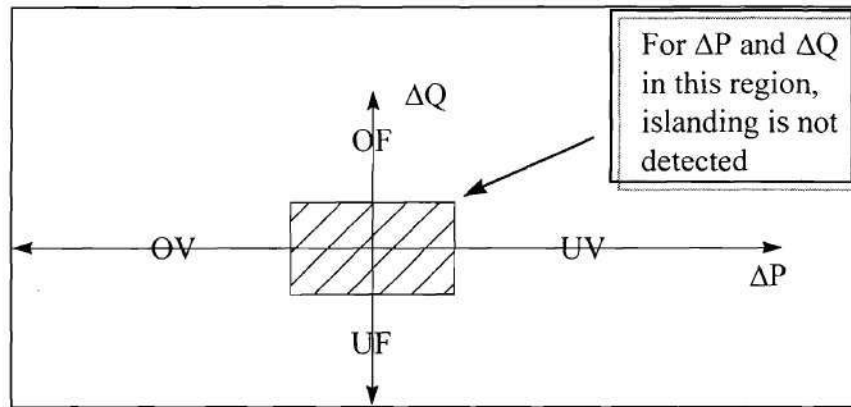
Figure 22.   Schematic demonstration of the nondetection zone in which the standard four relays cannot detect PV system islanding for a fixed RLC load.

protection be incorporated into PV systems, and this additional protection is the subject of the next section.

Methods of reducing the NDZ: Passive methods

Passive methods for islanding prevention involve monitoring the PCU's terminal voltage (v_a) for some condition that indicates islanding. These methods are discussed below.

Voltage harmonic monitoring

In this method, the PV PCU monitors the total harmonic distortion (THD) of v_a and shuts down if this THD exceeds some threshold. There are two mechanisms that can cause the harmonics in v_a to increase when islanding begins. One of these is the PV PCU itself. A PV PCU will produce some current harmonics in its AC output current, as all switching power converters do. A typical requirement for a grid-connected PV

PCU is that it produce no more than 5% THD of its full rated current [38,39]. Under normal operation, the utility, being a "stiff" voltage source, forces an "undistorted" sinusoidal voltage (THD $\approx$ 0) across the load terminals, causing the (linear) load to draw an undistorted sinusoidal current. Summing at node **a**, when the switch is closed the harmonic currents produced by the PCU will flow out into the grid. Because these harmonic currents are kept small and the impedance of the utility is in general low, these harmonic currents interact with the very small utility impedance to produce only a very small amount of distortion in the node-**a** voltage. When the switch opens, the harmonic currents produced by the PCU will flow into the load, which in general has a much higher impedance than the utility. The harmonic currents interacting with the larger load impedance will produce larger harmonics in v_a [40]. These voltage harmonics, or the change in the level of voltage harmonics, can be detected by the PCU, which can then assume that the PV system is islanding and discontinue operation.

The second mechanism which may cause the harmonics to increase is the voltage response of the transformer shown in Figure 21. If the switch that disconnects the utility voltage source from the island is on the primary side of the transformer, as shown in Figure 21, the secondary of the transformer will be excited by the output current of the PV system. However, because of the magnetic hysteresis of the transformer, its voltage response is highly distorted [40] and will increase the THD in v_a.

In theory, the voltage harmonic monitoring method promises to be highly successful in detecting islanding under a wide range of conditions [40], and its effectiveness should not change significantly in the multiple-inverter case. However, it suffers from a serious implementation difficulty: it is not always possible to select a trip threshold that provides reliable islanding protection but does not lead to nuisance tripping of the PV system. It is clear that a threshold must be selected that is: a) higher than the THD that can be expected in the grid voltage; but b) lower than the THD

63

that will be produced during islanding by the two mechanisms described above. Let us assume that the PV PCU produces 5% THD in its output current, the maximum allowable limit. For a resistive load fed by this current, in the absence of the utility voltage source, the THD of v_a will also be 5%. The proof of this is straightforward: if the current is represented by its Fourier series

$$i_{PV} = \sum_{n=1}^{\infty} I_{PV,n} \sin(n\omega_0 + \phi_n) \tag{29}$$

where n=1 denotes the fundamental component of i_{PV}, then the voltage response of a pure resistance to this current is simply

$$v_a = Ri_{PV} = R \sum_{n=1}^{\infty} I_{PV,n} \sin(n\omega_0 + \phi_n) \tag{30}$$

Let THD_{iPV} be the total harmonic distortion in the current described above. The total harmonic distortion in the voltage, THD_{va}, is given by

$$THD_{va} = \frac{\sqrt{\sum_{n=2}^{\infty} R^2 I_{PV,n}^2}}{RI_{PV,1}} = \frac{R}{R} \frac{\sqrt{\sum_{n=2}^{\infty} I_{PV,n}^2}}{I_{PV,1}} = THD_{iPV} \tag{31}$$

When the load is not purely resistive, the situation changes. The magnitude response of a parallel RLC can cause there to be less distortion in the voltage response than in the exciting current. The node-**a** voltage for a distorted current feeding an RLC load with impedance Z is

64

$$v_a = Z(\omega)i_{PV} \qquad\qquad (32)$$

where the dependence of Z on the frequency ω is explicitly indicated. The magnitude response (the magnitude of Z as a function of frequency) of a parallel RLC load with R = 14.4 Ω, L = 10 mH, and C = 703.6 μF is plotted in Figure 23, along with a line indicating the position of the 60-Hz utility frequency. Since this load has a unity power factor (is resonant) at 60 Hz, this vertical line also indicates the frequency at which the magnitude of Z is a maximum. This means that the voltage response of the RLC load to
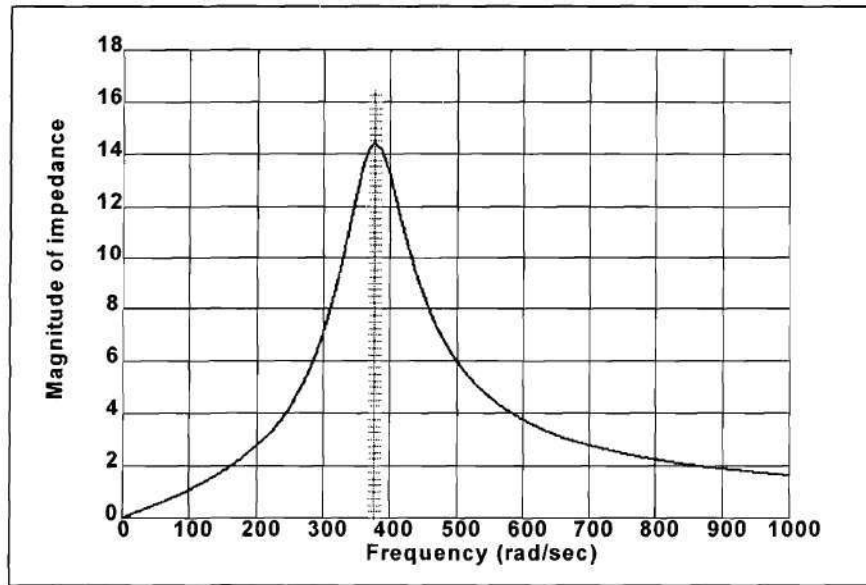
Figure 23. Demonstration of the magnitude response of a parallel RLC circuit. The vertical hatched line indicates the utility frequency, and (in this case) the RLC load's resonant frequency.

all current harmonics higher than the fundamental will be attenuated, and in this case where the load's resonant frequency is near the utility frequency, THD_{va} will be less than THD_{iPV}.

It is therefore clear that the THD threshold will have to be set lower than 5%. In reality, the utility voltage distortion that we assumed to be ≈ 0 in the foregoing discussion can actually be expected to be 1-2% under normal conditions (because of the interaction of harmonic currents drawn or supplied by loads with the utility source impedance), but there are many conditions, such as the presence of power electronic converters that produce current harmonics at frequencies at which the utility system has resonances, which can cause this value to increase significantly [41]. Also, transient voltage disturbances, particularly large ones such as those that accompany the switching of capacitor banks [42], could be interpreted by PV PCUs as a momentary increase in THD, depending on the measurement technique used. It is clear that in some cases it is not possible to select a threshold that meets criteria a) and b). It may be possible to overcome this problem using digital signal processing and harmonic signature recognition, but these techniques cannot be implemented cost-effectively in small PV PCUs. For these reasons, the harmonic monitoring technique has not been used commercially.

Transient phase change or phase jump detection

Another method of islanding prevention, phase jump detection (PJD), involves monitoring the phase between the inverter's terminal voltage and its output current for a sudden "jump" [31,40]. Under normal operation, the PCU's output current waveform will be synchronized to the utility voltage by detecting the rising (or falling) zero crossings of v_a. This is done through the use of a phase-locked loop (PLL) whose control

action is such as to bring i_{PV} into phase with v_a [43,44]. The PLL is the central element in the implementation of many islanding prevention schemes, and because of its importance a brief discussion of PLLs and their operation is warranted at this time.

A schematic of the basic PLL circuit is shown in Figure 24. The input signal, or "reference" signal, is usually band-pass filtered and fed as one input into a device called a phase comparator. The PLL's output signal is the other input to the comparator. The output of practical phase comparators usually has unwanted AC components, so the phase comparator output is low-pass filtered by the loop filter before being used to control the frequency of a voltage-controlled oscillator (VCO). The operation of an analog PLL circuit is as follows. If a phase difference arises between the PLL input and output signals, the phase comparator generates an output voltage which is proportional to the phase error. This (filtered) voltage commands the VCO to change its frequency in the direction which reduces the phase error. When the input and output signals of the PLL are in phase (the PLL has "acquired" the input signal), the phase comparator's output is zero, and the VCO maintains its frequency. Thus, the control action of the PLL acts to bring its output signal into phase with its input signal by changing the frequency of the output signal.

The operation of a digital PLL is slightly different. In the digital case, the "input filter" block in Figure 24 contains not just a filter but also a zero-crossing detector which produces a pulse at either a rising or falling zero crossing. A similar device must also be inserted between the VCO and the phase comparator, so both inputs to the phase comparator are digital pulses. The digital phase comparator then determines the phase error by measuring the time difference between the pulses.

An alternative variant on the PLL configuration would be to replace the VCO by a digital reference waveform generator, which may be a microprocessor or a look-up table. In this case, frequently the rising zero crossing of the input signal is used as a "reset"

67
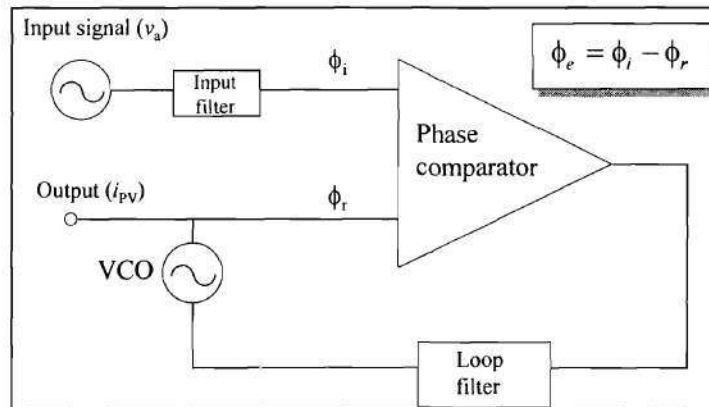
Figure 24. Schematic of a phase-locked loop (PLL).

signal for the reference generator, so that the PV output current cycle always starts at approximately the same time as the voltage cycle, guaranteeing synchronism.

In digital systems, since the synchronization in such a system occurs only at zero crossings, the PV system is in a sense in "open-loop mode" between zero crossings. In this work, it is generally assumed that the PLL is digital, since this is the type used in most PV PCUs.

Armed with this understanding of PLL operation, the PJD mechanism is now easily understood. When the utility is disconnected, the voltage v_a is no longer rigidly fixed by the utility voltage source. However, the PV current i_{PV} is fixed, since it is still following the waveform template provided by the PLL (because the system is between zero crossings). Therefore, suddenly it is the PV current i_{PV} that becomes the fixed phase reference. Since the frequency has not yet changed, the phase angle of the load must be the same as before the utility switch opened, and therefore v_a must "jump" to

68

this new phase as shown in Figure 25. At the next rising zero crossing of v_a, the resulting phase error between the "new" voltage and the PCU's output current can be used to detect islanding. If this phase error is greater than some threshold value, the controller can shut down the PCU.
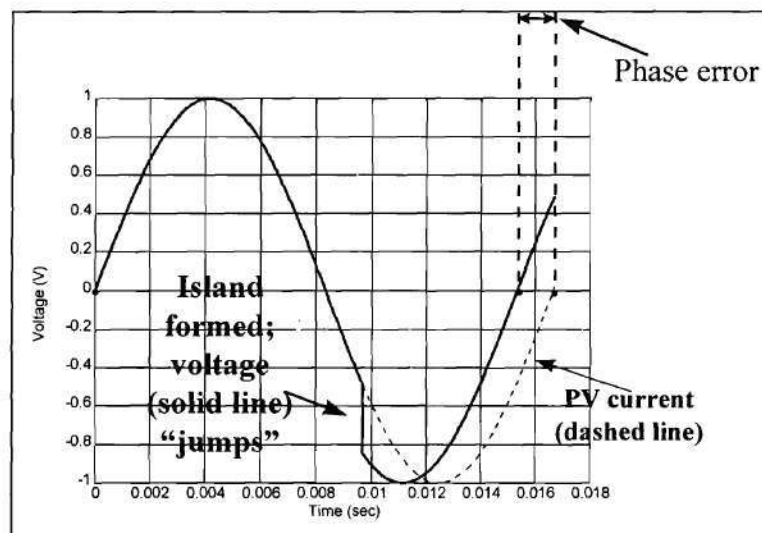
Figure 25. Figure explaining the operation of the phase jump detection method.

One of the biggest advantages of PJD is ease of implementation. Since the PV PCU requires a PLL for utility synchronization anyway, all that is required to implement PJD is to add a device which deactivates the PCU if the filtered output of the phase comparator exceeds some threshold. Unfortunately, PJD clearly has an NDZ for unity dpf loads, within the existing NDZ of the four standard relays; a load with a zero phase angle at the utility frequency will not produce a phase error when the utility is

disconnected. This NDZ can be moved away from the unity-dpf load region by operating the PCU at a nonunity power factor, but this requires the PCU to be capable of bidirectional power flow, which would make it more expensive. An additional difficulty, similar to the harmonic detection case, is that it is difficult to choose thresholds which provide reliable islanding detection but do not result in frequent nuisance trips. The starting of large loads, particularly motors or other loads with large reactances, often causes transient phase jumps of significant size, and these will deactivate the PV system if the thresholds are set too low. PJD thresholds could be altered for a given installation site, but such site-specific parameters increase the difficulty in installing utility-interactive PV systems.

Slide-mode frequency shift

In the slide-mode frequency shift (SMS) method, the current-voltage phase angle of the PCU, instead of always being controlled to be zero, is made to be a function of the frequency of v_a as shown in Figure 26 [31]. The S-shaped phase response curve of the PCU is designed such that the phase of the inverter increases faster than the phase of most unity-dpf loads in the region near the utility frequency ω_0. This makes ω_0 an unstable operating point for the PCU [31]. While the utility is connected, it stabilizes the operating point ω_0 by providing the phase and frequency reference. However, after the switch opens, the phase-frequency operating point of the load and PV system must be at an intersection of the load line and PCU phase response curve. Consider the load line of the unity-dpf load shown in Figure 26. The load line and PCU curve intersect at $(\omega_0, 0)$, but if there is any small perturbation of the frequency of v_a away from ω_0, the instability of the PCU at ω_0 causes the PCU to reinforce the perturbation and drive the system to a new operating point, either at ω_1 or ω_2 depending on the direction of the
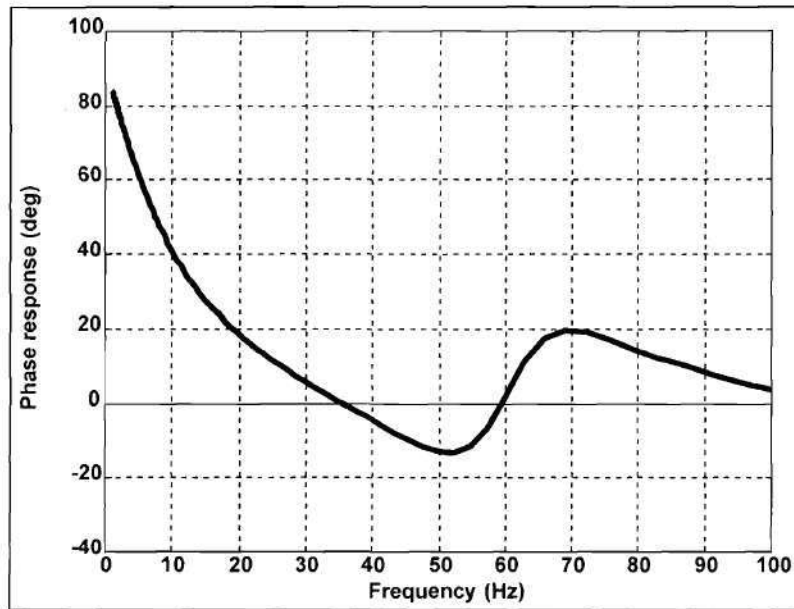
Figure 26. Plot of the phase vs. frequency characteristic of a PCU utilizing the SMS islanding prevention method.

perturbation. The PCU phase curve can be designed in such a way that ω_1 and ω_2 lie outside the NDZ of the OFR/UFR.

SMS is implemented through the design of the input filter to the PLL. To understand how SMS works, consider the PLL-parallel RLC load system under islanded conditions, shown schematically in Figure 27. At Point 1, the physical signal of interest is the PV system output current i_{PV}, which is a scaled copy of the PLL's output waveform (the gain block between the PLL and the load, which contains the switching command generator, MPPT, and PCU power stage, is not shown). It is assumed that i_{PV} may be represented by a phasor, $I_{PV} \angle \phi_{PV}$. The parallel RLC load has transfer function $Z \angle \phi_Z$, and it "converts" i_{PV} to v_a, which is the signal of interest at Point 2. The transfer function of

71
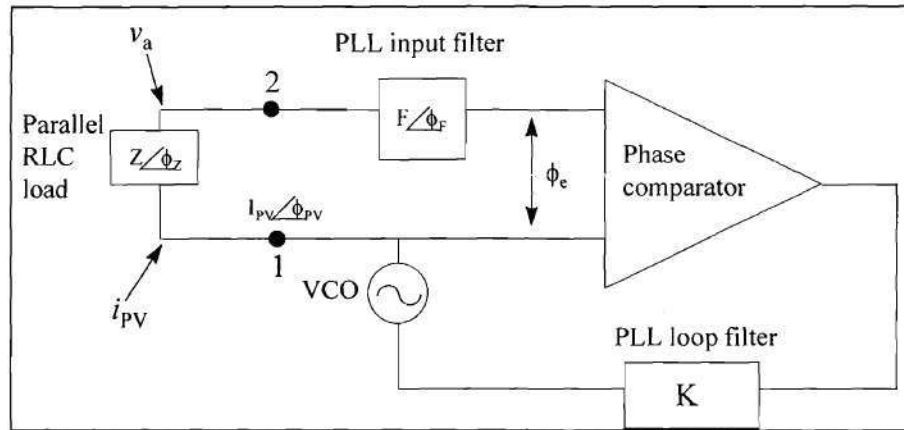
Figure 27. PLL schematic redrawn to explain the SMS islanding prevention method.

the input filter to the PLL is denoted $F\angle\phi_F$. Since this transfer function acts on the phase of the reference signal for the PLL, the phase response of this transfer function will be the phase response of the PLL and therefore of the PV PCU. The transfer function $F\angle\phi_F$ is designed such that it has the phase-frequency characteristic shown in Figure 26. The phase characteristics of the loop filter are ignored, so the loop filter is represented only by a gain K. The zero phase reference will be taken at Point 1 in the figure, so $\phi_{PV} = 0$. If one proceeds around the loop from Point 1 to Point 2, through ϕ_e, and back to Point 1, one finds that

$$\phi_e = \phi_F + \phi_Z \tag{33}$$

This means that the condition for steady state, i.e. the condition under which $\phi_e = 0$, is $\phi_F = -\phi_Z$. The phase vs. frequency characteristics of parallel RLC loads generally have

72

negative first derivatives; that is, they slope downward from left to right, as shown in Figure 28 for two RLC loads with the indicated parameters.

With this background, consider first the case in which the PLL input filter does not have SMS. In this case, $\phi_F = 0$ for all ω. If the frequency in the island were perturbed upward, the PLL would detect a negative phase error and would reduce its frequency to bring i_{PV} and v_a into phase. Now consider the case in which the phase versus frequency characteristic of $F\angle\phi_F$ is the SMS curve in Figure 26. When the frequency increases, ϕ_z becomes negative, but ϕ_F becomes positive and has a larger magnitude than ϕ_z. Therefore, ϕ_e is positive, and the PLL increases its frequency. The PLL's control action acts *in the wrong direction* to correct the phase error. This condition persists until $\phi_F = -\phi_z$. This demonstrates the instability of SMS; it acts to drive the operating point of the system away from the utility frequency, because the SMS phase increases *faster than* and *in the opposite direction from* the phase of the RLC load.

This scheme has been shown to be highly effective, both theoretically and experimentally [31]. It works for purely resistive loads, whose phase response curves lie on the frequency axis in Figure 26. It also works for a wide range of RLC loads. However, it is known [36] that some RLC loads have phase response curves such that the phase of the load increases faster than the phase of the PV PCU. This makes the nominal line frequency a stable operating point and renders SMS ineffective. We have performed computer modeling to demonstrate this fact, and the results are shown in Figure 29 and Figure 30. In these simulations, an SMS phase response curve from a commercial inverter [31] is plotted against the phase responses of several parallel RLC loads. To avoid confusion brought on by the minus sign in the equilibrium condition $\phi_F = -\phi_z$, in plots of this type the RLC frequency response curves are shown inverted (multiplied by -1). In this way, to find loads for which SMS fails one must simply look
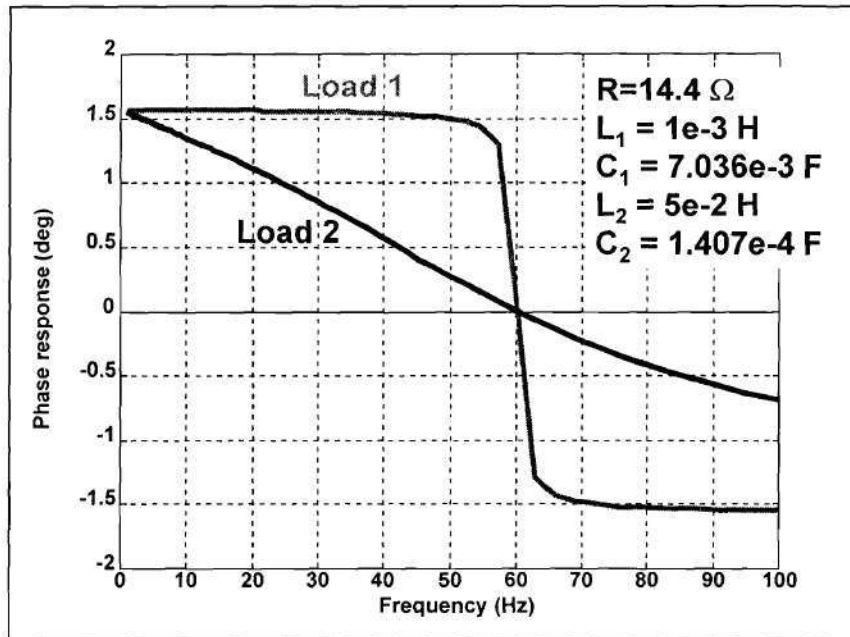
Figure 28. Phase vs. frequency behavior of parallel RLC loads.

for loads with phase curves with a larger slope than the phase curve of SMS. These examples show that SMS has an NDZ for RLC loads with relatively small values of L but large values of C (Figure 29), or low-power loads in which R is large (Figure 30). An additional problem with SMS is that it relies on an uncontrollable, externally-supplied perturbation, which makes predictions of the run-on time of an SMS-equipped PV system difficult. Theoretically, if a situation were to arise in which there were no perturbation at all, SMS could fail for nearly any load. However, since only tiny perturbations are necessary and since such perturbations are always present in practice due to such factors as noise and measurement inaccuracy, nondetection due to a lack of a perturbation is not a concern in actual systems.
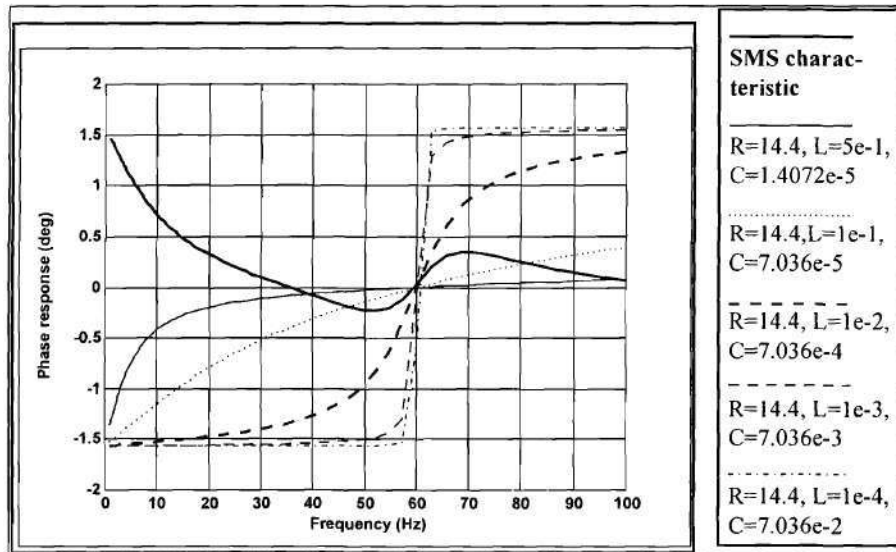
Figure 29. Plot of an actual SMS phase-frequency characteristic and the phase responses of several RLC loads. The dark S-shaped curve is the SMS phase characteristic; the other curves are the RLC phase responses (inverted; see Equation (33)). R is held fixed; L and C are varied, maintaining unity power factor at 60 Hz. For the bottom three loads in the legend, SMS cannot detect islanding.
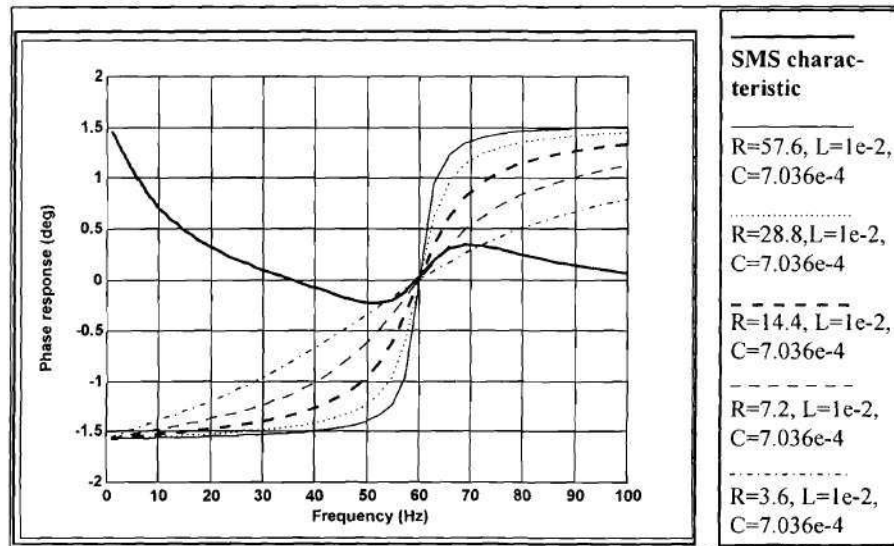
Figure 30. Plot of an actual SMS phase-frequency characteristic and the phase responses of several RLC loads. The dark S-shaped curve is the SMS phase characteristic; the other curves are the RLC phase responses (inverted; see Equation (33)). L and C are fixed and resonant at 60 Hz; R is varied. For the top two loads in the legend, SMS cannot detect islanding.

Methods of reducing the NDZ: Active methods

In order to eliminate the shortcomings of the passive NDZ elimination methods, several active methods have been developed. Active methods involve changing the system configuration or control of i_{PV} in such a way as to cause a change in v_a when islanding. The active methods include:

Output variation or "impedance measurement"

Since the PV system appears as a current source to the utility supplying current

$$ i_{PV} = I_{PV} \sin\left(\omega_{PV}t + \phi_{PV}\right) \tag{34} $$

there are three output parameters that may be varied: the amplitude I_{PV}, the frequency ω_{PV}, and the phase ϕ_{PV}. In the output variation method, a variation is continuously imposed upon one of these parameters [40]. If the utility is disconnected, this variation will force a detectable change in v_a that can be used to prevent islanding. In effect, the PCU is measuring dv_a/di_{PV}, and for this reason this method is often called the impedance measurement method [45]. Its primary advantage is that theoretically it has no NDZ; for a single PV system with any local load, if the load and PV powers are balanced upon disconnection of the utility, the output variation of the PCU will upset this balance and cause the UVR to trip. However, output variation has significant disadvantages. One of the most serious is that its effectiveness decreases in the multi-inverter case. This happens even if all PCUs in the island are using output variation, unless the variation is somehow synchronized. The reason is that as more PCUs are added to the island, the amount of variation introduced by each PCU into the total i_{PV} being generated by all PV systems is reduced, and eventually the variation becomes so

77

small that the change in v_a becomes undetectable. This phenomenon is demonstrated in Figure 31. In the top panel, a single PCU's output is shown. This system is designed to reduce its output power by 20% every 20 time units. This single PCU probably would not island if feeding a single load, because the 20% power drop would most likely lead to a large enough drop in voltage to trip the UVR. For example, considering a resistive load and utilizing the expression $V^2 = RP$, where P is the PV power, the 20% power reduction would lead to almost an 11% reduction in voltage, larger than the 8%
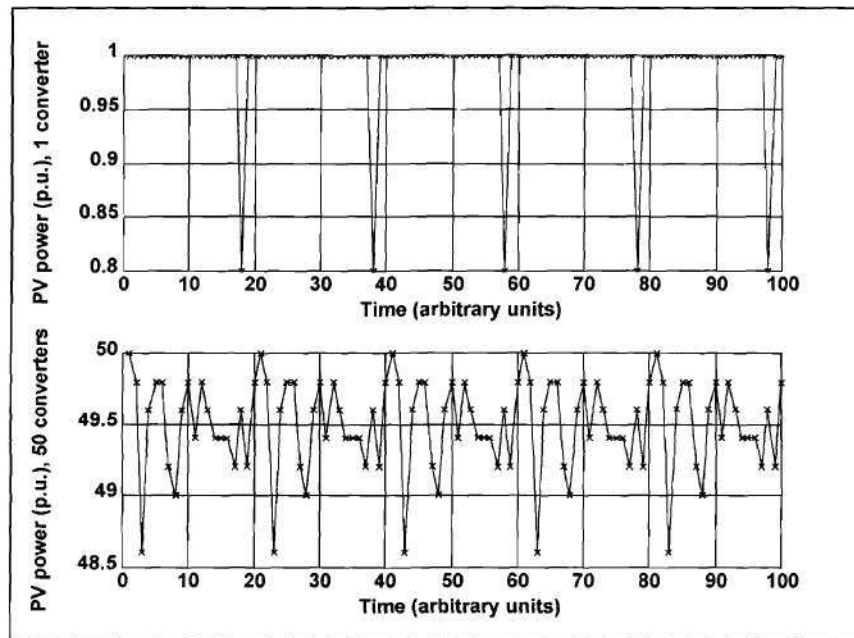
Figure 31. Demonstration of the failure of the impedance measurement method in the multiple-inverter case.

78

reduction required by IEEE-P929 for an undervoltage trip [35]. However, the lower panel shows the power production of 50 PCUs, all identical to the one in the top panel except that their 20% power "dips" are not synchronized. The maximum variation from the mean power production of the 50 PV systems is less than 2%, and the UVR no longer detects a trip condition. Also, output variation can lead to grid instability, voltage flicker, and several other problems. These problems would all worsen for increases in either the level of PV power or the utility source impedance.

These difficulties imply that output variation is not suitable either for multiple small systems or for single large systems. It can be a very reliable islanding detection method, but only in the case in which the PV power production is much less than the load's power demand and only one PCU is connected in the potential island. These disadvantages have led many to conclude that this method is of little practical value [46].

Reactance insertion

The reactance insertion method [26,27] is unique among islanding prevention methods in that it does not rely on the PCU to detect the islanding condition. Instead, a large reactance, usually a capacitor bank, is installed on the utility system inside the potential island at point **b** as shown in Figure 32. The switch is normally open. When the recloser opens, the capacitor bank switch closes after a short delay. This causes a sudden drop in ω_{res}, leading to a frequency decrease that the UFR can detect. This method offers several advantages. It is highly effective in preventing islanding [26,27] as long as the small delay is allowed between the time of recloser opening and the time of capacitor insertion to ensure that insertion of the capacitor will not actually create a balanced situation between the PV system and a lagging load. Capacitors of this type are readily available, and utilities have a great deal of experience with them. The same

79

capacitor bank could also be used for reactive power (voltage) support, with only minor changes in the switching logic to allow it to maintain its anti-islanding function. However, two readily-apparent drawbacks to the reactance insertion method are: 1) there may be multiple switches in series leading into the potential island, meaning that each series switch might need to be equipped with a switchable capacitor bank (depending on the load configuration); 2) this method cannot prevent short-term islanding, partially because of the speed of action of the capacitor switches and partially because of the necessary delay in switching. This method actually has a third problem that is more political than technical: it requires the installation of equipment on the utility side of the point of common coupling, which is usually taken to be the utility's electric meter. Utilities generally look unfavorably on such an arrangement.
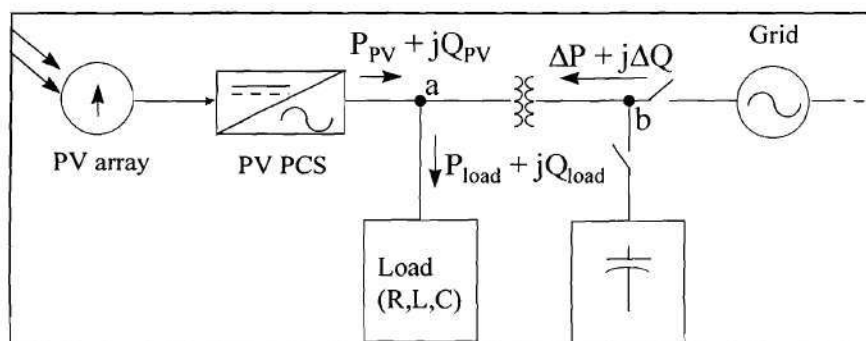
Figure 32. The reactance insertion method. This is the configuration of Figure 21, now equipped with a switchable capacitor bank at point b.

Power line carrier communications

Another intriguing possibility for islanding prevention is the use of power line carrier (PLC) communications systems. A complete treatment of these systems is beyond the scope of this thesis, but the method offers sufficient promise that mention of the use of PLC communications for islanding prevention is warranted. In PLC systems, communications signals are sent directly over the power lines; that is, the power lines themselves are the communications channel. If some sort of standardized control signal were sent from a point "upstream" from the switch (that is, from a point nearer to the utility voltage source), then a receiver in the PV PCU could test the continuity of the line by simply checking to see whether this signal was still being received. If the switch is opened, the signal path is disrupted, the PCU detects the loss of the control signal, and PCU operation can be safely discontinued. This method has a great deal of support in the PV community [47].

One of the primary strengths of PLC communications for islanding prevention, and the main reason for the interest in it, is that its behavior is theoretically independent of the makeup of the load, and therefore it should have no NDZ. In addition, the number of PCUs in the island should also have no effect on the operation of the PLC system, and thus the multiple-inverter problem is overcome by this method. Finally, such a system could be used for much more than islanding prevention. Many different types of control and integration would be possible, and the system would be applicable to all types of independent generation, not just PV. However, several significant challenges must be overcome before PLC communications could be applied to islanding prevention:

1.) The communications signal must contain information that cannot be accidentally reproduced by loads in the island, and have a high transmission rate which enables

81

rapid islanding detection. In other words, simply sending a carrier wave of unusual frequency would be insufficient as this sort of signal can be reproduced by many types of loads, including power electronics and asymmetrically-loaded motors.

2.) The signal would have to be standardized, and either all utilities would have to agree to provide it, or the PV system installer would be required to install a PLC transmitter somewhere within the utility's system "upstream" from any switches which have a probability of creating an island.

3.) The signal must be able to pass through all of the components of the distribution system, including transformers, without experiencing unacceptable attenuation. This means that the frequency selected will have to be fairly low, since the series inductances of transformers block the propagation of high-frequency signals.

4.) The amount of bandwidth available on the power lines is very limited, partially because of the behavior of distribution transformers just noted, and utilities may wish to use this bandwidth for other purposes including automated meter reading and load control [48,49], and in fact commercial systems for this application have already been developed. These other uses for the bandwidth result in economic benefits to the utility, whereas using the bandwidth for islanding prevention does not.

It is the belief of the author, after having studied islanding and islanding prevention methods extensively, that PLC communications are the best islanding solution and should be studied and promoted vigorously. However, the second and fourth drawbacks listed above are very serious. Many utilities have stated flatly that they will not allow any PLC signals on their systems, often referring to such signals as "pollution". Those that are willing to use PLC systems have expressed understandable reluctance to surrender valuable bandwidth for a purpose which presently has very few

applications and does not economically benefit the utility, when the other possible purposes have literally millions of potential applications that increase the profitability of the utility [48,49].

Active Frequency Drift

One active method that has received recent attention is the active frequency drift (AFD) or frequency bias method [46], a method that is easily implemented in a PV power conditioner with a microprocessor-based controller. In this method, the waveform of the current injected into node **a** by the PV system is slightly distorted such that, when islanding occurs, the frequency of v_a is forced to drift up or down, augmenting the "natural" frequency drift indicated by Equation (28). An example of a PV output current (i_{pv}) waveform that implements upward AFD is shown in Figure 33, along with an undistorted sine wave for comparison. T_{Vutil} is the period of the utility voltage, T_{Ipv} is the period of the sinusoidal portion of the current output of the PV system, and t_z is a dead or zero time. The ratio of the zero time t_z to half of the period of the voltage waveform, $T_{Vutil}/2$, is referred to as the "chopping fraction" (cf):

$$cf = \frac{2t_z}{T_{Vutil}} \tag{35}$$

During the first portion of the first half-cycle, the PV system's current output is a sinusoid with a frequency slightly higher than that of the utility voltage. When the PV output current reaches zero, it remains at zero for time t_z before beginning the second half cycle. For the first part of the second half-cycle, the PV output current is the negative half of the sine wave from the first half-cycle. When the PV current again reaches zero, it remains at zero until the rising zero crossing of the utility voltage. It is
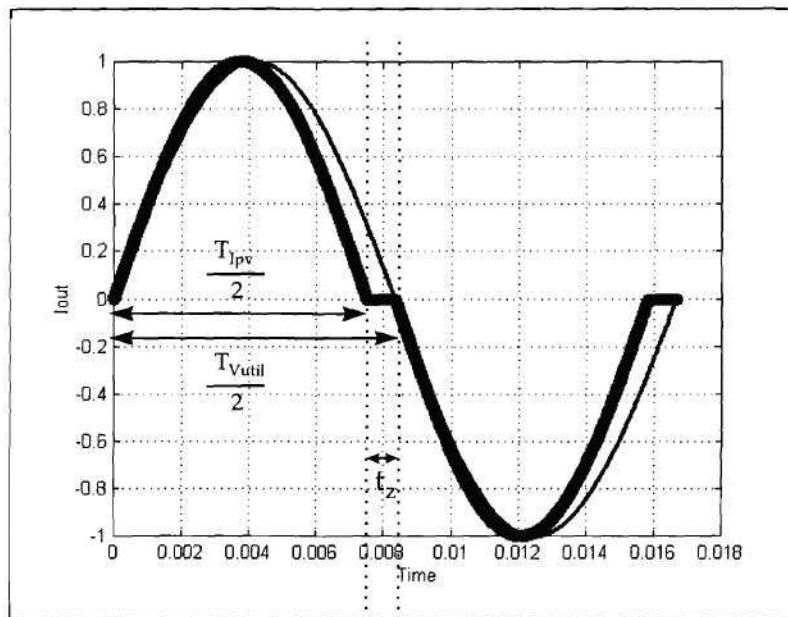
Figure 33. **Example of a waveform used to implement the AFD method of islanding prevention. A pure sine wave is also shown for comparison.**

important to note that the zero time in the second half cycle is not fixed and need not equal t_z. Such a waveform is implemented using a PLL with a digital waveform reference generator.

When this current waveform is applied to a resistive load, its voltage response will follow the distorted current waveform and go to zero in a shorter time ($T_{Vutil} - t_z$) than it would have under purely sinusoidal excitation. This causes the rising zero crossing of v_a to occur sooner than expected, giving rise to a phase error between v_a and i_{PV}. The PV system then increases the frequency of i_{PV} to attempt to eliminate the phase error. The voltage response of the resistive load again has its zero crossing advanced in time with respect to where it was expected to be, and the PV system still detects a phase

84

error and increases its frequency again. This process continues until the frequency has drifted far enough from ω_0 to be detected by the OFR.

Experiments have been conducted on PCUs equipped with upward-drifting AFD for purely resistive and for RC loads [46]. It has been shown that, as expected, AFD prevents islanding for purely resistive loads. However, it fails for RC loads with small amounts of capacitance. The reason for this is that a slightly capacitive load will have a tendency to drive the frequency downward, and if the value of the capacitance is exactly right this downward drifting tendency will exactly cancel the upward-drifting tendency being caused by the converter. Another problem with AFD is that, if its use is to be widespread, there must be agreement among manufacturers and standards-making bodies as to whether PCUs should cause the frequency to drift up or down. Otherwise, in the multiple-inverter case, it would be possible to have some PCUs in an island attempting to increase the frequency while being counteracted by other PCUs attempting to decrease the frequency. It has been very difficult to achieve such agreement for a variety of reasons [47]. AFD has not been studied for other types of loads, including RLC, nonlinear and motor loads.

Summary of existing islanding prevention methods

Table 3 summarizes the islanding prevention methods discussed here. Each islanding prevention scheme is categorized according to the types of load conditions under which it can prevent islanding, and the "Remarks" column addresses issues not easily quantified elsewhere in the Table. It is clear from the Table that no "perfect" islanding prevention scheme has yet been devised; all existing methods involve a tradeoff between effectiveness in islanding prevention, power quality, simplicity and cost-effectiveness. None of the methods simultaneously meets all three of the goals defined previously.

Table 3. Comparison of existing islanding prevention methods.

		Islanding protection[b]: Under which of these conditions does the given method protect against islanding?				
Islanding protection method	Works in multi-inverter case?[a]	$\Delta P^-\neq 0$	$\Delta Q^-\neq 0$	$\Delta P^-=\Delta Q^-$ ≈ 0, purely resistive load	$\Delta P^-=\Delta Q^-$ ≈ 0, resonant RLC load	Remarks
OVR/UVR	**Yes**	**Yes**	No	No	No	Small NDZ around $\Delta P^-=0$ because thresholds cannot be set arbitrarily small
OFR/UFR	**Yes**	No	**Yes**	No	No	Small NDZ around $\Delta Q^-=0$ because thresholds cannot be set arbitrarily small
PJD	**Yes**	No	**Yes**	No	No	Can be highly effective, but NDZ lies within that of OFR/UFR, OVR/UVR
Harmonic detection	**Yes?**	See re-marks	See re-marks	See remarks	See remarks	Detection not dependent on power matching, but rather on THD of v_a. Threshold setting is a problem for this method.
Output variation/im-pedance meas	No	**Yes**	**Yes**	**Yes**	**Yes**	Fails in multi-inverter case, can cause stability/flicker problems for large PV systems, reduces system efficiency
SMS	**Yes?**	No	**Yes**	**Yes**	**Yes**	Experimentally shown to be highly effective, but has NDZs for low-power loads and low L, high C loads
AFD	**Yes?**	**Yes**[c]	**Yes**	**Yes**	No	Ineffective for low L, high C loads that are near unity dpf at utility frequency; requires output current distortion
Reactance insertion	**Yes**	**Yes**	**Yes**	**Yes**	**Yes**	Requires installation of equipment on utility side of point of common coupling; cannot prevent short-term islanding.

[a]Assuming all inverters to be using the same islanding prevention scheme. If multiple schemes are used, the particular combination in question would have to be analyzed. A question mark denotes that in theory the method should be effective in this case but no modeling or simulation data is available.

[b]These columns describe the load circumstances *under which each scheme is **designed** to prevent islanding.*

[c]Success of these methods depends strictly on the L-C makeup of the load; they will work for any ΔP^- if phase conditions are met.

Subtask 2.1: Determination of the probability of encountering a load within the NDZ of the four standard relays

Background

As was mentioned in the Literature Search, there is considerable disagreement within the PV community as to whether there is actually a need for the advanced islanding prevention techniques described in the previous section. PV PCU manufacturers obviously want to avoid adding islanding prevention schemes into their PCUs which are excessively expensive and complex, and which degrade the output power quality of the PCU. One very common argument made by PCU manufacturers and PV advocates is that islanding is of no concern because in all practical cases the four standard relays, the OFR/UFR/OVR/UVR, will prevent islanding. This is equivalent to stating that no real-world loads exist which match the PV system's power output and which have resonant frequencies near the utility frequency, the emphasis being on the latter half of this argument. However, utilities are reluctant to accept this argument because real-world loads can have parameter values spanning a very wide range, meaning that the claim that the four standard relays alone provide adequate islanding protection is on shaky ground at best without some sort of verification.

The purpose of the work under Subtask 2.1 is to investigate the accuracy of this claim. This will be accomplished by attempting to quantify the probability of encountering a load on a utility system that lies within the NDZ of the four standard relays, a quantity referred to as the "NDZ probability". This study indicates that practical conditions exist under which the NDZ probability can be significant and

87

suggests that additional islanding prevention measures beyond the four standard relays are in fact necessary.

Methodology

As previously discussed, the existence of the conditions that could lead to a failure of the four standard relays to detect islanding corresponds to an event where the real powers of the PV system and load are closely matched, *and* the load's resonant frequency falls within the trip limits of the OFR/UFR. In order to calculate the probability of this occurrence, a realistic method for representing the load was first established.

Ideally, this representation would be as accurate but still as general as possible. Recall from the literature search that whether the OVR/UVR can detect islanding depends on the match between the PV and load real power, and the criterion for whether an (RLC) load lies within the OFR/UFR NDZ is whether its resonant frequency lies within the OFR/UFR trip thresholds. Therefore, if $R(t)$, $L(t)$ and $C(t)$, the operating voltage of the load, and $P_{PV}(t)$ were known as functions of time, the probability of that load being within the NDZ of the four standard relays could be determined with good precision. Load parameter measurements of this type have been made by others for a wide variety of loads, but unfortunately this data was unavailable for use in this study. An attempt was made to circumvent this problem by synthesizing the necessary parameters, but it was quickly realized that the probability of the existence of the conditions for OFR/UFR/OVR/UVR failure could be made to be almost anything by proper selection of the parameters, particularly the load dpf. Clearly, real-world dpf data was required. As a partial solution to this problem, measured real and reactive power (P and Q) data was collected from a number of U.S. utility companies. The utilities supplied P and Q data from recorders monitoring feeders in their distribution systems. It is important to note that this data is measured at the substation level (13.5-

45 kV), and therefore represents the characteristics of an aggregate load. For maximum accuracy and statistical significance, data sets were selected that had measurements at 15 minute or shorter intervals and spanned at least one year. The utilities also supplied the location at which the measurements were made and a general description of the load composition (residential, commercial, industrial, and whether power factor correction capacitors [PFCCs] were employed on the feeder being monitored). Data was collected for primarily residential loads, with some light commercial load allowed. (This was necessary because almost all of the residential-area data sets available had some small amount of light commercial load, representing neighborhood grocery stores, gasoline stations, etc. The amount of light commercial load was restricted to less than 10% of the total load on the feeder in this study). Data sets were collected from urban areas with and without PFCCs, and from rural areas.

It is of critical importance that the reader understand the usage of the measured data in this study. There are two parameters which are of primary interest: the load's demand shape and displacement power factor, both as functions of time. Recall that attempts were made to find data which models as accurately as possible the residential load in which this study is primarily interested, but R(t), L(t), and C(t) data, or even P and Q data, measured at the residential level was unavailable for this study. The data used here is a compromise, and the assumption is explicitly being made that the aggregate load characteristics can be accurately applied to individual loads.

Next, the output of a PV system at the location of the measured data was simulated. In each case, the PV system was oriented due-south with latitude tilt. PV system simulations were carried out using the program PVGRID with meteorological data from the TMY2 database. PVGRID supplies hourly PV system power outputs. Linear interpolation was used to obtain sub-hourly values for comparison with the sub-hourly utility data. In the PV system simulations, the values used for the various loss

89

mechanisms were the same as those used for our simulations of the GTAC PV system (see Table 1).

Then, criteria were derived in terms of the available parameters to determine whether the load demand and PV output at a given time point were matched. The criterion for a real power match was derived by assuming that all of the real power is dissipated in the resistive part of the parallel RLC load. Given a real power measurement P_k at time k, and assuming a utility voltage V_0, the value of the resistance at time k is

$$R_k = \frac{V_0^2}{P_k} \tag{36}$$

If the utility were suddenly disconnected, assuming that the PV system acts as a current source, the new PV system terminal voltage V_k is determined by R_k and the PV system power output $P_{pv,k}$ at time k according to

$$V_k = \sqrt{R_k P_{PV,k}} \tag{37}$$

Substituting (36) into (37) gives

$$\frac{V_k}{V_0} = \sqrt{\frac{P_{PV,k}}{P_k}} \tag{38}$$

Using the known threshold values for the OVR/UVR, which are 92% and 110% of the nominal voltage V_0 [35], we can therefore determine whether a real power match exists at a given time point k by checking whether the expression

$$(0.92)^2 \le \frac{P_{PV,k}}{P_k} \le (1.1)^2 \tag{39}$$

is satisfied. If this expression is true, the voltage relays will not detect islanding.

A "reactive power match" exists if the resonant frequency of the load, ω_{res}, lies within the frequency trip thresholds of the OFR/UFR. However, ω_{res} cannot be determined from the available P and Q data. The load displacement power factor (dpf) can be obtained as follows:

$$dpf_k = \cos\left\{\tan^{-1}\left[R_k \cdot \left(\omega_0 C_k - \left(\omega_0 L_k\right)^{-1}\right)\right]\right\} = \frac{P_k}{\sqrt{P_k^2 + Q_k^2}} \tag{40}$$

but unfortunately the dpf at the utility frequency ω_0 is not a unique function of ω_{res}. This can be shown using Equation (40) together with the fact that $\omega_{res} = (LC)^{-0.5}$ as follows:

$$dpf_k = \cos\left\{\tan^{-1}\left[\omega_0 R_k C_k\left(1 - \frac{\omega_{res}^2}{\omega_0^2}\right)\right]\right\} \tag{41}$$

If ω_{res} is set equal to one of the trip thresholds, the dpf obtained will be that of a "boundary load"; that is, a load on the boundary of the NDZ of the OFR/UFR. There are

many different C_k values, corresponding to different values of L, that give the same ω_{res}, but each of these will give a different value of dpf. This problem is illustrated in Figure 34, which shows the results of Equation (41) for several values of C and R and with ω_{res} set equal to the frequency trip thresholds of the OFR/UFR, which are 59.5 Hz and 60.5 Hz [35]. Each curve in Figure 34 is actually a pair of curves lying atop each other, one corresponding to loads with a 59.5-Hz resonant frequency (a leading dpf at 60 Hz), the other corresponding to loads with a 60.5-Hz resonant frequency (a lagging dpf at 60 Hz). Each pair of curves corresponds to a different value of R, and Equation (41) shows that the region above each pair of curves (at higher dpf values) is the region of loads for which the OFR/UFR will fail to detect islanding, since the ratio of ω_{res} to ω_0 approaches 1 as dpf increases. The range of C on the x-axis, 1 μF to 1 mF, is believed to correspond to that which is practical. Values of C in the hundreds of μF range are possible when cable capacitances, dynamic load characteristics, and PFCCs are taken into account [48,49, 50,51,62]. Values of C smaller than the 1 μF value at the origin of the x-axis may be possible as well, but the values of L required to resonate with them would be in the single-digit henries range, which is probably larger than is possible in practice. The possible range of R values is thought to be from about 5 Ω to around 250 Ω, which at 240V (typical residential service voltage) translates into a power range of about 11.5 to 0.23 kW [52].

Several facts become apparent from Figure 34. First, the previously mentioned problem, that dpf is not a unique function of resonant frequency, is evident. This means that it is not possible to determine precisely the probability of the conditions for failure of the OFR/UFR/OVR/UVR from the available data. Also, note that the dpfs of these boundary loads begin to drop rapidly as the capacitance increases, indicating that the range of RLC loads that could cause the OFR/UFR to fail is increasing. The dpfs of the boundary loads also decrease with increasing resistance (decreasing real power).

Even though a unique dpf threshold for the OFR/UFR cannot be set, the highest and lowest possible values of dpf threshold can be found from Equation (41) or Figure 34, since maximum and minimum values of R_l, L_l, and C_l have been determined. Also, note from Figure 34 that if it is assumed that the load parameters remain within a narrow range for any given load, then the frequency thresholds of the OFR/UFR may be approximated by a dpf threshold; that is, the curves shown may be approximated by a straight line over a narrow range of C_l and R_l. In equation form, the criterion for this condition is

$$\frac{P_k}{\sqrt{P_k^2 + Q_k^2}} \geq \left[\text{dpf threshold}\right] \tag{42}$$

These facts allow the following procedure to be adopted. By assuming that the load falls within a narrow range about the smallest possible values of R_l and C_l, which yields the highest possible value of the dpf threshold, the lowest probability of the load falling into the NDZ for the given P and Q data may be calculated. This highest possible dpf threshold is virtually equal to 1. Similarly, by assuming the load to have R and C that remain near the largest possible values (upper bounds), yielding the lowest value of dpf threshold, the highest possible probability of the load falling into the NDZ for the given data may be found. Equation (41) shows that this lowest possible dpf threshold is about 0.54; however, this is considerably less than the minimum value of load dpf ever observed in the utility data. When the dpf threshold value becomes less than the minimum load dpf, the OFR/UFR will *always* fail, and the probability of failure conditions is no longer dependent on the dpf threshold, being limited only by the real power criterion. It is therefore unnecessary to calculate probabilities for any value of
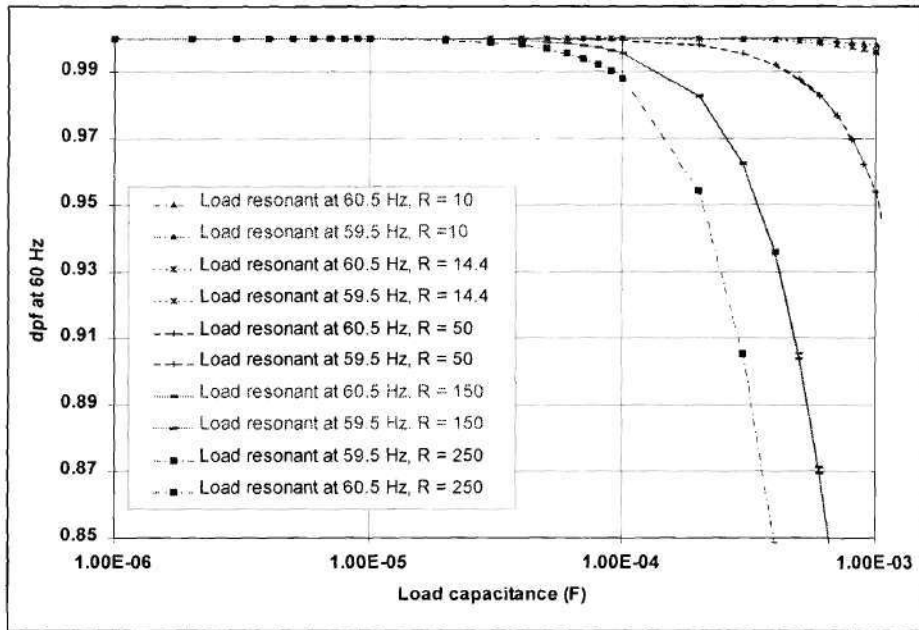
Figure 34. 60-Hz dpfs of loads whose resonant frequencies correspond to the OFR/UFR trip limits of ±0.5 Hz. Pairs of curves correspond to different values of R.

dpf threshold less than the minimum dpf found in the load data set. The probabilities found using the minimum and maximum dpf thresholds will *span the range* of possible probabilities for the given load data. Note that these extreme R and C values will not be the most likely ones. The most **likely** range of capacitances is expected to be 1e-5 F to 1e-4 F [48,49,50,51], and the most likely range of resistances should be from about 10 Ω to about 250 Ω [52]. With these values, the most **likely** range of dpf criteria falls between 0.988 and 0.9999998, still quite a wide range.

For clarity, let us review the assumptions that have been made here.

1.) The load can be represented by a parallel RLC circuit.

2.) The OFR/UFR/OVR/UVR thresholds are set according to the recommendations in the IEEE-P929 prestandard [35].

3.) The P-Q data acquired from the utilities adequately represents a typical residential load. For example, the residential load data acquired for a small city without PFCCs is representative of residential loads that meet this same description, regardless of size (power consumption).

4.) The practical ranges of R, L and C are as given above.

In this study, two different sets of probabilities were calculated. The first is the total probability of simultaneous satisfaction of both criteria (Equations (39) and (42)) during all daylight hours over the entire period over which the data was taken, as a function of PV system size, for several different values of dpf threshold that span the range of practical values. This probability is referred to as the "total NDZ probability". "Daylight hours" are defined as any hour in which the PV system is producing nonzero power, as predicted by PVGRID. In order to calculate this probability, a MATLAB program was written that compares the measured load P and Q data and modeled PV data point-by-point, checking at each point to see whether the criteria are met. If they are, a counter is incremented, and at the end of the simulation the probability is computed as the total number of points at which both criteria are met divided by the total number of time points.

However, the matching of PV and load powers can be modeled as a random process, meaning that the probability of simultaneously meeting both criteria is not constant but varies as a function of time of day. To reflect this, the conditional probability that both criteria will be met as a function of time of day has also been

found for several different values of PV system size. This probability is called the "conditional NDZ probability" and was calculated by limiting the data set to all the points that fall within a time interval and repeating the above-described procedure on this limited data set.

At this point, note that this study makes no assumptions about the stability of an island, or whether upon utility disconnection a transient may occur that would alter the system's behavior. For example, during the transient after the utility is disconnected, the load's reactive power requirements will be supplied from the energy storage (capacitors) in the output of the PV PCU(s), and clearly there is a limit to the amount of Q the PV system(s) can supply. This fact has been ignored.

Results

The total NDZ probabilities, taken over the entire measurement period for three different data sets, are shown in Figure 35, Figure 36, and Figure 37 as a function of the PV system size. Three data sets were used:

- Data Set #1, from a small city, primarily residential, without PFCCs;

- Data Set #2, from a major metropolitan area, residential, with PFCCs;

- Data Set #3, from a rural area, primarily residential but with large (10-30 hp, or 7.46-22.4 kW) induction motors driving pumps and no PFCCs.

For generality, the PV system size has been normalized by the average real power demand of the load over the entire measurement period. The four dpf threshold values used in each figure correspond to the minimum dpf of the measured load, the dpfs that bound the range of "most likely" dpfs just described, and the maximum practical dpf, also described previously. In all cases the probability of matching of both criteria is zero for PV systems whose power ratings are much smaller than the load's average real power demand, no matter what dpf threshold is selected, because a real power match is never achieved. Figure 35 shows the total NDZ probability using data

taken from Data Set #1. The total NDZ probability vanishes for all PV system sizes for a dpf threshold greater than about 0.99995, but reaches 20% for a dpf threshold of 0.8701, the minimum dpf of the load. At the low end of the range of "likely" dpf thresholds, the probability reaches about 1.6% for a PV system rated at 120% of the load's average real power demand. In Figure 36, Data Set #2 is used. In this case a log-lin plot has been used because even for a dpf threshold of 1.0, the probability is nonzero. Also, note that the total NDZ probabilities over the "likely" range of dpf thresholds are almost the same as the range spanned by the extreme values. Finally, Figure 37 shows the total NDZ probabilities calculated using Data Set #3. A major portion of the load in this location is three-phase induction motors powering irrigation pumps, and their low power factor has the expected effect on the total NDZ probability: it remains at zero until the dpf threshold is relatively low (~0.99). However, it exceeds 2% for the lowest value of "likely" dpf threshold and reaches nearly 16% when the dpf threshold is equal to the minimum load power factor. The figures clearly show that it is possible for the total NDZ probability to be significant under real-world conditions. Even for the low-dpf load shown in Figure 37, a significant total NDZ probability can be obtained for reasonable values of dpf threshold.

The results of computing the conditional NDZ probability for the same three data sets are shown in Figure 38, Figure 39 and Figure 40, and the results in Figure 38 are reproduced in three-dimensional format in Figure 41. The most important conclusion demonstrated by these figures is that the probability of the failure conditions is in fact a function of time, and as a function of time of day it can be many times the daylight-
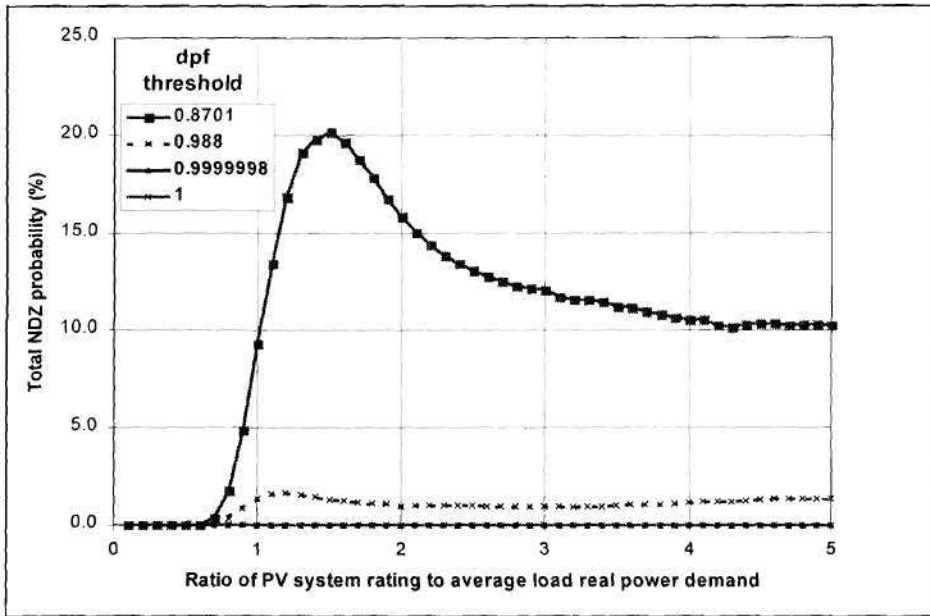
Figure 35. Total NDZ probability as a function of (normalized) PV system size, for several different values of dpf threshold. Data from Set #1.
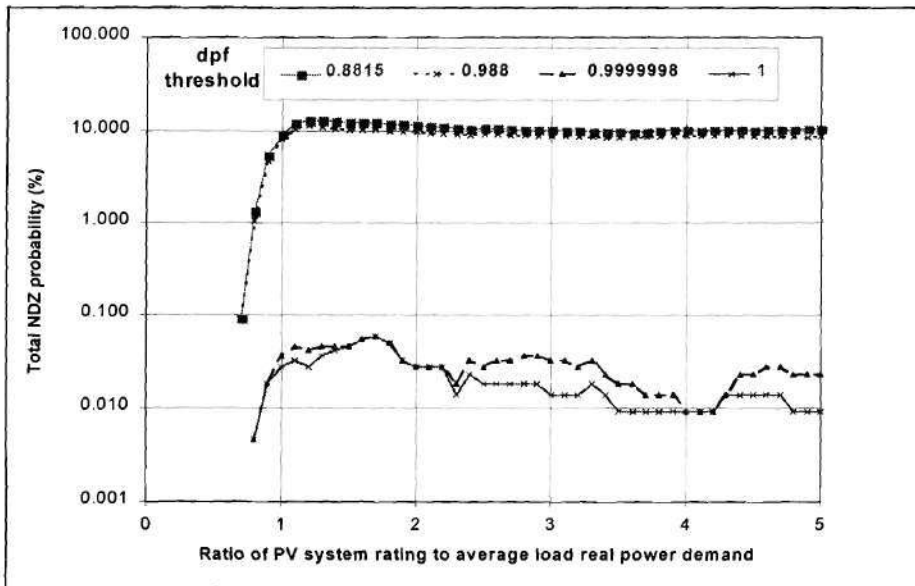
Figure 36. Total NDZ probability as a function of (normalized) PV system size, for several different values of dpf threshold. Data from Set #2.

98
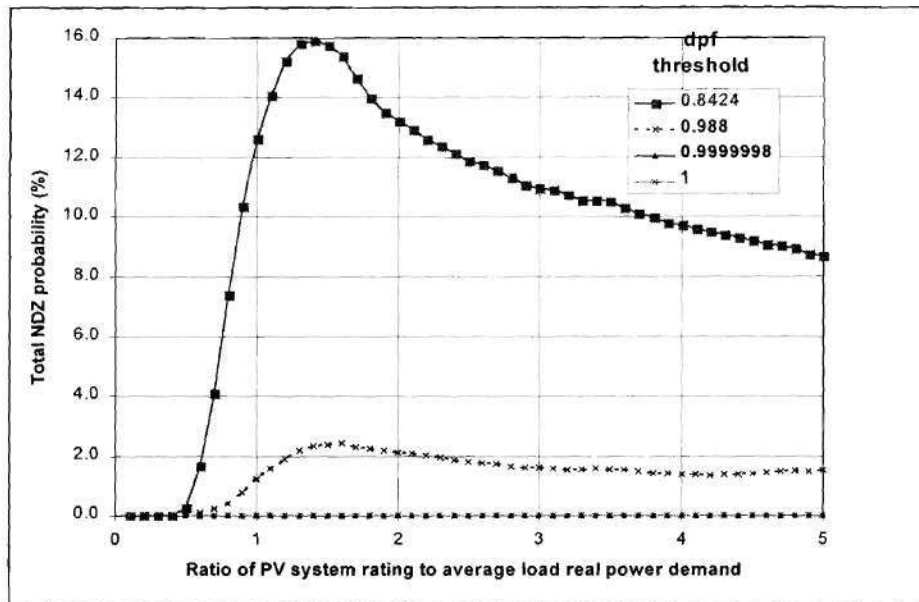
Figure 37. Total NDZ probability as a function of (normalized) PV system size, for two values of dpf threshold. Data is from Set #3.
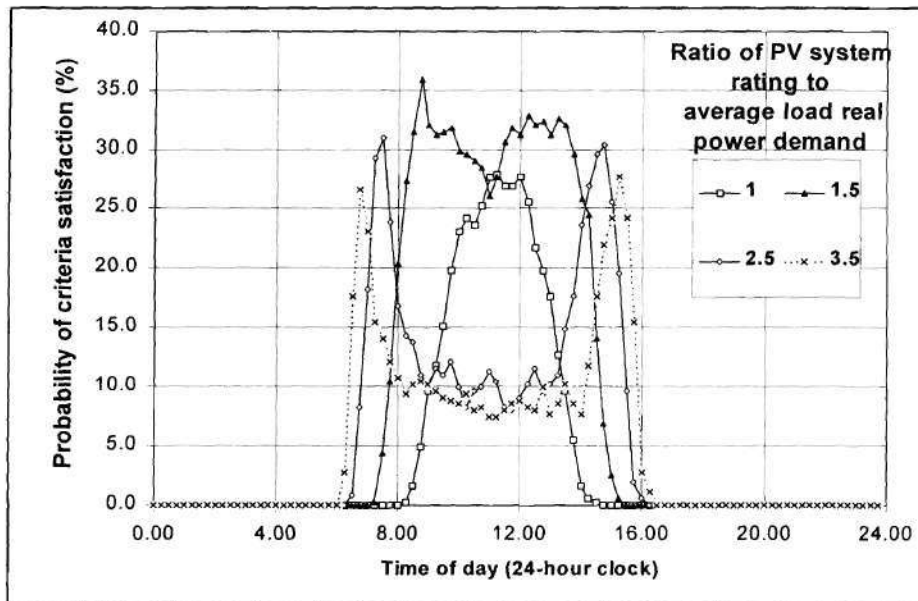
Figure 38. Conditional NDZ probability for several different values of (normalized) PV system size. Data from Set #1. The dpf threshold was set at 0.95.
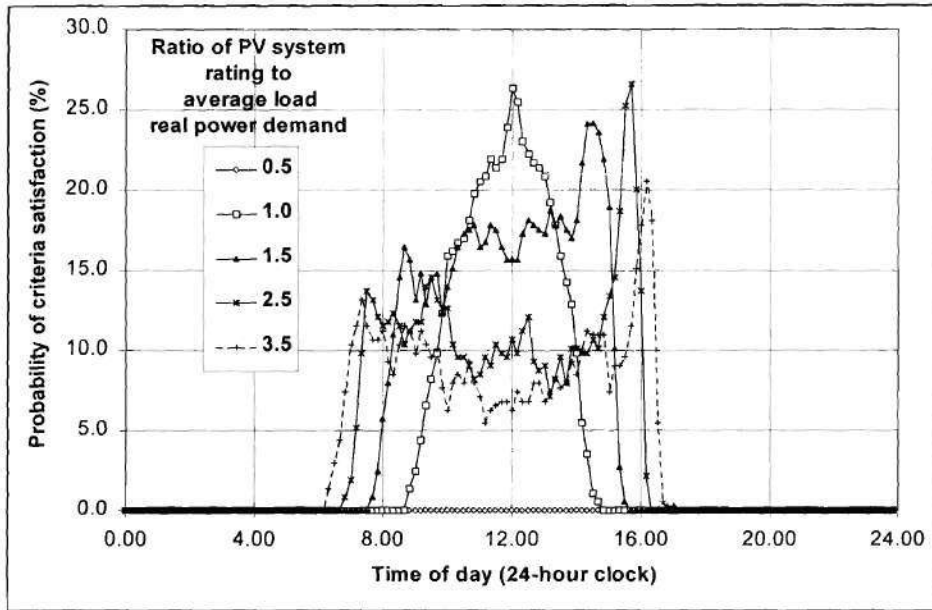
Figure 39. Conditional NDZ probability for several different values of (normalized) PV system size. Data from Set #2. The dpf threshold was set at 0.95.
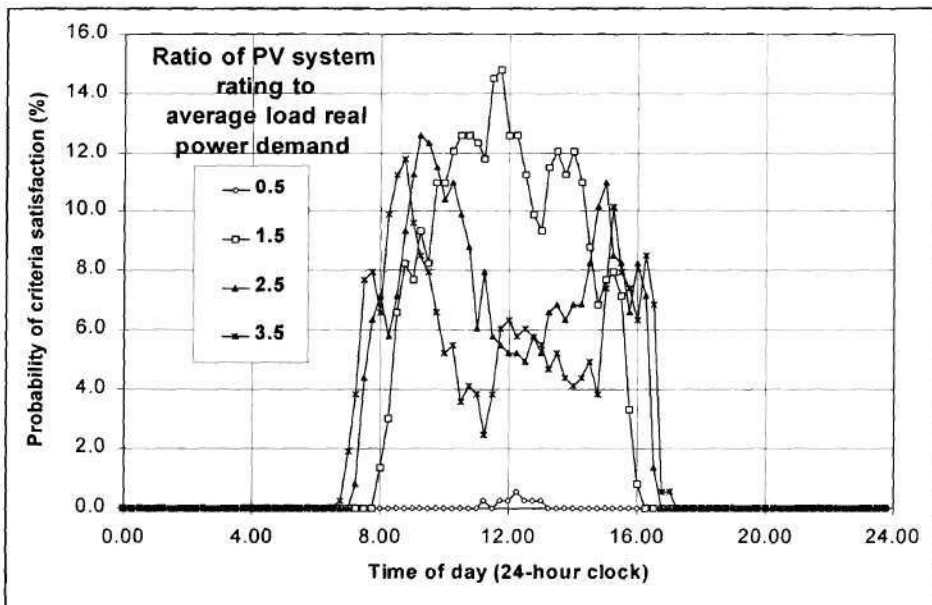
Figure 40. Conditional NDZ probability for several different values of (normalized) PV system size. Data from Set #3. The dpf threshold was set at 0.95.
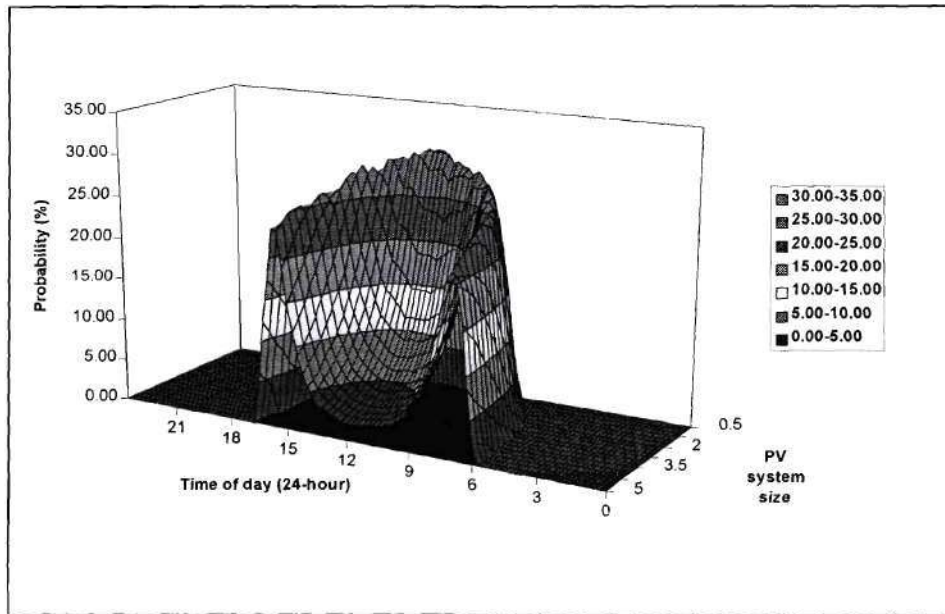
Figure 41. Three-dimensional plot of the conditional NDZ probability as a function of PV system size (power rating). Data from Set #1. The dpf threshold was 0.95.

hours total probability. Also, as one might intuitively expect because of the time behavior of the real power production of the PV system, the probability at times near sunrise and sunset increases to a nearly-constant value as the size of the PV system increases, and the probability near midday drops.

To summarize: the intent of this systematic study was to determine whether the OFR/UFR and OVR/UVR alone provide sufficient islanding protection. A statistical study of measured aggregate load data from U.S. utilities compared with modeled PV system performance data at the same locations was employed. The difficulties encountered in setting accurate failure criteria for the frequency relays have been

demonstrated. Finally, two sets of probability calculations have been presented, one showing the total probability of the conditions that lead to failure of the OFR/UFR/OVR/UVR over the entire period of the measured data, and the other showing the probability of the conditions that lead to failure of the OFR/UFR/OVR/UVR as a function of time of day. The results of this study show that, under real-world conditions, at times there exist conditions under which it is possible to have loads that are sufficiently closely matched to the PV system power production and have sufficiently high power factors that none of the relays would trip if the utility were disconnected at those times. This is particularly true when the probability as a function of the time of day is considered. This study provides evidence that the four relays are not sufficient for islanding protection, and further protective measures are required for grid-connected PV systems.

Limitations of this study

It is important to note that this study does have limitations.

1.) As previously mentioned, the load has been represented by measured aggregate load data in order to realistically model the load shape and power factor. The results of this study should hold for all loads whose demand pattern and power factor behavior are represented adequately by this data.

2.) It was stated that transients at utility turn-off have been ignored, but in cases in which the load requires a great deal of reactive power, even if the PCU(s) in the island are capable of providing it (which may not always be true), such a transient may occur, and this transient may be such as to cause one of the four standard relays to trip.

3.) A third difficulty is indicated by the fact that the probability of failure of the four standard relays can range from zero to over 10% depending on the value of dpf threshold used. This is in turn dependent on the values of R, L and C of the load.

Clearly, if more accurate or higher time-resolution load data, particularly probability density functions for R(t), L(t), and C(t), were available, a more accurate study would be possible.

A final point must also be mentioned. This study does NOT find the "probability of islanding", but rather the probability that, at any given time, the PV power and load power will be sufficiently closely matched that the OFR/UFR/OVR/UVR would fail to detect islanding should the utility be disconnected at that time, a probabilitiy which has been called the "NDZ probability". This is *not* the same as the probability that a PV system actually will island. Even if the load were known exactly, the "probability of islanding" depends on several additional factors, including the probability of the utility actually being disconnected from the PV system and the probability of a transient at turn-off. This situation is depicted schematically in Figure 42, which shows a total event space Ω (the space containing all possible outcomes). Within the event space are two subspaces, the subspace of events in which the load lies within the NDZ of the four standard relays, $\Omega(\text{NDZ})$, and a subspace of events in which the utility is disconnected, $\Omega(\text{D})$. Only in the intersection of these two spaces, $\Omega(\text{Isl})$, is islanding possible, and this demonstrates that the "probability of islanding" (the ratio of the areas of $\Omega(\text{Isl})$ and Ω) will be lower than the NDZ probability. However, the reader must keep in mind that at present it is the responsibility of PV PCU manufacturers to devise PCUs which do not island to within a reasonable certainty. Utilities and standards-making bodies require that PV PCUs have this behavior regardless of any external conditions [35]. This research is concerned with ascertaining whether PCUs do in fact have the desired characteristics and will disconnect from the point of common coupling (node **a**) when the utility does. Therefore, for the purposes of this research, the "probability of islanding" is actually irrelevant. The "probability of islanding" is important in the debate over how much effort is justified in preventing islanding, but not in the

103

discussion of the effectiveness of islanding prevention methods. The probabilities calculated here are important because they show that, to a first approximation, the OFR/UFR/OVR/UVR acting alone are not sufficient to guarantee the safety and integrity of people and property, and therefore additional islanding protection is needed for UIPV systems.
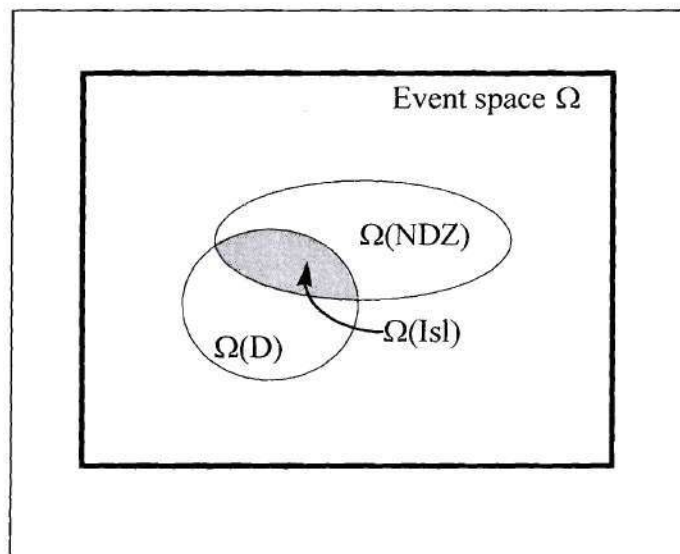
Figure 42. Graphical depiction of the difference between the NDZ probability and the "probability of islanding".

Subtask 2.2: Comparison of existing islanding prevention methods on the basis of NDZ location

Background

The literature review indicates that may different methods for preventing islanding are available, and the work just described under Subtask 2.1 shows that the use of such methods is required to produce non-islanding PCUs for PV systems. Manufacturers of PCUs would like to have islanding prevention techniques which give the best possible protection against islanding with minimal complexity and cost, and with the smallest possible penalty in output power quality. Unfortunately, it is difficult to draw conclusions about the relative islanding prevention effectiveness of existing islanding prevention schemes from the literature because no quantitative comparison of these methods has been made. Each method has been touted as "highly effective"—in fact, manufacturers using the SMS method have declared its islanding protection to be "perfect" [53] and to have "no dead bands" [54]—but none of these papers has compared islanding prevention methods against each other to determine which is "best".

However, the concept of a nondetection zone (NDZ) previously introduced in this work provides a method by which such a quantitative comparison may be accomplished. If the exact range of loads for which each islanding prevention method fails (which, by definition, is the NDZ) could be determined and mapped, the methods could be compared on the basis of the sizes and locations of their NDZs. The use of NDZ size in the comparison is intuitive, but the location of the NDZ is also important. For example, if Method A had a larger NDZ than Method B, but Method A's NDZ fell into a range of loads which is rarely seen in practice (for example, strongly capacitive loads

or negative-resistance loads) but Method B's NDZ falls into a more common range of loads, Method A could actually be preferable to Method B.

A brief review of the definition of "NDZ" being used in this work is in order at this point. Recall that the definition of NDZ adopted here is the second one given in the Literature Search: the NDZ of an islanding prevention method is that range of parallel RLC loads for which the method fails to detect islanding, assuming that the real powers of the load and PV are matched ($\Delta P = 0$). Comparisons of NDZs of methods have been made in the past [37,53]; however, these past comparisons have mapped the NDZs into a "power mismatch space" like that in Figure 22, using the first definition of NDZ given in the Literature Search. Unfortunately, this can lead to an incomplete, and therefore misleading, view of the NDZ location. This is because the absolute values of R, L, and C of the RLC load have a significant impact on the behavior of the islanded PV-load system, but the real and reactive power mismatch between PV and load are not unique functions of these parameters. In other words, there are many values of R, L and C that give the same ΔP and ΔQ but result in quite different islanded system behavior. This fact, which will be demonstrated shortly, is the reason for using the second definition of the NDZ.

For those islanding prevention methods that rely on a change in frequency to detect islanding, a simple method for determining their NDZ locations using expressions called *phase criteria* can be derived. This is made possible by the fact that the following two statements hold for UIPV systems: 1) when islanding begins, the frequency of the PV system's output current i_{PV} will change under the control action of the PLL, which acts in such a way as to bring i_{PV} into phase with the point of common coupling (POCC) voltage, v_a; and 2) the phase shift between v_a and i_{PV} under islanded conditions is determined by the phase angle of the parallel RLC load (see Figure 28), which is a function of frequency. The frequency will continue to change until the phase of the RLC

106

load is such that the phase comparator in the PLL "sees" a zero phase difference between its inputs. This relationship in general makes it possible to express the frequency under which the PLL reaches steady state in terms of load parameters. If this steady state frequency is attained before the trip mechanism for the islanding prevention method is triggered, then the method will fail and islanding can continue. Therefore, for islanding prevention methods which rely on a frequency shift, it is in general possible to compute the ranges of RLC loads for which these methods will fail by writing expressions for the PLL's steady-state frequencies in terms of the phase of the RLC load and then repeatedly solving these expressions using different values of R, L and C to determine for which RLC combinations islanding is not detected. These expressions are the phase criteria. The phase criteria can be used to map the NDZs of the methods into an RLC space, and then quantitative comparison is possible.

In this work, instead of using the "power mismatch" space traditionally used in the literature, the NDZ locations are plotted on graphs that show the load inductance L on the horizontal axis and a *normalized capacitance*, C_{norm}, on the vertical axis. The normalized capacitance is defined as the ratio of the actual load capacitance C to that capacitance that resonates with the corresponding L (on the horizontal axis) at the utility frequency ω_0; that is, $C_{norm} = C_{load} \div C_{res}$. The mapping is repeated for several values of R, thereby quantifying the islanding detection behavior as a function of all three load parameters. Throughout this section, MATLAB programs were used to automate the repeated calculations required to locate the boundaries of the NDZs of the various methods.

NDZ of the OFR/UFR/OVR/UVR

Procedure

If no additional islanding prevention beyond the four standard relays is used, recall that the PLL in the PV PCU will cause the frequency in the island to change until the phase shift between i_{pv} and v_a is zero, which occurs at the load's resonant frequency, $\omega_{res} = (LC)^{-0.5}$. Mathematically, the PLL will cause the frequency to change until the following condition is satisfied:

$$
\arg\left\{ \frac{1}{\frac{1}{R} + j\omega C - \frac{j}{\omega L}} \right\} = -\tan^{-1}\left\{ R \cdot \left(\omega C - \frac{1}{\omega L} \right) \right\} = 0 \tag{43}
$$

At ω_{res}, the phase criterion is satisfied, steady state is reached, and no further change in ω occurs. If ω_{res} lies outside the trip limits of the OFR/UFR, islanding will not occur; however, if ω_{res} lies within the OFR/UFR trip thresholds, detection failure results. Equation (43) may be solved for C as follows:

$$
C = \frac{1}{\omega^2 L} \tag{44}
$$

If an L is selected and ω is set equal to each of the OFR/UFR trip thresholds ($2\pi \times 59.5$ Hz or $2\pi \times 60.5$ Hz), this equation directly yields the capacitances at the edges of the OFR/UFR NDZ.

Next, the action of the OVR/UVR must be considered. Since it has already been stipulated that $\Delta P = 0$, the OVR/UVR will not trip right away. However, there is another

mechanism by which the amplitude of v_a can change. Just as the phase of parallel RLC loads is a function of frequency (Figure 28), the magnitude of these loads varies with ω as well. This is demonstrated in Figure 43, a plot of the magnitudes of the impedances of two parallel RLC loads as a function of frequency. Both loads are resonant at 60 Hz, which is equivalent to stating that they have their maximum impedances at 60 Hz. One load has a relatively small L and large C, whereas the other load has a relatively large L and small C. For the large L, small C case, the magnitude response is fairly flat, and the dependence of the magnitude of the load's impedance on frequency is relatively weak. However, as C increases and L decreases, the magnitude response of the RLC load becomes "sharper", decreasing more rapidly as the frequency is varied away from the resonant frequency. Therefore, for some loads, the change in the frequency of i_{PV} away from the nominal value caused by the PLL will cause a significant change in the load's impedance. Since $v_a = i_{PV} \times Z_{load}$, assuming the amplitude of the PV output current constant over the time interval of interest, a decrease in the magnitude of Z_{load} will lead to a decrease in the magnitude of v_a. If this decrease is sufficiently large, the UVR will trip, and islanding will be prevented. Therefore, for a load to fall within the NDZ, not only must Equation (43) be satisfied within the OFR/UFR trip limits, but

$$V_{a,low} \leq I_{PV} Z_{load}(\omega) \leq V_{a,high} \tag{45}$$

where $V_{a,low}$ and $V_{a,high}$ are the OVR/UVR trip thresholds, must also be true. Since $\Delta P = 0$, Equation (45) may be divided by the nominal voltage at node **a**, $V_{a,nom}$, to yield
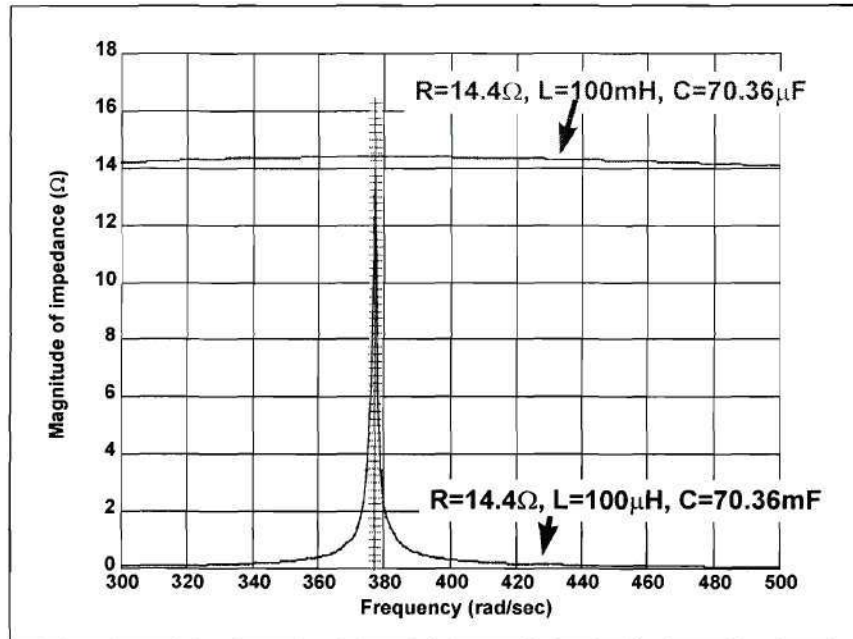
Figure 43. Magnitudes of two parallel RLC loads as a function of frequency.

$$\frac{V_{a,low}}{V_{a,nom}} \le Z_{load}(\omega)\frac{I_{PV}}{V_{a,nom}} \le \frac{V_{a,high}}{V_{a,nom}}$$

$$0.92 \le \frac{Z_{load}(\omega)}{Z_{load}(\omega_0)} \le 1.1$$

(46)

where the values 0.92 and 1.1 are the thresholds of the OVR/UVR, as dictated by IEEE-P929 [35]. Thus, the magnitude of the impedance of the load can be calculated at the final frequency reached by the system, and this value must satisfy Equation (46) if the load is to fall within the NDZ.

Results

Repeating the procedure above for several values of L, the mapping of the NDZ of
the OFR/UFR/OVR/UVR shown in Figure 44 is obtained. The NDZ is denoted by the
shaded region, and the heavy lines are the boundaries of the NDZ. Over most of the
range being considered, the frequency relays dominate the behavior of the system, and
the NDZ boundaries are a pair of horizontal lines; that is, the values of C_{norm} at which
the OFR/UFR fail are constants, independent of L. Also, since the resonant frequency
does not depend on R, the NDZ of the OFR/UFR is independent of its value as well. The
narrowing of the NDZ as L becomes smaller is because of the change in the impedance
of those loads with frequency. These loads have small L and large C values, and their
magnitude responses are becoming sharper as L decreases (see Figure 43). Therefore,
the OVR/UVR (Equation (35b)) dominate the behavior of the system in this range.

Note that the horizontal portion of the NDZ boundaries may have been found by
examining the definition of C_{norm}. C_{res}, the denominator of the ratio, is defined to be the
capacitance that resonates with the corresponding L on the horizontal axis at the
nominal utility line frequency ω_0. In addition, for the OFR/UFR, at the NDZ boundaries
the resonant frequencies are simply those that correspond to the OFR/UFR trip
thresholds. Since for any RLC load $\omega_{res} = (LC)^{-0.5}$,

$$\frac{C_{NDZ\ boundary}}{C_{res}} = \frac{\omega_{threshold}^2 L}{\omega_0^2 L} = \frac{\omega_{threshold}^2}{\omega_0^2} \tag{47}$$

Since the $\omega_{threshold}$ values of the OFR/UFR are constant, the NDZ boundaries are
horizontal lines at $C_{norm} = \left(\frac{59.5}{60}\right)^2$ or $\left(\frac{60.5}{60}\right)^2$ in the range in which the frequency
relays dominate.
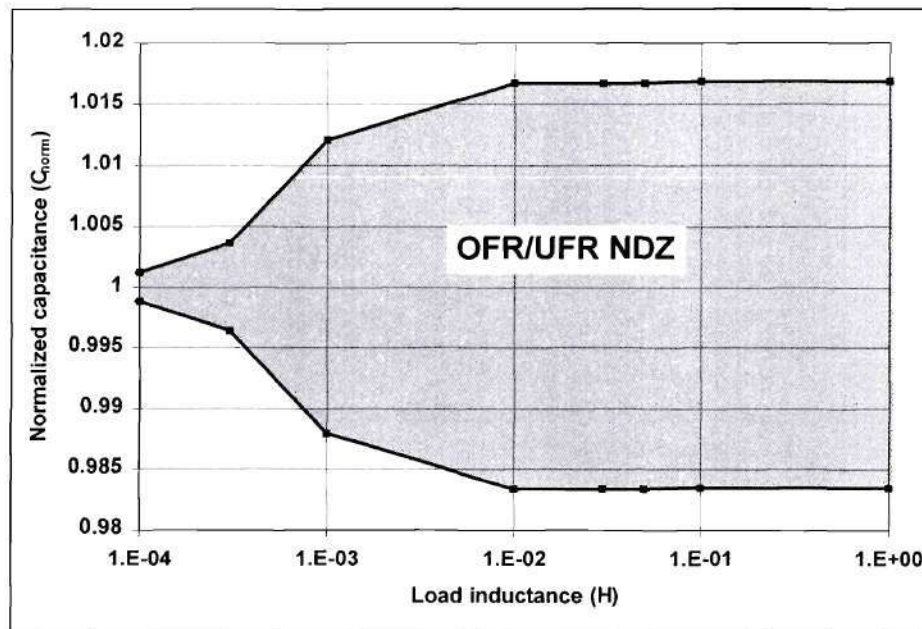
Figure 44. The NDZ of the OFR/UFR. The shaded region between the lines is the NDZ.

NDZ of PJD

Procedure

When the PJD method is used, again the PLL causes i_{PV} and v_a to come into phase with each other. Therefore, the phase criterion for this method is very similar to that for the OFR/UFR and may be written directly from the description of the operation of PJD given in the literature search. If the simplifying assumption is made that the system response is instantaneous (that is, the system moves in one cycle from the utility frequency ω_0 to the load's resonant frequency ω_{res}), then the approximate phase criterion for PJD is:

$$\left| \tan^{-1}\left\{ R \cdot \left[\omega_0 C - \frac{1}{\omega_0 L} \right] \right\} \right| \geq \phi_{th} \tag{48}$$

where ϕ_{th} is the phase threshold at which a stop signal is generated. _If_ Equation (48) is satisfied, then islanding will <u>not</u> occur. Again, this equation may be solved for C:

$$C = \frac{1}{\omega_0}\left[\frac{1}{\omega_0 L} + \frac{1}{R}\tan\phi_{th} \right] \tag{49}$$

Results

As before, Equation (49) may be used to map the NDZ of PJD into the C_{norm} vs. L plane by selecting L, R, and ϕ_{th}, yielding the C at the NDZ boundary corresponding to the selected parameter values. It was assumed here that $\phi_{th} = 2°$, which is the smallest value used to date in a commercial PV PCU [31]. The result is shown in Figure 45, along with the NDZ of the OFR/UFR. The NDZ gets narrower for larger C and smaller L (that is, as one moves to the left on the plot), indicating that PJD becomes more effective there. Note also that the NDZ of PJD gets wider as the value of the resistance decreases, showing that PJD becomes less effective as the real power demand of the load increases. However, most importantly, note that the NDZ of the OFR/UFR lies within the NDZ of PJD no matter what the value of R is. This indicates that the PJD method, as implemented here, provides essentially no additional islanding protection beyond that already provided by the OFR/UFR.

A note is in order at this point about the assumption that the system's response is instantaneous. This assumption holds reasonably well for RLC loads with a relatively

113

large value of C and a relatively small value of L. However, as L increases and C decreases, the rate at which the frequency changes from ω_0 to ω_{res} is reduced. This means that the phase error which will be detected by the PLL from one cycle to the next is decreased as well, leading to a further decrease in the effectiveness of PJD which will manifest itself as an even greater widening of the PJD NDZ as L increases in Figure 45.

Another important point to note is that, as the method is described here, PJD either detects islanding in the first cycle after the utility is disconnected, or it fails to detect islanding at all. However, there are variants of PJD for which this may not be true. In fact, such a scheme was implemented in the Teslaco PCU, a commercially-available PCU manufactured in the early 1980's [31]. This PCU used a PJD variant
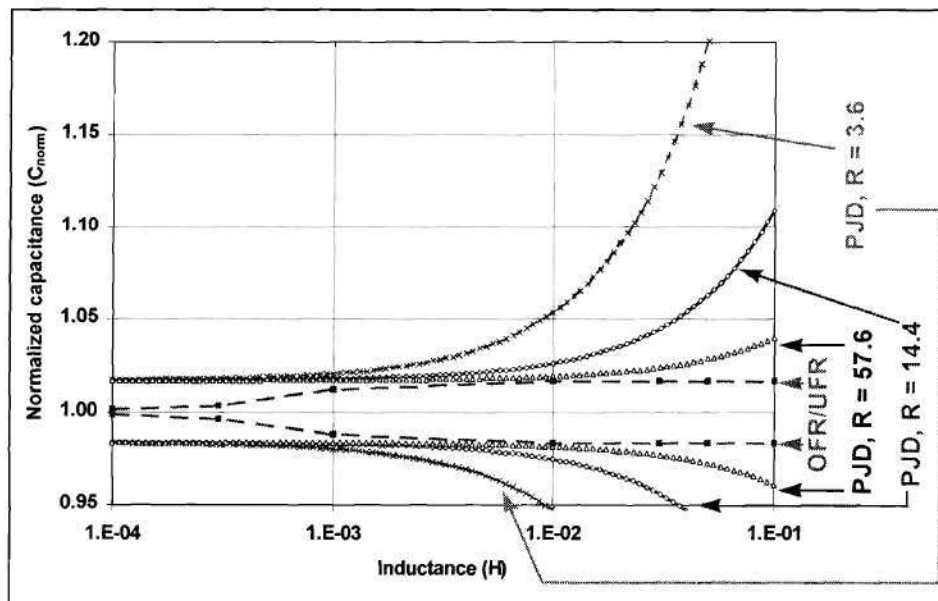
Figure 45. The NDZ of PJD as found using the phase criterion in Equation (35).

114

called unstable PJD in which a one-cycle delay was inserted in the PLL between the loop filter and the VCO. This one-cycle delay resulted in a "classical" instability (that is, a right-half-plane pole in the PLL's transfer function). In this case, the above phase criterion would be altered such that the phase error in the kth cycle is compared with the phase error in the previous $(k-1)^{th}$ cycle, and if this difference is greater than the threshold a shutdown results:

$$\left| \tan^{-1}\left\{ R \cdot \left[\omega_{k-1}C - \frac{1}{\omega_{k-1}L} \right] \right\} - \tan^{-1}\left\{ R \cdot \left[\omega_{k}C - \frac{1}{\omega_{k}L} \right] \right\} \right| \geq \phi_{th} \tag{50}$$

The NDZ of such a scheme would be somewhat narrower than that shown. However, it has been found that in general this improvement to PJD still results in unacceptably long run-on times [55,56].

NDZ of SMS

Procedure

The case for SMS is slightly more complicated because the operation of the PLL is different. When the PLL phase comparator detects a zero phase error, the phase difference between i_{PV} and v_a need not be zero, because the input to the PLL is not v_a but a filtered version of v_a, and this filtered version has intentionally had its phase altered. As in the case of PJD, an approximate phase criterion was extracted from the physical operation of the SMS method. This was achieved by redrawing the block diagram of the SMS-RLC load system given in Figure 27 as shown in Figure 46. If the loop equation for this system is solved for a closed-loop phase shift of zero, the solution is $\theta = -\phi$, or

115

$$\tan^{-1}\left\{R\cdot\left[\omega C-\frac{1}{\omega L}\right]\right\}=\arg\left\{H(j\omega)\right\} \qquad (51)$$

where $H(j\omega)$ is the transfer function of the input line filter. For loads with a near-unity dpf, if Equation (51) has more than one solution, the solution at the utility frequency is unstable and islanding will not occur. If $H(j\omega)$ is known analytically, this equation also may be solved for C as has been done in the previous two cases. However, for this study, a slightly different approach is adopted. First, an RLC load was selected and checked to see at what frequency Equation (51) was satisfied. If this frequency was within the OFR/UFR trip thresholds, the slope of the load's phase response was compared with the slope of the SMS curve at the intersection point of the two. If the load's phase response curve has a steeper slope than the SMS curve at that point, then the RLC load lies within the NDZ of SMS.

The reader must note that the SMS method actually relies on the OFR/UFR/OVR/UVR to trip the PV system. For this reason, it is technically incorrect to speak of the "NDZ of SMS"; rather, the NDZ is that of the OFR/UFR/OVR/UVR under the influence of SMS. SMS changes the NDZ of the OFR/UFR/OVR/UVR. To avoid confusion, the term "NDZ of SMS" will be used in this work, but this technicality must be borne in mind when viewing the NDZ plots.

<u>Results</u>

A mapping of the NDZ of SMS into the C_{norm} vs. L plane is given in Figure 47. In these simulations, the SMS curve used was that from the APCC SunSine PCU [31].

116
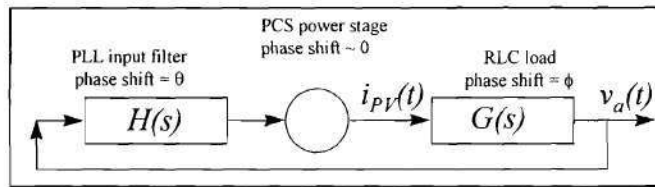
Figure 46. Block diagram of SMS-RLC load system.
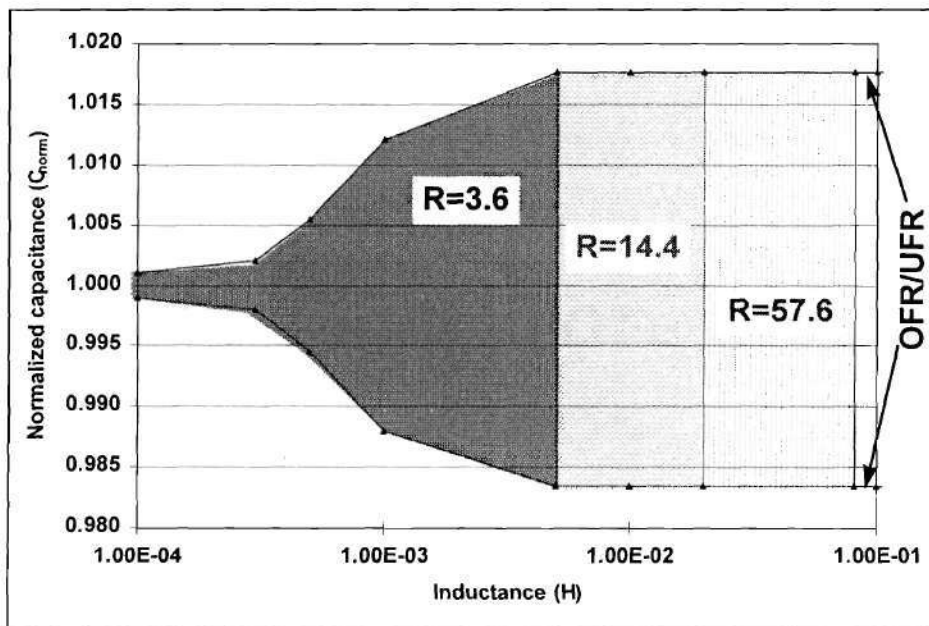
Figure 47. The NDZ of SMS. The SMS curve used is the one from the APCC SunSine [31]. NDZ locations are shown for three values of R.

On the right side of Figure 47, where L is large and C is small, SMS has no NDZ. However, for loads falling toward the left, SMS fails; that is, it does not alter the existing

NDZ of the OFR/UFR/OVR/UVR. Therefore, the effect of SMS is to "chop off" the NDZ of the OFR/UFR/OVR/UVR on the right side of the C_{norm} vs. L plane, with the cut-off point being dictated by the value of R. Note that the size of the SMS NDZ increases as the value of R increases, indicating that SMS becomes less effective as the real power demand of the load drops.

As was the case with PJD, it is possible to improve SMS somewhat by adding a one-cycle delay in the PLL between the loop filter and the VCO. This scheme also has been implemented in a commercially-available PCU, the APCC "SunSine" converter made in the late 1980s. The addition of the one-cycle delay adds a right-half-plane pole to the PLL's transfer function, and this "classical" instability could result in a narrowing (but not elimination) of the SMS NDZ.

Discussion

On the basis of the sizes and locations of the NDZ maps in the previous section, it appears clear that SMS is the most effective of the existing islanding prevention methods. Its NDZ is the smallest (that is, includes the least number of RLC loads, or equivalently has the lowest area in C_{norm} vs. L space), and its NDZ lies in a range of loads with larger values of C and smaller values of L. Most real-world loads do not have large values of C, although other sources of capacitance (PFCCs and distribution lines) certainly do exist in the utility system. In addition, adding the one-cycle delay to the SMS PLL would probably further reduce the size of the NDZ and increase the effectiveness of the method.

Another critical conclusion may be drawn from the previous section. As was mentioned in the introduction to Subtask 2.2, looking at the NDZs of islanding prevention methods in a "power mismatch space" results in a critical loss of information, leading to incorrect conclusions about the methods' effectiveness. The NDZ locations determined in the previous section clearly indicate that the islanded

118

behavior of PV systems does depend on the values of R, L and C, but there are many values of R, L and C which can lead to the same levels of real and reactive power mismatch between PV and load. This is best explained by an example. Consider a 4-kW PCU utilizing the SMS method undergoing islanding testing with a real and reactive power mismatch of zero. This point lies at the origin of the power mismatch space. Assume further that the PCU is being tested at 100% of its rated load using a parallel RLC load with L = 10 mH, C = 703.6 µF, and R = 3.6 Ω (at 120V). The result of this test would be that this condition lies outside the PCU's NDZ, as indicated by Figure 47. However, now consider the same PCU being tested with the same zero real and reactive power mismatch but at a power level of 1 kW, or 25% of the PCU's real power rating. At 120V, this means that the value of R has increased to 14.4 Ω. Figure 47 shows that for this load the PCU would in fact run on, but these two opposite behaviors would map into the same location (the origin) in "power mismatch space". The same conclusion may be reached by keeping R fixed and varying L and C, maintaining resonance between them. Therefore, it is not possible to uniquely identify the locations of NDZs within the "power mismatch space" unless it is somehow done as a function of the load parameters.

As a part of this work, a MATLAB program which automatically calculates the NDZ locations of several of the islanding prevention methods discussed here was created. A listing of the code for this program is provided in Appendix II.

Limitations of this study

Several important limitations of the study in Subtask 2.2 must be borne in mind. The simplification and fundamental understanding made possible by the phase criterion approach comes at the cost of a significant loss of information about the system. This loss of information is manifest in the following ways:

1.) The phase criterion approach assumes that no transients occur when the utility is disconnected. Such transients could possibly act to lengthen or shorten the run-on time of a PCU.

2.) The dynamics and internal operation of the PCU power stage have been neglected. It has been assumed that the PCU can be modeled essentially as a constant gain, but this idealization may not hold for transient conditions lasting for significant lengths of time. In addition, no allowance has been made for disturbances, which may arise from a variety of sources. These dynamics and disturbances could act to lengthen or shorten the run-on times.

3.) Only those aspects of the PCU control scheme which are directly involved in islanding prevention have been considered. Other aspects could have a significant impact as the run-on time increases. In particular, the MPPT will render invalid the above-mentioned assumption that the power stage may be modeled as a constant gain if the time period under consideration is sufficiently long. In general, the operation of the MPPT will destabilize an island and lead to shorter run-on times, particularly in cases in which indefinite run-on is predicted.

4.) Combinations of protective schemes have not been considered. However, it is likely that certain methods used in combination could be more effective than the methods are alone. In fact, in most commercial PCUs, more than one islanding prevention method is used.

Subtask 2.3: Analysis and characterization of AFD and its NDZ

Background

Active Frequency Drift (AFD), or frequency bias, is a relatively new islanding prevention method. The operation of this method was outlined in the Literature Search section, as was the fact that before this work this method had not been analyzed or thoroughly characterized. In particular, only one attempt to locate its nondetection zone was found in the literature [37], but this was for a narrow and unspecified range of loads (as evidenced by the fact that the mapping was done in the "power mismatch" space). Experimentally, limited data was available showing that AFD works for purely resistive loads but fails for resistive loads with a small amount of added capacitance (that is, RC loads with certain values of C) [46,60,61].

The purpose of the work under Subtask 2.3 is to address this lack of information by characterizing the behavior of AFD and mapping its NDZ, using an approximate phase criterion and also a full time-domain numerical simulation.

Analytical approach

Procedure

In order to facilitate the comparison of AFD with the other methods characterized in Subtask 2.2, a phase criterion for AFD was derived. However, unlike the methods previously studied, the needed understanding and analytical tools for AFD were not available in the literature. To address this problem, a simple analytical approach using the describing function analysis technique [38,57] was developed.

First, it was noted that the system can be separated into linear and nonlinear subsystems as shown in Figure 48. The PV PCU, with the PLL and AFD, is the nonlinear portion of the system. The linear subsystem is the parallel RLC load. Next, it was noted that the "chopping fraction" cf could not be arbitrarily large, or else the total harmonic distortion introduced into i_{PV} by AFD would become unacceptable. To quantify this effect, the Fourier coefficients of the AFD waveform for several different values of "chopping fraction" cf were calculated using the FFT function in MATLAB, and from these the total harmonic distortion in the AFD waveform was calculated for several different values of cf. The Fourier spectra are shown in Figure 49, and the THD_{iPV} values are given in Figure 50. Even for "chopping fraction" (cf) values of 5%, the largest harmonic components of the current have amplitudes of around 0.1% of the fundamental amplitude. Also, since it is necessary to keep THD_{iPV} below 5%, Figure 50 shows that the maximum allowable value of cf is also 5%, and therefore this value gives the worst case in terms of harmonic distortion. The fact that the higher-order harmonics of i_{PV} are so small suggests that in a first-order approximation they may be neglected without significantly sacrificing accuracy; that is, i_{PV} may be reasonably approximated by its fundamental component, $i_{PV,1}$. Thus, it can be further assumed
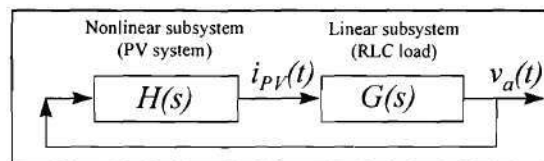
Figure 48. Block diagram of the system in Figure 20 after utility disconnection.

122
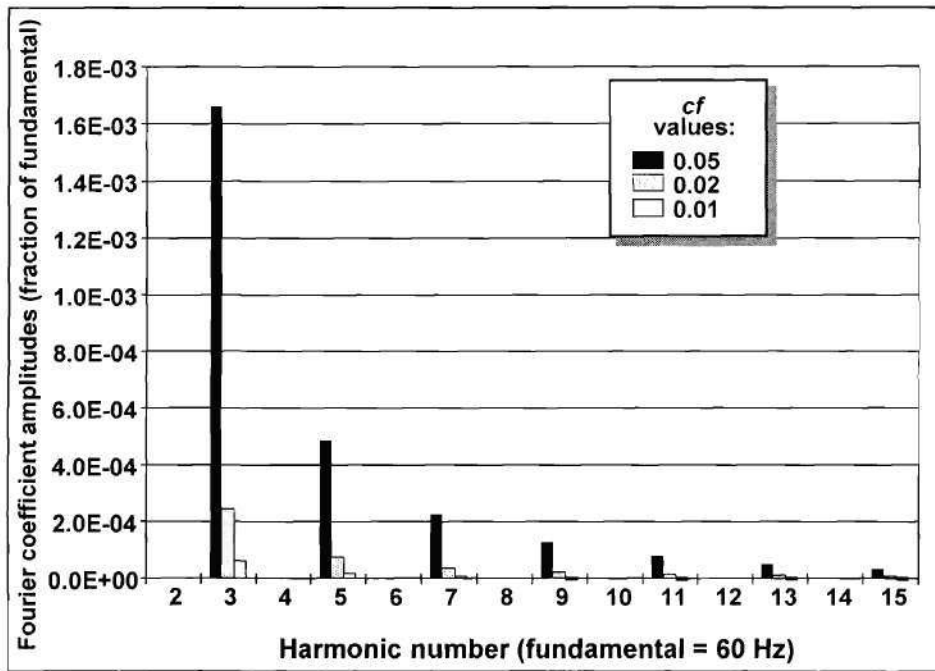
Figure 49. Fourier spectra of the AFD waveform (Figure 33) for several values of *cf*.
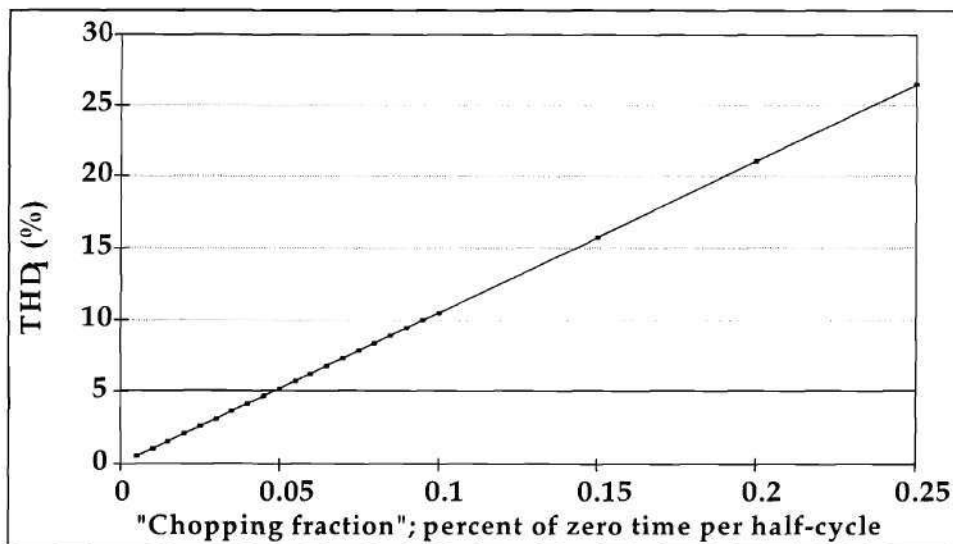
Figure 50. Plot of THD$_{IPV}$ vs. chopping fraction for the AFD waveform (Figure 33).

that v_a is a function only of $i_{PV,1}$ [57]; that is, the parallel RLC load "sees" and reacts to $i_{PV,1}$ only. Consider also that the AFD waveform in Figure 33 with its zero times has neither odd nor even symmetry about the origin. Because of this, the Fourier series representation of this waveform will have both sine and cosine terms [58]. From Fourier theory, this is equivalent to saying that $i_{PV,1}$ will have a phase shift with respect to i_{PV}. The amount of this phase shift can be determined using Figure 51. In this figure, the zero phase reference has been redefined by moving it by $-t_z/2$, thus creating a waveform i_{PV}^*. The shift results in i_{PV}^* having odd symmetry $(i_{PV}^*(t) = -i_{PV}^*(-t))$, and therefore its Fourier series consists only of sine terms, and the fundamental component of i_{PV}^*, $i_{PV,1}^*$, has no phase shift with respect to i_{PV}^* [57]. The time difference between the zero crossing of $i_{PV,1}^*$ and the start of the sinusoidal portion of i_{PV}^* is $t_z/2$, and the phase difference is therefore $\omega t_z/2$. This is the same as the time relationship between i_{PV} and $i_{PV,1}$, since i_{PV} and i_{PV}^* differ only by the assignment of the starting point (zero phase reference). As a cross-check, the phase shift of $i_{PV,1}$ with respect to i_{PV} was computed directly using the complex Fourier series coefficients, and this result was compared with the results found by computing $\omega t_z/2$. The results, given in Table 4, indicate that the simplified treatment gives the correct result. The agreement between the two phase shifts improves as the sampling rate for the directly-computed values is increased.

Recall that the phase of the load becomes zero when the frequency of v_a reaches the load's resonant frequency. However, since v_a is dominated by the load's response to $i_{PV,1}$, not i_{PV}, at the resonant frequency of the load the voltage v_a will be in phase with $i_{PV,1}$ and not i_{PV}. Therefore, since $i_{PV,1}$ leads i_{PV} by $\omega t_z/2$ rad, when the system reaches the load's resonant frequency, v_a still leads i_{PV} by $\omega t_z/2$ rad. The PLL in the PV PCU will continue to increase the frequency of i_{PV} since it still detects a phase error between i_{PV}

124

and v_a. The PLL will detect a zero phase shift between i_{PV} and v_a when the frequency of v_a is such that phase shift of the load is equal to and opposite from the phase between

Table 4. Comparison between directly-computed phase shifts and those found by the simplified treatment described in the text.

Chopping Fraction (%)	Phase shift predicted by simplified treatment (degrees)	Phase shift computed directly from Fourier series coefficients (degrees)
0.5	0.45	0.4939
1	0.90	0.9439
3	2.70	2.7439
5	4.50	4.5439

Parameters: Sampling rate = 491.52 kHz; one complete cycle analyzed; fundamental frequency = 60 Hz.
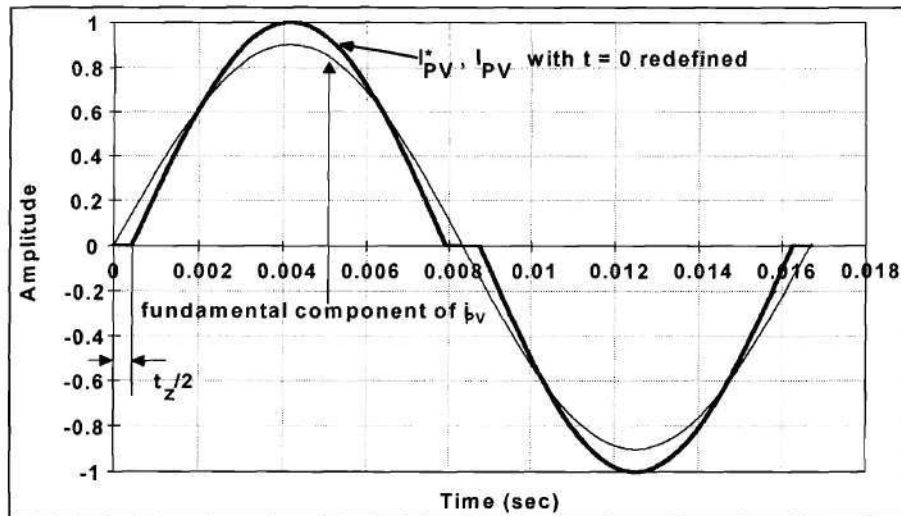
Figure 51. Plot of i_{PV}^* and $i_{PV,1}^*$. i_{PV}^* described in the text.

125

i_{PV} and $i_{PV,1}$. Thus, the frequency at which i_{PV} and v_a are in phase must satisfy

$$\tan^{-1}\left\{R\left[\omega C - \frac{1}{\omega L}\right]\right\} = \frac{\omega \cdot t_z}{2}$$
$$= \frac{1}{2}\frac{2\pi}{T}t_z \qquad (52)$$
$$= \frac{1}{2}(2\pi)\frac{cf}{2}$$
$$= \frac{\pi \cdot cf}{2}$$

Once the frequency of v_a has reached the ω that satisfies Equation (52), there is no phase error between v_a and i_{PV}, and the PLL no longer increases the frequency of i_{PV}, resulting in a steady state. This equation may be solved for C:

$$C = \frac{1}{\omega}\left[\frac{1}{\omega L} + \frac{1}{R}\tan\left(\frac{\pi}{2}\cdot cf\right)\right] \qquad (53)$$

By choosing R, L and cf, and by setting ω equal to one of the OFR/UFR thresholds, this equation gives the C at the edge of the AFD NDZ corresponding to the selected parameters.

As before, the operation of the OVR/UVR due to the effect of the frequency change on the load's impedance, and subsequently on v_a, must also be accounted for. Thus, Equation (46) must be used together with Equation (52) to map the NDZ of AFD into the C_{norm} vs. L plane. MATLAB was used to carry out these calculations.

<u>Results</u>

Figure 52 shows an example of the results of this procedure for R = 14.4 Ω, cf = 1%, 5% and 10%, and several values of L and C. (R = 14.4 Ω corresponds to a 1-kW load at 120 V_{RMS}.) The light dashed lines indicate the NDZ of a PV system using only the OFR/UFR/OVR/UVR, without AFD. The reader should bear in mind that AFD, like SMS, actually relies on the four standard relays to trip the PV system, and thus AFD changes the NDZ of the OFR/UFR/OVR/UVR. Technically, AFD has no NDZ of its own, although in this work the NDZ of the four standard relays as modified by AFD will be called the "NDZ of AFD".

Note that, for large values of L (toward the right in Figure 52), AFD bends the NDZ of the OFR/UFR into a range of leading-dpf loads. However, as L decreases and C increases, the NDZ slopes downward toward loads with higher and higher dpfs, eventually becoming centered about unity-dpf loads. Note also that the width of the NDZ decreases rapidly for inductances smaller than about 1 mH. This is because of the sharpness of the resonant peak of the load's magnitude response in that range; with large C and small L, small deviations from nominal frequency lead to large changes in the magnitude of the load impedance, leading to a detectable voltage deviation (assuming the magnitude of i_{PV} fixed; that is, the time period under consideration is short enough that the MPPT does not change the amplitude of i_{PV}) and PV system shutdown. With large L and small C, the magnitude response of the load is much flatter, and therefore the voltage trips do not play a role in that range.

Figure 53 shows the results of varying R on the NDZ of AFD for a fixed cf. Again, the light horizontal dashed lines indicate the NDZ of the OFR/UFR/OVR/UVR. Increasing R (that is, decreasing the load real power demand) causes the NDZ to bend back toward the NDZ of the OFR/UFR/OVR/UVR, indicating that AFD's behavior becomes more like that of the OFR/UFR/OVR/UVR for low-power (high-R) loads.

127
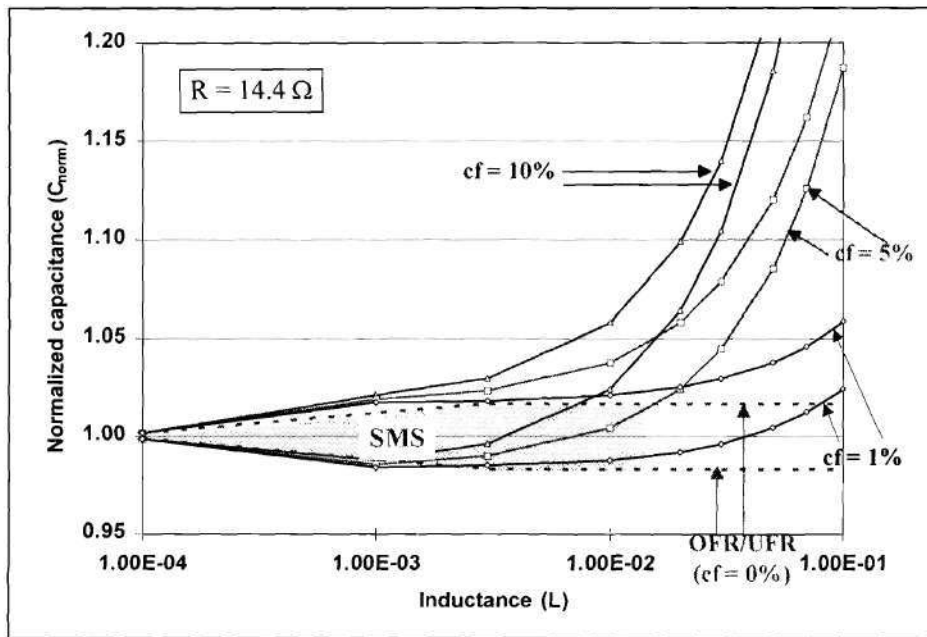
Figure 52. The NDZ of AFD found by the simplified analytical model for several values of *cf*. In these simulations, R=14.4 Ω. The dashed lines are the boundaries of the OFR/UFR/OVR/UVR NDZ, and the shaded region is the NDZ of SMS for R=14.4 Ω.
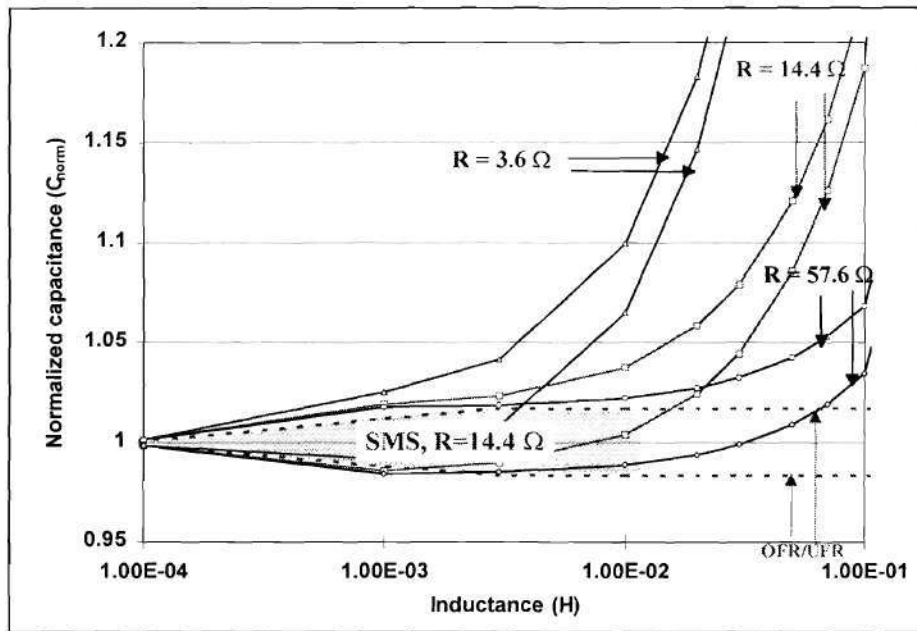
Figure 53. The NDZ of AFD found by the simple analytical model for *cf* = 5% and several values of R. The horizontal dashed lines are the boundaries of the OFR/UFR/OVR/UVR NDZ, and the shaded region is the SMS NDZ for R=14.4 Ω.

Time-domain simulation approach

Procedure

As a second approach to the analysis just described, a time-domain numerical simulation of the system shown in Figure 20 was developed in the MATLAB environment. This model contains three sections: a PV system model, a load/v_a model, and a zero crossing detector (ZCD) model, as shown in the block diagram in Figure 54.
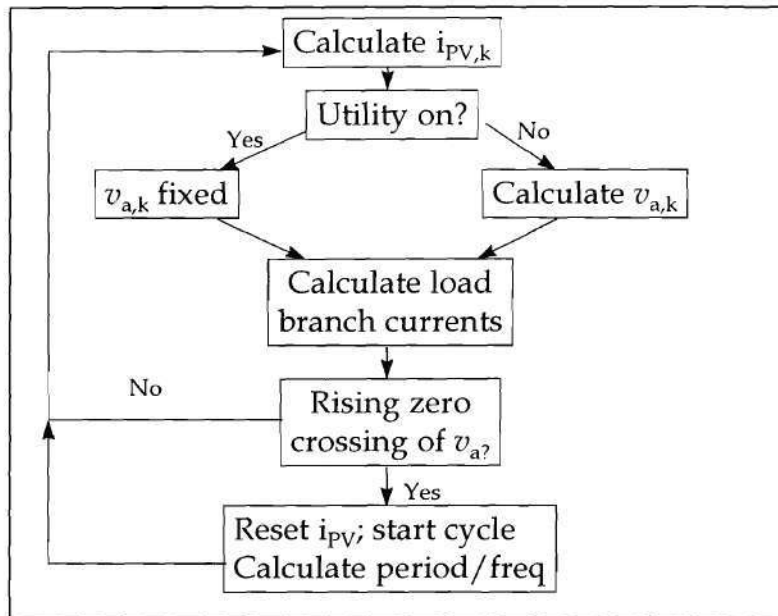
Figure 54. Block diagram of the MATLAB simulation of the AFD-equipped PV system and a parallel RLC load.

The solution procedure is as shown in the block diagram. First, the value of PV output current at time step k, $i_{PV,k}$, is calculated. The PV system is modeled as a programmable current source whose output is the AFD waveform in Figure 33. It is assumed that the PV system current jumps to zero and begins a new cycle on each rising zero crossing of v_a, regardless of the previous value of the output current. (This is a result of neglecting the PCU power stage dynamics.) Under most circumstances, this assumption makes no significant difference because the values of cf being used are small. It is also assumed that the amplitude of i_{PV} remains constant; that is, it is assumed that the MPPT does not act during the time interval of interest.

Next, the node-**a** voltage v_a is computed. If the utility is connected, it fixes v_a. The utility voltage is

$$v_{util,k} = \sum_{h=0}^{\infty} V_{util,h} \sin[ht_k (2\pi f_{util})] \tag{55}$$

where $V_{util,h}$ is the amplitude of the hth harmonic of the utility voltage and f_{util} is the utility voltage frequency in Hertz. In this work, only the fundamental harmonic was included in the utility voltage, and in what follows the h's will be dropped from that quantity for simplicity. This simplification is essentially equivalent to assuming that v_a can be effectively band-pass filtered without introducing a phase shift.

Next, consider the case in which the utility is disconnected. For the linear (RLC) load model, the currents drawn by the three load components are

$$i_{C,k} = C \frac{dv_a}{dt}\bigg|_{t=t_k} ; \quad i_{L,k} = \frac{1}{L} \int_{t=0}^{t=t_k} v_a dt ; \quad i_{R,k} = \frac{v_{a,k}}{R} \tag{54}$$

The POCC voltage $v_{a,k}$ is then determined by the interaction between the load and the current output of the PCU. Under this condition, $v_{a,k}$ may be found by using Kirchhoff's Current Law at **a**:

$$i_{PV,k} = i_{R,k} + i_{L,k} + i_{C,k} \tag{56}$$

where $i_{PV,k}$ is a discretized version of a sine wave ($i_{PV,0} = 0$) scaled in order to give the desired power output. This equation can be solved for $v_{a,k}$ using MATLAB's built-in

131

differential equation solver and Equations (54). However, for the present problem, this approach led to extremely long computation times. Therefore, to simplify the model and speed up the calculations, the integrals and derivatives in Equations (54) were approximated by sums and differences, respectively. During the time when the utility is connected, then, the following model equations were used:

$$v_{a,k} = V_{util} \sin\left(f_{util} \cdot 2 \cdot \pi \cdot t_k\right)$$

$$i_{L,k} = i_{L,k-1} + \frac{1}{L}\left(v_{a,k}\right)\left(t_k - t_{k-1}\right)$$

$$i_{C,k} = C \frac{v_{a,k} - v_{a,k-1}}{t_k - t_{k-1}} \tag{57}$$

$$i_{R,k} = \frac{v_{a,k}}{R}$$

The time interval $t_k - t_{k-1}$ is the sampling interval, and it must be chosen small enough that this linear approximation is significantly less than the time constant of the RLC load.

When the utility is not connected, Equations (57) are substituted into Equation (56), and since $i_{PV,k}$ is known, Equation (56) can then be solved for $v_{a,k}$, yielding:

$$v_{a,k} = \frac{\left[i_{PV,k} - i_{L,k-1} + \dfrac{Cv_{a,k-1}}{t_k - t_{k-1}}\right]}{\dfrac{t_k - t_{k-1}}{L} + \dfrac{C}{t_k - t_{k-1}} + \dfrac{1}{R}} \tag{58}$$

After v_a is calculated, the ZCD model detects the rising zero crossing of v_a by detecting the appropriate change in polarity. It also measures the period of v_a by

subtracting the time at which the previous rising zero crossing occurred from the time of the present zero crossing. The measured period of v_a is updated every cycle.

To check whether Equation (46) is satisfied, the magnitude of the load impedance at the frequency attained at the end of the simulation is compared with that at ω_0.

To map the NDZ of AFD using this simulation, the MATLAB program was run in batch mode. The amplitude of i_{PV} was first chosen so that $\Delta P^- \approx 0$. L, R, and *cf* were then fixed, and C was swept to find its values at the NDZ boundaries. This procedure was repeated for several values of L and R. The criteria for selecting whether a load was within the NDZ were taken directly from IEEE-P929 [35]: if the system ran on for longer than two seconds before either the frequency or the voltage went out of bounds, the load was included in the NDZ. The simulation parameters are given in Table 5. Note that the longest value of sampling interval (32.6 μsec) is more than an order of magnitude less than the smallest value of RLC load time constant (506.7 μsec, calculated using the formula in [59]), ensuring good accuracy of the linear approximations of the integrals and derivatives.

Table 5. Simulation parameters used in Subtask 2.3.

Parameter	Minimum value	Maximum value
R	3.6 Ω	57.6 Ω
L	1e-1 H	1e-4 H
C	7.036e-5 F	7.036e-2 F
cf	0 %	5 %
$t_k - t_{k-1}$	32.6 μsec	2.03 μsec

Results

Figure 55 shows a plot of the frequency calculated at each rising zero crossing of v_a as a function of time for the case R = 14.4 Ω, L = 1 mH, cf = 5%, and C varying over a narrow range about the value C = 7.036 mF that resonates with the given L at 60 Hz. The range of power factors of these loads is about 80% lagging to about 75% leading. The frequency of v_a increases or decreases initially, but then levels off, and for C = 7.0 and 7.1 mF the final frequency is within the ±0.5 Hz trip thresholds. Using the above-described, the NDZ of AFD for *cf* = 5% was mapped and compared with the results obtained using the phase criterion. This comparison is shown in Figure 56. The agreement is very good, within 5% over the entire range of L and C considered. The reason for the deviation of the phase criterion results from those of the full simulation at higher L values (smaller C values) is that the assumption that v_a is only a function of the fundamental of i_{PV} is less valid there.
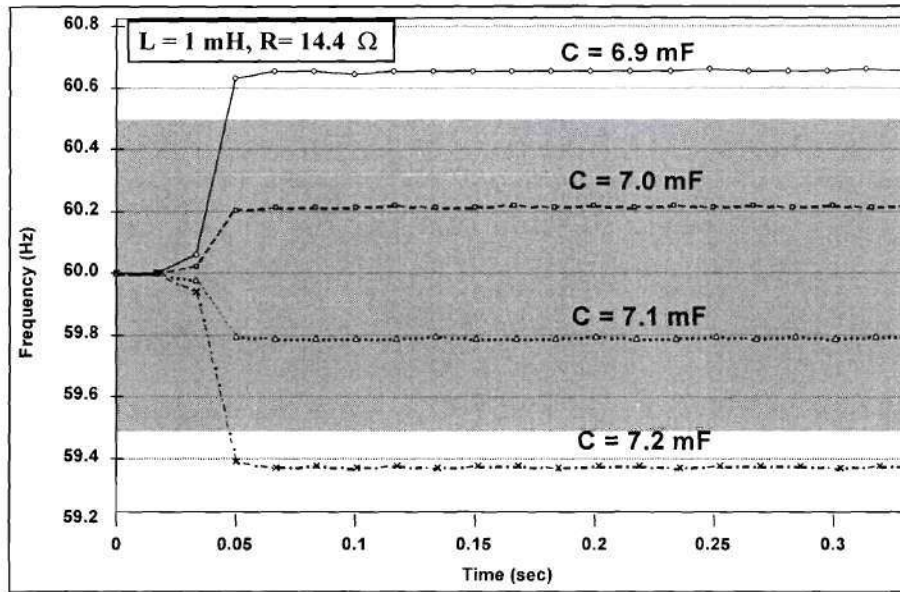
Figure 55. Plot of frequency vs. time for cf = 5%, L = 1 mH, R = 14.4 Ω, and several values of C.
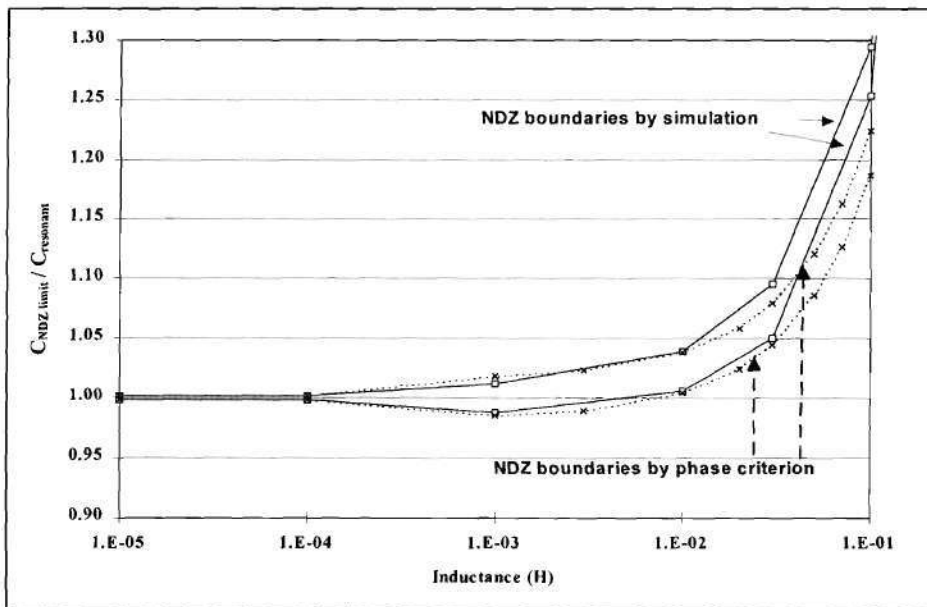
Figure 56. Comparison of the NDZ of AFD for cf = 5%, R = 14.4 Ω, as computed by the full simulation model and the phase criterion.

Experimental corroboration of the modeling results

In the Background portion of this Subtask, it was mentioned that experiments conducted by manufacturers indicated that AFD could be made to fail by adding a small amount of capacitance to a purely resistive load [46,60,61]. One manufacturer specified that they tested their own PCU, and power resistors and large AC capacitors were used to simulate the RC load. At the outset of this work, these were the only experimental results available. Therefore, to test the validity of the modeling results, it was required to examine these results for RC loads.

First, consider the location of a purely resistive load within the C_{norm} vs. L space in which NDZs are plotted in this work. A resistive load may be considered to be an RLC load in which the impedances of the inductive and capacitive branches are infinite, meaning that the value of L is infinite and that of C is zero. Furthermore, if one calculates the C which resonates with an infinite L from Equation (44), the value is zero. A purely resistive load, with $L = \infty$, $C = 0$, and $C_{res} = 0$, therefore lies at positive infinity on the horizontal axis in C_{norm} vs. L space. If any amount of capacitance is added, the ratio of the load capacitance to the resonant capacitance becomes infinite. An RC load therefore lies at plus infinity on both horizontal and vertical axes in L-normalized-C space.

Now consider the expected behavior of the NDZ of AFD as the RLC load approaches an RC load. Begin with a finite L and increase its value toward plus infinity. As L increases, one should expect the NDZ of AFD to move off of the horizontal axis and toward positive infinity on the vertical axis, which is the location of the known NDZ of AFD. Figure 52, Figure 53, and Figure 56 all indicate that both the simplified and the full time-domain models do indeed predict this behavior. In addition, simulations were run using RC loads ($L = 1 \times 10^{90}$ H), and it was found that the addition

of 14.4 to 14.6 μF of capacitance to a 14.4 Ω resistance would result in a load within the NDZ of AFD with cf = 5%. Exact values of capacitance, resistance and cf from the experiments were not available, but it is clear that the model does indeed accurately predict the known experimentally-demonstrated behavior of AFD, and therefore the models' accuracy and validity are supported by the available experimental data.

Discussion

In the introduction to Subtask 2.2, it was pointed out that the location of the NDZ of a method, and not just its size, is important in determining its effectiveness. In the case of AFD, it is clear from the NDZ mappings that it "bends" the NDZ of the OFR/UFR/OVR/UVR away from unity-dpf loads into a range of leading-dpf (capacitive) loads. Recalling that these are far less common in practice than lagging-dpf loads, the fact that AFD moves the NDZ into the leading-dpf range could be considered an advantage over the OFR/UFR/OVR/UVR alone.

Unfortunately, Figure 52 also shows that cf must be fairly large (greater than 1%) for these benefits to be significant. Figure 50 clearly shows that this will introduce significant distortion, and therefore AFD involves a somewhat unfavorable tradeoff between islanding detection effectiveness and PCU output power quality.

In conclusion, the NDZ locations mapped using the method described in this section illustrates the following points:

1.) AFD "bends" the NDZ of the OFR/UFR/OVR/UVR toward capacitive (leading-dpf) loads at values of L larger than about 1 mH.

2.) For values of L smaller than about 1 mH, the NDZ of AFD falls within the NDZ of the OFR/UFR/OVR/UVR without AFD; that is, for loads with a relatively small L and a correspondingly large resonant C, AFD gives little added protection over the

OFR/UFR/OVR/UVR. Another way of saying this is that AFD becomes less effective as L drops and C rises.

3.) The action of AFD is attenuated as the value of R of the load increases. In other words, for lower-power loads, the "bending" of the OFR/UFR/OVR/UVR NDZ into leading-dpf loads is reduced, and as R is increased AFD gives less protection over the OFR/UFR/OVR/UVR alone.

Limitations of this study

The limitations of the study in Subtask 2.3 are essentially the same as limitations 2 and 3 outlined under Subtask 2.2:

1.) The dynamics and internal operation of the PCU power stage and the effects of any disturbances have been neglected.

2.) Only those aspects of the PCU control scheme which are directly involved in islanding prevention have been considered, but other aspects, such as the MPPT, have been omitted.

The reader is cautioned to bear these limitations in mind, especially when examining the frequency-vs.-time results in Figure 55. In practice, the system will in all likelihood not level off at a constant frequency, but rather it will exhibit complex behavior which will not be accurately accounted for by this model. Also, as the run-on time becomes long, several of the assumptions made in this study begin to fail (for example, the assumption that the amplitude of i_{PV} is constant). However, recall that the purpose of this research is to attempt to determine what range of RLC loads can lead to failure of the method to detect islanding. The experimental corroboration allows confidence, in spite of the many simplifications and limitations, that the models can be used for this purpose with reasonable accuracy.

138

Subtask 2.4: Development of an improved AFD using positive feedback

Background

The results under Subtask 2.3 show that AFD does not compare favorably with existing islanding prevention methods, particularly SMS (see Figure 52). However, it is possible to modify AFD to dramatically improve its effectiveness. In this Subtask, a new islanding prevention scheme called active frequency drift with positive feedback (AFDPF) is introduced and studied. It is shown that this new method is significantly more effective than AFD, and in fact can be made to be more effective than SMS, making AFDPF one of the most effective islanding prevention techniques available. Experimental corroboration of the modeling results shows that although the simplified models do not accurately predict the frequency-vs.-time behavior of the system, they do predict the location of the NDZ with reasonable accuracy. In addition, several real-world concerns about the performance of AFDPF with respect to power quality are addressed, and finally it is shown that AFDPF is effective in the multi-inverter case, even if not all PCUs in the island use AFDPF.

Procedure

Definition of AFDPF

The effectiveness of the SMS method clearly indicates how valuable instability can be in preventing islanding. This suggests that one way of increasing the effectiveness of AFD would be to make it unstable when the utility is not present. Therefore, a scheme was developed in which positive feedback is used to increase the

139

chopping fraction cf with increasing deviation of the frequency of v_a (ω) away from nominal:

$$cf_k = cf_{k-1} + F(\Delta\omega_k)$$ (59)

where cf_{k-1} is the chopping fraction in the previous (k-1th) cycle, and $F(\Delta\omega_k)$ is a function of the sampled frequency error $\Delta\omega_k = \omega_k - \omega_0$. This scheme is called active frequency drift with positive feedback (AFDPF). The basic principle of AFDPF is that, when ω deviates from the nominal utility frequency ω_0, cf is adjusted in such a way as to make the frequency deviation larger. This will prevent the frequency from leveling off as early as was the case with AFD. Thus, if the utility has been disconnected, this positive feedback on cf will cause $\Delta\omega$ to increase to a larger value than was the case with AFD, giving a greater chance of tripping the OFR/UFR. In order to clarify this, consider the following. The AFDPF implementation shown in Equation (59) has been called "cumulative AFDPF" because the deviation of cf away from cf_0 accumulates over time. This can be clearly seen by rewriting Equation (59) in the following form:

$$cf_k = cf_0 + \sum_{n=0}^{\infty} F\left(\Delta\omega_{k-n}\right)$$ (60)

If the summation in Equation (60) is dropped ("non-cumulative AFDPF", which will be discussed in more detail in a later section):

$$cf_k = cf_0 + F\left(\Delta\omega_{k-n}\right)$$ (61)

140

then a phase criterion may be written for AFDPF by substituting the expression for cf_k into Equation (52):

$$\tan^{-1}\left\{R\left[\omega_k C - \frac{1}{\omega_k L}\right]\right\} = \frac{\pi}{2}\left[cf_0 + F(\omega_k - \omega_0)\right] \tag{62}$$

Equation (62) helps to clarify the action of AFDPF. With AFD, since cf was fixed, as the frequency deviated away from ω_0, the phase of the load would change until it became equal to the right-hand side of Equation (52), and steady state would result. However, with AFDPF, as the frequency ω_k deviates from ω_0, the second term on the right side of Equation (62), the F term, increases in magnitude. Thus, the phase of the load on the left-hand side must increase even further to move toward the steady-state condition. This process continues, impeding the ability of the system to reach a steady state until much larger frequency deviations are attained. This results in a narrowing of the NDZ.

The function F may be any function which has the following property: $F(\Delta\omega_k)$ should have the same sign as $\Delta\omega_k$. If a function were selected which did not have this property (for example, $F(\Delta\omega_k) = K (\Delta\omega_k)^2$, where K is a gain), then a negative frequency deviation would result in a positive cf deviation. This would result in negative, or regulating, feedback, which would act to *increase* run-on times.

One candidate for $F(\Delta\omega_k)$ which has the above property plus the advantage of simplicity is a linear function:

$$cf_k = cf_{k-1} + K^*(\omega_k - \omega_0) \tag{63}$$

141

where K is a gain (with units of sec/rad, for AFDPF as shown). This "linear AFDPF" will be the type of AFDPF studied and analyzed through most of this work to demonstrate the effectiveness of the method.

Locating the NDZ of AFDPF using the time-domain simulation approach

In order to investigate AFDPF and its advantages over AFD, linear cumulative AFDPF as defined by Equation (63) was incorporated into the time-domain simulation engine used to study AFD in Subtask 2.3. The resulting MATLAB code is provided in Appendix IV. In order to map the NDZ of AFDPF, the same procedure was applied as in the case of AFD, using the parameter values given in Table 5 with the initial chopping fraction, cf_0, corresponding to cf. Four values of gain K were used: 0, 1e-3, 1e-2, and 1e-1. Values of cf_0, the gain K, and the load inductance and resistance L and R were chosen, and then C was swept in order to discover at what C values AFDPF would fail.

Results

The results of simulations performed using this model indicate clearly the above-described operation of AFDPF, that it prevents the frequency of v_a from leveling off. To show this clearly, the frequency-vs.-time results provided by the MATLAB simulation using K = 0.1 Hz^{-1}, R = 14.4 Ω, L = 1 mH, and four values of C, are shown in Figure 57. The upper panel shows the frequency vs. time of an AFD-equipped system with cf = 5% (reproduced from Figure 55). Recall that, for two of the four loads shown, the frequency of v_a (note that f (Hz) is shown, not ω (rad/sec)) levels off within the shaded region (the OFR/UFR NDZ), and AFD fails to prevent islanding. However, in the lower panel, the frequency vs. time behavior of an AFDPF-equipped system with the same loads and cf_0 = 5% is shown. With the addition of the positive feedback, the frequency of v_a does not

level off within the OFR/UFR NDZ for any of the loads shown. AFDPF prevents islanding in cases in which AFD does not.

The NDZ boundaries located by the above-described method are shown in Figure 58, along with the NDZs of AFD, SMS, and the OFR/UFR. In these simulations, K = 0.1 Hz⁻¹, R=14.4 Ω and L = 1 mH. Again, the action of AFDPF is apparent—adding positive feedback to AFD has reduced the width of its NDZ throughout the range of loads under consideration.
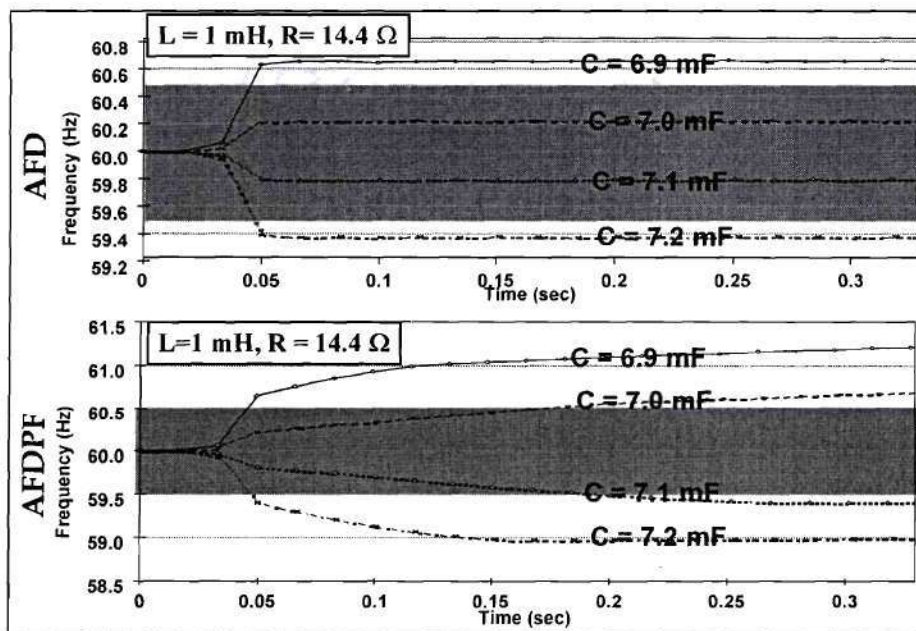
Figure 57. Demonstration showing that AFDPF prevents the frequency leveling noted using AFD. In these simulations, R = 14.4 Ω, L = 1 mH, cf_0 = 5%, and gain K=0.1 Hz⁻¹.
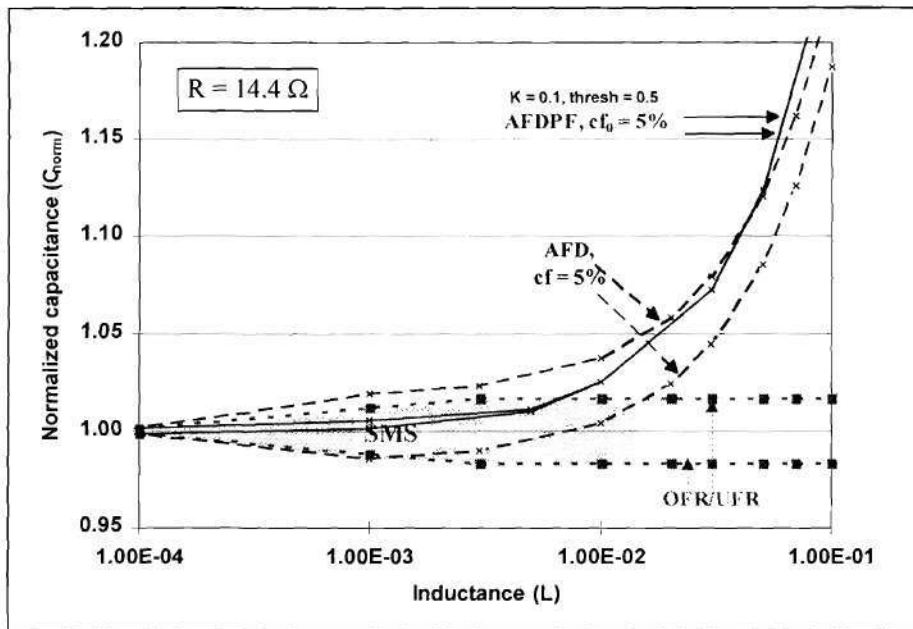
Figure 58. The NDZs of AFD and linear AFDPF, for $cf = cf_0 = 5\%$, gain $K = 0.1$ Hz^{-1}, and R=14.4 Ω. Also shown are the NDZs of SMS for R=14.4 Ω and the OFR/UFR.

Linear AFDPF does still have an NDZ, but throughout the range of L shown the range of capacitances that lead to nondetection for each inductance is significantly reduced. This subject is taken up in more detail in the Results section.

Experimental verification of the AFDPF modeling results

The AFDPF concept was well-received by manufacturers of PV PCUs [60,61] and also by utilities [48,49,62]. Several PCU manufacturers immediately initiated work on implementing AFDPF or variants of it in their PCUs. One manufacturer, Ascension Technology, Inc. (ATI), was contracted by Sandia National Laboratories to build an anti-islanding evaluation unit (AIEU) based on their SunSine 300 PCU. The SunSine 300 is a 300 W PCU which is descended from the SunSine PCU manufactured by the American

144

Power Conversion Corporation (APCC) in the mid-1980s [31]. ATI modified the design for module-integrated (AC array) application and digital control. The AIEU was a SunSine 300 which had built into it several different islanding prevention methods that could be switched on and off, along with data acquisition circuitry to capture and record the PCU's measured output current and terminal voltage frequency (the frequency of v_a). One of the methods built into the AIEU was a variant of AFDPF called Sandia Frequency Shift (SFS). Without delving into the operation of SFS, the primary difference between SFS and AFDPF is that the dead zone is applied entirely at the end of the current cycle; there is no dead zone before the zero crossing at mid-cycle.

ATI also built an islanding test setup in their laboratory. This apparatus, which is shown schematically in Figure 59, includes a large inductive load implemented using a transformer with one winding open-circuited, and a switchable capacitor bank which allows ATI experimenters to step the value of capacitance over a range in order to zero out the reactive power consumption of the inductor. Resistance could be added in a similar
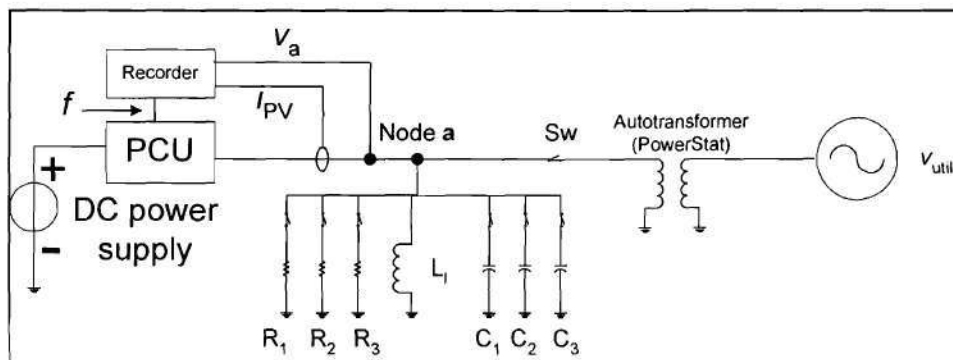
Figure 59. Schematic of islanding test setup.

way as capacitance. This type of setup is ideally suited to experimental verification of the type of NDZ mapping done in this thesis.

ATI graciously agreed to perform a series of experiments planned by the author in order to obtain verification of the modeling procedure described above. However, before undertaking the task of experimental verification, let us summarize briefly what the models have shown and what the experiments can be expected to demonstrate.

1.) The NDZ of AFDPF, like that of AFD, becomes wider as L decreases and C increases; that is, the effectiveness of AFDPF decreases with increasing C and decreasing L values (Figure 58). Another way of viewing this prediction is that it should be easier in an experimental setting to find loads which produce long run-on times when L is small and C is large. If L is large and C is small, the NDZ becomes so narrow that it would be difficult to match the experimental load parameters to those of the NDZ loads with sufficient precision. Therefore, it is expected that longer run-on times will be found for loads with small L and large C.

2.) The NDZ of AFDPF, like that of AFD, becomes wider as the value of R increases; that is, the effectiveness of AFDPF decreases as the value of R increases. Again considering the implications of this prediction from a practical standpoint, it is expected that it will be easier to make the PCU run on when the real power consumption of the load is low. Thus, it is expected that longer run-on times will be measured for loads with low values of R than for higher-power loads.

3.) The NDZ of AFDPF, like that of AFD, "bends" into the leading-dpf load range (C_{norm} >1) when there is a nonzero cf_0 (Figure 58). Therefore, as the value of L is increased, it is expected that the C_{norm} at which run-on times are longest will also increase.

146

In order to test whether these general predictions are in fact representative of the behavior of the real system, the following experiment was designed:

1.) Deactivate all islanding prevention methods other than SFS (the OFR/UFR/OVR/UVR are not switchable; these are always active).

2.) Select RLC loads according to the following matrix:

R	L	C
"high" (>110 Ω)	"high" (>300 mH)	Sweep over the range $0.8 \leq C_{norm} \leq 1.2$.
"low" (<70 Ω)	"high" (>300 mH)	Sweep over the range $0.8 \leq C_{norm} \leq 1.2$.
"high" (>110 Ω)	"low" (<50 mH)	Sweep over the range $0.8 \leq C_{norm} \leq 1.2$.
"low" (<70 Ω)	"low" (<50 mH)	Sweep over the range $0.8 \leq C_{norm} \leq 1.2$.

3.) Run a series of four tests. For the first and second tests, L will be fixed at its "high" value. In the first test, an R ("high") will be chosen, and C_{norm} will be swept over the prescribed range. In the second test, R will be changed to its "low" value, and C_{norm} will again be swept over the prescribed range. For the third and fourth tests, L will be set to its "low" value. In the third test, R will be returned to its "high" value (or a value as near it as allowed by practical considerations), and C_{norm} will again be swept, and in the fourth test R will be set to its "low" value, and C_{norm} will again be swept. In this way, all combinations of R, L and C_{norm} will be tested.

4.) For each test, in each line cycle, record frequency of v_a, magnitude or RMS of v_a, the length of the run-on, and PCU current output.

ATI performed the experiments and provided the requested data. The actual load parameters used in the experiment are given in Table 6. Unfortunately, the available values of L in the laboratory setup do not meet the requirements set forth in

147

the experimental plan, but the inductances used represent the largest available span of L values. The measured run-on times of the AIEU as functions of C_{norm} are shown in Figure 60 and Figure 61. Each figure shows the results for one value of inductance, and in each figure there are two curves, each corresponding to a different value of resistance. In addition, in Figure 62, the frequency-vs.-time and voltage-vs.-time behavior of the AFDPF-equipped system with L = 96.6 mH, C = 69.5 µF, and R = 108.1 Ω is plotted, and in Figure 63 the same plots are shown for a load with L = 345.4 mH, C = 20.467 µF, and R = 134.4 Ω. Finally, the run-on time data is consolidated in the three-dimensional chart plotted in Figure 64 as functions of R (high or low) and L (high or low). Note that this chart was plotted using four data points (at the corners of the surface).

Table 6. RLC load parameters for ATI islanding experiments using AFDPF (SFS).

R (Ω)	L (mH)	C (µF)	Maximum run-on time	C_{norm} at which max run-on happens
108.1	96.6	67.5, 69.5, 70.5, 71.22, 72.22, 73.22, 74.22, 75	125	0.954
73.4	96.6	67.5, 69.5, 70.5, 71.22, 72.22, 73.22, 74.22, 75	16	0.978
134.4	345.4	19.72, 19.97, 20.22, 20.467, 20.72, 20.967, 21.22, 21.467, 21.72, 21.967, 22.22	26	1.005
71.7	345.4	19.72, 19.97, 20.22, 20.467, 20.72, 20.967, 21.22, 21.467, 21.72, 21.967, 22.22	7	1.091
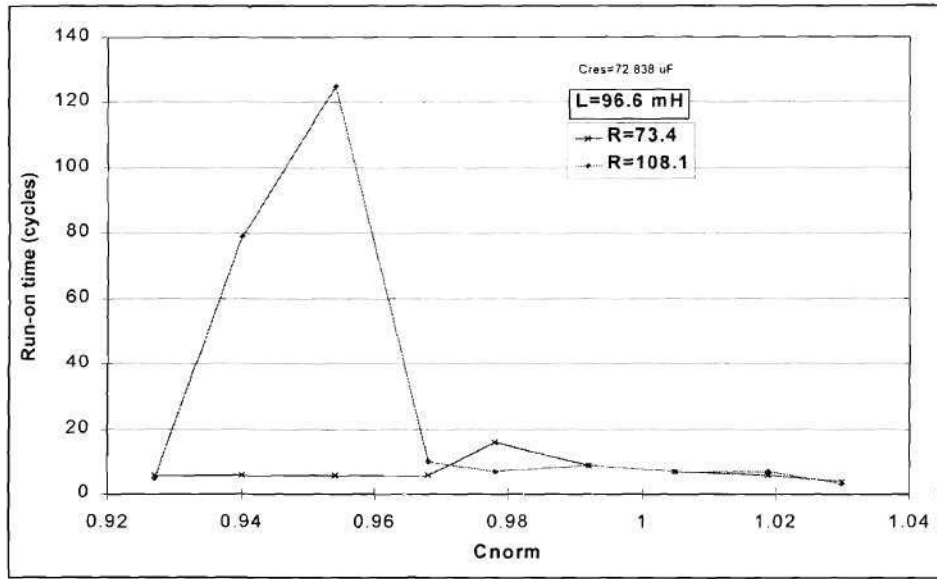
Figure 60. Run-on time of the ATI AIEU as a function of C_{norm} for two values of load resistance. For these experiments, L = 96.6 mH.
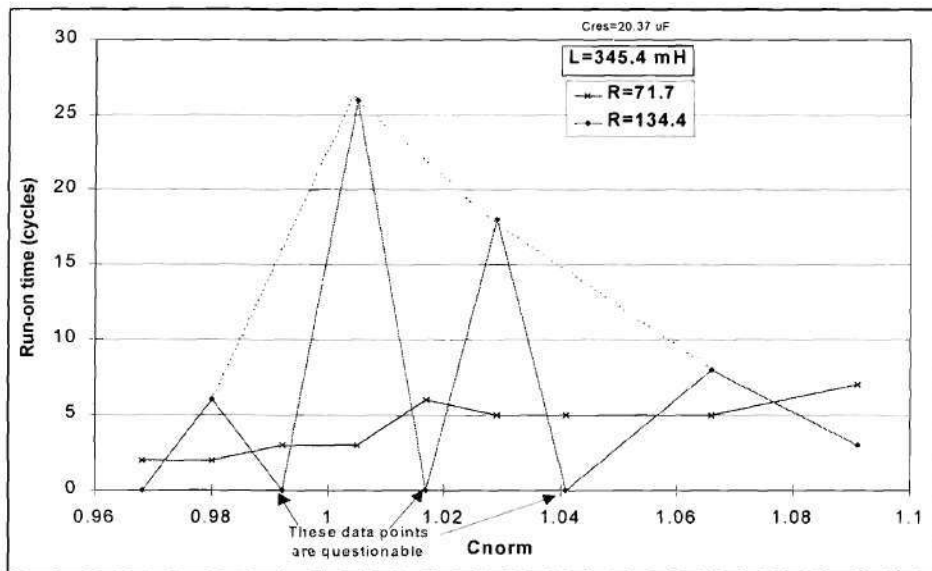
Figure 61. Run-on time of the ATI AIEU as a function of C_{norm} for two values of load resistance. For these experiments, L = 345.4 mH.
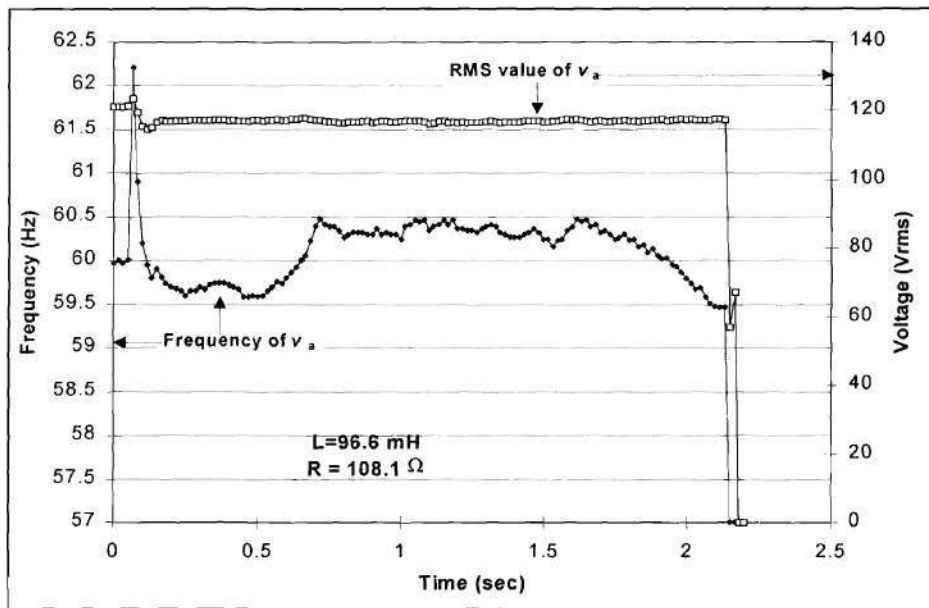
Figure 62. Frequency vs. time and RMS voltage vs. time during an example long run-on with L = 96.6 mH, R = 108.1 Ω, and C = 69.5 μF.
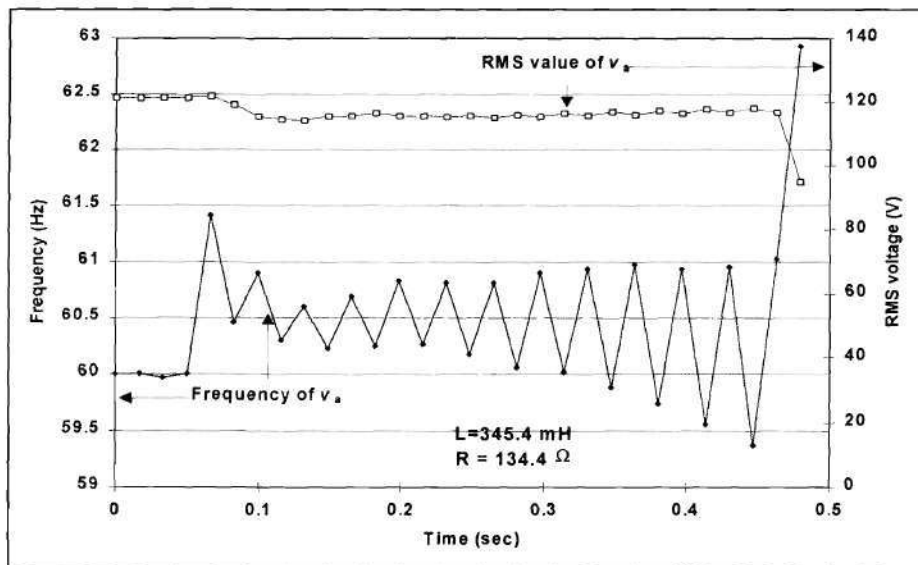
Figure 63. Frequency vs. time and RMS voltage vs. time during an example long run-on with L = 345.4 mH, R = 134.4 Ω, and C = 20.467 μF.

Discussion

Experimental data vs. modeling results

The plots of run-on times in Figure 60 and Figure 61, and the 3-D chart of the data in Figure 64 offer many significant insights. First and foremost, the data shows that the following behaviors are correctly predicted by the model:

1.) Longer run-on times were obtained for loads with large values of C and small values of L, and that were near resonance at ω_0. This corroborates the expected narrowing of the NDZ of AFDPF at larger values of L and smaller values of C.

2.) Longer run-on times were observed for low-power loads than for high-power loads. This verifies the finding that the NDZ of AFDPF is narrower for high-power loads.

3.) The value of C_{norm} at which the longest run-on times are obtained increased as L increased. This illustrates that the NDZ of AFDPF does in fact bend upward under the influence of a small amount of frequency bias (nonzero cf_0).

Further validation of the models was provided by the experimenters at ATI and also at Sandia National Laboratories, who indicated that the worst-case loads observed during their anti-islanding experiments were loads with small inductors, large resistors, large capacitors, and dpfs very near unity [61,64,63]. Therefore, the predictions of the location of the NDZ of AFDPF, which are the primary goal of this research, seem to be well-supported by the experimental evidence. The model has demonstrated significant value in determining the locations of the worst-case loads in RLC space, significant because it can serve as a guide for experimentation and also as an aid for developing a test of the islanding protection of PV PCUs.

151

However, as was indicated previously, the experimental data also indicates some weaknesses of the models used in this work. Note in Figure 62 and Figure 63 that the frequency-vs.-time behavior is very different from that predicted by the models as plotted in Figure 57. For the small-L, big-C case shown in Figure 62, there is a significant initial transient in frequency, followed by a "meandering" behavior until the PCU finally trips on underfrequency. (The system actually runs on for more than 2 seconds, indicating that for this load it does not meet the specifications called for in IEEE-P929 [35].) Even more surprising is the behavior seen in the big-L, small-C case in Figure 63, in which the frequency measurement actually oscillates before finally shutting down. This is significant because it appears that at larger inductances and smaller capacitances, the behavior of the AIEU may be dominated by mechanisms not accounted for in the modeling. However, experimenters at Sandia National Laboratories report that this behavior was not seen in other converters [64], so it is believed that the oscillation itself is specific to the AIEU, and is not an inherent property of AFDPF. Furthermore, note the fact that the oscillation is slowly growing in amplitude. This growing amplitude is believed to be because of the presence of the positive feedback; in other words, if the system were using AFD and not AFDPF, the oscillation would be expected to be much more constant in amplitude, and run-on times would be much longer. Because the positive feedback makes the system less stable, it is not believed that this oscillation could increase run-on times so significantly as to change the predicted NDZ location.

Note also that in Figure 60 the maximum run-on times are obtained for loads with $C_{norm} < 1$; that is, loads which are slightly inductive, and slightly off of resonance. It is suspected that this is an indication of the influence on the load of the large capacitors in the output of the AIEU, an influence which is not included in the model. In fact, the PCU itself seems to contribute some amount of capacitance to the load, or

152

equivalently the PCU is capable of supplying a significant amount of reactive power to the load. This would have the effect of offsetting the NDZ of AFDPF to lower values of C_{norm}. A second peculiarity is evident in Figure 61. Note that several of the data points are marked as "questionable". This is because in each case a sharp upward frequency transient like that shown in Figure 62 tripped the PCU immediately when the switch was thrown to form the island. Clearly, these points do not illustrate the behavior of AFDPF, but they are important because they illustrate the importance of Limitation 2 pointed out in Subtask 2.1, which stated that potential transients at utility shutoff were ignored. Clearly, such transients are in fact possible and can significantly impact the behavior of the system in some cases.

In summary, in spite of the differences between the experimental system and the system that was modeled, and in spite of the simplicity of the model, the modeling described in this work has proven highly valuable to the PV community because it accurately describes the ranges of loads in which islanding prevention methods can be expected to fail (or at least perform the least well). Such knowledge has already directly led to improved islanding prevention techniques, and also a test to determine whether a PV PCU may be certified as "non-islanding".
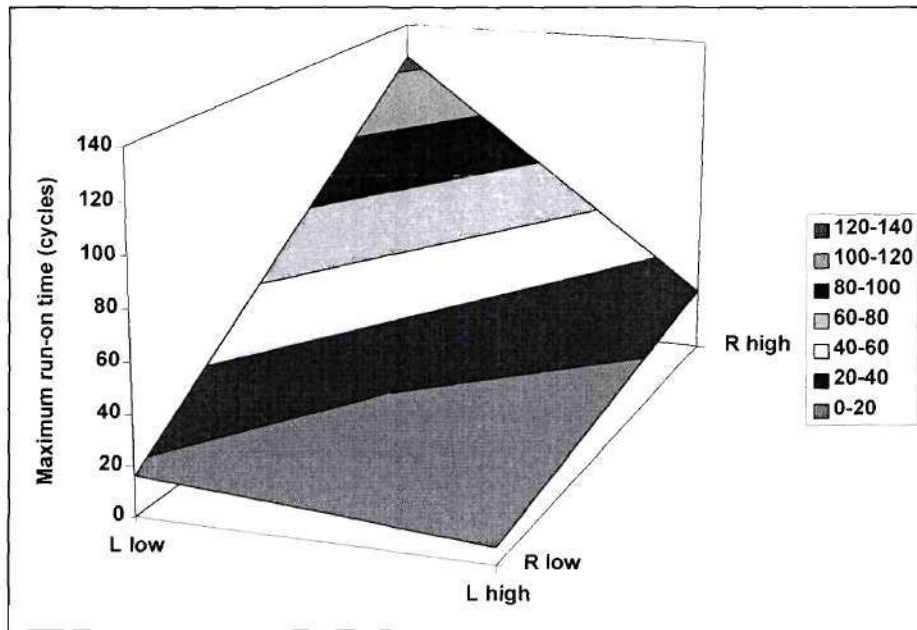
Figure 64. Three-dimensional plot showing trend in maximum run-on times as functions of the R and L of the RLC load. Note that this plot was created using only four data points (at the corners of the surface).

The effectiveness of AFDPF vs. other methods

The NDZ locations predicted by the models have, in general, been experimentally validated. Therefore, it may be concluded that the NDZ results indicate that AFDPF is among the most effective islanding prevention methods available, in terms of its ability to prevent islanding. The addition of positive feedback leads to dramatic improvements over the performance of AFD. The width of the AFDPF NDZ ("width" being defined as the difference between the capacitances at the NDZ boundaries for a given value of L) is at least an order of magnitude less than the width of the AFD NDZ, and for L > about 1

mH the AFDPF NDZ is six orders of magnitude narrower than that of AFD. An examination of Figure 57 indicates that AFDPF has significant advantages over SMS as well. In particular, in the "midrange" of inductances between about 1 and 100 mH, the NDZ of AFDPF is narrower than that of SMS. At larger L values, AFDPF has an NDZ where SMS does not, but this NDZ is extremely narrow, and if a nonzero cf_0 is used it lies in a range of leading-dpf loads ($C_{norm} > 1$), which are much less likely in practice than lagging-dpf loads ($C_{norm} < 1$). Therefore, AFDPF can arguably be declared to be the best islanding prevention method among those presented in this thesis.

Effect of AFDPF on PCU output power quality: distortion of i_{PV}

Under normal operating conditions (with the utility connected), the PCU will periodically detect deviations in ω. These deviations could be caused by switching of large loads, particularly large loads with low dpfs, or by the switching of large utility reactances; nonlinear load components that inject sufficient harmonic current to lead to appreciable distortion of v_a; and noise and other disturbances, both in the system itself and in the PCU's measurement of ω. In an AFDPF-equipped PCU, these will cause cf to fluctuate while the utility is still connected, and as is demonstrated in Figure 50, this will increase the amount of distortion in i_{PV}. Therefore, AFDPF will always cause greater output distortion than would AFD with the same starting value of cf. Since it is required to keep THD_{iPV} below 5% [38,39], the fact that AFDPF increases THD_{iPV} will impose a limit on how large the positive feedback gain can be. Instead of reducing the gain, one might impose a threshold on cf, so that it would saturate at some value chosen to keep THD_{iPV} within limits. However, either of these approaches will also reduce the islanding detection effectiveness by widening the NDZ. The effect of reducing the gain on NDZ size is demonstrated in Figure 65. The NDZ for a gain of 0.1 Hz^{-1},

which is the one plotted in Figure 58 is compared with the AFDPF NDZ with a gain of 0.01 Hz^{-1}. In both cases, cf_0 = 5%.
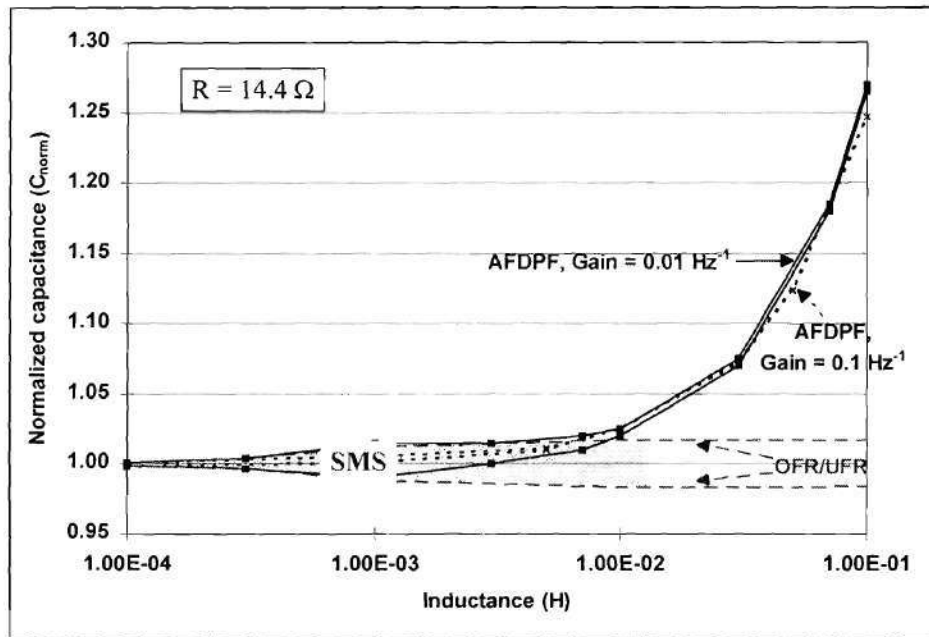
Figure 65. NDZ of AFD for two different values of gain. Also shown are the NDZs of the OFR/UFR (dashed lines) and SMS for R = 14.4 Ω (shaded).

Another practical consideration that impacts THD_{iPV} must be introduced at this time. Consider a case in which the frequency of v_a, ω, is perturbed in one direction or the other but returns to zero without a deflection in the opposite direction. In this case, AFDPF as presented in Equation (63) would alter its value of cf but would never return to the original value. If several such deflections occurred, this could lead to large values of cf_k and correspondingly large values of THD_{iPV}. To prevent this, some mechanism must be provided that causes cf_k to return to cf_0 when several cycles pass without any

156

deviation in ω. Such a mechanism has been referred to as "centering" or "forgetting". This mechanism may take any of several forms. One is simple forgetting, in which older values of cf_k are multiplied by a coefficient that decreases as the cf_k values become older. Note that Equation (63) may be rewritten as

$$cf_k = cf_0 + K^* \sum_{n=1}^{\infty} \left[\left(\omega_{k-n} - \omega_0 \right) \right] \tag{64}$$

To implement simple forgetting, all that is required is to multiply the summation term by a "forgetting factor" (*FF*) which decreases as the index n increases:

$$cf_k = cf_0 + K^* \sum_{n=1}^{\infty} FF_n \cdot \left[\left(\omega_{k-n} - \omega_0 \right) \right] \tag{65}$$

where *FF* may be $1/n$, exp(-n), or any similar factor. An alternative to using *FF* would be to use an AFDPF function in which cf_k does not depend on cf_{k-1}:

$$cf_k = cf_0 + K^* \left(\omega_k - \omega_0 \right) \tag{66}$$

This is "non-cumulative" AFDPF, which the reader will recall was used earlier in the derivation of an AFDPF phase criterion. Non-cumulative linear AFDPF is much simpler than AFDPF with forgetting, but it has a wider NDZ unless *K* is fairly large.

A third alternative would be to use a sliding window, so that AFDPF uses only a finite number of past cf_k values:

$$cf_k = cf_0 + K^* \sum_{n=1}^{N} \left[\left(\omega_{k-n} - \omega_0 \right) \right] \qquad (67)$$

This alternative is more effective than non-cumulative AFDPF but requires less computing power than using forgetting factors. In this work, both the non-cumulative and sliding window approaches were investigated. If the sliding window used is fairly long (N > about 30), the NDZ of AFDPF with the sliding window is practically identical to that of cumulative AFDPF. Also, at the high gains used in this work, the NDZ of non-cumulative AFDPF is nearly the same as that of cumulative AFDPF, but the difference becomes larger at smaller gains.

The maximum allowable value of the gain is a complex function of several mechanisms that are not considered in the models presented here. A maximum gain of 0.1 Hz^{-1} has been used in the linear AFDPF demonstrated in this work. This value was derived by assuming that the maximum allowable frequency deviation is 0.5 Hz (larger frequency deviations would trip the OFR/UVR). Since to maintain THD$_{ipv}$ of less than 5% it is required to keep cf less than 5% (Figure 50), the gain is selected such that the maximum frequency deviation of 0.5 Hz leads to a cf of 0.05, or 0.1 Hz^{-1}. This assumes that $cf_0 = 0$, and that "centering" has been employed. However, in practice, the true maximum gain allowable would need to be determined by testing of the PCU.

Effect of AFDPF on PCU output power quality: system transient response

In general, the utility voltage source, as seen from node **a**, is not an ideal voltage source with zero impedance. In particular, the transformers used to step the distribution voltage down to household voltage have non-negligible series resistance and inductance. Since the series impedance of distribution lines is *in general* very small

158

[65], the transformer impedances dominate the source impedance as seen from the point of common coupling.

Consider the system configuration shown in Figure 66. This is the now-familiar PV-load-utility interconnected system, except that this time the impedance of the utility source is explicitly shown. When large loads switch on or off, v_a will in general exhibit
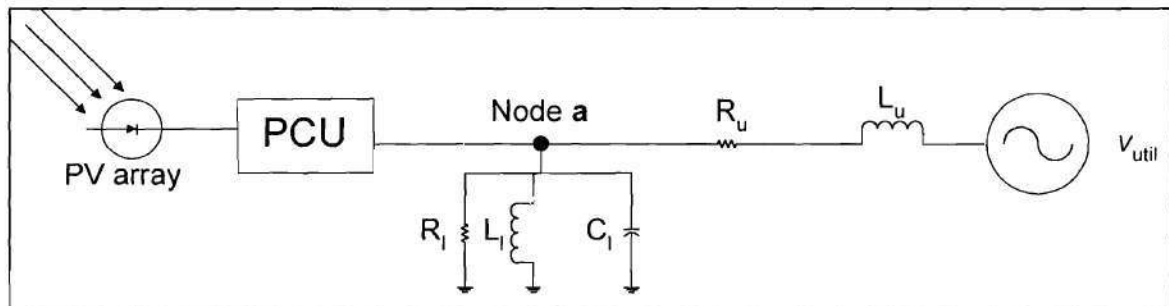
Figure 66. Schematic of PV-load-utility system showing utility series impedances.

a short transient. The magnitude and settling time of this transient will depend primarily on the size of the change in the load, and on the impedance of the utility voltage source. If the PV PCU in Figure 66 were equipped with AFDPF, it will react in such a way as to increase the magnitude of the frequency transient. Therefore, the potential impact of AFDPF on the system transient response must be investigated.

To model the system in Figure 66, a state-space model was used. The derivation of this model follows the procedure outlined in the literature [66]. The load inductor

current i_{Ll}, load capacitor voltage v_{Cl}, and utility inductor current i_{Lu} were selected as the state variables, resulting in a third-order system:

$$
\begin{bmatrix} x_1 \\ x_2 \\ x_3 \end{bmatrix} = \begin{bmatrix} i_{Ll} \\ v_{Cl} \\ i_{Lu} \end{bmatrix}
$$

(68)

The derivatives of the state variables are:

$$
\begin{bmatrix} \dot{x}_1 \\ \dot{x}_2 \\ \dot{x}_3 \end{bmatrix} = \begin{bmatrix} \dfrac{di_{Ll}}{dt} \\ \dfrac{dv_{Cl}}{dt} \\ \dfrac{di_{Lu}}{dt} \end{bmatrix} = \begin{bmatrix} \dfrac{1}{L_l} v_{Ll} \\ \dfrac{1}{C_l} i_{Cl} \\ \dfrac{1}{L_u} v_{Lu} \end{bmatrix}
$$

(69)

To derive the state equations, Kirchhoff's Current and Voltage Laws are used to analyze the system and solve for v_{Ll}, i_{Cs}, and v_{Lu} in terms of linear combinations of the state variables:

$$
\dot{x}_1 = \frac{1}{L_l} x_2
$$

$$
\dot{x}_2 = \frac{1}{C_l}\left(-x_1 - \frac{1}{R_l} x_2 + x_3 + i_{PV} \right)
$$

(70)

$$
\dot{x}_3 = \frac{1}{L_u}\left(-x_2 - x_3 R_u - v_{util} \right)
$$

160

Equation (70) can be written in the matrix form $\dot{x} = Ax + Bu$, where

$$
A = \begin{bmatrix} 0 & \dfrac{1}{L_l} & 0 \\[2mm] -\dfrac{1}{C_l} & -\dfrac{1}{R_l C_l} & \dfrac{1}{C_l} \\[2mm] 0 & -\dfrac{1}{L_u} & -\dfrac{R_u}{L_u} \end{bmatrix} \quad ; \quad B = \begin{bmatrix} 0 & 0 \\[2mm] \dfrac{1}{C_l} & 0 \\[2mm] 0 & \dfrac{1}{L_u} \end{bmatrix} \quad ; \quad u = \begin{bmatrix} i_{PV} \\[2mm] v_{util} \end{bmatrix} \qquad (71)
$$

The MATLAB program used previously was modified to use this state equation model (instead of the algebraic model in Equation (58)) and to run in batch mode, as shown in Appendix V. To simulate the switching of a large load, a step change in load was utilized in which the load impedance increases by a factor of five. The load parameters used are listed in Table 7. This simulates the turning off of a high-power load. In each simulation, the step change occurred at $t = 0.25$ sec (30 line cycles). The PV system output power was matched to the original load power (before the step change).

Table 7. Load parameters used in modeling system transient response.

Parameter	Initial value	At step change, value changes to
R	14.4 Ω	72 Ω
L	10 mH	50 mH
C	703.6 µF	140.7 µF

161

It has been previously noted that in general the utility source impedance is dominated by the series impedance of the pole-mounted transformer used to step the distribution voltage down to customer-level voltage. However, this impedance depends on the size (i.e. power rating) of the transformer and on the voltages at its windings. In order to model the utility source impedance realistically, parameter values for commonly used transformers were supplied by a manufacturer [67]. These values are listed in Table 8. Finally, simulations were performed using four different values of AFDPF gain, namely 0, 0.001, 0.01, and 0.1. In all simulations, $cf_0 = 0$. To summarize: a total of twenty simulations were performed. For each of the five transformers in Table 8,

Table 8. Parameters of Howard Industries 7.62kV-240V distribution transformers.

Transformer power rating (kVA)	R (mΩ)	L (μH)
10	135	169
15	77.3	162
25	36.3	115
37.5	22.2	100
50	15.0	57

simulations were run using each of the four gains. In all simulations, the step change in the load was of the same magnitude (increased by 5x) and at the same time ($t = 0.25$ sec).

Examples of the results of these simulations for the smallest and largest transformers are shown in Figure 67, Figure 68, Figure 69, and Figure 70. The most

162

important result of these simulations is that in no case does AFDPF cause the transient to be significantly larger than it would be without AFDPF (the zero gain case). This is evident from the fact that in all four figures all four curves lie essentially atop one another. Therefore, this modeling suggests that the effects of AFDPF on the system's transient response will be negligible. However, one interesting point to note is that the effect of AFDPF on the transient response is greater for the lower-impedance (higher-power) transformer. This at first seems somewhat counterintuitive; one might expect that a higher utility source impedance would lead to larger problems. However, apparently the higher impedance of the lower-powered transformer serves to damp the oscillations introduced by the AFDPF-equipped PCU, and this damping effect is reduced as the utility source impedance decreases. This effect could be significant and warrants further attention. (Note: the slight "jump" at the beginning of each simulation is due to a small mismatch between the initial conditions used and those required for a correct steady-state startup. Exact determination of the true steady-state initial conditions proved to be very difficult, but the match achieved is actually very close, as indicated by the fact that the "jump" is very small in all cases.)
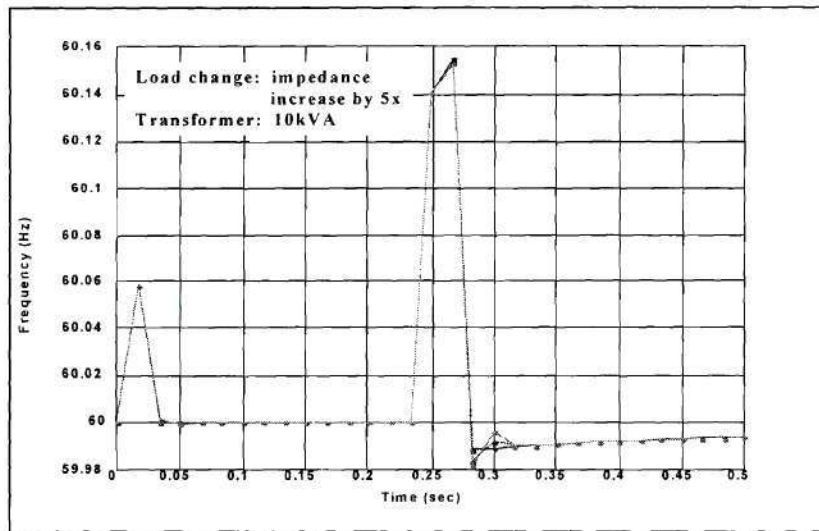
Figure 67. Frequency of v_a vs. time, showing the effect of a step change in the RLC load, for the 10-kVA transformer (highest impedance). Four curves, one for each gain value, are shown.
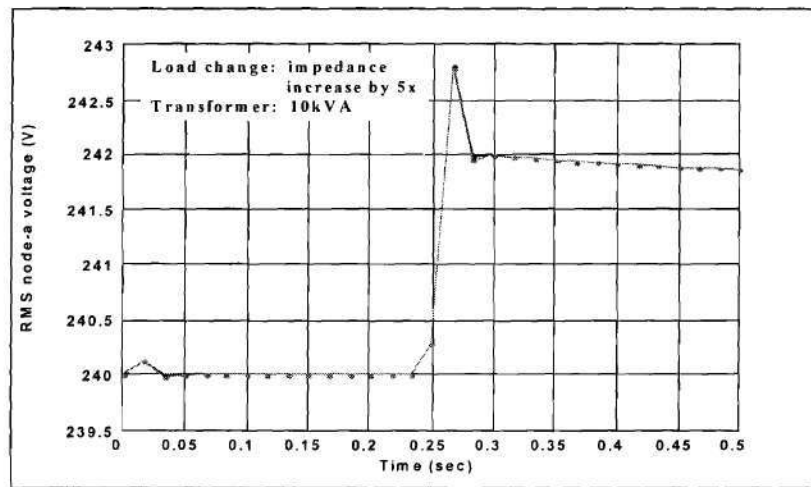
Figure 68. RMS value of v_a vs. time, showing the effect of a step change in the RLC load, for the 10-kVA transformer (highest impedance). Four curves, one for each gain value, are shown.
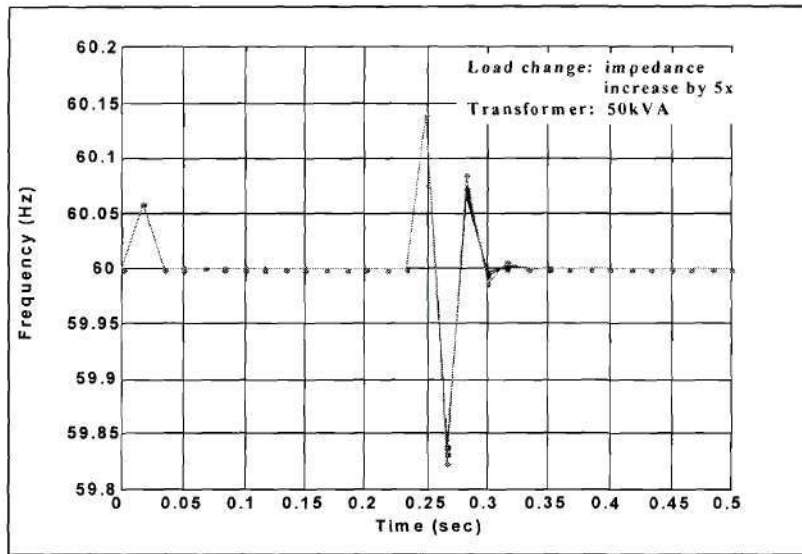
Figure 69. Frequency of v_a vs. time, showing the effect of a step change in the RLC load, for the 50-kVA transformer (lowest impedance). Four curves, one for each gain value, are shown.
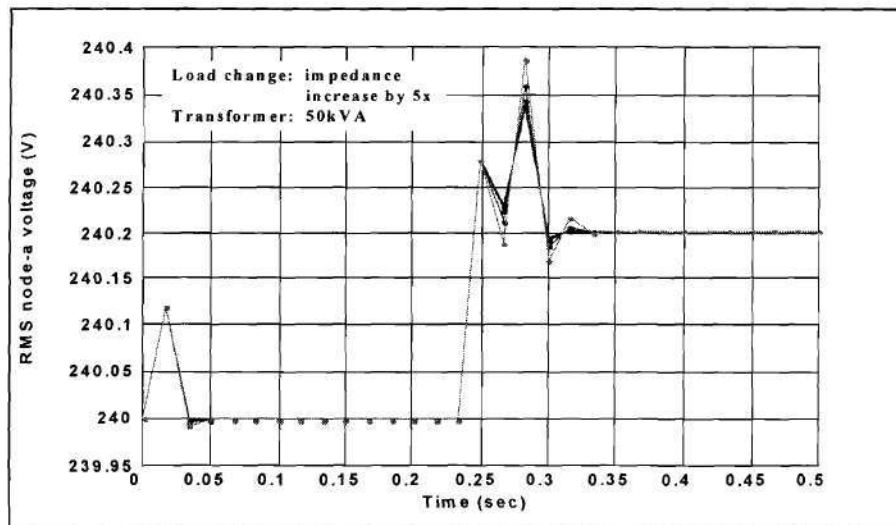
Figure 70. RMS value of v_a vs. time, showing the effect of a step change in the RLC load, for the 50-kVA transformer (lowest impedance). Four curves, one for each gain value, are shown.

Effectiveness of AFDPF in the multiple inverter case

AFDPF has the potential to eliminate the problem of reduced effectiveness in the "multiple inverter case" in which there are many PV systems within the island. This is because the positive feedback action enables an AFDPF-equipped PV system to reinforce whatever frequency deviation is produced by the other PV systems, or by any other device in the island. If all PV systems in the island were equipped with AFDPF, they would detect islanding as a group in the same way that they would individually, albeit perhaps in a slightly longer time due to differences in gains and other practical considerations such as impedances between the PCUs. However, it is not required that all PV systems use AFDPF for this synergistic effect to occur. To illustrate this, consider a simplified simulated island containing four PV systems, as shown in Figure 71. In this system, the top PV system is equipped with linear AFDPF, while the other three have no islanding prevention methods beyond the four standard relays. The total power of the four PV systems is always set to match the load's real power requirement (the PV generation to load ratio is approximately 1). Impedance between the PCUs is ignored, which is essentially the same as assuming that there are no transformers between the PCUs and the POCC. The load has R = 14.4 Ω, L = 10 mH, and C = 700 μF, corresponding to a C_{norm} of 0.995. This load lies within the NDZ of the OFR/UFR/OVR/UVR, but outside that of AFDPF. A MATLAB program has been written to simulate this system, and the results of the simulations are plotted in Figure 72. This plot shows the frequency of the system as a function of time. Each
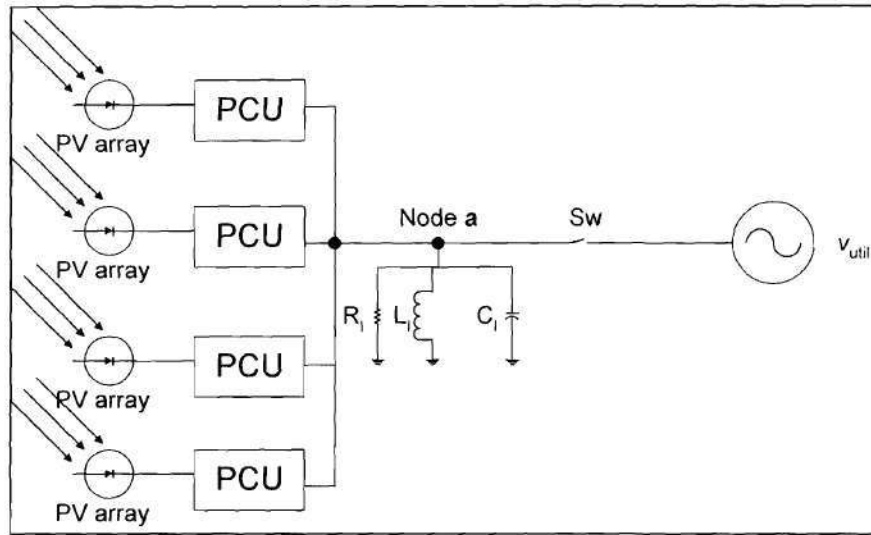
Figure 71. Schematic of a system used to investigate the so-called "multiple-inverter case".
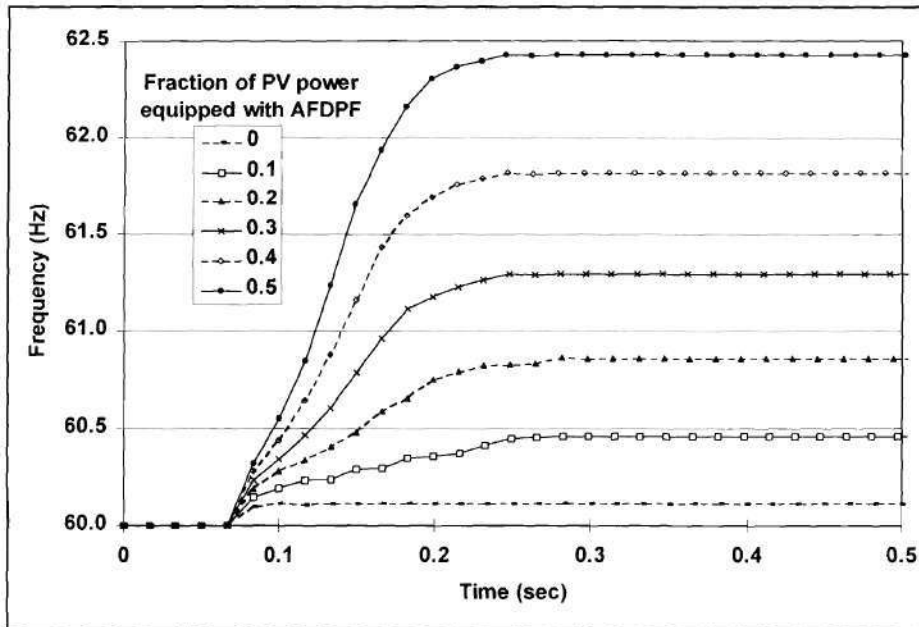
Figure 72. Frequency of v_a vs. time for the system in Figure 71. Only one PCU is equipped with AFDPF (linear; gain = 0.1 Hz^{-1}).

curve corresponds to a different fraction of the PV power being equipped with AFDPF. In other words, the single AFDPF-equipped PV system is varied in size (power rating), and the other three systems equally share the remaining real load power demand. The gain of the AFDPF system is 0.1 Hz^{-1}. The results of this simulation show that even if only a small amount of the total PV generation within the island is equipped with AFDPF (20% or more), the frequency within the island can still be driven outside the OFR/UFR trip limits. Thus, this simulation demonstrates that AFDPF can help prevent islanding even if not all of the PCUs within the island are using it.

In addition, AFDPF would work in conjunction with PV systems using other islanding prevention schemes. For example, it would enhance the islanding protection of a PCU using harmonic detection, because the THD of the AFDPF system's output current will increase when islanding begins, thereby increasing the THD of v_a. A PCU using phase-jump detection also may work better because AFDPF will increase the rate of change of the frequency in the island, leading to a larger phase jump from one cycle to the next.

Other choices for the positive feedback function $F(\Delta\omega_k)$

For all the AFDPF work described up to this point, the linear $F(\Delta\omega_k)$ was used. However, any $F(\Delta\omega_k)$ which satisfies the condition that $F(\Delta\omega_k)$ have the same sign as $\Delta\omega_k$ could be used to implement AFDPF. This includes nonlinear and piecewise-linear functions. In fact, it may be desirable to use some other function under certain conditions. For example, an $F(\Delta\omega_k)$ might be selected in which the gain increases as the frequency deviation increases. Such a function would shorten run-on times in cases where the load was near the NDZ edge. Conversely, if the grid to which a PV system is connected were weak and frequency deviations were common, an $F(\Delta\omega_k)$ might be

selected in which the gain *decreases* as the frequency deviation decreases in order to improve power quality. However, care must be exercised when selecting $F(\Delta\omega_k)$. To illustrate, the AFDPF MATLAB model in Appendix IV allows the user to enter an exponent x which acts on the $\Delta\omega$ term:

$$ cf_k = cf_{k-1} + K^*\left(\omega_k - \omega_0\right)^x \tag{72} $$

The exponent x may have any odd value (1, 3, 5...), and the result will be a function that meets the above-mentioned condition, that $F(\Delta\omega_k)$ have the same sign as $\Delta\omega_k$. Linear AFDPF corresponds to the $x = 1$ case, but simulations were also performed with $x = 3$, the "cubic AFDPF" case. These simulations showed that, in order to get from the $x = 3$ case approximately the same NDZ as in the linear case, the gain must be extremely large, on the order of 10^3. The reason is simple: for small deviations in ω, the cubed frequency deflection is so small that the change in *cf* is negligible. If such large gains are not used, the NDZ of cubic AFDPF is actually considerably larger than that of linear AFDPF.

Subtask 2.5: Investigation of the effect of the load composition on islanding prevention

Background

In most analytical or simulation studies of islanding of PV systems, the local load is usually represented by a parallel RLC circuit [31,32,38]. A concern that could

rightfully be raised is the validity of representing real-world loads in this manner because such loads exhibit many characteristics which cannot be modeled by a constant-parameter parallel RLC. These include nonlinear (harmonic-producing) loads, induction motors connected directly to the utility supply, and constant-power loads, such as (to a first approximation) adjustable-speed drives (ASDs) and switching computer power supplies. The first two types of loads are extremely common, and the third is rapidly increasing in number. Therefore, because of their increasing importance, the effect of these types of loads on the behavior of AFD and AFDPF will be addressed at this time.

Nonlinear loads

Procedure

There is an ever-increasing component of the utility load that draws harmonic currents from the utility; that is, loads whose input currents contain components at frequencies other than the nominal line frequency and are therefore nonlinear. All switching power converters fall into this category to some extent. However, probably the most common nonlinear load is a load which is interfaced to the utility through an uncontrolled rectifier. In addition to being one of the most common nonlinear loads, the rectifier is more nonlinear than most power converters in the sense that it draws a much more distorted current. Therefore, in order to investigate the effect of the presence of a nonlinear load component on islanding protection systems in a meaningful way, a load model has been derived which includes a parallel RLC load and a half-wave rectifier consisting of a diode D and capacitor C_{rect}, shown in Figure 73 [68]. The diode will be "off" whenever $v_{o,rect} > v_{in}$ (in our case, $v_{in} = v_a$), and

$$v_{o,rect} = \frac{q_{Crect}}{C_{rect}} \qquad (73)$$
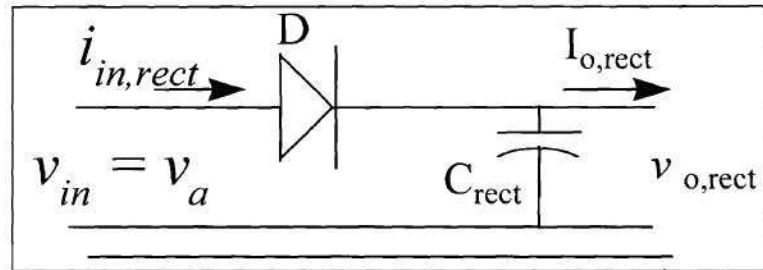
Figure 73. Half-wave rectifier.

where q_{Crect} is the charge on C_{rect}. C_{rect} will be assumed to be fully charged at the beginning of the simulation. The change in q_{Crect} during each time interval of the simulation becomes

$$\Delta Q_{Crect} = (i_{in,rect,k} - I_{o,rect}) \cdot \Delta t \qquad (74)$$

where Δt is the length of the time step. At each time t_k, using (73) and (74), $V_{o,rect}$ may be computed. During the conduction interval of the diode, the rectifier input current at time step k $i_{in,rect,k}$ is given by

$$i_{in,rect,k} = C_{rect} \left. \frac{dv_a}{dt} \right|_{t_k} + I_{o,rect} \quad (> 0) \qquad (75)$$

171

As before, the derivative will be approximated by a difference, and the time step between solution points will be kept small (less than 10 μsec) to ensure accuracy. Armed with Equations (73) to (75), it is now possible to calculate the rectifier input current at each time step. To find the equation for v_a when the utility is disconnected, the rectifier current term is added to Equation (56):

$$i_{PV,k} = i_{R,k} + i_{L,k} + i_{C,k} + i_{in,rect,k} \qquad (76)$$

When the utility is disconnected but D is not conducting, Equation (58) is used to find v_a. When D is conducting, the equations for the currents drawn by the load components are substituted in to Equation (76), which is then solved for v_a:

$$v_{a,k} = \frac{\left[i_{PV,k} - i_{L,k-1} + \dfrac{(C + C_{rect})v_{a,k-1}}{t_k - t_{k-1}} - I_{o,rect} \right]}{\dfrac{t_k - t_{k-1}}{L} + \dfrac{(C + C_{rect})}{t_k - t_{k-1}} + \dfrac{1}{R}} \qquad (77)$$

This nonlinear load model was incorporated into the MATLAB program. In order to ascertain the effect of the nonlinear load, numerous simulations were performed with linear and nonlinear loads for comparison. In each case, the total real power of the load was kept constant at 4 kW. The rectifier parameters were C_{rect} 2.9 mF (chosen to give a 5% output voltage ripple) and $I_{o,rect}$ = 2.95 A (approximately 1 kW of load at an output voltage of $240\sqrt{2}$ V, or 25% of the total real power). For the linear (RLC) portion of the load, the parameters selected were R = 14.4 Ω (if the rectifier was not present) or 19.2 Ω (if the rectifier is present), L = 1 mH, and C = 7.1 mF. This represents a load which lies

172

just outside the NDZ of AFD when the rectifier is not present. This choice will demonstrate whether the addition of the rectifier could somehow widen the NDZ such that such loads now lie within the NDZ and result in failure to detect islanding.
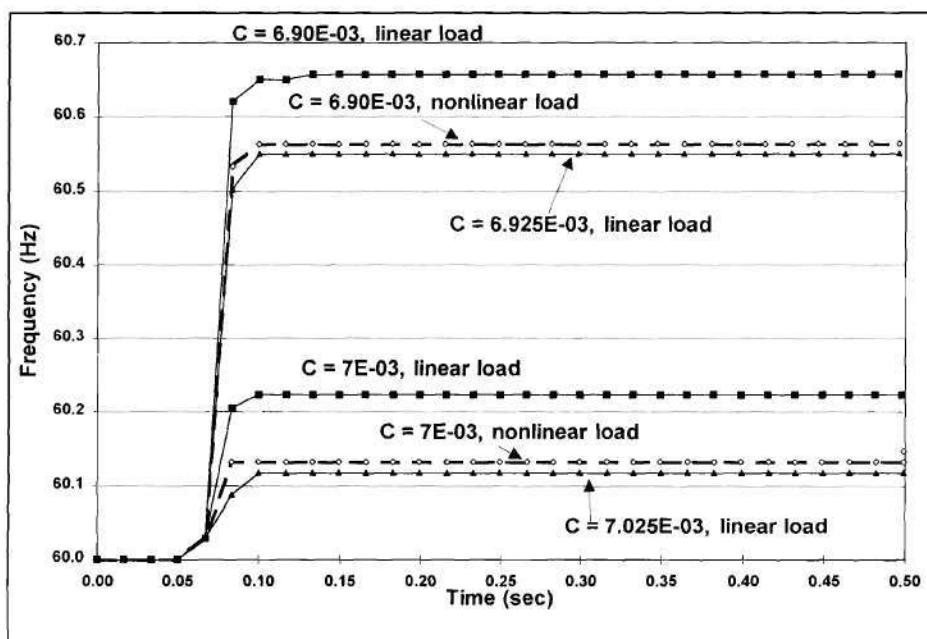
Figure 74. Frequency-vs-time behavior of an AFD-equipped PV system with a linear (RLC) load and a nonlinear load (RLC plus the half-wave rectifier). Dashed heavy lines with hollow markers indicate curves for the nonlinear load; solid lighter lines with filled markers indicate curves for the linear load.

Results

An example of the results is shown in Figure 74. This figure shows the frequency-vs-time behavior of the AFD-equipped system for two of the loads shown in Figure 55. Interestingly, the results in Figure 74 indicate that the system behaves as if the load were a linear parallel RLC combination but with a slightly larger capacitor. In fact, if a "time averaged" value of C_{rect} is calculated by multiplying it by the ratio of the diode conduction time per period to the total period (the duty cycle of the diode), and this time-averaged C_{rect} is added in parallel with that already present in the RLC load, keeping the total real power consumption constant, then the frequency-vs-time behavior of this new RLC load corresponds very closely to that of the RLC-plus-rectifier load. This also is demonstrated in Figure 74. The nonlinearity of the rectifier appears not to have affected the function of AFD at all. Thus, computer modeling and theoretical considerations both suggest that such nonlinear loads will not have a significant effect on the operation of AFD or AFDPF.

The islanded behavior of induction motors connected to the utility supply

Procedure and results

The dynamic behavior of single-phase induction motors is complex. Fortunately, there are several excellent texts on the subject [69,70,71], and these will be drawn upon heavily in this section. There are two basic relationships which govern this behavior. The first is the "swing equation", which basically is Newton's law $F = ma$ applied to the rotor of the motor:

$$\omega_m J \frac{d\omega_m}{dt} = P_{elec} - P_{mech} \tag{78}$$

174

where ω_m is the mechanical (rotational) frequency, J is the rotational inertia of the motor and its rotating load, P_{elec} is the electrical power input to the motor, and P_{mech} is the mechanical power output of the motor. The second relationship is the motor's equivalent circuit, shown in Figure 75. It interrelates the electrical parameters and also accounts for the rotation of the motor through the parameter **S**. **S** is called the "slip" and is a measure of how much the rotor is "slipping" with respect to the rotating magnetic fields in the machine. **S** is defined by

$$S = \frac{\omega_s - \omega_m}{\omega_s}$$

(79)
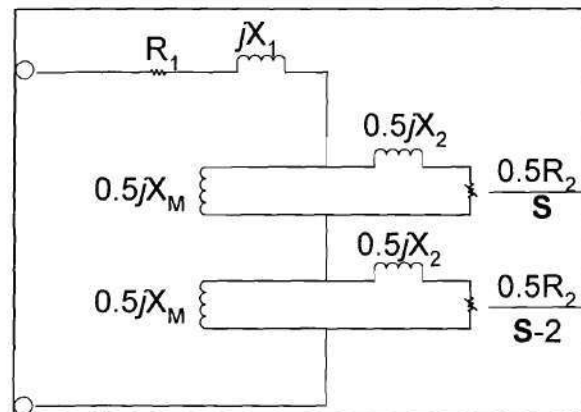
Figure 75. Schematic of a single-phase induction motor.

175

where ω_s is the synchronous speed of the motor (the electrical frequency divided by the number of pole pairs in the motor). When the motor is running and in steady state, **S** will be a small nonzero number (on the order of 0.05, depending on the design of the machine).

A highly simplified treatment of the single-phase induction motor's behavior as part of the load in an island is possible if one assumes that the difference between electrical power input and mechanical power output remains small (a "small-disturbance" case). In this case, the swing equation indicates that the rotational frequency of the motor will not change appreciably ($\frac{d\omega_m}{dt} \approx 0$). With this assumption, under islanding conditions and assuming that the PV power and load power are closely matched and have a similar power factor, the impedance of the motor will change as the PV PCS alters the frequency of the exciting current (i_{PV}) due to the changes in the impedances of the reactances and the changes in the resistances because of the change in the slip. The change in slip is apparent from Equation (35), since the motor's rotational frequency is assumed constant over the time interval being considered. The derivative of Equation (79)

$$\frac{dS}{d\omega_s} = \frac{\omega_m}{\omega_s^2} \tag{80}$$

shows that the change in **S** will have the same sign as the change in ω_s; that is, if ω_s increases, **S** will increase. When an induction machine is operating under normal conditions, **S** is small (≈ 0.05). Likewise, the changes in **S** caused by the PV PCS will be small for small changes in ω_s. If the case of a sudden increase in frequency (the worst-

176

case scenario which will give the largest impedance change in the motor) is considered, the impedance of the motor will change, but the amount of the change will not be large. Therefore, this simple model suggests that the presence of an induction motor in the island would not significantly affect the performance of either AFD or AFDPF. In fact, it suggests that the motor can cause the islanding prevention method to work better, because as the impedance changes the motor's current draw will change and cause the voltage in the island to change, introducing another method by which the PV system can detect the islanded condition and trip.

This reasoning is best illustrated by an example. Consider a 60-Hz, 120 V, 4-pole, single-phase induction machine with the following parameters [68]:

$$R_1 = 10\Omega$$
$$X_{L1} = X_{L2} = 12.5\Omega$$
$$R_2 = 11.5\Omega$$
$$X_m = 250\Omega$$
$$S = 0.05$$

Under normal conditions, the rotational frequency of the motor is 28.5 Hz from Equation (79), and the motor's equivalent series impedance is 71.67 + j76.16 Ω (104.6∠46.74°--notice that the power factor of the motor is very low, 0.685 lagging). The motor draws a current of 1.15∠-46.74° A. Assume that there is sufficient capacitive compensation in the island that the PV system does not trip immediately on a phase error, and disconnect the utility. Now if the PV system suddenly increased the frequency to 60.5 Hz (the largest upward jump which would not trip the OFR) while keeping the power constant, since the motor's rotational frequency cannot change that rapidly the slip becomes 0.058. With this parameter, the motor's new series impedance is found to be 70.30 + j67.78 Ω (97.65∠43.95°). The change in the magnitude of the

177

motor's series impedance is 6.6%, which is not large enough to cause a voltage trip by itself. If the current being fed into the motor has the same magnitude as before the utility was disconnected (1.15 A), then the new voltage at the motor terminals would have a magnitude of 112.3 V, which is comfortably within the voltage trip limits of the PV system. Thus, according to this simplified treatment, the change in impedance with frequency caused by the presence of the motor will not cause a change in the NDZ of AFD or AFDPF.

Similarly, if the frequency were to undergo a step change in the downward direction to 59.5 Hz, the slip would suddenly change to 4.2%, and the impedance of the motor would increase. In this case also, the change is not large enough to cause a voltage trip.

Two important facts, one general fact and one caveat regarding this simplified treatment, should be noted at this point. The general fact is this: it was pointed out that the above real-world single-phase induction motor has a very low power factor, 0.685 lagging. Not all induction motors have power factors this low, but all do have a lagging power factor. Islanding of a motor of this type, if it were not capacitively compensated by some other part of the local load, could easily be prevented by phase jump detection or by the OFR/UFR.

The other fact, the caveat, is this: the above modeling essentially ignores the interaction between the electrical and mechanical systems. This has been justified by the assumption that $P_{elec} - P_{mech} \approx 0$, so that the mechanical speed of the rotor could be assumed constant. The swing equation is thus effectively removed from the model. Such a simplification may not be justified in practice, with real motors and real loads.

Experimental results

Unfortunately, the results of recently-conducted experiments at Sandia National Laboratories and elsewhere appears to contradict the results of the simplified treatment

of the motor. Many researchers have concluded that in fact the presence of induction motors in islands tends to increase run-on times of converters using islanding prevention methods which depend on a frequency change [31,60,61]. In fact, one recent study suggested that, in the case of AFDPF and schemes like it, the worst-case load was a capacitively-compensated induction motor with a large rotational inertia, such as a bench grinder [63]. In this study, run-on times as long as 180 cycles were reported for high-Q, resonant, parallel RLC loads, but indefinite run-on times (requiring operator intervention to stop the PCU) were obtained when the load consisted of a capacitively-compensated induction motor attached to a pair of large grinding wheels that acted as flywheels.

The commonly-believed explanation for this behavior is that the kinetic energy of the rotating load drives the induction motor as a generator, supplying a voltage at the motor's terminals that counteracts the normally-expected change in frequency. However, an examination of Equations (78) and (79) along with Figure 75 does not appear to support this theory. In order for the motor to generate, the slip must become negative, so that a negative resistance appears in the equivalent circuit. The simplified treatment indicates that even with a step change from the nominal to minimum frequencies allowed without tripping the UFR, the slip never becomes negative. In order to fully understand what is happening in this case, detailed dynamic modeling of the capacitively-compensated motor load is required, and such a treatment is beyond the scope of the present work.

Interestingly, there is another factor which may also need to be considered. Recall that, in general, the dpf of single-phase induction motors is quite low, and therefore in order to obtain a load which draws no reactive power a large capacitor must be connected in shunt across the motor's terminals. The reactive power draw of induction motors can be large, indicating that a large capacitance would be required to

compensate. This work has shown repeatedly that the presence of large capacitors reduces the effectiveness of AFDPF, and therefore it may be the large capacitor and not the motor which leads to the longer run-on times.

The parameters of the loads used in the tests described above are listed in Table 9. The inductance used in the parallel RLC load case (no motor) drew approximately 95 VARs at 117 V_{RMS}, meaning that the value of L was approximately 381 mH. This L would be compensated at 60 Hz by a capacitance of about 18.4 μF. However, the induction motor used in the tests drew 247.7 VARs at 117 V_{RMS}, which would be an equivalent inductance of about 147 mH. The compensating capacitance would be about 48 μF, more than twice the value used in the no-motor case. In both cases, the real power consumption of the load is relatively low, indicating that the value of R is relatively high. This factor also has been shown to decrease the effectiveness of AFDPF. It is possible that, at least in part, the longer run-on times seen with induction motors

Table 9. Comparison between RLC and induction motor load parameters used in comparisons of run-on times.

Parameter	Value in RLC load	Value (or equivalent) in induction motor load
Real power consumption (W)	58	112.8
Inductance (mH)	147	381
Compensating capacitance (μF)	18.4	48

in islands are due to the fact that such loads lie far to the left in the C_{norm} vs. L plane, where AFD and AFDPF are known to be less effective, and the value of R is high, which is known to reduce the effectiveness of both methods. Further investigation of this situation is warranted.

The islanded behavior of a constant-power load

Procedure

Constant-power loads are becoming more prevalent in many applications. This category includes any loads which have switching converters regulating their power. If we assume the efficiency of the switching converter to be constant, then its power input is regulated as well, and the utility effectively sees a constant-power load. Adjustable speed drives and switching power supplies for electronic equipment such as computers fall into this category. Note that most constant-power loads are actually also producers of harmonic current; however, it was shown previously that significant amounts of harmonic currents do not affect AFD, and therefore this nonlinearity of constant-power loads will be neglected.

Constant-power loads are usually designed to draw current at as close to unity dpf as possible. Therefore, a constant power load can be represented by a variable resistance r_P which depends on the utility voltage. If V_a is the RMS value of the PCS terminal voltage v_a and P is the constant power draw, then r_P can be found by

$$P = \frac{V_a^2}{r_P} \Rightarrow r_p = \frac{V_a^2}{P} \tag{81}$$

The impedance of a parallel RLC load with a constant-power component then becomes

$$Z = \cfrac{1}{\cfrac{1}{R_{load}} + \cfrac{P}{V_a^2} + j\left(\omega C - \cfrac{1}{\omega L}\right)} \qquad (82)$$

Let us first examine the effect of a constant-power load on $\left|v_a\right|$, the magnitude of the voltage v_a. Since

$$\left|v_a\right| = \left|i_{PV}\right|\left|Z_{load}\right| \qquad (83)$$

the magnitude of v_a may be expressed as

$$\left|v_a\right| = \cfrac{\left|i_{PV}\right|}{\sqrt{\left[\cfrac{1}{R_{load}} + \cfrac{P'}{\left|v_a\right|^2}\right]^2 + X^2}} \qquad (84)$$

where $P' \equiv 2P$ to compensate for the fact that $\left|v_a\right| = \sqrt{2}V_a$ and $X \equiv \left[\omega C - \cfrac{1}{\omega L}\right]$. Note that $\left|v_a\right|$ appears on both sides of Equation (84). Solving Equation (84) for this quantity yields

$$\left|v_a\right| = \left[\frac{1}{2}\left\{-\cfrac{2\cfrac{P'}{R_{load}} - \left|i_{PV}\right|^2}{\cfrac{1}{R_{load}} + X^2} \pm \sqrt{\left[\cfrac{2\cfrac{P'}{R_{load}} - \left|i_{PV}\right|^2}{\cfrac{1}{R_{load}} + X^2}\right]^2 - 4\cfrac{P'^2}{\cfrac{1}{R_{load}} + X^2}}\right\}\right]^{\frac{1}{2}} \qquad (85)$$

Recalling that X carries the frequency dependence of this function, Eequation (85) may be differentiated with respect to ω to obtain

$$\frac{d|v_a|}{d\omega} = \frac{1}{2}\left[\frac{1}{2}\left\{-b+\sqrt{b^2-4c}\right\}\right]^{\frac{1}{2}} \cdot \left[-\frac{db}{dX} + \left\{\frac{1}{2}\sqrt{b^2 4c}\right\} \cdot \left\{2b\frac{db}{dX} - 4\frac{dc}{dX}\right\}\right]\frac{dX}{d\omega} \quad (86)$$

where

$$b = \frac{2\,P'\!\!\Big/\!R_{load} - |i_{PV}|^2}{1\!\!\Big/\!R_{load}^2 + X^2}$$

$$c = -\frac{P'^2}{1\!\!\Big/\!R_{load}^2 + X^2}$$

From these definitions,

$$\frac{db}{dX} = -\frac{\left[2\,P'\!\!\Big/\!R_{load} - |i_{PV}|^2\right] \cdot [2X]}{\left[1\!\!\Big/\!R_{load}^2 + X^2\right]^2}$$

$$\frac{dc}{dX} = -\frac{2XP'^2}{\left[1\!\!\Big/\!R_{load}^2 + X^2\right]^2} \quad (87)$$

$$\frac{dX}{d\omega} = C + 1\!\!\Big/\!L\omega^2$$

183

Results

Expressions for $|v_a|$ and its rate of change with respect to frequency have now been derived. From these, plots of $|v_a|$ and its rate of change for R_{load} = 14.4 Ω, L = 1 mH, C = 7.03 mF, and several values of P' are shown in Figure 76 and Figure 77. Note also that $|i_{PV}|$ has been scaled so that, for each value of P, the load and PV power are balanced at 60 Hz. Figure 76 shows that the voltage magnitude response becomes steeper as the constant-power demand increases. The results in Figure 77 are consistent; the absolute value of the rate of change of $|v_a|$ increases more rapidly as the constant power load demand rises, although the change is very small. This suggests that the presence of a constant-power load in the island will reduce the size of the NDZ of AFD or AFDPF because the range of loads that does not lead to a voltage trip will be reduced. Also, the amount of this reduction will not be large.

To understand why this occurs, consider the example case used in Figure 76 and Figure 77. L and C are near resonance at 60 Hz (~377 rad/sec), meaning that $|Z|$ is near its maximum value. When the frequency begins to shift under the control action of AFD or AFDPF, the magnitude of Z begins to decrease. Since $|i_{PV}|$ is fixed, if $|Z|$ drops then Equation (83) tells us that $|v_a|$ must also drop. However, this decrease in $|v_a|$ leads to a reduction in r_p, and since $|Z|$ depends on the inverse of r_p this will cause an additional decrease in $|Z|$, beyond what would have occurred without the constant-power load component. Therefore, in a sense, there is a "positive feedback" action of the constant power load on the voltage magnitude; the presence of a constant power load causes any deviation in $|v_a|$ to be reinforced.
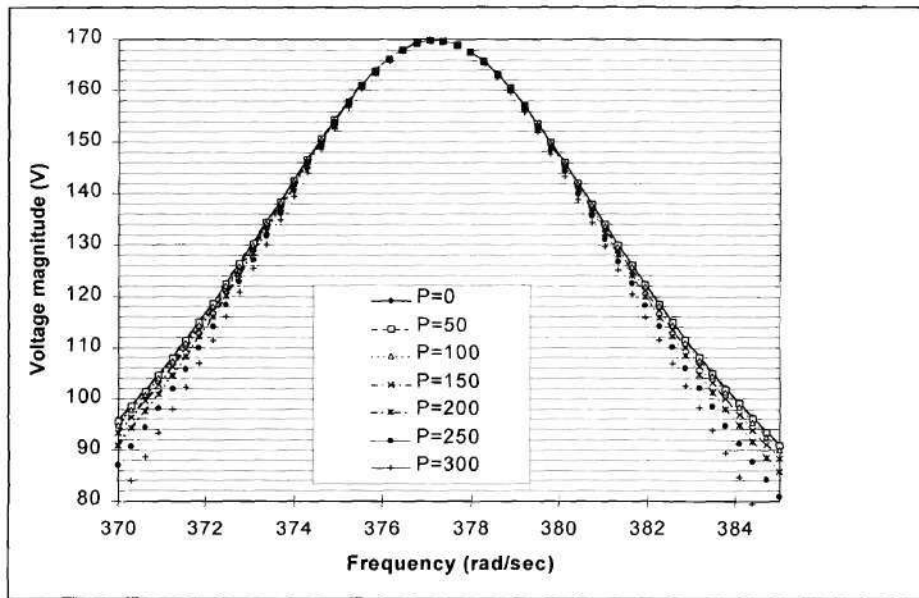
Figure 76. Voltage magnitude as a function of frequency in the presence of a constant-power load. Calculated using Equation (85).
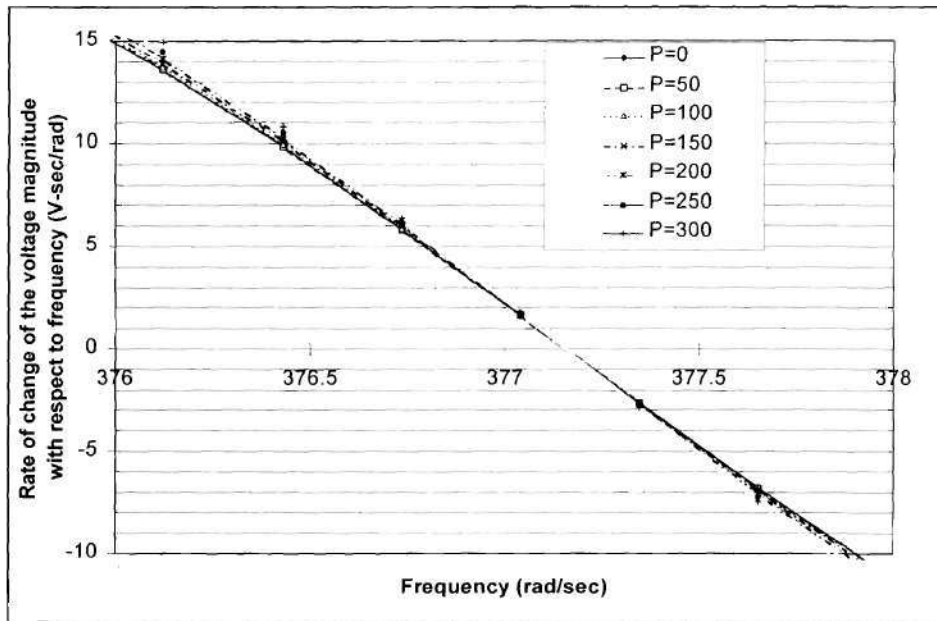
Figure 77. Plot of $\dfrac{d|v_a|}{d\omega}$, calculated from Equation (86).

CHAPTER IV

CONCLUSIONS

Results and contributions of this work

The work presented in this thesis provides several significant contributions to the field of photovoltaics.

1.) A simplified procedure for modeling curved PV arrays was developed and shown to be useful not only for designing and optimizing such systems but also for obtaining theoretical predictions about these systems which can be used diagnostically. This procedure involves the use of a new efficiency derating factor called the curvature derating factor. Methods for obtaining a value for this parameter from existing software were described, and it was shown experimentally, using the GTAC PV system, that the procedure yields valid results.

2.) A detailed study of the use of computer modeling in the design, optimization, and monitoring of a large UIPV system was conducted. The performance penalty incurred by the non-optimal orientation of the GTAC array was quantified, the PCU choice was justified on the basis of power rating and total system efficiency, and the general accuracy of the PV systems modeling programs was demonstrated.

3.) Quantitative evidence was provided to reveal that, in fact, the four standard relays alone are not sufficient islanding protection, and further islanding prevention methods are required to guarantee the safety of personnel and integrity of equipment.

4.) A quantitative comparison of existing islanding prevention methods is presented, including the first-ever mapping of their nondetection zones in C_{norm} vs. L space, and a determination of which of these methods is the most effective in preventing islanding. The conclusion was that the best available islanding prevention method at the beginning of this work was the slide-mode frequency shift (SMS) method. It was further demonstrated that the mapping in C_{norm} vs. L space provides vital information about islanding prevention methods which is overlooked in mappings in the traditionally-used "power mismatch space".

5.) The first thorough and quantitative analysis and characterization of the AFD method of islanding prevention was presented. This analysis showed that, contrary to conventional wisdom, AFD has serious weaknesses and does not compare favorably with methods such as SMS.

6.) A novel improvement to AFD was developed through the addition of positive feedback to create AFDPF. AFDPF is described and analyzed, and it is shown to be among the best available, if not *the* best available islanding protection.

7.) An analysis of the effect of AFDPF on system transients and power quality was performed. This analysis was used to describe some practical considerations when using AFDPF, and it was shown that by proper selection of parameters it is not necessary that AFDPF create significant problems in the utility system. It was further shown that AFDPF remains effective in the multi-inverter case.

8.) An investigation was conducted of the impact of nonlinear (harmonic-producing) loads, direct-connected motors, and constant-power loads on the NDZs of AFD and AFDPF. This investigation indicated that nonlinear and constant-power loads have little or no effect on the NDZs, but the effect of induction motors is still unclear.

Recommendations for further work

Several possible avenues for future work have been revealed during the course of this research. Some of the most important are listed below.

1.) There is a need for a software package which integrates I-V curve modeling with POA irradiance calculations on multiple surfaces, or which at least automates the procedure described herein for modeling curved PV arrays. It is believed that the number of PV systems with curved arrays will rise dramatically within the next two decades as innovative PV building products are developed, and PV system designers will require tools which can deal with these systems with maximum accuracy and speed. A significant window of opportunity exists for developing user-friendly, Windows©-based software which can accomplish these tasks.

2.) The use of power line carrier (PLC) communications for islanding prevention is very much an open issue. Much study is possible on the types of signals best suited for this application; the optimum locations of PLC signal transmitters within the utility network; and multiple uses for PLC signals (for example, designing a receiver that uses a PLC signal normally used for automatic meter reading to detect utility disconnection reliably).

3.) In this work, the use of positive feedback to reinforce a deviation in frequency has been explored and shown to be highly effective in preventing islanding. However, it is also possible to use positive feedback to reinforce deviations in other parameters, such as the node-**a** voltage. Schemes of this type are being investigated by several researchers at this time, and in fact the SFS method mentioned under Subtask 2.4 has a companion islanding protection method called Sandia Voltage Shift (SVS) in which the PV system's output current is controlled in such a way as to increase any deviation in v_a. SVS has been shown experimentally to be highly effective in

189

islanding prevention, possibly even more effective than SFS. However, it poses several technical challenges in terms of converter/MPPT design and also in terms of the effects of such a scheme on steady-state power quality and transient response when penetration levels are high. More research is needed to determine whether these challenges may be overcome while still preserving the effectiveness of this method.

4.) The behavior of induction motors in islands warrants further examination. This work uncovered the fact that it is not known why induction motors tend to result in longer run-on times than RLC loads without induction motors. Perhaps if this question could be answered, more effective islanding prevention or more reliable PCU tests would result.

APPENDIX I: COMPLETE DESCRIPTION OF THE GEORGIA TECH

AQUATIC CENTER PHOTOVOLTAIC SYSTEM AND DATA ACQUISITION

SYSTEMS

Introduction

The Georgia Tech Aquatic Center (GTAC), located near the southwest corner of the Georgia Tech campus, was the site of the aquatic events of the 1996 Summer Olympic and Paralympic Games in Atlanta. Mounted on the roof of this facility, is the GTAC photovoltaic (PV) array. It is comprised of 2,856 modules and is rated at 342 kW. At the time of its installation, it was the world's largest roof-mounted PV array.

This Appendix describes the electrical and physical layout of the PV system, and the associated data acquisition system (DAS) which monitors the performance of the system and collects measurements of several important meteorological parameters. These systems were, in effect, the "experimental apparatus" used for the work performed under Task 1.

Electrical design of the PV system

The PV modules

The electrical design of the PV system begins with the PV modules themselves. The modules used in this installation are Solarex MSX-120 modules. Each module

contains 72 10 cm² multicrystalline silicon solar cells connected in series. The performance specifications of this module are given in Table A1- 1. These modules have a low-iron tempered glass front encapsulation, which also provides structural rigidity (i.e. the "structural front" design) and a Tedlar vapor barrier on the back, surrounded by a bronze-anodized extruded aluminum frame.

Array layout

The modules are connected in a DC array configuration. Twelve modules are connected in series to form a "series string" to provide the desired voltage for the system, and then 238 of these series strings are connected in parallel to achieve the desired power. This configuration is shown in Figure A1-1, and the resulting array parameters are given in Table A1- 2. Interconnection of the modules in this array was simplified by the plug-in pin-and-socket type connectors provided by Solarex. The pin-type ("male") connector from each module is the negative terminal; the socket ("female") is the positive.

The National Electric Code (NEC) states that photovoltaic systems cannot produce DC voltages in excess of 600V. Therefore, it is important to choose the number of modules in series such that the maximum voltage produced by the array will not exceed this limit. This maximum array voltage is its open circuit voltage, which increases as temperature decreases. Underwriters' Laboratories (UL) recommend using the lowest known ambient temperature at the site with the known module voltage derating coefficient in calculating this maximum voltage.

DC-side current collection

The DC-side current collection scheme is shown in Figure A1-2. Note that all the components in Figure A1-2 are part of the "+"-side of the array shown in Figure A1-1. The "-" leg, or return leg, is actually connected to ground.

Table A1- 1. Solarex MSX-120 module parameters.

Parameter	Value
Modules used	Solarex MSX-120 (24V configuration)
Module area	$1.1118 \text{ m}^2 = 11.97 \text{ ft}^2$
V_{OC}	42.6 V
I_{SC}	3.8 A
V_{mp}	34.2 V
I_{mp}	3.5 A
P_{mp}	120 W
Fill factor	0.7394
Module efficiency	10.8%
K_{voc}	-0.146 V/°C
K_η	-0.38 %/°C
NOCT	45°C
Test conditions	1 kW/m² irradiance with AM 1.5 spectrum, $T_{module} = 25°C$
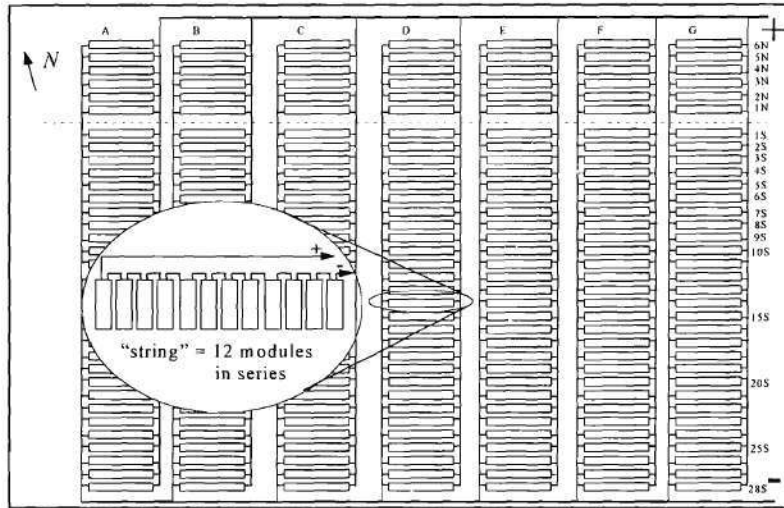
Figure A1-1. Schematic of Aquatic Center roof PV array configuration. The dotted line through the array is the crest of the roof curvature and the location of the access catwalk. Series strings shown above that line face north; all others face south.

Table A1- 2. Array parameters.

Parameter	Value
Array power rating	341280 kW$_p$
Array configuration	12(s) x 238 (p) = 2856 modules 504 modules on north-facing roof slope 2352 modules on south-facing roof slope
Nominal array voltage	410.4 V
Nominal array current	833 A
Array area	3162.1 m² = 34,037 ft²
Measured average array tilt: south-facing side	6.4° up from horizontal
Measured average array tilt: north-facing side	5.9° up from horizontal
Measured array azimuth	12° west of south
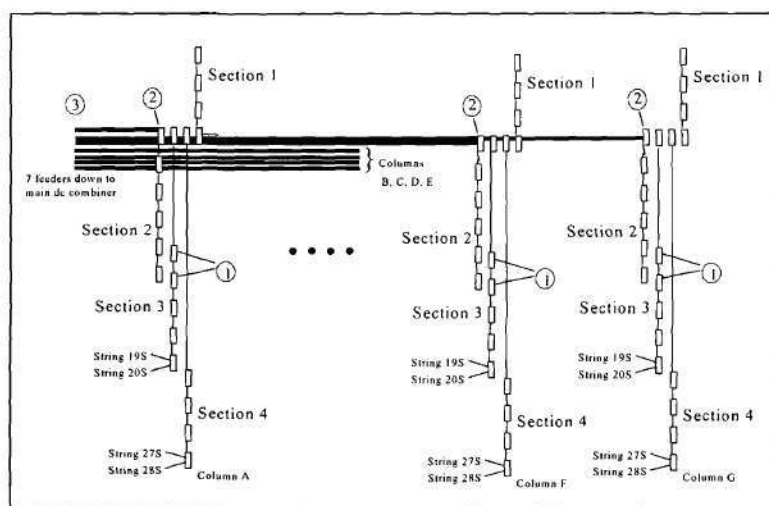
Figure A1-2. **DC-side current collection scheme showing combiner boxes (①),** **rooftop disconnect switches (②), collection circuits and feeders (③). Note also the** **further subdivision of the array into "sections". In each column, each of the four** **rooftop disconnect switches ② controls one "section".**

Series string combiners

The boxes labeled ① are string combiner boxes; each of these combines the output of two series strings. The combiner boxes used in this installation are Ascension Technology source circuit protectors. Fuse protection is provided for each series string connected to the box. The source circuit protectors contain the blocking diodes necessary in the DC array design configuration; each box contains one blocking diode per series string. These prevent shadowed or damaged series strings from operating in a region of the I-V curve in which they absorb power. A surge suppressor is provided in

the combiner box to prevent transients from getting to or from the series strings. The combiner boxes are series-connected up to the current limit of the device, for a maximum of five boxes in series. Thus, in each column, there are four "collection circuits" as shown in Figure A1-2. All conductors used on the roof are run through conduit, and the cables themselves are Type RHH/THHN, with insulation rated at 90° F. Type RHH/THHN cables are rated for use in humid or moist environments, and most can tolerate direct sun exposure. The boxes also include a ground lug to which is connected a bare copper wire for grounding the frames of the PV modules. Without this ground, it would be possible for the metal module frames to float above ground potential if a short should develop within the module which connected the cells to the frame. This failure mechanism is frequently seen; therefore, in this array, every single module frame is grounded to a ground lug in a combiner box.

Rooftop disconnect switches

The boxes labeled ② are the rooftop disconnect switches mounted on the catwalk. These contain three-pole DC disconnect switches and give the ability to isolate any of the four collection circuits in each column. These switches are wired such that, when the switch is thrown, the fuse is isolated, but the grounded negative leg of the circuit is not broken, thus maintaining ground continuity. A bar of copper with size chosen to match the conductor ampacity is inserted into the fuse bracket of the first pole. A jumper wire, again sized to match the conductors, is inserted between the first and third poles, and a fuse is inserted into the fuse bracket of the third pole, thus completing the circuit. This fuse is intended to protect against faults on the array itself. The second (middle) pole of the switch is not used. The box itself is connected to the system ground.

Each column in the array is separated into four sections, each with its own disconnect switch as shown in Figure A1-2. The arrangement of switches and

connections is as shown in Figure A1-2; a person standing in front of the switch boxes would see, from left to right, disconnect switches for sections 1, 4, 3, 2 in that order. The two boxes on the left are smaller because their ampacities need not be as high since fewer series strings are connected to them.

Power transport to the inverter room

Just downstream from the disconnect switches, the four collection circuits are combined to form a main DC feeder. At point ③, there are seven of these feeders, one for each column. The feeders run through conduit down from the roof, where they go underground and run the length of the building back to the inverter room.

The main DC collection switchboards

In the inverter room, the layout of which is diagrammed in Figure A1-3, there are two main DC collection switchboards. These switchboards, made by Siemens Energy and Automation Division, are near the corner of the inverter room in large grey cabinets. The seven lines from the roof first enter a switchboard (the "first DC switchboard") with a separate circuit breaker for each feeder (seven circuit breakers). These breakers protect against faults between point ③ in Figure A1-2 and the first DC switchboard. The seven feeders, after passing through the seven breakers, are joined on a common bus into one main feeder. This main DC bus is in turn connected through another circuit breaker, the main DC circuit breaker, to the power conditioning system (PCS). This breaker protects against faults between the DC collection switchboard and the PCS. This main breaker is wired in a slightly unusual way to ensure proper operation. It is a standard three-phase AC breaker. To ensure that it will trip under the proper conditions, all three poles must be energized; therefore, the positive leg of the DC bus passes through one pole and is doubled back through a second pole. The negative leg passes through the third pole. Note that the main breaker does break the

197

negative leg of the DC circuit. The ground leads coming down from the roof pass through the DC switchboard cabinets directly to the ground bus of the power conditioning system (PCS) without passing through any switches. This is necessary to allow the PCS to properly detect ground faults on the system. It should be noted that two of the ground leads from the roof are connected to the ground rail of the main DC breaker cabinet. Another, much smaller cable runs from this ground rail through the conduit to the system ground in the DC isolation switch box on the PCS cabinet, thus grounding the DC switchbox chassis. The reason for the connection of two of the roof grounds to the ground rail in the main DC breaker box is unclear; however, it introduces a situation of two heavy-gauge grounds being connected to earth ground via a lighter-gauge cable.

The power conditioning system (PCS)

Functional/electrical description of the PCS

The PCS in this installation is a 315 kW unit supplied by Trace Technologies, Inc. (formerly Kenetech Windpower). A block diagram of the PCS is shown in Figure A1-4. The PCS is equipped with a "no-load-break" switch which isolates it from the array; this switch is shown in Figure A1-4 between the array and the boost stage. The term "no-load-break" means that the switch does not have the capability to interrupt the full array current, and therefore **it cannot be opened while the DC-side line is energized.** The array must be disconnected by opening the main DC breaker, all seven main feeder breakers, or all 28 of the
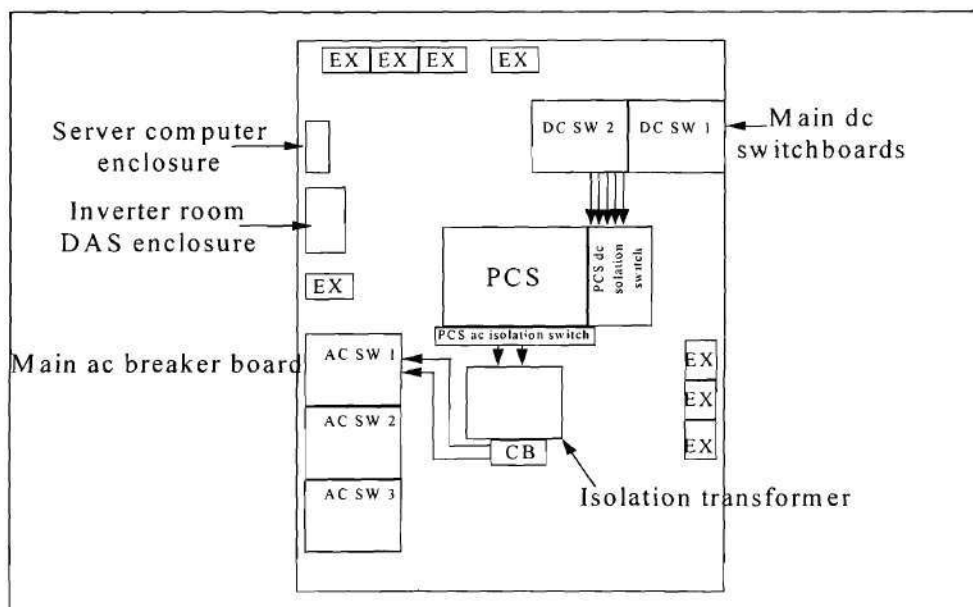
Figure A1-3. Layout of the inverter room. EX stands for "existing"; these are other devices (lighting panels, breaker boxes etc.) which are not part of the PV system. The first DC breaker box containing the seven feeder breakers is labeled "DC SW 1"; the main DC breaker cabinet is "DC SW 2". The arrows between components indicate the power cable conduit runs.
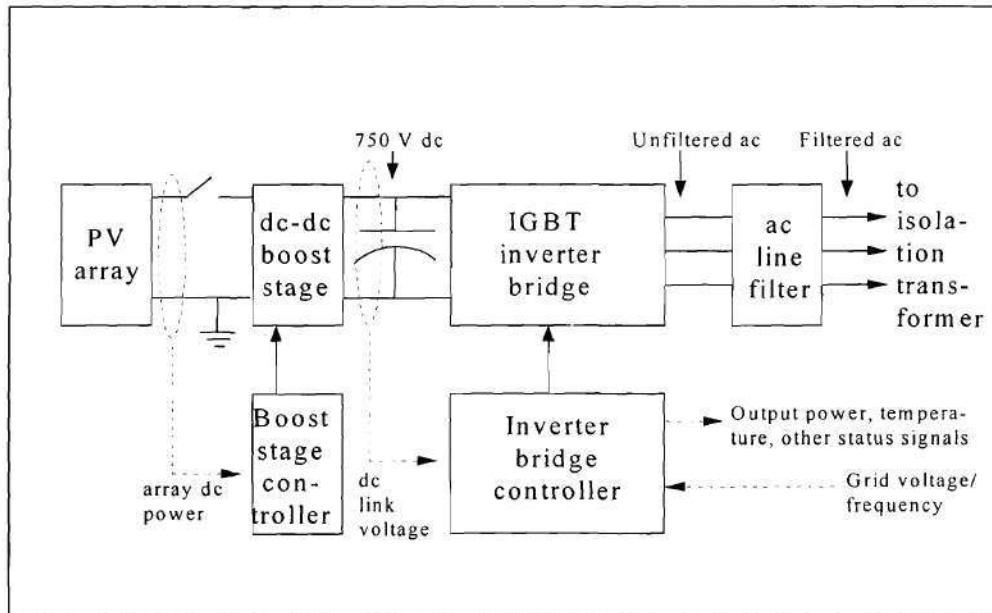
Figure A1-4. Block diagram of the Aquatic Center PV system power conditioning system (PCS). The boost stage steps the (variable) array voltage up to 750 V$_{DC}$; the inverter bridge is an IGBT bridge circuit that performs the inversion. The capacitor between the DC-DC boost stage and the inverter bridge is the "DC link".

rooftop disconnect switches before the no-load-break switch can be opened. A similar switch (not shown in Figure A1-4) is supplied on the AC side, to isolate the PCS from AC power. Both of these switches should be locked open before the inverter cabinet is opened. Normally, the switches should be locked in the closed ("1") position.

The power switching stages of the PCS uses 1200V, 1200A insulated gate bipolar transistors (IGBTs) as the semiconductor switches, switching at 6 kHz. The converter topology contains twelve IGBTs divided into two sets. One set forms a DC-DC "boost"-type converter, with the switches acting in parallel; the other is a six-switch, three-

phase inverter bridge. A pulse-width modulation (PWM) switching scheme is used in both the boost stage and the inverter bridge. In the boost stage, the control variable used to determine the PWM duty ratio is the array power output; the switching function is controlled so as to keep the array operating at its maximum power point. In the inverter bridge, by sinusoidal modulation of the duty ratio, an output waveform with a large fundamental-frequency component (at the frequency of the sinusoidal modulation) but with small low-order harmonic amplitudes is obtained, allowing for easy filtering to obtain the desired sinusoidal output current. The inverter bridge switching is also controlled in order to maintain the DC link voltage at 750 V. The bridge is self-commutated, allowing for a near-unity power factor. However, the line voltage waveform is used by the inverter controller as a template for the output current waveform (i.e. to modulate the IGBT duty ratios). The line filter just downstream from the inverter bridge removes unwanted harmonics from the bridge output, particularly harmonics at and above the switching frequency. Because of its size, the line filter is contained in a separate enclosure from the rest of the PCS. The manufacturer's specifications state that this configuration produces an output current waveform with less than 5% THD at full load.

It is important to note that the PWM output waveform of the inverter bridge is asymmetric about zero; that is, its maximum value is the voltage across the DC bus, and its minimum is zero, since the DC bus is not grounded at its center and is not neutral-point controlled. Therefore, this output waveform has a DC component approximately equal to half the DC bus voltage. To prevent injection of this component into the grid, a three-phase isolation transformer is provided on the AC side between the bridge and the grid. This transformer is Δ-Y connected, with the Y on the delta side. The center of the Y is grounded. This isolation transformer is the only mechanism in this inverter for prevention of DC injection into the grid.

Table A1-10, taken from the manufacturer's literature, collects some of the performance specifications of the PCS. The efficiency quoted for the PCS is its efficiency under "full load" conditions; that is, when the PV array is producing power equal to the PCS's continuous rating (315 kW). The efficiency is not constant under all loading conditions, however, and Figure A1-5 shows a curve of the PCS efficiency vs. PV array power production.

Table A1-10. Specifications of the Aquatic Center array PCS

Parameter	Value
Continuous rated DC (PV) power input	315 kW
Maximum rated DC (PV) power input	324 kW
Nominal DC-terminal voltage	380V
Maximum DC-terminal voltage	600V
Efficiency	95% at full load
Output power factor	1.00
THD of AC output current	$\leq$ 5%, in compliance with IEEE-519
Semiconductor switching device	IGBTs rated at 1200V, 600A
Switching frequency	6 kHz
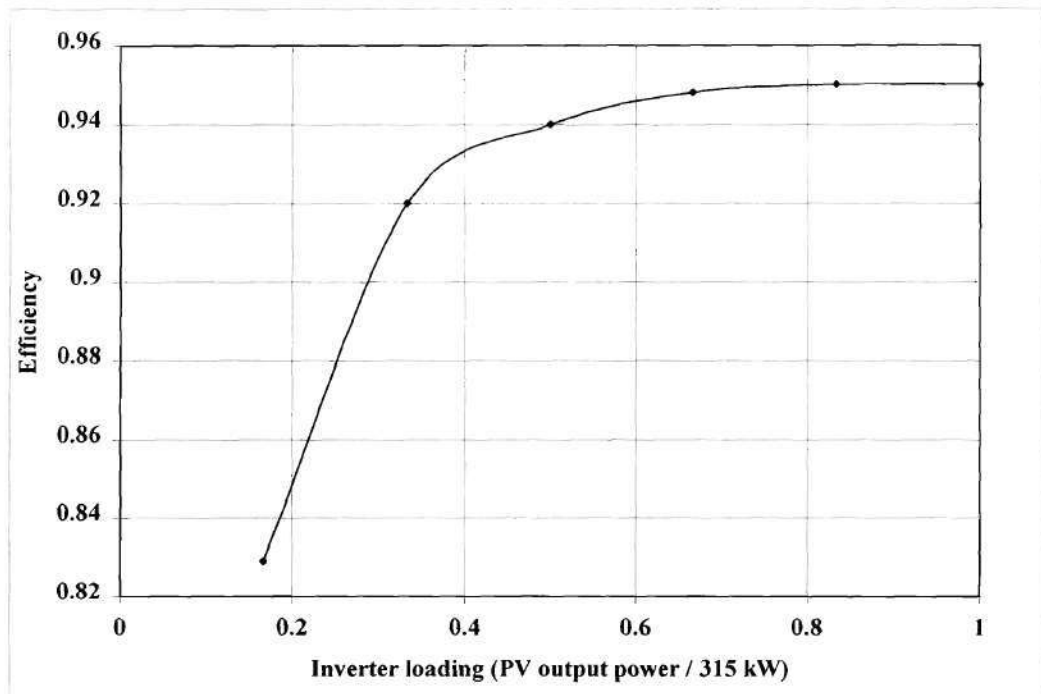
Figure A1-5. Efficiency of Trace 315 kW PCS as a function of PV power input. x-axis values are in terms of "fractional loading", which is the input power to the PCS (in this case the PV array's power production) divided by the PCS's continuous rating.

<u>Control functions</u>

The PCS provides many control and protection functions for the system.

a.) Maximum power point tracking: the PCS uses a "dithering" scheme in which the PV array's output current is changed in 5A increments and the resulting output power is calculated. If the power has increased since the last increment, the next 5A increment will have the same sign (i.e. be in the "same direction"); if the

power has decreased, the sign will be reversed in subsequent increments. The current is incremented as follows: to increase the current flowing through the inverter, the controller will increase the switch "on" time in order to raise the amount of current flowing in the (very large) inductor in the boost stage. As the boost stage increments the current from the array, the capacitor voltage will tend to increase. The inverter switching function is controlled to maintain the 750 V_{DC} across the link capacitor. In this way, the PV array current is controlled such that it operates at or near its maximum power point at all times.

b.) Self-protection: DC overvoltage and overcurrent and also overtemperature conditions are monitored by the PCS's control system. Device protection is accomplished in part by an "over-power" protection function: if the input power from the array attempts to go over 324 kW, the maximum power point tracking circuit acts as a limiter and prevents the array current from increasing, thus preventing the PV array output power from exceeding 324 kW.

c.) Islanding protection: AC-side over/undervoltage and over/underfrequency monitors are included in the PCS's control system to enable detection of islanding from the utility grid. In addition, if the grid voltage decays to zero, the template for the inverter bridge output current also goes to zero, meaning that the inverter output current in turn will vanish.

d.) DC-side ground-fault detection: the PCS is capable of shutting down the system in the event of a short to ground on the DC side. A current sensor is provided on the ground bus from the PCS to the actual earth ground. When large currents in the ground bus are detected, some type of ground fault exists and a command is generated to stop power production and disconnect the PV array. It is because this function is provided in the PCS that it is important for the array ground lines to pass directly from the roof to the PCS ground bus, with no other

204

ground path. If another ground path were provided, two conditions would exist: first, the PCS may not detect the ground fault because current flow would be divided between the multiple ground paths; and second, if the fault were detected, the PCS would be unable to interrupt it because the fault current could continue to flow through the other ground paths. The PV array would indefinitely feed the ground fault with essentially its short-circuit current, which would very likely lead to a fire.

e.) Lightning protection: MOV surge arrestors are provided on both the AC and DC terminals for the purpose of preventing high-voltage lightning-induced transients from reaching the semiconductor switches.

f.) Automatic normal start-up and shut-down: the PCS automatically begins conditioning power each morning when the array voltage exceeds 400V and remains above that level for five minutes. The extra time is inserted to prevent the system from "cycling", or starting and stopping repeatedly. Similarly, the system automatically "sleeps" at night, shutting down when the array power drops below 3kW and remains below that level for fifteen minutes. This long time interval is required to prevent the system from cycling during the passage of unusually dark clouds.

The isolation transformer

The AC output of the PCS is then fed into the main isolation transformer, which is 480 VΔ-480 VY connected. This transformer provides electrical isolation from the grid and also prevents passage of the DC component of the output of the inverter bridge into the grid. A circuit breaker is provided on one side of the cabinet. This breaker frequently trips during start-up due to inrush currents; more than one attempt is usually necessary to reclose it.

The main system circuit breaker

There are two main system circuit breakers. The first is a standard, three-phase AC breaker located on the system's AC switchboard. The second is a specific protection system made up of three different components. The first, called an 86 device, is a locking circuit breaker. This is the actual switch that disconnects the PV system from the building service entrance. This 86 device can be tripped by either of the other two components: a phase imbalance detector and a device called a "32 device".

The phase imbalance sensor monitors the current flows in the three phases coming from the PV system. In the event that an unbalance condition occurs, indicating any of a number of abnormal operating conditions, the phase imbalance sensor "trips" (opens) the 86 breaker, which locks open and disconnects the PV system from the grid.

The 32 device monitors the direction of power flow in the main isolation transformer. If the power flow attempts to reverse, flowing from the grid to the PV system, the 32 device trips the 86 breaker and disconnects the system. The threshold value of reverse power flow, above which the 32 device generates a trip, must be chosen carefully to avoid false trips due to the array going off-line at night. To avoid this problem, the designers of this installation realized that the core loss of the main isolation transformer will appear to the grid as a load when the PV system is off-line, and this is a normal condition in the case of nighttime PV system shutdown. Therefore, this core loss is used as the threshold value for reverse power flow. If the reverse power flow is at or below this threshold, no trip is generated. However, if reverse power flow exceeds this core loss, an abnormal condition exists, and the 86 device is tripped.

Lightning protection

The array is protected against lightning strikes by two air terminals, one located on each main steel support structure at either end of the roof. These air terminals were designed by Lightning Arrestor of America, Inc. Each is designed to provide a radius of protection of approximately 250 feet. The air terminals are bonded directly to the steel support structure and are thus grounded via this structure. There is no other ground connection for these terminals. The installer reports testing the resistance from the air terminal to ground at "not more than 5Ω", which is deemed sufficient for this application. One potential problem with this arrangement is that the aluminum roof skin is also electrically connected to the steel support structure and is thus in the ground path for the air terminals. In this way, the roof appears as a shunt-connected resistance between the two air terminal-to-ground paths, and in the event of a lightning stroke on either terminal, part of the current could travel through the roof structure to the other ground path. The resistance offered by the roof is unknown, however; it could well be much higher than the 5Ω specified for the air-terminal-to-ground path, and in that case the current through the roof could be negligible.

Physical design of the PV array

Module mounting scheme

The roof structure provides a convenient way to mount the PV array. In Figure A1-6, this structure, called a standing-seam design, is illustrated. The array is mounted to the roof using clamps that clamp directly to the aluminum standing seams, as shown in Figure A1-6. This mounting configuration results in an array-roof standoff height of 1.5 inches (the height of the clamps themselves) + 2 inches (the height of the

standing seams) = 3.5 inches between the roof deck and the bottom edge of the PV module frames. The array is laid out on the roof essentially as illustrated in Figure A1-1. There is a two-foot-wide aisle between columns of series strings. This allows a space along which maintenance workers may reach all parts of the array. Also, the Ascension Technology string combiner boxes and the conduit containing the conductors for each collection circuit are placed in these aisles.
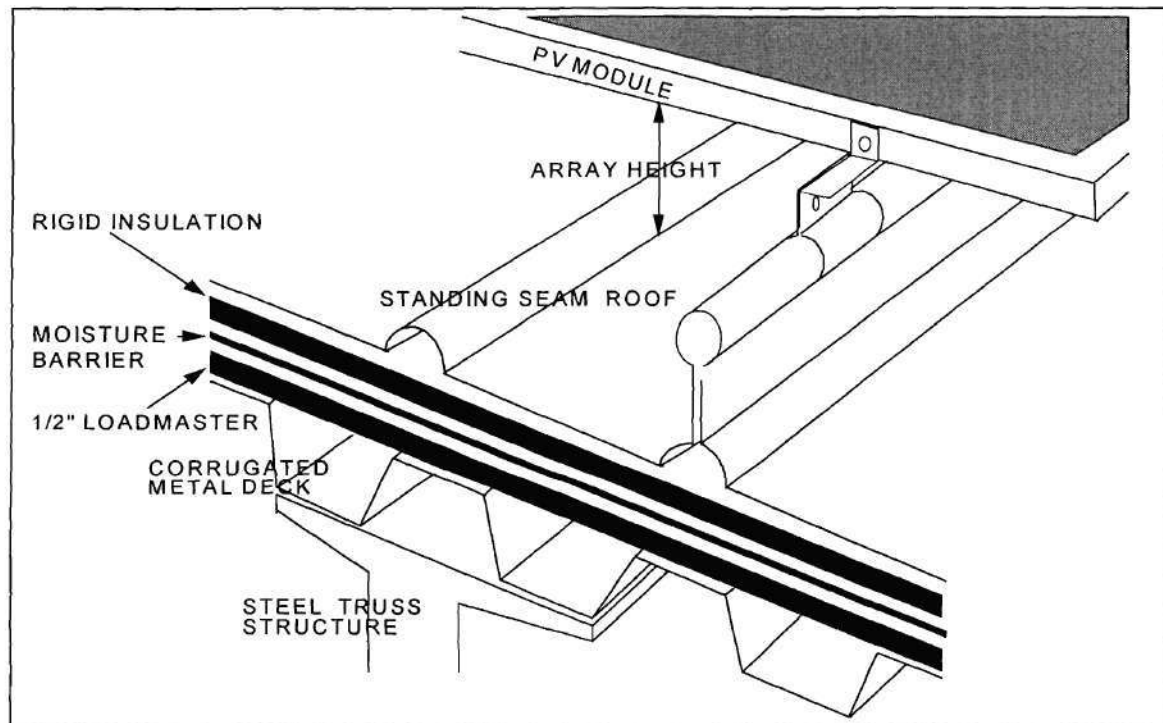
Figure A1-6. Method used in mounting PV modules to the Aquatic Center roof.

Module orientation

Since the array is flush-mounted to the roof, its tilt is continuously changing with the roof curvature, and thus the orientations of all of the rows of modules will be slightly different. The tilt angles of all rows of series strings were measured using a protractor with a self-leveling indicator needle. The results of this measurement are given in Table A1-11. (The row number-letter designations are taken from Figure A1-1.) Also, the azimuth angle of the entire array was measured using a magnetic compass. According to the magnetic declination chart supplied by the compass manufacturer, the magnetic declination correction required in Atlanta is, conveniently, 0°. For the south-facing modules, the measured azimuth angle was 12° west of south; for the north facing angles, it is 192° west of south, or 12° east of north.

Table A1-11. Measured module tilts on the Aquatic Center roof.

Row designation (from Figure 3-1)	Measured tilt angle, ° up from horizontal
6N	9.75
5N	8.0
4N	6.5
3N	5.0
2N	3.75
1N (north side of catwalk)	2.25
1S (south side of catwalk)	0.0
2S	0.0
3S	1.0
4S	1.0
5S	2.0
6S	2.5
7S	2.5
8S	3.0
9S	3.0
10S	4.5
11S	5.0
12S	5.5
13S	6.0
14S	6.0
15S	6.5
16S	7.25
17S	7.0
18S	9.0
19S	9.25
20S	9.25
21S	10.0
22S	10.0
23S	11.0
24S	11.0
25S	11.0
26S	11.5
27S	12.5
28S	13.0

The data acquisition system (DAS)

The Aquatic Center PV array is heavily instrumented for measurement of many performance and meteorological parameters, thus allowing for accurate determination of the array's performance and enabling thorough research of the system. This section describes the DAS, its function, and its operation. The DAS is divided into three functional parts: the rooftop DAS, the inverter room DAS, and the data communications system, as illustrated in Figure A1-7.
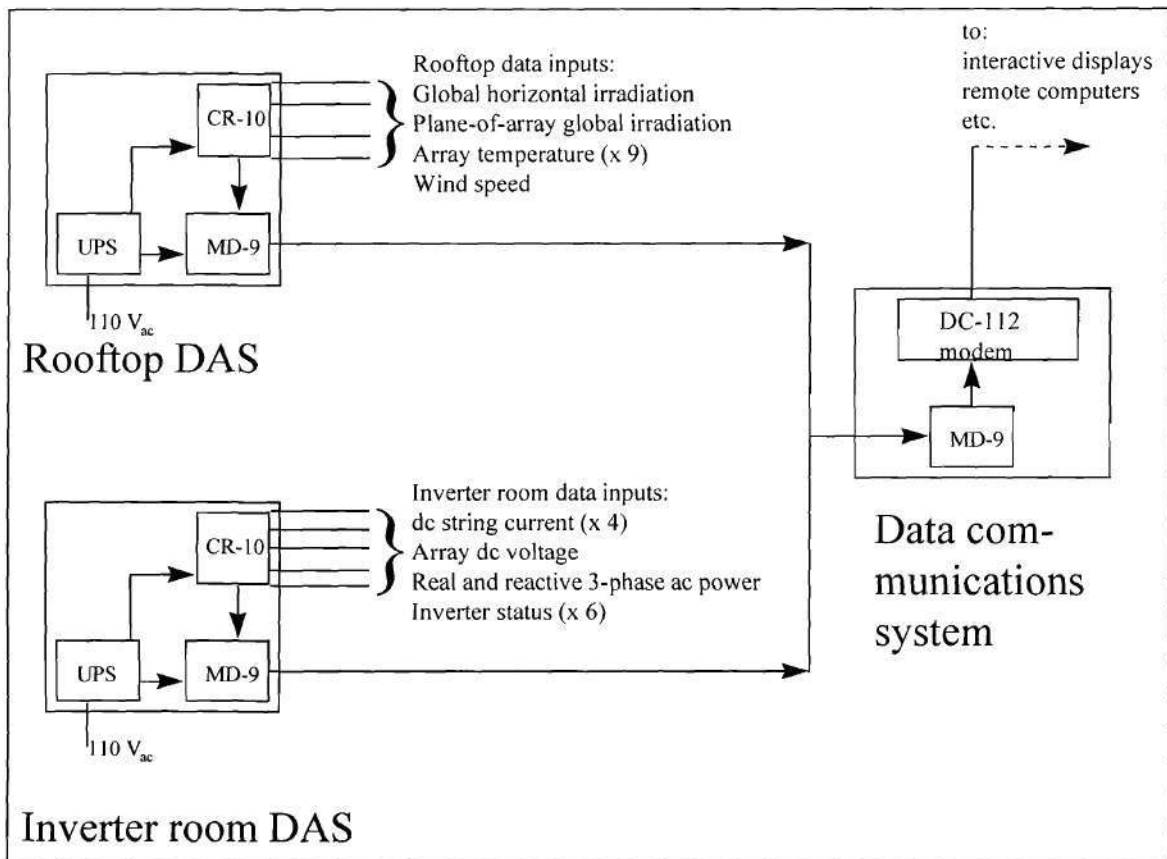
Figure A1-7. The Aquatic Center array data acquisition system (DAS), showing its three functional units: the rooftop DAS, which collects the meteorological parameters, the inverter room DAS, which collects system performance data, and the data communications system (which includes all three MD-9's), which allows remote retrieval.

Primary components of the DAS

Campbell Scientific CR-10 datalogger

The datalogger is the heart of the DAS. It performs several vital functions:

212

a.) It receives the raw data from the sensors or other outboard devices. This data can be in any of several forms, including analog voltage signals from thermocouples and pyranometers, digital signals such as the status indication from the inverter, and "pulse" type signals from anemometers.

b.) It performs initial data manipulation, such as conversion of the electrical signals into measurement data with the proper units (scaling, etc.) and averaging of a set number of data points. This averaging is very commonly done in order to reduce the required amount of data storage space. The datalogger can also identify maxima and minima, or compute standard deviations.

c.) It stores this manipulated data. The CR-10's long-term or "final" storage can hold over 29,000 processed values.

The rate at which the raw data from the various sensors is sampled, as well as the processing done before final storage, is set in the datalogger's program. This program is written on a PC using the PC-208 software provided by Campbell Scientific. PC-208 contains a subprogram called EDLOG which provides a programming language for setting up the instructions to be executed by the datalogger. In the Aquatic Center DAS, all data will be sampled every 10 seconds, and averages stored every 10 minutes for all the variables listed below. The PC-208 software also allows real-time monitoring and verification of the operation of the DAS. In addition, the program can generate tabular or graphical reports and check for missing or out-of-range data points.

Campbell Scientific MD-9 multidrop interface

The MD-9 interface "translates" serial-port data signals to or from a format that can be sent via coaxial cable. In this way, the MD-9's allow a coaxial "data bus" to be built which can connect all the data loggers to a single computer for long-term storage and remote access to this data. In the GTAC installation, use of coaxial cable facilitates the long cable runs necessary to connect the rooftop and inverter room DAS units.

Ribbon (serial) cable is much more susceptible to electrical noise and is much less physically robust, and would also be difficult to pull through conduit.

Rooftop DAS

The rooftop DAS is, as its name implies, mounted on the roof with the PV array itself. This unit of the DAS monitors four meteorological parameters as given in Table A1-12. All data from all sensors is collected by a CR-10 datalogger mounted in a Hoffman electrical enclosure situated roughly in the center of the catwalk on the roof. The two pyranometers are also located atop this enclosure. The CR-10 is connected to the communication system of the DAS by an MD-9 interface, which is also located in the Hoffman box on the roof. The CR-10 is powered by an uninterruptible power supply (UPS), which is connected to a standard 110 V_{ac} supply connected at the AC breaker board in the inverter room. The MD-9 is powered by the CR-10.

Table A1-12. Meteorological parameters measured by rooftop DAS.

Parameter	Sensor
Global horizontal irradiation	horizontal pyranometer
Plane-of-array global irradiation	pyranometer at average array tilt
Ambient (air) temperature	shielded thermistor
Array temperature	six (6) module-mounted thermocouples
Wind speed	anemometer mounted 2 feet above roof surface

Inverter room DAS

The configuration of this system is essentially the same as the one on the rooftop, except that the Hoffman box in which it is contained is wall-mounted on the north wall of the inverter room. It monitors the system performance parameters shown in Table A1-13.

Table A1-13. System performance parameters measured by inverter room DAS.

Parameter	Sensor
Inverter temperature	Thermocouple mounted on IGBT heat sink
Real AC power (3-phase, 480 V_{ac})	Available directly from inverter; also monitored independently by DAS sensors
Reactive AC power (3-phase, 480 V_{ac})	
DC string current (x 4)	Four Hall-effect current transformers
Total DC current	Available directly from inverter; also monitored independently by DAS sensors
Array DC voltage (inverter DC input voltage)	Available directly from the inverter; also monitored independently by DAS sensors
Inverter status (x 6)	Available directly from the inverter

Data communication system

The data communication system provides access to the DAS data from remote computers. Each DAS enclosure includes one MD-9 multidrop interface linking its datalogger to the coaxial cable "data bus". On the other end of this "bus" is another MD-9 which connects the coaxial network to a DC-112 Campbell Scientific modem which can be accessed by telephone from a remote computer running the PC-208 software from Campbell.

Operation of the PV system and the DAS

General operation of the PCS

Under most normal circumstances, it will not be necessary to intervene into the operation of the PCS. However, it is often necessary to observe the system parameters being measured by the PCS. These are continuously displayed on the front panel LCD. The parameter to be displayed may be selected using the up/down arrow keys.

It should not become necessary to change the PCS operation settings. However, this can be done from the front panel keypad by pressing the Menu key and entering the password 659. The menu of settable parameters is shown in the operator's manual. **DO NOT change these settings without first consulting Trace Technologies (formerly Kenetech Windpower).** Alteration of these settings without a thorough understanding of what they are and why they were set as they were could lead to extremely serious consequences such as compromising of the PCS's anti-islanding protection, loss of maximum power point tracking, and serious safety hazards.

Collection of data from the DAS

The server computer allows for easy collection of both real-time data and daily data files via modem. The telephone number of the modem is **(404) 894-7507**. The following procedure may be used to download data from the server using the Campbell Scientific software called GraphTerm.

a.)   First, you must set up a parameter file called a "station file" from which GraphTerm will obtain communications parameters. If you have not set up a station file, follow the following procedure: type "gt" at the DOS prompt, then enter the name you wish to give to the station file. When the parameter editing screen appears, enter the following:

Table A1-14. Communications parameters for the GTAC PV system DAS.

Station name	(enter here whatever you have called the station file, without extension)
Datalogger type	CR10
Security Code	0
Asynchronous Communications Adaptor	(whichever COM port on your computer your modem is connected to)
Communications Baud Rate	1200
Data File Format	Comma Delineated ASCII
Final Storage Collection Area	Area 1
Interface Device #1	Hayes Modem; phone # 894-7507
Interface Device #2	MD-9; address = 1 for the roof, 2 for the inverter room
Interface Device #3	End

Use Ctrl-P to exit the parameter editor and save your station file. (If you do not wish to save the station file, hit Esc.)

b.)   Then, run GraphTerm (by typing "gt" at the DOS prompt), and when it asks you for the station file name, give it the name you assigned to your station file. If you have set up the program correctly, it will dial your modem and contact either the roof or inverter room DAS.

c.)   When contact is established, a menu will pop up on the screen. You then enter the letter of your choice. If you wish to download the data from the datalogger,

you select "U" for collect U)ncollected data. You can also monitor the data in real time by selecting "M". If you select M and are monitoring the inverter room DAS, you will not see all of the data channels because the default setting for GraphTerm is to display only the first 12 data channels. You can increase this by typing "L" for L)ocations in the monitoring screen, then type "1..31". This will cause GraphTerm to display all of the inverter room data.

APPENDIX II: CODE FOR MATLAB PROGRAM NDZFINDER.M

This appendix contains a listing of a MATLAB code which uses phase criteria to plot the approximate NDZs of three islanding prevention methods. This code was used for a portion of the work under Subtask 2.2.

```
%=================================================================
%  GeneralNDZFinder.M
%
%  Mike Ropp
%  06.16.98
%  (ALWAYS back up your files!)
%
%  M-file to find the NDZs of several islanding prevention methods
%  based on phase criteria.
%=================================================================

clear all

%=================================================================
% U   U   SSS   EEEE   RRRR      IIIII  N    N PPPP  U   U  TTTTT  SSS
% U   U  S      E      R   R       I     NN   N P  P U   U    T   S
% U   U  SSSS   EEEE   RRRR        I     N N  N PPPP U   U    T   SSSS
% U   U     S   E      R   R       I     N  N N P    U   U    T      S
%  UUU   SSS   EEEE   R   R      IIIII  N   NN P     UUU     T    SSS
%-----------------------------------------------------------------
%  User input section:  the user needs to set the variables
%  in this section to whatever values are desired.
%-----------------------------------------------------------------

%Rmx=[3.6 14.4 57.6];                %Load resistance (ohms)

LineFreq=60;           %Utility line frequency (Hz)
UpperFreqThresh=60.5;
LowerFreqThresh=59.5;

IslStopMethod=menu('For which method do you want the
NDZ?','OFR/UFR','PJD','AFD');

RInPrompt={'Enter an array of resistances to be tested (ohms).'};
RInTitle='Load resistances';
RInLineNo=1;
RInDef={'[3.6 14.4 57.6]'};
RInInp=inputdlg(RInPrompt,RInTitle,RInLineNo,RInDef);
Rmx=str2num(RInInp{1});

OutMx=[];

switch IslStopMethod
```

```matlab
case 1,
    Prompt1={'Smallest inductance (enter only the power of ten desired)',...
            'Largest inductance (enter only the power of ten desired)',...
            'Upper frequency threshold (Hz)','Lower frequency threshold (Hz)'};
    Title1='OFR/UFR parameters';
    LineNo1=1;
    Def1={'-5','0','60.5','59.5'};
    Inp=inputdlg(Prompt1,Title1,LineNo1,Def1);
    L=logspace(str2num(Inp{1}),str2num(Inp{2}),100);
    UpperFreqThresh=str2num(Inp{3});
    LowerFreqThresh=str2num(Inp{4});
case 2,
    Prompt2={'Smallest inductance (enter only the power of ten desired)',...
            'Largest inductance (enter only the power of ten desired)',...
            'Phase trip threshold (degrees)'};
    Title2='PJD parameters';
    LineNo2=1;
    Def2={'-5','0','2'};
    Inp=inputdlg(Prompt2,Title2,LineNo2,Def2);
    L=logspace(str2num(Inp{1}),str2num(Inp{2}),100);
    PhaseTol=str2num(Inp{3});
case 3,
    Prompt3={'Smallest inductance (enter only the power of ten desired)',...
            'Largest inductance (enter only the power of ten desired)',...
            'Upper frequency threshold (Hz)','Lower frequency threshold (Hz)',...
            'Chopping fraction (fraction, not percent)'};
    Title3='AFD parameters';
    LineNo3=1;
    Def3={'-5','0','60.5','59.5','0.05'};
    Inp=inputdlg(Prompt3,Title3,LineNo3,Def3);
    L=logspace(str2num(Inp{1}),str2num(Inp{2}),100);
    UpperFreqThresh=str2num(Inp{3});
    LowerFreqThresh=str2num(Inp{4});
    ChopFrac=str2num(Inp{5});
end

RadLineFreq=2*pi*LineFreq;              %Convert line frequency to radians/sec
UpThreshRad=UpperFreqThresh*2*pi;
LoThreshRad=LowerFreqThresh*2*pi;
CRes=1./(RadLineFreq^2.*L);            %Finds resonant capacitor for each L.   (Note:
                                       %it's a mx.)


%  That's the end of the user inputs.
%===================================================================

%===================================================================
%  Main program
%  Finds NDZs for each method using phase criteria.
%===================================================================
for RInd=1:length(Rmx),
    R=Rmx(RInd);

    switch IslStopMethod
    case 1,   %OFR/UFR
        Cupper=1./(LoThreshRad^2*L);
```

```
      Clower=1./(UpThreshRad^2*L);
   case 2,   %PJD
      Cupper=1/LoThreshRad*(1./(LoThreshRad*L)+1/R*tan(PhaseTol*pi/180));
      Clower=1/UpThreshRad*(1./(UpThreshRad*L)+1/R*tan(-PhaseTol*pi/180));
   case 3,   %AFD
      Cupper=1/LoThreshRad*(1./(LoThreshRad*L)+1/R*tan(pi/2*ChopFrac));
      Clower=1/UpThreshRad*(1./(UpThreshRad*L)+1/R*tan(pi/2*ChopFrac));
   end

   CupperNorm=Cupper./CRes;
   ClowerNorm=Clower./CRes;
   OutMx=[OutMx; CupperNorm; ClowerNorm];
end

figure(1)
semilogx(L,OutMx);grid;xlabel('Inductance (H)');…
      ylabel('Normalized capacitance; C/Cres');
axis([10^str2num(Inp{1}) 10^str2num(Inp{2}) 0.95 1.2]);
%save d:\mer\COutMx.dat COutMx -ascii;
```

APPENDIX III: CODE FOR MATLAB PROGRAM AFD.M

This appendix contains a listing of the MATLAB code for the basic simulation
engine for the AFD anti-islanding method. This code is described under Subtask 2.3.
Several modifications of this basic simulation engine were used in the work; however,
for brevity, only this basic version is included here. All others may be derived from it.

```
%==================================================================================
%
%    AFD.M
%
%    Mike Ropp
%    REwritten 08.26.97
%    Always back up your files!
%
%    M-file to model the islanded behavior of a PV inverter.
%----------------------------------------------------------------------------------
%    Islanding prevention method:  AFD
%    Positive feedback implementation:  none
%    Load model:  constant-parameter parallel RLC, implemented using difference %
equations
%    iPV harmonics capability:  yes
%    Vutil harmonics capability:  yes
%    Va noise capability:  no
%    ZCD input filtering:  no
%    ZCD linear interpolation:  yes
%    Converter model:  ideal signal source
%==================================================================================

clear all

%----------------------------------------------------------------------------------
% Parallel RLC load model variables--user chooses these
Ll=1e-2;                  % Load inductance (H)
Cl=7.03e-4;               % Load capacitance (F)
Rl=14.4;                  % Load resistance (ohms)--4kW load @ 240 Vrms = 14.4
ohms
%----------------------------------------------------------------------------------

% Note:  to make it island, try Cl = 7.036e-3 F, Ll = 0.001 H.

%----------------------------------------------------------------------------------
% PV Model parameters
%----------------------------------------------------------------------------------

iPVAmp=27;                % Amplitude (NOT RMS!!!) of PV output current wave (A).
i3Amp=iPVAmp*0;           % 3rd harmonic amplitude
i5Amp=iPVAmp*0;           % 5th harmonic amplitude
```

```
i7Amp=iPVAmp*0;          %   7th harmonic amplitude
ChopFrac=0.0;            %   Chopping fraction; fraction of current zero time
                         %   per half-cycle.


%-----------------------------------------------------------------------
%  Utility parameters
%-----------------------------------------------------------------------

RMSUtilVoltageAmp=240;        %   RMS utility voltage amplitude
UtilVoltageAmp=sqrt(2)*RMSUtilVoltageAmp;
UtilityOffInd=3994;           %   Time-vector index at which the utility is shut
                              %   off.
                              %   Current UtilityOffInd:  Two complete cycles,
                              %   then 95% of next
                              %   cycle (position of UtilityOffInd in cycle #3 =
                              %   0.95).
UtilFreq=60;                  %   Nominal utility frequency (Hz).
Va3Amp=UtilVoltageAmp*0;      %   3rd harmonic amplitude of utility voltage
Va5Amp=UtilVoltageAmp*0;      %   5th harmonic amplitude of utility voltage
Va7Amp=UtilVoltageAmp*0;      %   7th harmonic amplitude of utility voltage
MeasLineFreq=UtilFreq;
MeasLineFreqVec(1)=MeasLineFreq;


%-----------------------------------------------------------------------
%  Flow control
%-----------------------------------------------------------------------

NumLineCycles=10;        %   This sets the length of the simulation; see the
                         %   end of the next section where the variable
                         %   "SimLength" is defined.



%-----------------------------------------------------------------------
%  Initialization
%-----------------------------------------------------------------------

NumPts=2^10;             %   Number of points per half cycle.  This is set as
                         %   a power of 2 because most of these inverters use
                         %   a binary counter with N points per half-cycle and
                         %   a look-up table to define their sine-wave references.
                         %   Watch the sample rate; most inverters won't be able
                         %   to use more than about 2^8 or 2^10 points per half-
                         %   cycle.
TimeInd=1;
TimeVec(1)=0;
PVInd=0;
ZeroCross(1)=0;
PrevZeroCross=(1/UtilFreq)/(2*NumPts);
ZCInd=1;
iPV(1)=0;
iL(1)=-UtilVoltageAmp*(1/(MeasLineFreq*2*pi))*(1/Ll); %Inductor current
                                                      %initial condition
%iL(1)=0;
SimLength=(1/UtilFreq)*NumLineCycles;   %   Simulation length is converted from
                                        %   a number
```

```
                                         %  of cycles to a length of time in this
line
ZCIndVec=[0];

h=waitbar(0,'% Completed');

%========================================================================
%  Main program
%
%  There are three separate counters, or indices, in this loop.  One,
%  TimeInd, is the index used in the timing (increment of the time
%  vector).  Another, PVInd, increments the sine-wave reference in the
%  inverter model.  The third, ZCInd, numbers the zero crossings of
%  Va.
%========================================================================

while TimeVec(TimeInd)<=SimLength,
    waitbar(TimeVec(TimeInd)/SimLength);
    PVInd=PVInd+1;
    TimeInd=TimeInd+1;
    delta_t=(1/(2*MeasLineFreq))*(1/NumPts);
    TimeVec(TimeInd)=TimeVec(TimeInd-1)+delta_t;

    %-------------------------------------------------------------------
    %Inverter model--frequency-shifted sine output waveform
    %  (The two if-else blocks simulate the two states of the unfolding
    %  bridge.)
    if PVInd<=NumPts,
        if (PVInd/NumPts)<=(1-ChopFrac),
            i3(TimeInd)=i3Amp*sin((3*PVInd/(NumPts*(1-ChopFrac)))*pi);
            i5(TimeInd)=i5Amp*sin((5*PVInd/(NumPts*(1-ChopFrac)))*pi);
            i7(TimeInd)=i7Amp*sin((7*PVInd/(NumPts*(1-ChopFrac)))*pi);
            iPV(TimeInd)=iPVAmp*sin((PVInd/(NumPts*...
            (1-ChopFrac)))*pi)+i3(TimeInd)+i5(TimeInd)+i7(TimeInd);
        else
            iPV(TimeInd)=0;
        end
    end
    if PVInd>NumPts,
        if ((PVInd-NumPts)/NumPts)<=(1-ChopFrac),
            i3(TimeInd)=-i3Amp*sin((3*(PVInd-NumPts)/(NumPts*(1-ChopFrac)))*pi);
            i5(TimeInd)=-i5Amp*sin((5*(PVInd-NumPts)/(NumPts*(1-ChopFrac)))*pi);
            i7(TimeInd)=-i7Amp*sin((7*(PVInd-NumPts)/(NumPts*(1-ChopFrac)))*pi);
            iPV(TimeInd)=-iPVAmp*sin(((PVInd-NumPts)/(NumPts*(1-
ChopFrac)))*pi)+i3(TimeInd)+i5(TimeInd)+i7(TimeInd);
        else
            iPV(TimeInd)=0;
        end
    end

    %-------------------------------------------------------------------
    %Load and Va model
    if TimeInd<=UtilityOffInd,
        Va3(TimeInd)=Va3Amp*sin((3*UtilFreq*2*pi)*TimeVec(TimeInd));
        Va5(TimeInd)=Va5Amp*sin((5*UtilFreq*2*pi)*TimeVec(TimeInd));
        Va7(TimeInd)=Va7Amp*sin((7*UtilFreq*2*pi)*TimeVec(TimeInd));
```

224

```
Va(TimeInd)=UtilVoltageAmp*sin((UtilFreq*2*pi)*TimeVec(TimeInd))+Va3(TimeInd)+Va
5(TimeInd)+Va7(TimeInd);
        iL(TimeInd)=iL(TimeInd-1)+(1/Ll)*(Va(TimeInd))*(delta_t);
        iC(TimeInd)=Cl*(Va(TimeInd)-Va(TimeInd-1))/delta_t;
        iR(TimeInd)=Va(TimeInd)/Rl;
    else
        iLP=iL(TimeInd-1);
        VaP=Va(TimeInd-1);
        Va(TimeInd)=(iPV(TimeInd)...
            -iLP+(Cl*VaP)/delta_t)/((delta_t/Ll)+(Cl/delta_t)+(1/Rl));
        iL(TimeInd)=iL(TimeInd-1)+(1/Ll)*(Va(TimeInd))*(delta_t);
        iC(TimeInd)=Cl*(Va(TimeInd)-Va(TimeInd-1))/delta_t;
        iR(TimeInd)=Va(TimeInd)/Rl;

    end


    %-------------------------------------------------------------------
    %Negative-to-positive zero crossing (of Va) detector
    if sign(Va(TimeInd-1))<0,
        if sign(Va(TimeInd))>=0,
            ZCInd=ZCInd+1;
            RealZeroCrossTime=TimeVec(TimeInd-1)+(-Va1*(TimeVec(TimeInd)...
                -TimeVec(TimeInd-1))/(Va2-Va1));
            TimeMeasErr(ZCInd)=-TimeVec(TimeInd)+RealZeroCrossTime;
            ZeroCross(ZCInd)=RealZeroCrossTime;
            MeasLineFreq=1/(ZeroCross(ZCInd)-PrevZeroCross);
            MeasLineFreqVec(ZCInd)=MeasLineFreq;
            PrevZeroCross=ZeroCross(ZCInd);
            PVInd=0;
        end

    end

end

iLoad=iR+iL+iC;
iPVprime=iPV/iPVAmp;
Vaprime=Va/UtilVoltageAmp;

%===================================================================
% Output section
%===================================================================

figure(1)
plot(TimeVec,iPVprime,'b:',TimeVec,Vaprime,'k.',...
    TimeVec(UtilityOffInd),iPVprime(UtilityOffInd),'ro');grid;...
    xlabel('Time (sec)');ylabel('Normalized PV current (in blue); normalized
    Va (in black)');

figure(2)
plot(ZeroCross,MeasLineFreqVec,'kd:',TimeVec(UtilityOffInd),UtilFreq,'ro');grid;
xlabel('Time (sec)');ylabel('Frequency (Hz)');

figure(3)
subplot(3,1,1)
```

```
plot(TimeVec,iL,'b.',TimeVec(UtilityOffInd),iL(UtilityOffInd),'ro');...
    grid;xlabel('Time');ylabel('Inductor current');
subplot(3,1,2)
plot(TimeVec,iC,'g.',TimeVec(UtilityOffInd),iC(UtilityOffInd),'ro');...
    grid;xlabel('Time');ylabel('Capacitor current');
subplot(3,1,3)
plot(TimeVec,iR,'k.',TimeVec(UtilityOffInd),iR(UtilityOffInd),'ro');...
    grid;xlabel('Time');ylabel('Resistor current');

figure(4)
plot(TimeVec,iC,'g',TimeVec,iL,'r',TimeVec,iR,'k',TimeVec,Va,'b',...
    TimeVec(UtilityOffInd),Va(UtilityOffInd),'ro');grid;xlabel('Time');
ylabel('iC (green), iL (red), iR (black), Va (blue)');


%   That's more than enough, I think.
```

APPENDIX IV: CODE FOR MATLAB PROGRAM AFDPF.M

This appendix contains a listing of the MATLAB code for the basic simulation engine for the AFDPF anti-islanding method. This code is described under Subtask 2.4. Several modifications of this basic simulation engine were used in the work; however, for brevity, only this basic version is included here. All others may be derived from it.

```
%==========================================================================
%
%     AFDPF.M
%
%     Mike Ropp
%     Edited 03.06.98
%     Always back up your files!
%
%     M-file to model the islanded behavior of a PV inverter.
%--------------------------------------------------------------------------
%     Islanding prevention method:  AFDPF
%     Positive feedback implementation:  cf(k)=cf(k-1)+ChopGain*(MeasLineFreq-
%     UtilFreq)^n.
%        Feedback is applied to cf, not to iPV frequency.
%     Load model:  constant-parameter parallel RLC, implemented using difference
%     equations
%     iPV harmonics capability:  yes
%     Vutil harmonics capability:  yes
%     Va noise capability:  yes
%     ZCD input filtering:  no
%     ZCD linear interpolation:  yes
%     Converter model:  ideal signal source
%==========================================================================

clear all

%--------------------------------------------------------------------------
%  Parallel RLC load model variables--user chooses these
Ll=1.74e-1;            %   Load inductance (H)
Cl=4.075e-5;           %   Load capacitance (F)
Rl=248;                %   Load resistance (ohms)--4kW load @ 240 Vrms = 14.4
                       %   ohms
%--------------------------------------------------------------------------

%  Note:  to make it island, try Cl = 7.036e-3 F, Ll = 0.001 H.

%--------------------------------------------------------------------------
%  PV Model parameters
%--------------------------------------------------------------------------

iPVAmp=0.4*sqrt(2);  %  Amplitude (NOT RMS!!!) of PV output current wave (A).
```

```
InitChopFrac=0.0;
ChopFrac=InitChopFrac;%   Chopping fraction; fraction of current zero time
                      %   per half-cycle.
ChopGain=0.02;
UpperChopThreshold=0.5;
LowerChopThreshold=-0.5;
FeedbackExp=1;
%----------------------------------------------------------------------
%   Utility parameters
%----------------------------------------------------------------------

RMSUtilVoltageAmp=120;        %   RMS utility voltage amplitude
UtilVoltageAmp=sqrt(2)*RMSUtilVoltageAmp;
UtilityOffInd=5400;           %   Time-vector index at which the utility is shut
                              %   off.
                              %   Current UtilityOffInd:  3/4 into cycle #3.
UtilFreq=60;                  %   Nominal utility frequency (Hz).
MeasLineFreq=UtilFreq;
MeasLineFreqVec(1)=MeasLineFreq;
VaNoise=UtilVoltageAmp*0.0*(2*(rand-0.5));

%----------------------------------------------------------------------
%   Flow control
%----------------------------------------------------------------------

NumLineCycles=60;       %   This sets the length of the simulation; see the
                        %   end of the next section where the variable
                        %   "SimLength" is defined.



%----------------------------------------------------------------------
%   Initialization
%----------------------------------------------------------------------

NumPts=2^10;              %   Number of points per half cycle.  This is set as
                          %   a power of 2 because most of these inverters use
                          %   a binary counter with N points per half-cycle and
                          %   a look-up table to define their sine-wave references.
                          %   Watch the sample rate; most inverters won't be able
                          %   to use more than about 2^8 or 2^10 points per half-
                          %   cycle.
TimeInd=1;
TimeVec(1)=0;
PVInd=0;
ZeroCross(1)=0;
PrevZeroCross=0;
%PrevZeroCross=(1/UtilFreq)/(2*NumPts);
ZCInd=1;
iPV(1)=0;
iL(1)=-UtilVoltageAmp*(1/(MeasLineFreq*2*pi))*(1/Ll); %Inductor current
                                                      %initial condition
%iL(1)=0;
SimLength=(1/UtilFreq)*NumLineCycles;   %   Simulation length is converted from
                                        %   a number
                                        %   of cycles to a length of time in
                                        %   this line
```

228

```
ZCIndVec=[0];

h=waitbar(0,'% Completed');
set(h,'name','AFDPF.M');

%=======================================================================
%  Main program
%
%  There are three separate counters, or indices, in this loop.  One,
%  TimeInd, is the index used in the timing (increment of the time
%  vector).  Another, PVInd, increments the sine-wave reference in the
%  inverter model.  The third, ZCInd, numbers the zero crossings of
%  Va.
%=======================================================================

while TimeVec(TimeInd)<=SimLength,
   waitbar(TimeVec(TimeInd)/SimLength);
   PVInd=PVInd+1;
   TimeInd=TimeInd+1;
   delta_t=(1/(2*MeasLineFreq))*(1/NumPts);
   TimeVec(TimeInd)=TimeVec(TimeInd-1)+delta_t;

   %-------------------------------------------------------------------
   %Inverter model--frequency-shifted sine output waveform
   %  (The two if-else blocks simulate the two states of the unfolding
   %  bridge.)
   if PVInd<=NumPts,
       if (PVInd/NumPts)<=(1-ChopFrac),
           iPV(TimeInd)=iPVAmp*sin((PVInd/(NumPts*(1-ChopFrac)))*pi);
       else
           iPV(TimeInd)=0;
       end
   end
   if PVInd>NumPts,
       if ((PVInd-NumPts)/NumPts)<=(1-ChopFrac),
           iPV(TimeInd)=-iPVAmp*sin(((PVInd-NumPts)/(NumPts*(1-ChopFrac)))*pi);
       else
           iPV(TimeInd)=0;
       end
   end

   %-------------------------------------------------------------------
   %Load and Va model
   if TimeInd<=UtilityOffInd,
       Va(TimeInd)=VaNoise+UtilVoltageAmp*sin((UtilFreq*2*pi)*TimeVec(TimeInd));
       iL(TimeInd)=iL(TimeInd-1)+(1/Ll)*(Va(TimeInd))*(delta_t);
       iC(TimeInd)=Cl*(Va(TimeInd)-Va(TimeInd-1))/delta_t;
       iR(TimeInd)=Va(TimeInd)/Rl;
   else
       iLP=iL(TimeInd-1);
       VaP=Va(TimeInd-1);
       Va(TimeInd)=VaNoise+(iPV(TimeInd)-iLP+(Cl*VaP)/delta_t)...
           /((delta_t/Ll)+(Cl/delta_t)+(1/Rl));
       iL(TimeInd)=iL(TimeInd-1)+(1/Ll)*(Va(TimeInd))*(delta_t);
       iC(TimeInd)=Cl*(Va(TimeInd)-Va(TimeInd-1))/delta_t;
       iR(TimeInd)=Va(TimeInd)/Rl;
```

```
        end

    %------------------------------------------------------------------
    %Negative-to-positive zero crossing (of Va) detector
    if sign(Va(TimeInd-1))<0,
        if sign(Va(TimeInd))>=0,
            ZCInd=ZCInd+1;
            RealZeroCrossTime=TimeVec(TimeInd-1)-Va(TimeInd-1)*…
                (TimeVec(TimeInd)-TimeVec(TimeInd-1))/(Va(TimeInd)-Va(TimeInd-1));
            TimeMeasErr(ZCInd)=-TimeVec(TimeInd)+RealZeroCrossTime;
            ZeroCross(ZCInd)=RealZeroCrossTime;
            MeasLineFreq=1/(ZeroCross(ZCInd)-PrevZeroCross);
            MeasLineFreqVec(ZCInd)=MeasLineFreq;
            PrevZeroCross=ZeroCross(ZCInd);
            PVInd=0;
            NextChopFrac=InitChopFrac+ChopGain*…
                (MeasLineFreq-UtilFreq)^FeedbackExp;
            SignFlag=sign(NextChopFrac);
            if NextChopFrac>=UpperChopThreshold|NextChopFrac<=LowerChopThreshold,
                if ChopFrac<UpperChopThreshold|ChopFrac>LowerChopThreshold,
                    SatTimeInd=TimeInd;
                    SatTime=RealZeroCrossTime;
                end
                if SignFlag<0,
                    NextChopFrac=LowerChopThreshold;
                elseif SignFlag>0,
                    NextChopFrac=UpperChopThreshold;
                end
            end
            ChopFrac=NextChopFrac;
        end
    end

end

close(h);

OutMx=[ZeroCross;MeasLineFreqVec];
save d:\mer\OutMx.dat OutMx -ascii;

iLoad=iR+iL+iC;
iPVprime=iPV/iPVAmp;
Vaprime=Va/UtilVoltageAmp;

%==================================================================
%  Output section
%==================================================================

figure(1)
plot(TimeVec,iPVprime,'b:',TimeVec,Vaprime,'k.',…
    TimeVec(UtilityOffInd),iPVprime(UtilityOffInd),'ro');…
    grid;xlabel('Time (sec)');ylabel('Normalized PV current (in blue);
    normalized Va (in black)');

figure(2)
```

230

```
plot(ZeroCross,MeasLineFreqVec,'kd:',TimeVec(UtilityOffInd),UtilFreq,'ro');…
    grid;xlabel('Time (sec)');ylabel('Frequency (Hz)');

figure(3)
subplot(3,1,1)
plot(TimeVec,iL,'b.',TimeVec(UtilityOffInd),iL(UtilityOffInd),'ro');…
    grid;xlabel('Time');ylabel('Inductor current');
subplot(3,1,2)
plot(TimeVec,iC,'g.',TimeVec(UtilityOffInd),iC(UtilityOffInd),'ro');…
    grid;xlabel('Time');ylabel('Capacitor current');
subplot(3,1,3)
plot(TimeVec,iR,'k.',TimeVec(UtilityOffInd),iR(UtilityOffInd),'ro');…
    grid;xlabel('Time');ylabel('Resistor current');

figure(4)
plot(TimeVec,iC,'g',TimeVec,iL,'r',TimeVec,iR,'k',TimeVec,Va,'b',…
    TimeVec(UtilityOffInd),Va(UtilityOffInd),'ro');grid;xlabel('Time');
ylabel('iC (green), iL (red), iR (black), Va (blue)');


%  Whew!  Made it.  That's the end.
```

APPENDIX V: CODE FOR MATLAB PROGRAM

AFDPFSTATEEQUSMODELBATCHMODE.M

This appendix contains a listing of the MATLAB code used to simulate the transient response of the system shown in Figure 66. It illustrates the use of MATLAB's state equations solver, conversion of a continuous system to a discrete-time system, and the necessary setup (loops) to run the program in batch mode.

```
%=========================================================================
%
%    AFDPFStateEqsModelBatchMode.M
%
%    Mike Ropp
%    Edited 09.15.98
%    Always back up your files!
%
%    M-file to model the islanded behavior of a PV inverter.
%-------------------------------------------------------------------------
%    Islanding prevention method:  AFDPF
%    Positive feedback implementation:  cf(k)=cf(k-1)+ChopGain*(MeasLineFreq-
%    UtilFreq)^n.
%      Feedback is applied to cf, not to iPV frequency.
%    Load model:  constant-parameter parallel RLC, implemented using state
%    equations
%    Utility impedance included:  yes
%    iPV harmonics capability:  yes
%    Vutil harmonics capability:  yes
%    Vutil noise capability:  yes
%    ZCD input filtering:  no
%    ZCD linear interpolation:  yes
%    Converter model:  ideal signal source
%=========================================================================

clear all

LuMx=[169e-6 162e-6 115e-6 100e-6 57e-6];
RuMx=[135e-3 77.3e-3 36.3e-3 22.2e-3 15e-3];
ChopGainMx=[0 0.001 0.01 0.1];
FreqOutMx=[];
VOutMx=[];
TimeVecMx=[];
FreqOutMx2=[];
VOutMx2=[];
```

```
TimeVecMx2=[];

h=waitbar(0,'% Completed');
set(h,'name','AFDPFStateEqsModelBatchMode.M');

for UInd=1:length(LuMx),
    waitbar(UInd/length(LuMx));
    for CGInd=1:length(ChopGainMx),
        CGInd

        %-------------------------------------------------------------------
        %  Parallel RLC load model variables--user chooses these
        Ll=1e-2;                    %  Load inductance (H)
        Cl=7.036e-4;                %  Load capacitance (F)
        Rl=14.4;                    %  Load resistance (ohms)--4kW load @ 240 Vrms =
                                    %  14.4 ohms
        %-------------------------------------------------------------------

        %  Note:  to make it island, try Cl = 7.036e-3 F, Ll = 0.001 H.


        %-------------------------------------------------------------------
        %  PV Model parameters
        %-------------------------------------------------------------------

        iPVAmp=240/Rl*sqrt(2);      %  Amplitude (NOT RMS!!!) of PV output current
                                    %  wave (A).
        InitChopFrac=0.0;           %  Starting cnopping fraction.
        ChopFrac=InitChopFrac;      %  Chopping fraction; fraction of current zero
                                    %  time
        %  per half-cycle.
        ChopGain=ChopGainMx(CGInd);              %  Gain coefficient in AFDPF
                                    %  formula.
        UpperChopThreshold=0.5;     %  Thresholds may be set.  If ChopFrac reaches
                                    %  either
        LowerChopThreshold=-0.5;    %  threshold, it will saturate at that value.
        FeedbackExp=1;
        %-------------------------------------------------------------------
        %  Utility parameters
        %-------------------------------------------------------------------

        RMSUtilVoltage=240;         %  RMS utility voltage amplitude
        UtilVoltageAmp=sqrt(2)*RMSUtilVoltage;
        UtilityOffInd=1e10;         %  Time-vector index at which the utility is
                                    %  shut off.
        %  Enter a negative number to disable.
        LoadJumpPoint=2^8*2*15;
        UtilFreq=60;                %  Nominal utility frequency (Hz).
        MeasLineFreq=UtilFreq;
        MeasLineFreqVec=[];
        MeasLineFreqVec(1)=MeasLineFreq;
        VutilNoise=UtilVoltageAmp*0.0*(2*(rand-0.5));

        Lu=LuMx(UInd);
        Ru=RuMx(UInd);

        VutilStartPhase=-0*atan((Lu*2*60*pi)/Ru);
```

233

```matlab
Vutil(1)=UtilVoltageAmp*sin(VutilStartPhase);

%------------------------------------------------------------------------
%  Flow control
%------------------------------------------------------------------------

NumLineCycles=30;       %  This sets the length of the simulation; see the
%  end of the next section where the variable
%  "SimLength" is defined.



%------------------------------------------------------------------------
%  Initialization
%------------------------------------------------------------------------

NumPts=2^8;                 %  Number of points per half cycle.  This is set as
%   a power of 2 because most of these inverters use
%   a binary counter with N points per half-cycle and
%   a look-up table to define their sine-wave references.
%   Watch the sample rate; most inverters won't be able
%   to use more than about 2^8 or 2^10 points per half-
%   cycle.
TimeInd=1;
TimeVec(1)=0;
PVInd=0;
ZeroCross(1)=0;
PrevZeroCross=0;
%PrevZeroCross=(1/UtilFreq)/(2*NumPts);
ZCInd=1;
iPV(1)=0;
SimLength=(1/UtilFreq)*NumLineCycles;  %  Simulation length is converted
%   from a number
%   of cycles to a length of time in this line
VaSumForRMS=0;
Vrms=[];
Vrms(1)=RMSUtilVoltage;
IUtilSumForRMS=0;
IUtilrms(1)=0;
ZCIndVec=[0];



%------------------------------------------------------------------------
%  Build state matrices
%------------------------------------------------------------------------
delta_t=(1/(2*UtilFreq))*(1/NumPts);
A=[0 1/Ll 0
   -1/Cl -1/(Rl*Cl) 1/Cl
   0 -1/Lu -Ru/Lu];

B=[0 0
   1/Cl 0
   0 1/Lu];

[Ad,Bd]=c2d(A,B,delta_t);
```

```
x=[-(2*pi*UtilFreq*UtilVoltageAmp*Cl);0;0*iPVAmp/2];
%  To get the initial conditions, assume that at the rising zero crossing
%  of Va (which
%  is where the simulation starts) the inductor current is approximately
%  equal to the
%  opposite of the capacitor current (they're resonating and the resistor
%  current = 0
%  since it's a voltage zero crossing).  That gives x(1) at t=0.  x(2) at
%  t = 0 is assumed
%  zero (zero crossing of Va).


%=======================================================================
%  Main program
%
%  There are three separate counters, or indices, in this loop.  One,
%  TimeInd, is the index used in the timing (increment of the time
%  vector).  Another, PVInd, increments the sine-wave reference in the
%  inverter model.  The third, ZCInd, numbers the zero crossings of
%  Va.
%=======================================================================

while TimeVec(TimeInd)<=SimLength,
    PVInd=PVInd+1;
    TimeInd=TimeInd+1;
    TimeVec(TimeInd)=TimeVec(TimeInd-1)+delta_t;
    %  These next "if" blocks change the state matrices to account for
    %  utility cutoff
    %  or a step change in the load parameters.
    if TimeInd==UtilityOffInd,
        A=[0 1/Ll
            -1/Cl -1/Rl*Cl];

        B=[0
            1/Cl];
        [Ad,Bd]=c2d(A,B,delta_t);
    end
    if TimeInd==LoadJumpPoint,
        Rl=Rl*5;
        Ll=Ll*5;
        Cl=Cl/5;

        A=[0 1/Ll 0
            -1/Cl -1/(Rl*Cl) 1/Cl
            0 -1/Lu -Ru/Lu];

        B=[0 0
            1/Cl 0
            0 1/Lu];
        [Ad,Bd]=c2d(A,B,delta_t);
    end


    %---------------------------------------------------------------
    %Inverter model--frequency-shifted sine output waveform
    %  (The two if-else blocks simulate the two states of the unfolding
    %  bridge.)
```

235

```
if PVInd<=NumPts,
    if (PVInd/NumPts)<=(1-ChopFrac),
        iPV(TimeInd)=iPVAmp*sin((PVInd/(NumPts*(1-ChopFrac)))*pi);
    else
        iPV(TimeInd)=0;
    end
end
if PVInd>NumPts,
    if ((PVInd-NumPts)/NumPts)<=(1-ChopFrac),
        iPV(TimeInd)=-iPVAmp*sin(((PVInd-NumPts)/(NumPts*(1-
        ChopFrac)))*pi);
    else
        iPV(TimeInd)=0;
    end
end


%-------------------------------------------------------------------
%Load and Va model
if TimeInd<UtilityOffInd,
    Vutil(TimeInd)=VutilNoise+UtilVoltageAmp...
        *sin((UtilFreq*2*pi)*TimeVec(TimeInd)+VutilStartPhase);
    x(:,TimeInd)=Ad*x(:,TimeInd-1)+Bd*[iPV(TimeInd);Vutil(TimeInd)];
else
    x(1:2,TimeInd)=Ad*x(1:2,TimeInd-1)+Bd*[iPV(TimeInd)];
    x(3,TimeInd)=0;
end

VaSumForRMS=VaSumForRMS+x(2,TimeInd)^2*delta_t;
IUtilSumForRMS=IUtilSumForRMS+x(3,TimeInd)^2*delta_t;



%-------------------------------------------------------------------
%Negative-to-positive zero crossing (of Va) detector
if sign(x(2,TimeInd-1))<0,
    if sign(x(2,TimeInd))>=0,
        ZCInd=ZCInd+1;
        RealZeroCrossTime=TimeVec(TimeInd-1)-x(2,TimeInd-1)*...
            (TimeVec(TimeInd)-TimeVec(TimeInd-1))/(x(2,TimeInd)-
            x(2,TimeInd-1));
        TimeMeasErr(ZCInd)=-TimeVec(TimeInd)+RealZeroCrossTime;
        ZeroCross(ZCInd)=RealZeroCrossTime;
        MeasLineFreq=1/(ZeroCross(ZCInd)-PrevZeroCross);
        MeasLineFreqVec(ZCInd)=MeasLineFreq;
        PrevZeroCross=ZeroCross(ZCInd);
        PVInd=0;
        NextChopFrac=InitChopFrac+ChopGain*(MeasLineFreq-
            UtilFreq)^FeedbackExp;
        SignFlag=sign(NextChopFrac);
        if
NextChopFrac>=UpperChopThreshold|NextChopFrac<=LowerChopThreshold,
            if ChopFrac<UpperChopThreshold|ChopFrac>LowerChopThreshold,
                SatTimeInd=TimeInd;
                SatTime=RealZeroCrossTime;
            end
            if SignFlag<0,
                NextChopFrac=LowerChopThreshold;
```

```
                    elseif SignFlag>0,
                        NextChopFrac=UpperChopThreshold;
                    end
                end
                ChopFrac=NextChopFrac;
                Vrms(ZCInd)=sqrt(1/(ZeroCross(ZCInd)-ZeroCross(ZCInd-
                        1))*(VaSumForRMS));
                VaSumForRMS=0;
                IUtilrms(ZCInd)=sqrt(1/(ZeroCross(ZCInd)-ZeroCross(ZCInd-
                        1))*(IUtilSumForRMS));
                IUtilSumForRMS=0;
            end
        end


    end

    FreqOutMx2=[FreqOutMx2; ChopGain Lu MeasLineFreqVec];
    VOutMx2=[VOutMx2; ChopGain Lu Vrms];
    TimeVecMx2=[TimeVecMx2;ChopGain Lu ZeroCross];

%       FHighOutMx(UInd,CGInd)=max(MeasLineFreqVec);
%       FLowOutMx(UInd,CGInd)=min(MeasLineFreqVec);
%       VHighOutMx(UInd,CGInd)=max(Vrms(15:length(Vrms)));
%       VLowOutMx(UInd,CGInd)=min(Vrms(15:length(Vrms)));
%       VFinalOutMx(UInd,CGInd)=Vrms(length(Vrms));

    end
end

save c:\mer\FreqOutMx2.dat FreqOutMx -ascii;
save c:\mer\VOutMx2.dat VOutMx -ascii;
save c:\mer\TimeVecMx2.dat TimeVecMx -ascii;


%save c:\mer\FreqOutMx.dat FreqOutMx -ascii;
%save c:\mer\VOutMx.dat VOutMx -ascii;
%save c:\mer\TimeVecMx.dat TimeVecMx -ascii;
%save c:\mer\FLowOutMx.dat FLowOutMx -ascii;
%save c:\mer\FHighOutMx.dat FHighOutMx -ascii;
%save c:\mer\VLowOutMx.dat VLowOutMx -ascii;
%save c:\mer\VHighOutMx.dat VHighOutMx -ascii;
%save c:\mer\VFinalOutMx.dat VFinalOutMx -ascii;
close(h);
```

PUBLICATIONS RESULTING FROM THIS WORK

1. **M. E. Ropp**, M. Begovic, A. Rohatgi, R. Long, "Roof-Installed Photovoltaic System on the Olympic Swimming Pool at Georgia Tech", in Proceedings of the 13th European Photovoltaic Solar Energy Conference, Oct. 23-27 1995, p. 965-968.

2. M. Begovic, **M. Ropp**, A. Rohatgi, R. Long, "World's Largest PV System on the Roof of the Georgia Tech Aquatic Center", conference paper for Tesla: The Third Millennium, Belgrade, Yugoslavia, October 1996.

3. **M. E. Ropp**, M. Begovic, A. Rohatgi, R. Long, "Design Considerations for Large Roof-Integrated Photovoltaic Arrays", *Progress in Photovoltaics* v. 5 p. 55-67, January/February 1997.

4. M. Begovic, **M. Ropp**, A. Rohatgi, S. Durand, A. Rosenthal, "Monitoring and Data Acquisition for a Large Roof-Mounted Photovoltaic Array", Proceedings of the IEEE Region 3 Conference (SECON '97), Blacksburg, VA, April 12-14 1997, p. 297-300.

5. D. H. Nall, J. R. Hardesty, A. Rohatgi, M. Begovic, **M. Ropp**, "Design and Operation of a 340 kW Utility Coupled Photovoltaic System", in press in the Proceedings of the American Institute of Architects Conference "Environmental and Economic Balance: the 21st Century Outlook", October 1997.

6. M. Begovic, **M. E. Ropp**, A. Rohatgi, R. Long, "Performance Evaluation of the Georgia Tech Aquatic Center Photovoltaic Array", Plenary Session paper, Proceedings of the 14th European Photovoltaic Solar Energy Conference (EPVSEC '97), Barcelona, Spain, p. 374-379.

7. R. Long, A. Rohatgi, M. Begovic, **M. Ropp**, "Photovoltaics in Architecture: The Design, Construction, and Monitoring of a Photovoltaic Power System on the Georgia Institute of Technology Aquatic Center", Proceedings of the 14th European Photovoltaic Solar Energy Conference (EPVSEC '97), Barcelona, Spain, p. 1941-1944.

8. **M. E. Ropp**, M. Begovic, A. Rohatgi, "Determination of the Curvature Mismatch Factor for the Georgia Tech Aquatic Center Photovoltaic Array", Proceedings of the 26th IEEE Photovoltaic Specialists Conference, Sept. 30-Oct. 3, 1997, p. 1297-1300.

9. M. Begovic, **M. E. Ropp**, A. Rohatgi, "Determining the Likelihood of Islanding of Photovoltaic Systems by Modeling and Statistical Analysis", accepted for publication and Plenary Session presentation at the 2nd World Conference on Photovoltaic Energy Conversion, to be held July, 1998, Vienna, Austria.

10. **M. Ropp**, M. Begovic, A. Rohatgi, "Analysis and Performance Assessment of the Active Frequency Drift Method of Islanding Prevention", accepted for Summer 1998 publication in the *IEEE Transactions on Energy Conversion*.

11. **M. E. Ropp**, M. Begovic, A. Rohatgi, "Prevention of Islanding in Grid-Connected Photovoltaic Systems", accepted for 1998 publication in *Progress in Photovoltaics*.

BIBLIOGRAPHY

[1] J.C. Lee, V. M. Fthenakis, S. C. Morris, G. A. Goldstein, P. D. Moskowitz, "Projected Photovoltaic Energy Impacts on U.S. CO_2 Emissions: An Integrated Energy-Environmental-Economic Analysis", *Progress in Photovoltaics* **5**(4) Jul-Aug 1997, p. 277-285.

[2] G. Almonacid, G. Nofuentes, J. D. Aguilar, J. de la Casa, A. Garrido, "Estimation of the Effects of an Intensive Solar Intervention in the Historical Centre of Jaen (Spain)", *Progress in Photovoltaics* **3**(3) May-Jun 1995, p. 197-209.

[3] M. Tatsuta, "New Sunshine Project and New Trend of PV R&D Program in Japan", *Renewable Energy* **8**(1-4) pt. 1, May-Aug 1996, p. 40-43.

[4] B. Decker, U. Jahn, "Performance of 170 Grid-Connected PV Plants in Northern Germany—Analysis of Yields and Optimization Potentials", *Solar Energy* **59**(4-6) pt. 4, Apr-Jun 1997, p. 127-133.

[5] U.S. Department of Energy Press Release, "Million Solar Roofs Initiative Responds to Global Climate Change, Strengthens American Solar Power Industry", June 27, 1997.

[6] Typical Meteorological Year User's Manual. National Climatic Data Center publication TD-9734, reprinted August 1988.

[7] W. Marion and K. Urban, User's Manual for TMY2s. National Renewable Energy Laboratory, June 1995.

[8] R. Hulstrom, ed., Solar Resources, MIT Press, Cambridge MA, 1989.

[9] S. R. Wenham, M. A. Green, M. E. Watt, Applied Photovoltaics, Centre for Photovoltaic Devices and Systems, University of New South Wales, Australia, 1994.

[10] R. Perez, R. Seals, P. Ineichen, R. Stewart, D. Menicucci, "A New Simplified Version of the Perez Diffuse Irradiance Model for Tilted Surfaces", *Solar Energy* **39**(3) 1987, p. 221-231.

[11] H. Häberlin, C. Beutler, "Highest Grid-Connected PV Plant in the World at Jungfraujoch (3454m): Excellent Performance in the First Two Years of Operation", *13th EPVSEC*, October 23-27 1995, P. 969-972.

[12] P. Ineichen, R. Perez, R. Seals, "The Importance of Correct Albedo Determination for Adequately Modeling Energy Received by Tilted Surfaces", *Solar Energy* **39**(4) 1987, p. 301-305.

[13] R. Perez, J. Doty, B. Bailey, R. Stewart, "Experimental Evaluation of a Photovoltaic Simulation Program", *Solar Energy* **52**(4) 1994, p. 359-365.

[14] S. Rahman, B. H. Chowdhury, "Simulation of Photovoltaic Power Systems and Their Performance Prediction", *IEEE Transactions on Energy Conversion* **3**(3) September 1988, p. 440-446.

[15] G. W. Braun, D. Kearney, D. S. Shugar, "Comparison of Bulk Power Solar Peaking Options in the 1990s", *Solar Energy Materials* **24**(1-4), December 2, 191, p. 108-120.

[16] J. F. Jockell, S. Rahman, "Application of High-Resolution Insolation Data for Photovoltaic System Design Analysis", *IEEE Southeastcon* 1989 v.3, p. 1430-1435.

[17] D. A. Bergman, M. C. Russell, "Off-Azimuth Photovoltaic Performance and Insolation Study", *18th IEEE PVSC* 1985, p. 240-245.

[18] J. W. Bishop, "Computer Simulation of the Effects of Electrical mismatch in Photovoltaic Interconnection Circuits", *Solar Cells* **25**(1), October 1988, p. 73-89.

[19] A. Rosenthal, Southwest Technology Development Institute at New Mexico State University, personal communication.

[20] J. Wiles, Southwest Technology Development Institute at New Mexico State University, personal communication.

[21] M. A. Green, Solar Cells, Prentice-Hall Inc., Englewood Cliffs NJ 1982, p. 81.

[22] Liu, B. Y. H, Jordan, R. C., "The Interrelationship and Characteristic Distribution of Direct, Diffuse and Total Solar Radiation", *Solar Energy* v. 4 no. 3, July 1960, p. 1-19.

[23] J. C. Wiles, *Photovoltaic Power Systems and the National Electric Code: Suggested Practices*, Photovoltaic Design Assistance Center, Sandia National Laboratories, March 1995.

[24] D. F. Menicucci, J. P. Fernandez, *User's Manual for PVFORM: Photovoltaic System Simulation Program for Stand-Alone and Grid-Interactive Applications*, Sandia National Laboratories publication SAND85-0376, October 1989.

[25] M. Buresch, Photovoltaic Power Systems, McGraw-Hill 1981.

[26] A. Kitamura, M. Okamoto, F. Yamamoto, K. Nakaji, H. Matsuda, K. Hotta, "Islanding Phenomenon Elimination Study at Rokko Test Center", Proceedings of the 1st IEEE World Conference on Photovoltaic Energy Conversion (1994) pt. 1, p. 759-762.

[27] A. Kitamura, M. Okamoto, K. Hotta, K. Takigawa, H. Kobayashi, Y. Ariga, "Islanding Prevention Measures: Demonstration Testing at Rokko Test Center for Advanced Energy Systems", Proceedings of 23rd IEEE Photovoltaic Specialists Conference (1993), p. 1063-1067.

[28] T. R. Sims, R. A. Jones, A. F. Imece, "Investigation of Potential Islanding Problems of a Line-Commutated Static Power Converter in Photovoltaic Systems", *IEEE Transactions on Energy Conversion* **5**(3) September 1990, p. 429-435.

[29] R. A. Jones, T. R. Sims, A. F. Imece, "Investigation of Potential Islanding of a Self-Commutated Static Power Converter in Photovoltaic Systems", *IEEE Transactions on Energy Conversion* **5**(4) December 1990, p. 624-631.

[30] A. F. Imece, R. A. Jones, T. R. Sims, C. A. Gross, "An Approach for Modeling Self-Commutated Static Power Converters for Photovoltaic Islanding Studies", *IEEE Transactions on Energy Conversion* **4**(3) September 1989, p. 397-401.

[31] R. A. Jones, T. R. Sims, A. F. Imece, *Investigation of Potential Islanding of Dispersed Photovoltaic Systems*, Sandia National Laboratories report SAND87-7027, Sandia National Laboratories, Albuquerque NM, 1988.

[32] G. Vachtsevanos, H. Kang, "Simulation Studies of Islanded Behavior of Grid-Connected Photovoltaic Systems", *IEEE Transactions on Energy Conversion* **4**(2) June 1989, p. 177-183.

[33] J. Stevens, "Utility Intertied Photovoltaic System Islanding Experiments", Proceedings of the 17th IEEE Photovoltaic Specialists Conference (1987), p. 1134-1138.

[34] P. Longrigg, "Effects on Electrical Distribution Networks of Dispersed Power Generation at High Levels of Connection Penetration", *International Journal of Ambient Energy* **3**(4) October 1992, p. 199-214.

[35] *IEEE-P929: Recommended Practice for Utility Interface of Photovoltaic (PV) Systems*, 7th draft of IEEE Prestandard P929, August 1998.

[36] S. Yuyama, T. Ichinose, K. Kimoto, T. Itami, T. Ambo, C. Okado, K. Nakajima, S. Hojo, H. Shinohara, S. Ioka, M. Kuniyoshi, "A High-Speed Frequency Shift Method as a Protection for Islanding Phenomena of Utility Interactive PV Systems", *Solar Energy Materials and Solar Cells* **35** 1994, p. 477-486.

[37] H. Kobayashi, K. Takigawa, "Statistical Evaluation of Optimum Islanding Preventing Method for Utility Interactive Small Scale Dispersed PV Systems", Proceedings of the First IEEE World Conference on Photovoltaic Energy Conversion (1994), p. 1085-1088.

[38] S. J. Ranade, N. R. Prasad, S. Omick, L. F. Kazda, "A Study of Islanding in Utility-Connected Residential Photovoltaic Systems, Part I: Models and Analytical Methods", *IEEE Transactions on Energy Conversion* **4**(3) Sept 1989, p. 436-445.

[39] R. H. Wills, "The Interconnection of Photovoltaic Systems with the Utility Grid: An Overview for Utility Engineers", a publication of the Sandia National Laboratories Photovoltaic Design Assistance Center, publication number SAND94-1057, October 1994.

[40] H. Kobayashi, K. Takigawa, E. Hashimoto, "Method for Preventing Islanding Phenomenon on Utility Grid with a Number of Small Scale PV Systems", Proceedings of the 21st IEEE Photovoltaic Specialists Conference (1991), p. 695-700.

[41] D. Handran, R. Bass, F. Lambert, J. Kennedy, "Simulation of Distribution Feeders and Charger Installation for the Georgia Tech Olympic Electric Tram System", Proceedings of the 5th IEEE Workshop on Computers in Power Electronics, August 11-14 1996, p. 168-175.

[42] T. E. Grebe, "Application of Distribution System Capacitor Banks and Their Impact on Power Quality", *IEEE Transactions on Industry Applications* 32(3), May/June 1996, p. 714-719.

[43] R. Best, Phase-Locked Loops: Theory, Design, and Applications, 2nd. ed., pub. McGraw-Hill Inc., 1993.

[44] P. V. Brennan, Phase-Locked Loops: Principles and Practice, pub. MacMillan Press Ltd., 1996.

[45] H. Becker, V. Gerhold, E. Ortjohann, B. Voges, J. Voβ, "Entwicklung, Aufbau und erste Testerfahrung mit einer Prüfeinrichtung zum Test der automatischen Netzüberwachung bei netzgekoppelten Wechselrichtern". Paper supplied by Dr. Paul Lynn, managing editor of *Progress in Photovoltaics*. Journal reference unavailable.

[46] G. Kern, "SunSine300: Utility Interactive AC Module Anti-Islanding Test Results", Proceedings of the 26th IEEE Photovoltaic Specialists Conference (1997).

[47] P. Toggweiler, Summary and Conclusions, Proceedings of the IEA-PVPS Task V Workshop "Grid Interconnection of Photovoltaic Systems", September 15-16, 1997, p. 15-17.

[48] B. Jones, Rochester Gas and Electric Co., personal communication.

[49] T. Duffy, Central Hudson Gas and Electric Co., personal communication.

[50] W. Mombauer, K.-H. Keck, "Load Modeling for Harmonic Flow Calculations", *European Transactions on Electrical Power Engineering* **3**(6), Nov.-Dec. 1993, p. 453-460.

[51] T. Shaw, Protection Engineer, Georgia Power Company, personal communication.

[52] Average residential load data supplied by Southern Company Services upon request.

[53] T. Ishida, R. Hagihara, M. Yugo, Y. Makino, "Anti-Islanding Protection Using a Twin-Peak Band-Pass Filter In Interconnected PV Systems, and Substantiating Evaluations", Proceedings of the First World Conference on Photovoltaic Energy Conversion (WCPEC), Dec. 5-9, 1994, p. 1077-1080.

[54] T. Ambo, "Islanding Prevention by Slip-Mode Frequency Shift", Proceedings of the IEA-PVPS Task V Workshop "Grid Interconnection of Photovoltaic Systems", September 15-16, 1997, p. 189-194.

[55] G. H. Atmaram, A. H. Ayoub, J. Benton, W. Bower, "Test Results of Islanding Experiments on Grid-Interactive Residential Power Conditioners", Proceedings of the 15th IEEE Photovoltaic Specialists Conference (1985), p. 1326-1335.

[56] W. Bower, Sandia National Laboratories, personal communication.

[57] J-J. Slotine, W. Li, Applied Nonlinear Control, Prentice-Hall 1991.

[58] B. P. Lathi, Linear Systems and Signals, Berkeley-Cambridge Press 1992.

[59] K. L. Su, Fundamentals of Circuit Analysis, Waveland Press Inc. 1993.

[60] R. Wills, Advanced Energy Systems, Inc., personal communication.

[61] G. Kern, Ascension Technology, Inc., personal communication.

[62] C. Sun, Pacific Gas and Electric Co., personal communication.

[63] G. Kern, "Status Report #6, Sandia Anti-Islanding Investigation", contract report to Sandia National Laboratories, May 27, 1998.

[64] S. Gonzalez, Sandia National Laboratories, personal communication.

[65] A. R. Bergen, Power Systems Analysis, pub. Prentice-Hall, Inc. 1986.

[66] R. W. Erickson, Fundamentals of Power Electronics, pub. Chapman & Hall (International Thompson Publishing) 1997.

[67] C. Bryant, Howard Industries, Inc., personal communication.

[68] A. S. Sedra, K. C. Smith, Microelectronic Circuits, 3rd ed., Saunders College Publishing, 1991.

[69] M. S. Sarma, Electric Machines 2nd ed., pub. West Publishing Co. 1994.

[70] L. Matsch, J. D. Morgan, Electromagnetic and Electromechanical Machines, 3rd ed., pub. Harper and Row 1986.

[71] A.E. Fitzgerald, C. Kingsley, S. D. Umans, Electric Machinery, 5th ed., pub. McGraw-Hill, Inc. 1990.

BIOGRAPHY

Michael Ropp was born on September 26, 1968, on Ellsworth Air Force Base in Rapid City, SD. He grew up in western Nebraska and eastern Wyoming, where he acquired a deep appreciation of nature and a concern about the lack of sustainability in modern American life. Michael attended the University of Nebraska-Lincoln from August 1986 to May 1993, majoring in Music (low brass and low strings) and earning the B.A. in Music in August of 1992. He then entered the Electrical Engineering program at the Georgia Institute of Technology in Atlanta, GA, in June of 1993. He earned his M.S.E.E. in March of 1996, with a minor in Mechanical Engineering. Michael's interests lie within the areas of Energy Conversion, Systems and Controls, and Power Electronics, and his intention is to apply himself to problems relating to a sustainable economy such as renewable energy sources, energy storage, and electric transportation.